Quantitative single molecule imaging deep in biological samples using adaptive optics

Corey Butler

THÈSE PRÉSENTÉE

POUR OBTENIR LE GRADE DE

DOCTEUR DE L'UNIVERSITÉ DE BORDEAUX

ÉCOLE DOCTORALE DES SCIENCES DE LA VIE ET DE LA SANTÉ

SPÉCIALITÉ : **BIOIMAGERIE**

PAR **COREY BUTLER**

QUANTITATIVE SINGLE MOLECULE IMAGING DEEP IN BIOLOGICAL SAMPLES USING ADAPTIVE OPTICS

SOUS LA DIRECTION DE **JEAN-BAPTISTE SIBARITA**

SOUTENUE LE 4 JUILLET 2017

MEMBRES DU JURY

SIBARITA, Jean-Baptiste	Ingénieur de Recherche, *CNRS*	Directeur de Thèse
LEVEQUE-FORT, Sandrine	Directeur de Recherche, *Université Paris-Sud*	Rapporteur
RADENOVIC, Aleksandra	Associate Professor, *EPFL*	Rapporteur
COGNET, Laurent	Directeur de Recherche, *Université de Bordeaux*	Examinateur
LEVECQ, Xavier	Ingénieur, *Imagine Optic*	Examinateur
NAGERL, U Valentin	Professeur, *Université de Bordeaux*	Président

INTERDISCIPLINARY INSTITUTE FOR NEUROSCIENCE
CNRS UMR 5297

Université de Bordeaux – Centre Broca Nouvelle Aquitaine
146 rue Léo-Saignat
33076 Bordeaux, France

Abstract

Optical microscopy is an indispensable tool for research in neurobiology and medicine, enabling studies of cells in their native environment. However, subcellular processes remain hidden behind the resolution limits of diffraction-limited optics which makes structures smaller than ~300nm impossible to resolve. Recently, single molecule localization (SML) and tracking has revolutionized the field, giving nanometer-scale insight into protein organization and dynamics by fitting individual fluorescent molecules to the known point spread function of the optical imaging system. This fitting process depends critically on the amount of collected light and renders SML techniques extremely sensitive to imperfections in the imaging path, called aberrations, that have limited SML to cell cultures on glass coverslips.

A commercially available adaptive optics system is implemented to compensate for aberrations inherent to the microscope, and a workflow is defined for depth-dependent aberration correction that enables 3D SML in complex biological environments. A new SML technique is presented that employs a dual-objective approach to detect the emission spectrum of single molecules, enabling 5-dimensional single particle imaging and tracking (x,y,z,t,λ) without compromising spatiotemporal resolution or field of view. These acquisitions generate ~GBs of data, containing a wealth of information about the localization and environment of individual proteins. To facilitate quantitative acquisition and data analysis, the development of biochemical, software and hardware tools are presented. Together, these approaches aim to enable quantitative SML in complex biological samples.

Keywords

Superresolution Microscopy, Single Molecule Localization Microscopy, Adaptive Optics, Spectral, Single Particle Tracking

Imagerie quantitative des molécules uniques en profondeur dans les échantillons biologique à l'aide d'optiques adaptatives

Résumé

La microscopie optique est un outil indispensable pour la recherche de la neurobiologie et médecine qui permets l'étude des cellules dans leur environnement natif. Les processus sous-cellulaire restent néanmoins cachés derrière les limites de la résolution optique, ce qui rend résoudre les structures plus petites que ~300nm impossible. Récemment, les techniques de la localisation des molécules individuelles (SML) ont permis le suivi des protéines de l'échelle nanométrique grâce à l'ajustement des molécules unique à la réponse impulsionnelle du system optique. Ce processus dépend critiquèrent sur la quantité de lumière recueillit et rends ces techniques très sensibles aux imperfections da la voie d'imagerie, nommé des aberrations, qui limitent l'application de SML aux cultures cellulaires sur les lamelles de verre.

Un system commerciale d'optiques adaptatives est implémenté pour compenser les aberrations du microscope, et un flux de travail est défini pour corriger les aberrations dépendant de la profondeur qui rend 3D SML possible dans les milieux biologiques complexe. Une nouvelle méthode de SML est présentée qui utilisent deux objectifs pour détecter le spectre d'émission des molécules individuelles pour des applications du suivi des particule uniques dans 5 dimensions (x,y,z,t,λ) sans compromis ni de la résolution spatiotemporelle ni du champ de vue. Pour faciliter les analyses de manière quantitative des Go de données générés, le développement des outils biochimiques, numériques et optiques est présenté. Ensemble, ces approches ont le but d'amener l'imagerie quantitative des molécules uniques dans les échantillons biologiques complexes.

Mots clés

Microscopie de superresolution, localisation des molécules individuelles, Optiques Adaptatives, Spectrale, Suivi des particules uniques

Acknowledgements

"All living things contain a measure of madness that moves them in strange, sometimes inexplicable ways."
— Yann Martel, Life of Pi

I would remiss to begin my acknowledgements without thanking Eric Hosy and Daniel Choquet for accepting me for a Master 2 internship in 2013. Eric introduced me to the IINS, to the world of research, to superresolution microscopy and its application to the vast multidisciplinary domain of neuroscience, and finally to Jean-Baptiste Sibarita, who would become not only my PhD advisor but a kind of life coach. JB, thank you for affording me the right combination of independence and guidance to complete this project, and for pushing me inside and outside the lab to become a more well-rounded, functional individual. From you, I learned the importance of the intangible work-life balance and have become stronger, both physically and mentally.

Of course, a huge thanks to all my fellow group members, from my PhD big brother Adel Kechkar to Rémi Galland for his day-to-day guidance, Anne Beghin and Marine Cabillic for all of the kiwi breaks, and Pierre-Olivier Strahl for being an early-riser and always having the coffee ready in the morning. A huge thank you to all of my coworkers at Imagine Optic, specifically Grégory Clouvel and Audrius Jasaitis, who warmly welcomed me to the IO family and were always available for discussions.

My PhD work relied heavily on collaborations with many other talented people in the IINS, to whom I am extremely grateful: Ingrid Chamma, Benjamin Compans, Julia Goncalves, Julien Dupuis, Ezequiel Saraceno and the countless others whom I solicited as the "neuron trashcan" for my spectral tracking experiments. Special thanks to Julie Angibaud and Charlotte Rimbault for always knowing how to put a smile on my face.

I have to thank my family for their flexibility and comprehension for spending nearly 5 years overseas. Their wholehearted support of my independence (academic, professional, cultural and otherwise) allowed me to fully invest myself and flourish in this foreign environment.

Lastly, and perhaps most importantly, thank you to those whom I have forgotten to thank, those quiet yet influential ambient voices that helped guide (and sometimes carry) me along this path.

TABLE OF CONTENTS

ABBREVIATIONS

(s)CMOS – (scientific) Complementary Metal Oxide Semiconductor
ADU – Analog to Digital Units
AFP – Actual Focal Plane
AMPA - α-amino-3-hydroxy-5-methyl-4-isoxazolepropionic acid receptor
AO – Adaptive Optics
CCD – Charge-coupled device
COT - cyclooctatetraene
DM – Deformable Mirror
DMD – Digital Micromirror Devise
DNA-PAINT – DNA Points Accumulation in Nanoscale Topography
DoL – Degree of Labeling
dSTORM – direct Stochastic Optical Reconstruction Microscopy
EM – Electro-magnetic
EMCCD – Electron Multiplying Charge-Coupled Device
FOV – Field of View
FRC - Fourier Ring Correlation
FWHM – Full Width at Half Maximum (Frequently used as resolution criteria)
GA – Glutaraldehyde
Glox – Glucose Oxidase
GPU – Graphics Processing Unit
GSDIM – Ground State Depletion Microscopy followed by Individual Molecule Return
HCS – High Content Screening
IM – Interaction Matrix
LIMA – Light-induced molecular adsorption
LSM – Light Sheet Microscopy
mStrav – Monomeric Streptavidin
NA - Numerical Aperture
NFP – Nominal Focal Plane
NIR – Near Infrared
Nlg1 – Neuroligin1
OPL – Optical Path Length
PAINT – Points Accumulation for Imaging in Nanoscale Topography
PALM – Photoactivated Localization Microscopy
PCA – Pair Correlation Analysis
PFA - Paraformaldehyde
PFS – Perfect Focus System
PSF – Point Spread Function
SAF – Supercritical Angle Fluorescence
SIM – Structure Illumination Microscopy

SLM – Spatial Light Modulator
SMLM – Single Molecule Localization Microscopy
SMS – Single Molecule Switching (see also, SMLM)
SNR – Signal to Noise Ratio
SPIM – Selective Plane Illumination Microscopy
SPT – Single Particle Tracking
sptPALM – Single Particle Tracking Photoactivate Localization Microscopy
SRM – Super Resolution Microscopy
STED – Stimulated Emission Depletion Microscopy
STORM – Stochastic Optical Reconstruction Microscopy
TIRF – Total Internal Reflection of Fluorescence
uPAINT – Universal Points Accumulation in Nanoscale Topography
UV – Ultraviolet
WFS – Wavefront sensor

INTRODUCTION

Historically, fundamental advances in human knowledge occur as a direct result of scientific and technological progress. Over our evolution as a society, we have begun narrowing our attention in an attempt to comprehend how the interaction of a complex network of small microscale events act together to induce a macroscale effect. This is particularly true in biology, where the advent of the microscope in the 16th century enabled the visualization of individual cells and their interactions together. The microscope has allowed us to gain a wealth of knowledge not only about the human body, but also about our surrounding environment.

However, optical microscopy has been restricted to visualization of ~micrometer scale structures due to physical limits that govern the propagation of light. Within the past decades, techniques have emerged that push optical microscopes to their technical limit, allowing for the first time the visualization and tracking of individual proteins in live cells. These so-called super-resolution microscopes are capable of resolving nanometer scale structures, but the full capabilities of these young techniques have yet to be fully exploited. In particular, the optical sensitivity combined with the huge amount of data generated by these techniques has conventionally limited their applications to cells cultured on glass coverslips, preventing quantitative nanoscale biology in more complex but physiologically relevant environments like tissue.

This thesis aims to address some of these limitations by the development of new biological, optical and software tools in an effort towards enabling the quantitative study of nanoscale protein interactions in complex biological samples. This work was part of a CIFRE collaboration with Imagine Optic, a company at the forefront of advanced optical tools for metrology and microscopy. Finally, this work was made possible thanks to the collaborative environment of the Interdisciplinary Institute for Neuroscience, where the lines between chemistry, biology, optics and computer science are blurred through collaboration.

Organization of the Thesis: Chapter Descriptions

This dissertation is composed of an introductory chapter and 3 main chapters that represent 3.5 years of work on individual paths towards improving single molecule localization microscopy

along separate vectors, with the ultimate goal of enabling quantitative single molecule biology of multiple proteins in physiological biological environments.

In Chapter 1, I introduce the notion of fluorescence microscopy and its fundamental limits in terms of imaging speed and resolving power. I detail the decade-new discovery of super resolution fluorescence microscopy and its capacity to uncover nanometer-scale protein localization and dynamics. I cover the requisite notions of single molecule localization microscopy (SMLM), from sample labeling techniques to efficient fluorophore excitation and detection, highlighting the current limitations that restrict its application to a subset of biological models.

In Chapter 2, I detail several distinct collaborative paths I explored during this thesis towards improving single molecule localization microscopy to help enable quantitative biological imaging. I begin with a photopatterning technique to create quantitative single molecule assays for characterizing the photophysical properties of single molecule labels in absence of cellular noise. I then introduce a novel automated acquisition pipeline for high content single molecule imaging to facilitate dSTORM, DNA-PAINT and (spt)PALM imaging in multi-well plates. To address the issue of quantitative analysis of SMLM data, I detail a new method of cluster analysis based on Voronoï segmentation constructed from the localized molecule coordinates. I detail its application to DNA origami structures that serve as excellent metrological tools for single molecule localization microscopy (SMLM), as well as a quantitative investigation of AMPA receptor clustering in hippocampal neuron cultures.

Chapter 3 tackles the topic of 3D single molecule imaging and the limitations that restrict conventional 3D SMLM methods close to the coverslip surface. I introduce the concept of adaptive optics for single molecule localization microscopy, a field of optics pioneered for astronomy to correct for atmospheric distortions in land-based telescope images. As part of the CIFRE collaboration with Imagine Optic, I detail the development of a plugin for the MetaMorph acquisition environment, which facilitates the use of adaptive optics for wavefront correction in single molecule imaging. I describe the implementation of a plug-and-play adaptive optics kit and discuss how it is used for correction of wavefront aberrations, allowing for thicker 3D imaging than conventional methods as well as SMLM imaging up to 10µm away from the coverslip, notably facilitating 3D dSTORM in hippocampal brain slices.

In the final fourth chapter, I outline the development of a microscope that retains high spatiotemporal resolution of conventional epifluorescence collection while adding spectral discrimination abilities through a second collection objective placed in the transmission geometry. By using a dispersive element in the second optical path, the average emission wavelength of each single emitter can be estimated, allowing for simultaneous 3D multicolor structural imaging and protein tracking without compromises. I discuss our unique implementation of the method using two commercial microscopy bodies in an effort to maximally stabilize the system and make it as accessible to users as possible. I conclude with several applications of the method for a variety of biological models and fluorescent probes, demonstrating the sensitivity and versatility of the technique for 5-dimensional single particle tracking.

CHAPTER 1 Optical Single Molecule Fluorescence Microscopy

This introductory chapter establishes the foundation of the burgeoning field of single molecule localization microscopy, which has given unprecedented insight into nanoscale biological structure and dynamics over the past 2 decades thanks to an order of magnitude improvement in resolution.

A complete understanding of super-resolution microscopy techniques requires a thorough introduction to the contrast mechanism used to pinpoint individual molecules in the protein-dense cellular environment. I begin by briefly describing the theory of the light-matter interaction known as fluorescence, highlighting in particular its advantages and utility as a specific marker for biological imaging, and discuss its fundamental limitations. I then focus on methods that circumvent the optical resolution limits in so-called super-resolution imaging, specifically techniques based on single molecule blinking and localization. I cover non-exhaustively the most important aspects of single molecule imaging in the context of optimizing image resolution, from sample labeling with fluorescent probes to their efficient excitation and sensitive detection.

Improving these three criteria form the foundation for my PhD work, with the ultimate goal of extending single molecule imaging beyond the coverslip into more biological complex and physiologically relevant samples.

1.1 Introduction to Optical Fluorescence Microscopy

Specificity is a fundamental issue in any optical imaging system, particularly in the domain of microscopy, where images are frequently used for decorticating complex biological circuits or diagnosing medical diseases. The ability to separate a specific protein or structure of interest from its surrounding environment is critical in successfully achieving this. For decades, the light-matter interaction known as fluorescence has been utilized to distinguish molecules from its neighbors. By selectively attaching such a fluorescent molecule, known as a fluorescent probe or

tag, to a certain protein of interest, the field of fluorescence microscopy has become an integral tool for research in biology and medicine.

1.1.1 Motivation and Principles of Fluorescence Microscopy

The process known as **fluorescence** occurs as the result of a specific interaction between a molecule and an incident electromagnetic (EM) wave. When a fluorescent molecule absorbs an EM wave, its electrons are excited from an energetic ground state to a higher-energy excited state. Briefly, these energy levels are a result of the quantized nature of energy that discretizes the energy of a given molecule into a combination of distinct atomic rotational, vibrational and electronic states. Figure 1.1a depicts the electronic energy levels of a molecule during its fluorescence cycle, commonly referred to as the **Jablonski diagram**. During the photon absorption process, the fluorescent molecule gains a discrete amount of energy (E) inversely proportional to the wavelength (λ) of the incident photon:

$$E = h\nu = h\frac{c}{\lambda} \quad (1.1)$$

where ν is the light's frequency and $c \approx 6.626\times10^{-34}$ J • s is Planck's constant. Absorption of the incident photon's energy induces a molecular transition to a higher electronic energy state, where it remains on the order of nanoseconds before relaxing to the ground state. When relaxing, it releases energy by a non-radiative transfer of energy to a lower-energy state, or by emitting this energy in the form of photons. Notably, these emitted photons contain less energy than the excitation photon due to energy loss in the form of vibrational relaxation in the upper electronic state. The energy difference between the excited and the emitted photons is called the **Stokes Shift**. Furthermore, the large number of vibrational states within each electronic state causes variability of the energy of each emitted photon, resulting in broad fluorescence excitation and emission spectra (**Figure 1.1**b).

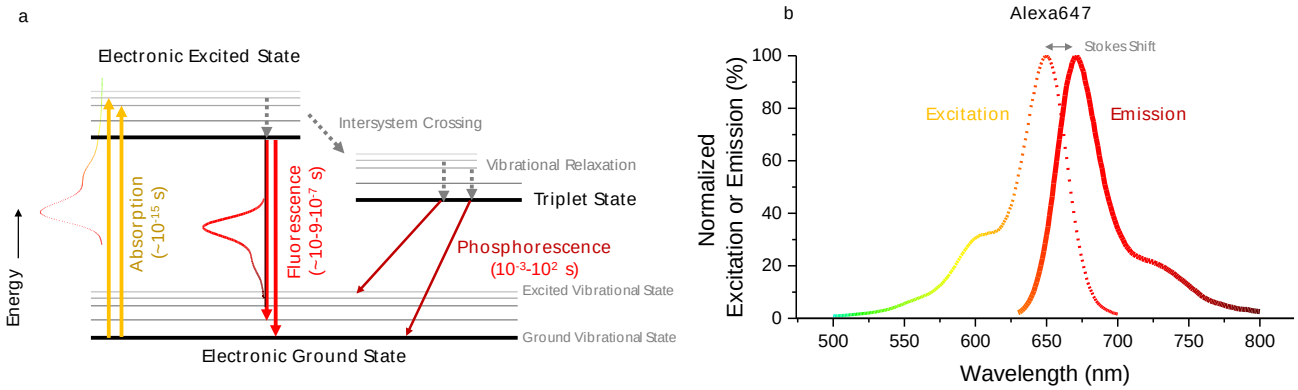

Figure 1.1: The Principle of Fluorescence. (a) Jablonski Diagram showing the timeline of fluorescence. The molecule is raised to an excited electronic state through the absorption of an incident photon (yellow). It releases this energy either in the form of a fluorescence photon (red), or may transition to a long-lived, lower energy triplet state, from which it can emit higher wavelength phosphorescence photons. (b) The large number of energetic sub-states from vibrational and rotational modes allow the Alexa647 fluorescent molecule to absorb and emit a spectrum of photons. The energy lost due to internal conversion and vibrational relaxation results in a red-shift of the fluorescence spectrum with respect to the emission spectrum, called the Stokes Shift.

Fluorescence is just one of many processes by which a molecule can internally transfer its energy. An energy transfer which induces a change in electron spin pushes the molecule in to a **triplet state** via a process known as **intersystem crossing**. These triplet states have a much longer

lifetime than singlet excited states because depopulating these quantum mechanically forbidden energy levels requires emitting the appropriate amount of energy and simultaneously changing electron spin in order to emit a photon in a process known as **phosphorescence**. When considering the timeline of single molecule photophysics, these triplet states are commonly considered as "dark states", as the molecule can reside here from milliseconds to hundreds of seconds before returning to the electronic ground state where it can begin a new fluorescence cycle.

This cycle of energy absorption and re-emission can occur indefinitely as long as the system is not perturbed. However, for most fluorescent molecules, this fluorescence lifecycle typically ends with a structural change to the chemical bonds of the molecule known as **photobleaching**, which prevents it from absorbing further photons.

Fluorescence microscopy has proven to be a powerful method for studying biology due to its simple implementation into an optical system. Many molecules which possess the ability to fluoresce can be easily and specifically tagged to single proteins, rendering them visible on the microscope. Combining the physical process of fluorescence as a proxy for the biological structure to image, fluorescence microscopy has given protein-specific contrast to biological structures. Fluorescence excitation sources such as fluorescence lamps or lasers are now commonly available, as are a wide range of filters at various wavelengths and spectral bandwidths used to selectively allow only photons in the emission spectrum of the fluorescent molecule to be imaged by the system.

Historical Aside: The term fluorescence was first coined by Sir George Gabriel Stokes in 1843, where he observed the phenomenon with his own eyes using sunlight as an excitation source for calcium fluoride (Stokes 1852). The first fluorescence microscopes, originally developed by the Carl Zeiss company in the early 20th century, exploited the autofluorescence of various biomolecules as a contrast mechanism. Later, the advent of fluorescent tags that specifically target individual proteins brought about rapid growth of the field of fluorescence microscopy.

1.1.2 Resolution in Fluorescence Microscopy

While fluorescence microscopy adds inherent specificity and contrast, it is subject to the laws of light propagation and diffraction, limiting the theoretical resolution of the technique to the micrometer scale.

Perhaps the most common metric used to measure the power of a microscope or other optical system its capacity to separate two point sources from each other, a quantity commonly referred to as **resolution**. This resolution ultimately determines the finest details the microscope can image.

When considering the resolution of a microscope, it is essential to understand how the imaging system creates an image of an infinitesimally small source of light, known as a **point source**. There are two key notions to consider when imaging a single emitting point source, the fluorescence of which propagates radially outward from the point source. The first is that only a finite portion of the radiations can be collected, resulting in incomplete or "lossy" photon collection. Second, the radiated photons periodically interfere with each other due to the wave nature of light in a process called diffraction. Considering an optical system where the photons

emitted from a single molecule are collected with a simple lens, it is mechanically impossible to collect the entirety of the emitted light with one single lens. When quantifying the collection efficiency of an optical element or system, it is common to reference the maximum emission angle of light collected by this lens, known as its **numerical aperture (NA)**, mathematically formalized as

$$NA = n \sin \alpha \quad (1.2)$$

where n is the refractive index and α is the half-angle of the cone of light that enters the lens, as shown **Figure 1.2**a.

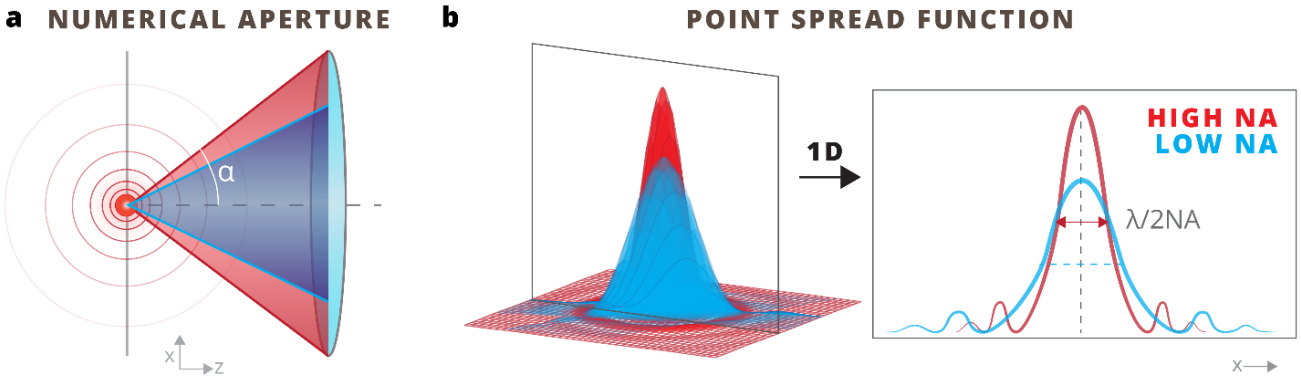

Figure 1.2 Consequences of the Limited Photon Collection of an Optical Imaging System. (a) The numerical aperture (NA) of an imaging system is defined by its ability to collect a given angle, α, of emission light from a point source. A high-NA system (red) collects more light than a low-NA system (blue). (b) The partial collection of light from a single point source results in a 2D Airy diffraction pattern at the focal plane called the point spread function. High-NA systems (red) that collect more light more perfectly interfere, resulting in a narrower and more intense central peak.

1.1.2.1 The Point Spread Function: The Result of Incomplete Collection

As a result of this limited collection ability, the focused fluorescence emission from a single fluorescent emitter does not perfectly interfere. Practically, a single point source of light therefore appears as an image with a finite size, in a blurry representation known as the **point spread function (PSF)**. The wave nature of light underlies the PSF's representative spatial distribution in the form of a 2-dimensional Airy Function (**Figure 1.2**b), with most of the energy concentrated in a large central peak and several peaks and troughs emanating radially from the emitter's center. The width of the main lobe of this airy function depends critically on two factors: the wavelength of the emitted photon, as well as the amount of light collected by the imaging system, introduced previously as the numerical aperture of the system. Collecting more light from the emitted source (by increasing the objective's NA, for example) results in a more perfect interference between the collected EM radiation, reducing the effective size of the PSF. Similarly, light with smaller wavelengths results in a narrower interference pattern and reduces the PSF size.

If we consider an imaging system as an optical signal processor, the point spread function is essentially the microscope's impulse response, and any image created by the system is simply a linear superposition of the PSFs of each emitting fluorescent molecule, a process called **convolution**. The image of a complex sample can be considered as the sum of the point spread functions of all each individual fluorescing molecule inside the sample. Thus, understanding the point spread function is essential to defining the resolving capabilities of an imaging system.

1.1.2.2 Spatial Resolution: Rayleigh Limit vs. Abbe Limit

Using the point spread function as the fundamental unit of an optical imaging system, the ability to discriminate the point spread functions emanating from two adjacent single emitters defines the system's spatial **resolution**. Formally, several mathematical descriptions of this criteria exist, differing only in their definition of the minimum distance necessary to effectively separate the two airy functions (**Figure 1.3**a).

Ernst Abbe [1], however, was the first to mathematically formalize this notion in 1873 by calculating the spot size, d, of a point source imaged through a microscope objective as

$$d = \frac{\lambda}{2NA} \qquad (1.3)$$

Shortly thereafter, Lord Rayleigh in 1879[2], expanded on this notion by defining the minimum discernable separation between the spatial intensity distribution of two converging point sources, called the **Rayleigh criteria**, imposing this distance such that the maximum of one point spread function is placed exactly at the first minimum of its adjacent PSF. Mathematically, this was formalized as

$$\Delta x_{airy} = 0.61\frac{\lambda}{NA} \qquad (1.4)$$

and is commonly used as a reference for resolution in microscopy, and is as small >200nm for visible light (λ =400nm-700nm, NA=1.4) used in biological applications.

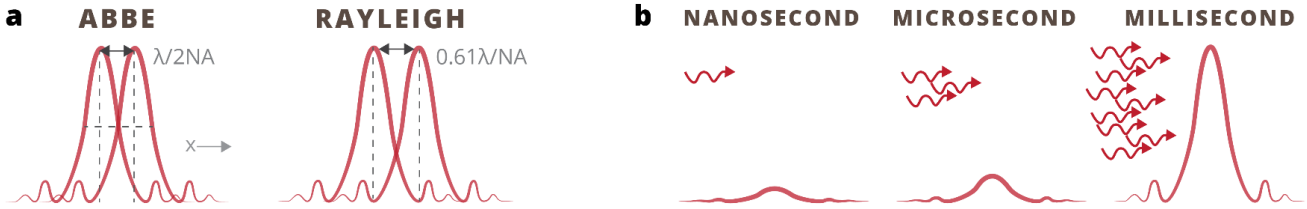

Figure 1.3: Spatiotemporal Resolution Considerations. (a) Two common definitions exist for defining the capability of an imaging system to resolve two adjacent emitters, but the resolution of an optical system is generally simplified as λ/2NA. (b) Several hundreds of photons must be acquired to create an accurate image of a single emitter. This schematic representation ignores noise sources (from an imaging sensor or the stochastic photon emission process) in a simple illustration that longer exposure time allows accumulation of more photons for higher SNR.

It is important to distinguish the lateral resolution, discussed above, and the axial resolution, that is the ability of the imaging system to discriminate two point sources which have the same lateral *xy* position but differ in their *z* axial position. Again, calculating the spatial profile of the interference of the collected EM waves and using the Rayleigh criteria for separation, this axial resolution is given by

$$\Delta z_{Airy} = 2n\frac{\lambda}{NA^2} (1.5)$$

and is typically >800nm, ~3-4x larger than the lateral spatial resolution.

Aside: Choosing a Wavelength for Fluorescence Imaging in Biological Samples

Following Rayleigh's resolution criterion, one would postulate the maximizing resolution is as simple as minimizing the wavelength. While mathematically valid, complications arise when applying fluorescent to biological studies. Due to their molecular structure, water, blood and

tissue have an electromagnetic attenuation minimum between λ=600nm – 1μm. This is frequently referred to as the biological window, as light in this spectral range can be easily transmitted without scattering. Lower wavelengths, towards the ultraviolet (UV), contain a biologically harmful amount of energy and should be used sparingly in biological imaging. Much work is taking place in pushing microscopy towards the near infrared (NIR), although excitation sources and fluorescent probes in this range remain scarce and/or expensive.

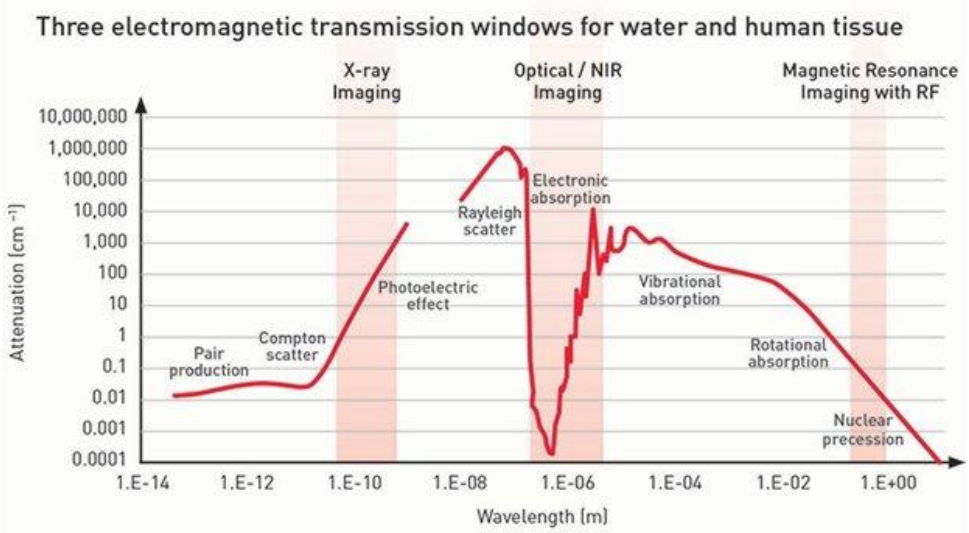

Figure 1.4: Electromagnetic Transmission Window for Biological Studies. Water and biological tissue have a transmission window in the visible and near-infrared wavelengths. Future laser and probe development further in the near infrared wavelength range is promising for biological applications of optical microsopy.

From: https://www.osa-opn.org/home/articles/volume_26/september_2015/features/optics_in_the_molecular_imaging_race/

1.1.2.3 Temporal Resolution: Fluorescence Lifetimes

The resolving power of a microscope extends beyond its ability to spatially discriminate point sources. Another critical notion to understanding the resolution of a microscope is its ability to temporally distinguish these point sources.

The fundamental limit to the temporal resolution of a fluorescence imaging system can be considered as the single emitting molecule to complete its fluorescence cycle. Revisiting the Jablonski diagram in **Figure 1.1**a, we notice that once excited by an incident photon (a process which occurs on the order of picoseconds), the fluorescent molecule with remain in its excited state for a time on the order of nanoseconds before emitting radiation in the form of a fluorescence photon or transitioning to a lower-energy state.

The theoretical temporal resolution of an optically perfect imaging system capable of imaging single photons is therefore on the order of nanoseconds. To accurately create an image of a fluorescent sample, several hundreds of photons are required, resulting in typical exposure times on the order of microseconds to milliseconds (**Figure 1.3**b).

1.1.3 Improving Axial Resolution by Removing Out of Focus Light

While diffraction optically limits the far-field resolution of an imaging system, there are means to improve the capacity of the optical system to resolve structures by optimizing contrast. A common idea used to improve the effective resolution of a microscope is to limit the thickness

of the specimen effectively imaged by the optical system. There are two straightforward ways to implement this: by confining the excitation or the detection to a thin slice of a thick specimen. In both cases, limited the effective thickness of the imaged sample results in greatly improved axial resolution.

One of the first implementations of this confined excitation exploits the ability to limit excitation light inside the coverslip on which the sample is imaged. While widefield or epifluorescence imaging illuminates an entire sample, focusing a laser source near the extremity of the back focal plane of the microscope objective results in a beam that is totally internally reflected in the coverslip due to the refractive index difference between the glass and the imaging medium. This causes an evanescent wave to propagate along the coverslip surface, whose intensity decreases exponentially with the axial distance into the sample. Known as **Total Internal Reflection Fluorescence (TIRF)** microscopy[3], this evanescent wave can be used to excited fluorescent markers several hundred nanometers from the coverslip, the exact distance of which can be carefully calibrated and controlled based on the position of the focused incident beam in the back focal plane of the objective (**Figure 1.5**a). The result is an extremely high contrast signal thanks to the optical confinement of the excitation light.

One major drawback to the TIRF method is intrinsic to the physics that power the technique: TIRF is inherently restricted close to the coverslip surface and therefore cannot be used to image many cellular structures deeper into the cell. A slight variation of the technique, informally referred to as "dirty TIRF" or **oblique** excitation, brings the laser excitation slightly close to the optical axis such that the light is no longer internally reflected, but instead creates a highly inclined thin optical sheet that provides enhanced contrast over widefield imaging when imaging within several microns from the coverslip[4] (**Figure 1.5**b). A more advanced technique enables deeper imaging at the expense of slightly weaker optical sectioning. **Light Sheet Microscopy**, or **Selective Plane Illumination Microscopy (SPIM)**, dissociates the excitation light from the detection plane, typically by employing two objectives in a perpendicular geometry (**Figure 1.5**c), creating a strong optical sectioning effect that can be exploited for cellular, tissue, or even entire-organism imaging.

An alternative method to improve contrast is to provide a widefield excitation but prevent the out-of-focus background light from reaching the detector. By placing a pinhole in a plane optically conjugate to the image plane, only the in-focus light rays are permitted to pass the spatial filter and onto the photodetector (**Figure 1.5**d). These **confocal microscopes** typically employ a point scanning excitation, where an excitation laser is focused on the sample plane and raster scanned through the field of view, with a single photodetector collecting the emission sequentially from each point. This technique is temporally limited by the ability to rapidly scan the laser and detect a sufficient number of photons per point. However, a slight optimization to the conventional confocal microscope with an array of spinning pinholes and a 2-dimensional imaging sensor have made **spinning disk microscopy** an exceedingly used technique in biological studies of fixed tissue due to its high contrast and fast imaging speed.

Finally, **multiphoton microscopy** is a laser-scanning based technique that benefits from excitation-based optical sectioning without the need for a detection pinhole by exploiting temporal properties of advanced laser sources (**Figure 1.5**e). In two photon microscopy, femtosecond laser pulses with twice the desired excitation wavelength are used, allowing only

fluorophores very close to the focus simultaneously absorb two photons and reducing the effective excitation to very small focal volume (~0.1μm²)[5].

The optical sectioning capabilities of these illumination techniques are overviewed in **Figure 1.5** and will be treated in greater detail in section 1.4.2.

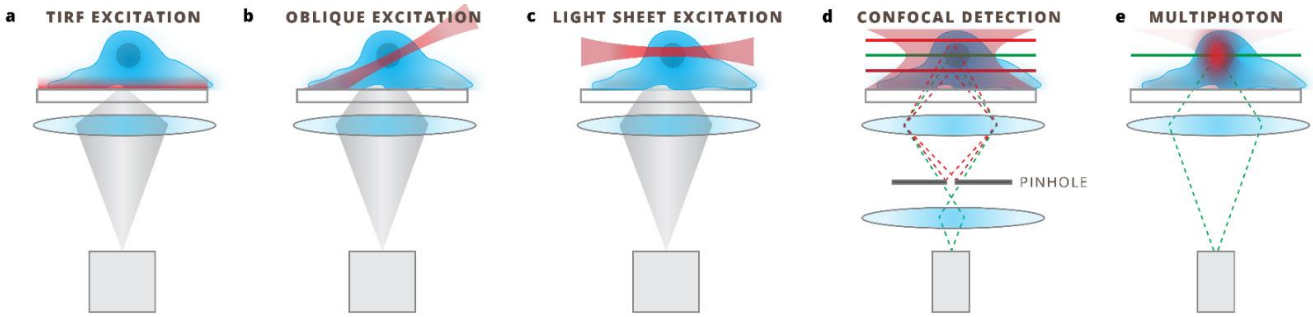

Figure 1.5: Improving Axial Resolution by Optical Sectioning. (a) Total Internal Reflection excitation confines the excited fluorophores to several hundred nanometers from the coverslip surface. (b) Oblique or HiLo excitation creates a thin, highly inclined optical sheet that allows imaging within several micrometers from the coverslip surface. (c) Light sheet, or selective plane, illumination decouples the excitation and detection, enabling imaging up to organism scale. (d) Widefield laser scanning based approaches can benefit from optical sectioning with a confocal detection pinhole, allowing only excited light from the focal plane to reach the detector. (e) Multiphoton excitation techniques confine the excitation volume by requiring multiple photons to be simultaneously absorbed.

1.1.4 Circumventing the Diffraction Barrier: Super-Resolution Microscopy

TIRF, light-sheet, multiphoton and confocal microscopy improve axial resolution using a common notion: limiting the collected fluorescence to an axial subset of fluorescent molecules prevents interference from out-of-focus molecules. While the result is improved contrast and improved axial resolution, the resolution of these techniques is still limited by the diffraction of light.

In 2014, Nobel Prize in Chemistry was awarded to three scientists instrumental to the creation of the first so-called "super-resolution" microscopes, capable of circumventing the diffraction barrier to image fluorescent molecules with nanometer precision. These super-resolution methods do not break the fundamental laws of EM wave propagation, but rather play clever tricks to increase the effective image resolution in the far-field.

Structured Illumination Microscopy (SIM)[6] achieves a two-fold improvement over conventional diffraction-limited microscopy through a combination of patterned excitation and image processing that increase the acquired spatial frequencies and thus image resolution. The sample is excited with specific patterns that make high spatial frequencies accessible by diffraction-limited optics. SIM offers a 2x gain in resolution for little compromise in terms of image acquisition time, setup complexity, or required laser power, and is an ideal choice for live-cell imaging of structures ~100nm in size.

A second superresolution approach called **Stimulated Emission Depletion (STED) Microscopy**[7] extends upon a traditional point scanning microscope with confocal detection, adding a second excitation laser that quenches the fluorescence around the excitation point. It is achieved by shaping the spatial profile of the depletion laser in a doughnut-shaped ring concentric with the fluorescence excitation laser. The excitation and depletion laser are scanned

simultaneously using a high-precision galvanometric scanner, generating an image of the fluorescent sample where only the fluorophores in the sub-diffraction limited area inside the quenching ring contribute to the image. The resolution of this method is theoretically infinite, as the inner radius of the quenching ring decreases with increasing laser power. Practically, however, laser power must be limited when imaging biological samples to prevent damage to the fluorescent markers or to the underlying biological structure.

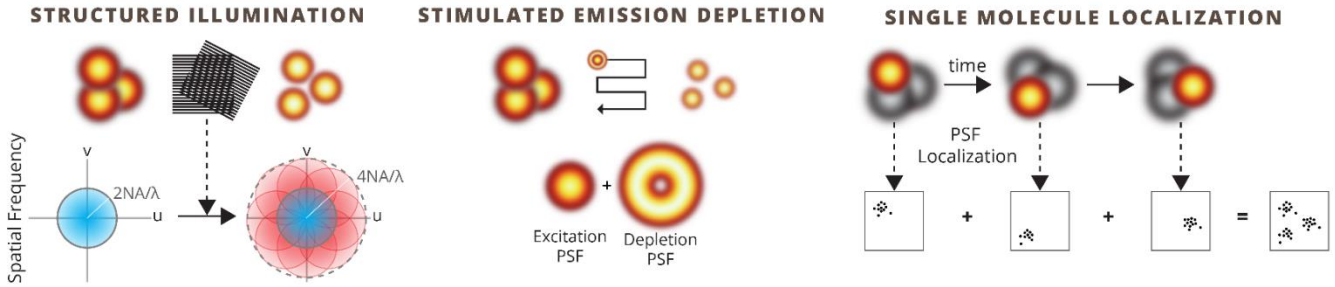

Figure 1.6: Comparison of Superresolution Methods. (a) Structure Illumination Microscopy (SIM) achieves a 2x improvement in resolution by using patterned illumination to fold higher spatial frequencies into the diffraction limit. (b) Stimulated Emission Depletion (STED) microscopy uses a second laser beam with a doughnut spatial profile to quench fluorescence outside of a tight focus. (c) In Single Molecule Localization Microscopy (SMLM), stochastic activation of spatially overlapping fluorophores allows localization of single emitters with a precision an order of magnitude greater than the diffraction-limited resolution.

Whereas STED uses advanced illumination techniques and precise knowledge of the location of the excitation beams to acquire a sub-diffraction limited image, **single molecule localization** based techniques exploit temporal separation of spatially overlapping fluorophores to numerically estimate their position with nanometer precision. By accumulating tens of thousands of imaging frames and reconstructing a single image containing the localizations of hundreds of thousands of molecules, in 2006 *Betzig et al* first demonstrated fluorescence photoactivated localization microscopy ((f)PALM[8]) and shortly thereafter *Rust et al* stochastic optical reconstruction microscopy (STORM[9]) for sub-diffraction limited imaging. Fundamentally, PALM, STORM differ only in their means of rendering optical sparsity to spatially overlapping fluorescent molecules, and will be discussed in further detail in section 1.3.3.

By giving access to nanometer-scale protein localization and dynamics, these techniques and their derivatives have enabled biologists to study the complex cellular circuitry and protein interactions at a new level.

1.2 SINGLE MOLECULE LOCALIZATION MICROSCOPY

Single molecule imaging techniques combine conventional full field microscopes with new stochastically-activated fluorescent probes that allow a single molecule to fluoresce amongst a sea of otherwise dark molecules. If only a single molecule is imaged in a diffraction-limited area, its image on the camera sensor will appear as a diffraction-limited and pixel-binned representation of the airy-distributed point spread function. This condition of a single molecule underlying the imaged PSF is exploited to determine the centroid of the PSF, usually by fitting the fluorescence distribution to a model point spread function. The result is an estimate of the molecule's position with an order of magnitude higher resolution than the optically-limited

image (Section 1.2.6 discusses the validity of this assumption and the consequences of its violation).

In **Single Molecule Localization Microscopy (SMLM)**, this localization process is repeated for up to hundreds of thousands of image frames, ideally until all fluorescent molecules have been localized, accumulating the spatial coordinates of fluorescent molecules to reconstruct one final image with up to millions of localization points. The tradeoff for spatial resolution is evident: a single reconstructed image requires several tens of seconds to tens of minutes in order to effectively image and localize all fluorophores in a given sample. The term SMLM encompasses a variety of individually-named techniques including (non-exhaustively) (spt)PALM[8,10], STORM[11], dSTORM[12], (u)PAINT[13,14], and GSDIM[15]. While the variety of terminology can be daunting, the techniques are fundamentally identical, distinguished primarily by the type of fluorescent tags used and how they obtain sufficient spatial sparsity for single molecule localization.

A high-level overview of the analytical approach to single molecule localization and reconstruction is given here. For a more thorough analysis, I refer the reader to a recent review article by *Lee et al.*[16], which provides a comprehensive look at each analytical step.

1.2.1 The SMLM Microscope: Simplicity and Efficiency

SMLM can be performed using relatively simple optical system as shown in Figure 1.7a, typically composed of two distinct optical paths: the **excitation path** (light red), where one or multiple light sources are projected onto the sample plane through a system of lenses, and the **collection or detection path** (dark red), where the light emitted from the sample plane is collected and imaged via a tube lens onto a photosensitive device, such as a camera. In a commonly employed geometry, the **inverted microscope**, these two paths share a common element: the microscope objective; the excitation light is focused through the objective onto the sample, and the fluorescence emission is back-collected using the same objective, after which a wavelength-sensitive dichroic mirror is used to separate the fluorescence emission from the excitation light. Coupling the two optical paths through the microscope objective allows for both the excitation and detection to take advantage of the benefits of these highly precise optical elements, but also imposes some constraints that will be detailed in section 1.4.

Establishing imaging conditions where only a single fluorescent molecule is emitting in a diffraction-limited area differs depending on the specific technique. It is generally accomplished by very low-power photoactivation (PALM-like), by immerging the sample in an imaging buffer that heavily favors molecular dark states (dSTORM) or by adjusting the concentration of antibodies coupled to a fluorophore (PAINT-like). Under these **single molecule** conditions, a single exposure frame contains from ten to hundreds of spatially distinct fluorescent spots.

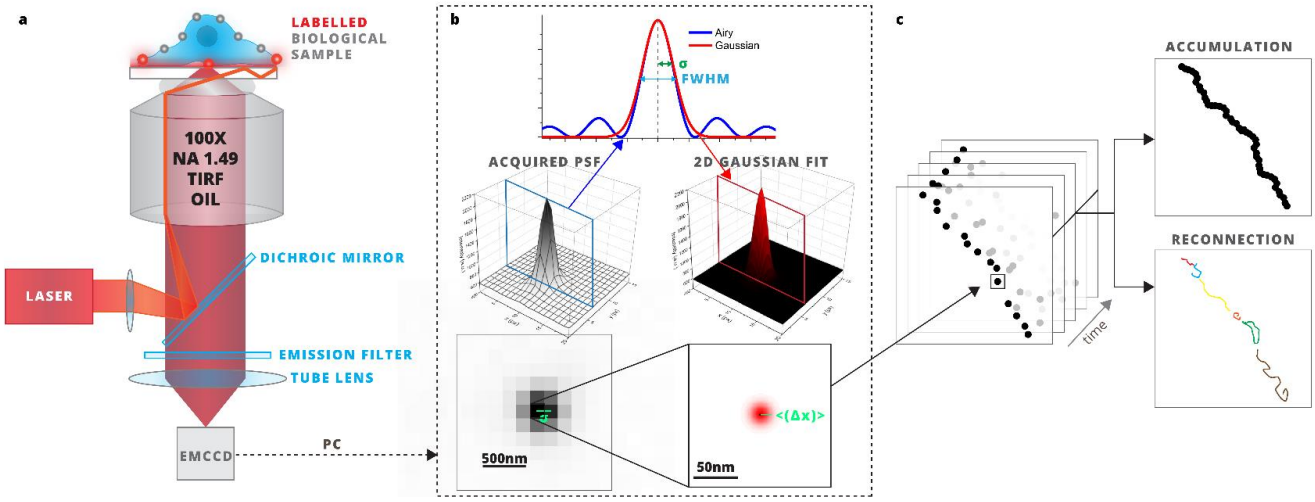

Figure 1.7: A Standard Single Molecule Localization Microscope with Gaussian Fitting Routine. (a) A standard inverted microscope geometry is typically employed in single molecule localization microscopy. An excitation laser is injected into the back focal plane of a high numerical aperture, high magnification microscope objective, exciting fluorescent markers in the biological sample. The emitted fluorescence is collected through a back-reflection geometry and focused onto a sensitive detector. (b) Individual images of fluorescent single molecules are segmented from the image and fit to a 2D Gaussian function of width σ (full width at half maximum ~2.35σ). This fitting process has a precision of Δx, generally in the tens of nanometers. (c) Hundreds of localizations from tens of thousands of frames can either be accumulated into a density map or temporally reconnected to form single molecule trajectories

1.2.2 The Localization Process: Accuracy

For well aligned optical systems, these individual fluorescent spots can be considered as accurate representations of the diffraction-limited point spread function of the microscope. In order to gain spatial information below the diffraction limit, these individual PSFs are fitted numerically to a model point spread function of the microscope, generally a Gaussian approximation of the Airy function, with the primary purpose of retrieving the position of the fluorophore at the epicenter of the fluorescence emission (Figure 1.7b).

1.2.2.1 The Validity of a Gaussian Fit Approximation (2D)

As mentioned in section 1.1.2.1, the intensity profile of a single molecule is imaged as an airy disk, whose width depends directly on the wavelength of emitted light and inversely on the numerical aperture of the collection objective. However, numerically fitting an airy function is not only a calculation-intensive task, but the spatial sampling and number of photons collected from a single fluorescing molecule limit the detectability of even the first side lobes. For these reasons, it is common practice to use a numerically simpler yet physically similar fitting model, namely a Gaussian curve:

$$I(x) = \mathrm{I}_{bg} + \frac{I_0}{\sigma\sqrt{2\pi}} e^{\left(-\frac{(x-x_0)^2}{2\sigma^2}\right)} \quad (1.6)$$

The width of the Gaussian fit, σ, is related to the full width at half maximum of the PSF via the following relationship:

$$FWHM = 2\sqrt{2\ln 2}\sigma \approx 2.3548\sigma \quad (1.7)$$

While a 2-dimensional Gaussian fit is generally used for single molecule localizations, the fitting process is more easily visualized in 1-dimension (Figure 1.7b), where the similarity of a theoretical Airy and its Gaussian fit is particularly apparent in the central peak of the Airy function.

1.2.2.2 Theoretical Localization Precision

The ability to numerically extract the central coordinates of this Gaussian approximation to the point spread function, in part, limits the effective resolution in SMLM (other factors contributing the resolution of SMLM images will be discussed in 1.2.5.1). Quantitatively, this is referred to as the **localization precision**. The theoretical variance of the coordinates of the single molecule, given by the Cramer-Rao lower bound, is detailed by *Ober et al.* [17] and gives a fundamental limit to the localization precision. More practically, in 2002, *Thompson et al.* first quantitatively investigated the uncertainty with which the center position of a single fluorophore can be extracted from its image through a real optical system, with sensor noise and finite pixel size[18].

$$\langle(\Delta x)^2\rangle_{Thompson} = \frac{\sigma^2 + {a^2}/{12}}{N} + \frac{8\pi\sigma^4 b^2}{a^2 N^2} \quad (1.8)$$

Mortensen et al. later refined this uncertainty to include excess noise from the electron multiplication process in EMCCDs commonly used in SMLM, resulting in the slight modification [19]:

$$\langle(\Delta x)^2\rangle_{Mortensen} = \frac{{\sigma_a}^2}{N}\left(\frac{16}{9} + \frac{8\pi {\sigma_a}^2 b^2}{Na^2}\right) \quad (1.9)$$

with $\sigma_a = \sigma + a^2/12$ and $a \leq \sigma$ where σ is the standard deviation of the PSF (1/e value for Gaussian approximation), a is the effective pixel size of the imaging system, N the number of photons collected, and b is the background noise.

In most cases and for EMCCD cameras, the background noise caused by readout error or dark current can be considered negligible, and the localization process finds itself in a regime limited principally by photon shot-noise. In this case, the second background term is ignored, and the approximate uncertainty with which a single molecule can be localized reduces to

$$\langle(\Delta x)\rangle_{Shot\ noise\ limited} = \frac{\sigma_a}{\sqrt{N}} \quad (1.10)$$

Simply stated, a single fluorescent emitter imaged through a digital imaging system like a microscope can be localized with greater certainty by increasing the number of photons collected in a single image frame or by reducing the standard deviation of the PSF (discussed in detail previously in 1.1.2.2), accomplished by reducing the wavelength of emitted light or increasing the numerical aperture of the collection objective. For example, a molecule that emits 100 photons, as is typical in PALM imaging, could theoretically be localized 10x more precisely thanks to the fitting processs. While this idealistic simplification is often used for localization precision estimates, it should be noted that it is only truly valid when the sensor noise is low compared to the signal and is less applicable in PALM imaging (where the signal per localization is quite low) or when using an sCMOS camera as a detector (where in individual pixel noise can greatly influence the fitting process). Furthermore, other sources of background noise like out of focus excited fluorophores add stochastic variability to the background and decrease the localization precision.

This localization and fitting process is applied to the array of molecules (~hundreds) in a single image frame, and by acquiring several tens of thousands of such single molecule images, a final reconstructed image can be generated. These localizations can be accumulated into a single density map, or localizations in the subsequent frame gives access to building single molecule trajectories with nanometer-scale precision (**Figure 1.7**c).

1.2.3 Single Molecule Tracking by Temporal Reconnection

Imaging single molecules has opened the doors to a wealth of biologically-relevant information about protein dynamics that are rendered invisible by the ensemble averaging of conventional bulk fluorescence imaging. The idea of temporally tracking single molecule fluorescence images was demonstrated as early as 1982, when *Barak et al* measured single receptor diffusion coefficients using bright fluorescent probes[20]. Localization-based approaches soon followed, allowing tracking of membrane molecules[21] and motor proteins[22] at the nanometer scale.

The advent of photoactivable fluorescent proteins like PA-GFP and Eos-FP decoupled the protein labeling density from the fluorescence imaging by allowing a small, stochastically activated subset of fluorescent tags to be imaged. By genetically fusing these photoactivable fluorescent proteins to proteins of biological interest, high-density mapping of protein populations with several orders of magnitude more tracks could now be obtained, revealing previously hidden heterogeneities in single protein dynamics with sptPALM[10]. Over the past decade, these high-density localization-based single particle tracking methods have allowed cellular biologists to peer even deeper in to protein dynamics and structure with spatial resolutions around 30nm[23-25].

While a high-level introduction of these approaches is outlined here, the interested reader is referred to two recent review articles that detail further advances in dynamic single molecule localization imaging [26,27].

1.2.3.1 Temporal Localization Reconnection and Trajectory Analysis

Temporally reconnecting spatially proximate localizations in adjacent image frames forms individual trajectories of individual molecules from which protein dynamics can be extracted (Figure 1.8a). For high-density SPT acquisitions, this can become a very computationally complex task requiring multiple-particle tracking, and therefore *a-priori* knowledge of the expected maximum velocity of the protein is frequently used to define a maximal spatial radius for track reconnection. Presently, dozens of software packages and methods are available to perform these trajectory reconnections. In a collaboration between more than 30 participating researchers, *Chenouard et al* present an excellent review of the state of the art of particle tracking methods[28], ultimately concluding that while no single software package is flawless, most methods work for a strong signal to noise ratio (SNR).

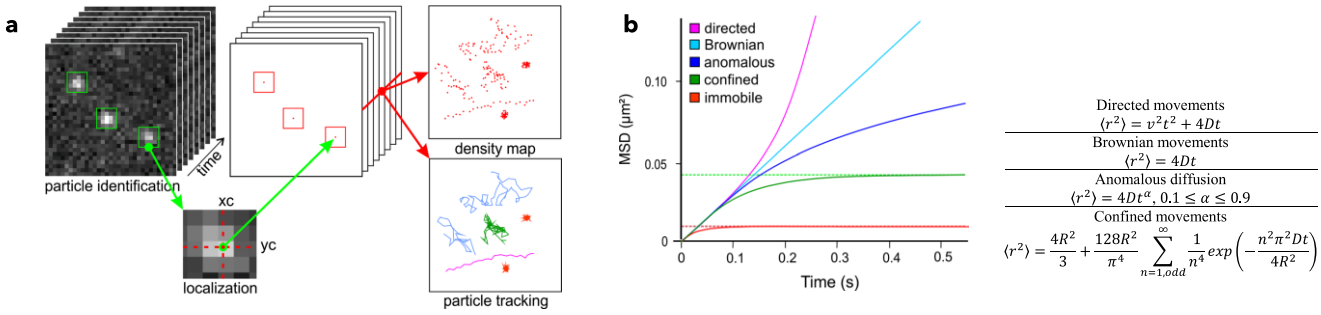

Figure 1.8: Single Particle Tracking and Mean Squared Displacement. (a) Localizations from individual single molecules are temporally reconnected across subsequent imaging frames, generating single particle trajectories that contain information and protein position and dynamics. (b) The mean square displacement is commonly used to define protein motion in complex cellular environments.

From *Sibarita et al* [27]

Spatiotemporal analysis of these trajectories can reveal not only how these proteins move in their local biological environment, but also how they interact with other proteins. The **Mean Square Displacement (MSD)** is one such commonly used analysis, extracting the diffusion coefficient of a freely diffusing molecule by quantifying the area that the molecule explores over time. As shown in **Figure 1.8**b, fitting the MSD data with several different model motion curves can unveil if a molecule is being actively directed, confined, or moving stochastically due to Brownian motion[29]. Furthermore, the MSD curve can be used to calculate a global diffusion coefficient per trajectory in addition to instantaneous diffusion coefficients per image frame for each trajectory, giving insight into the evolution of individual molecule's dynamics over time.

1.2.3.2 Spatiotemporal considerations and limitations of single molecule tracking

Essential to the analysis and interpretation of these single molecule dynamics is the comprehension of the technique's limitations. The MSD data must be carefully interpreted as a function of the fluorescent probe and linker's size and bio-accessibility[26]. Ultimately, the molecular diffusion coefficients are bound by the acquisition speed of the single molecule image stack (upper) and localization precision (lower). The imaging parameters must be carefully adjusted to consider the speed of protein motion, as any translation motion during camera exposition can blur the resulting image and induce localization error, especially when using a Gaussian fit model[30].

1.2.4 Real-time Online Localization and Tracking

The Gaussian fitting process can provide a very accurate estimation of the position of the fluorescent molecule underlying the PSF, but it is a computationally intensive task. The processing time for several hundred localizations per image frame can take as much computation time as the SMLM acquisition itself. To expedite the localization process, an alternative method for estimating the molecule's position based on the computationally inexpensive Wavelet transform was initially proposed by *Izeddin et al.* in 2012 [31]. By segmenting the PSF in the Wavelet space, the image is much less sensitive to noise and background than in the direct image space, and the centroid can be used as a proxy for the molecule's position with relatively high accuracy (**Figure 1.9**).

The reduced computational complexity of a wavelet domain centroid-based localization method, as well as its parallelizable nature, allowed for *Kechkar et al.* to create a localization tool

that performs the localization process in real-time on the acquisition system by exploiting the graphics processing unit (GPU) for parallel computation (**Figure 1.9**)[32].

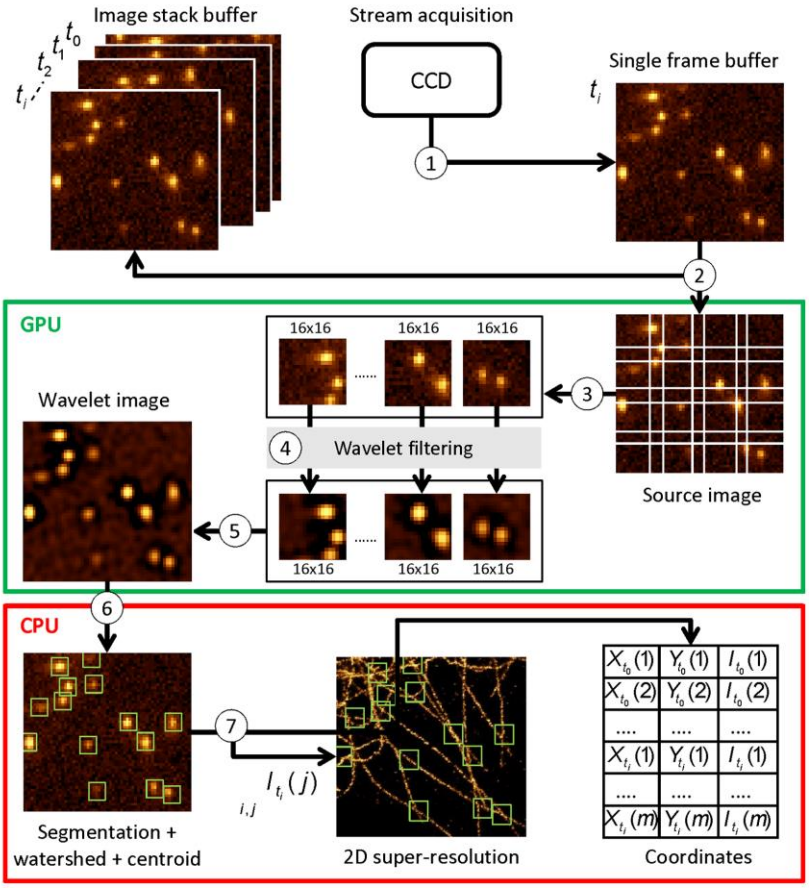

Figure 1.9: Real-time localization with GPU-based Wavelet Segmentation. GPU parallelization of single molecule localization highly multiplexes the localization process and allows for simultaneous real-time localization of hundreds of localizations.

From *Kechkar et al* [32]

A key advantage to localizing single molecule signatures in real-time during the acquisition is the ability to modify experimental conditions on-the-fly. For example, the number of activated molecules can be adjusted to optimize acquisition time, or even dynamically modulated over the course of the acquisition to maintain a constant number of localizations. Similarly, real-time super-resolution reconstruction can validate the correct level of protein expression or immunostaining, or alert the experienced experimenter of potential artifacts. This direct feedback is essential to facilitating SMLM more widespread application. On-line localization and image generation also alleviate one major numerical constraint that limits SMLM applications: saved data size. While SMLM image stacks can easily reach multiple gigabytes per image, online localization affords the ability to save only a single reconstructed image and/or a localization file containing all the localization and fit information for each individual localization, reducing the data storage required by nearly 2 orders of magnitude to hundreds of megabytes.

Critically, the ability to generate a super-resolution reconstruction during the acquisition addresses one key issue in SMLM: how many images are needed before the reconstruction can be considered "completed," or, more quantitatively, what is the effective molecular density desired in the super-resolution reconstruction.

1.2.5 Resolution and Applicability of SMLM

While there are multiple ways to define resolution in conventional microscopy, these definitions are based on semantic differences, as the true resolution is ultimately limited optically by the size of the point spread function. This, unfortunately, is not the case in single molecule localization microscopy, where the definition of resolution is a more complex notion.

1.2.5.1 Resolution in SMLM

In the field of microscopy, a notion known as the **resolution tradeoff** has been a longstanding dogma: there is inherent compromise between spatial resolution, temporal resolution, spectral resolution, imaging depth, or biocompatibility (with respect to the total dose of light inflicted on the sample). This tradeoff is even more important in SMLM due to the limited number of photons that a single molecule can emit before photobleaching. This **photon budget** has restricted SMLM acquisition speed and biological applicability of the technique to single cultured cells close to coverslip, as imaging into complex biological tissue results in a loss of collected photons that either degrades resolution or completely prevents single molecule localization.

Two independent factors together contribute to the final localization density in a SMLM reconstructed image, and therefore to its resolution: localization precision and labeling density.

The first, localization precision, is the SMLM analog to optical resolution, and has been previously discussed in section 1.2.2.2. To summarize, in the absence of noise, the uncertainty with which a single molecule's position can be estimated from an image of its fluorescence emission varies linearly with the PSF size and inversely with the square root of the number of photons collected above the background in that image. Bright fluorescent probes allow more precise PSF fitting and therefore less error in the centroid calculation.

The second factor, **labeling density**, is slightly more esoteric with no conventional microscopy analog, and yet can be related to the Nyquist criterion in a traditional signal processing perspective. Applying this theorem to the case of SMLM data, it implies that there must be a molecular probe at least every $n/2$ nanometers along the entirety of the structure to achieve a resolution of n nanometers, although some suggest that even a labeling spacing of $n/20$ (10x Nyquist sampling) is barely sufficient for high-quality single molecule reconstructions[33]. Similarly, the notion of **linker length**, the distance between the protein of interest and its fluorescent tag caused by the ligand that binds the two, and **probe size**, both typically disregarded in conventional microscopy, become critical at the nanometer scale of single molecule imaging.

Example Biological Model: Microtubule Network

To visually illustrate the inherent difficulties in single molecule imaging in a biological context, this chapter will investigate the single molecule labeling and imaging of the microtubule structure. Microtubules are one of several cytoskeletal proteins, forming an intricate network of hollow tubes ~25nm in diameter. Their small size, highly dense protein composition, and biological relevance have rendered microtubules ideal structures for super-resolution imaging.

Deschout et al. [34] give an excellent demonstration of the joint effects of localization precision, linker length and labeling density with respect to microtubule imaging (**Figure 1.10**b). In the cases of long linker length, low labeling density, and low localization precision, individual fluorescent molecules are able to be localized without error, but the final reconstruction bears little resemblance to the original microtubule structure; precise, accurate, and dense localizations are required to effectively reconstruct the underlying biological structure.

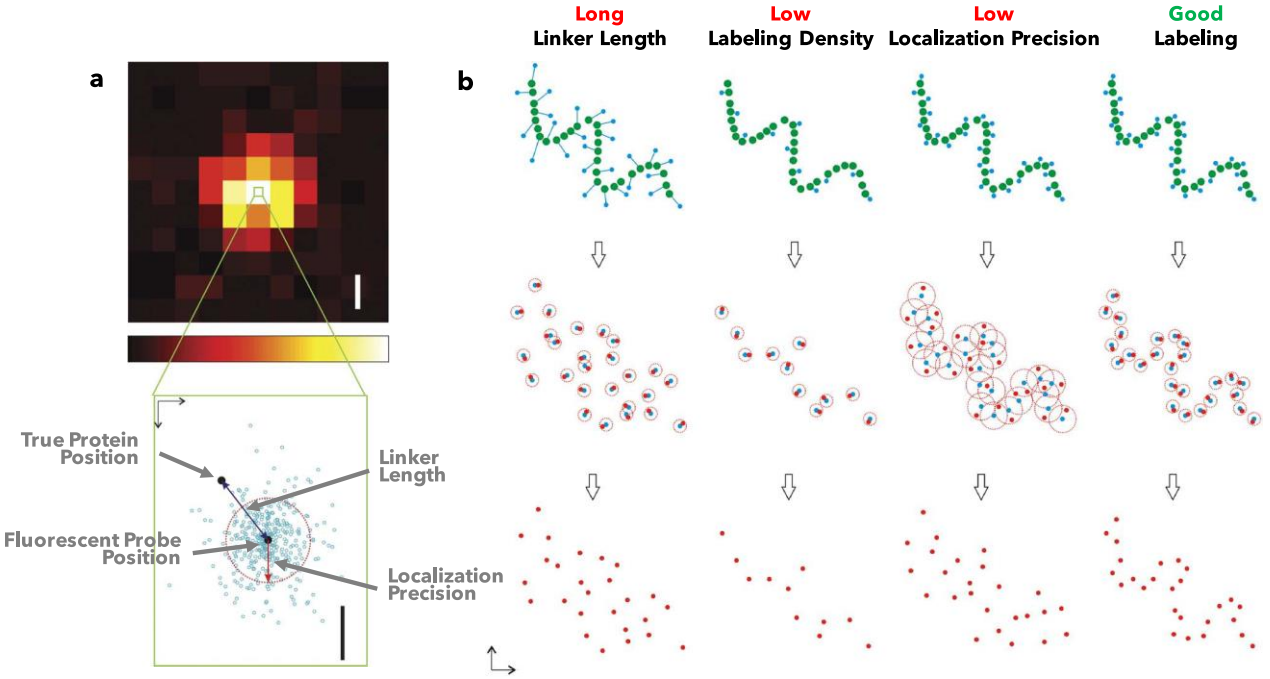

Figure 1.10: Resolution in SMLM requires precise localization of accurate, densely labeled probes. (a) Schematic representation of the critical notions behind resolution in single molecule localization microscopy. Successive localizations of an individual fluorescent probe create a cloud of localizations whose spatial confinement is given by the localization precision. This localization cloud is offset from the true position of the tagged protein by a distance given by the linker length. (b) Long linker length, low labeling density, or low localization precision results in inaccurate structural imaging with SMLM.

Adapted from *Deschout et al.*[34]

Measuring Experimental Resolution in SMLM

The combination of independent factors contributing to the overall image resolution in SMLM prevents a simple, single, measurable metric from being used to quantify resolution. As labeling density and accuracy are difficult to quantify, measures for experimental localization precision are often given as an approximation of a maximal resolution, assuming sufficient localization density in the reconstruction. These values can be simply estimated by calculating the standard deviation of the localizations emanating from a single molecule[34]. For highly dense samples, it is difficult to spatially separate single molecules, and *Endesfelder et al.* [35] demonstrated the use of a nearest neighbor calculation in the subsequent image frame to estimate the true localization precision, assuming that a single molecule will be imaged in several consecutive frames. Importantly, this precision varies for each localization across an imaging field of view, resulting in a variable effective resolution throughout the image that makes assigning a single value for image "resolution" difficult.

Methods do exist, however, the take into account both localization precision and labeling density for calculating the effective resolution of SMLM images. One method, the Fourier Ring

Correlation[36] (FRC), was originally implemented in electron microscopy and can give an estimation of the image resolution by computing a Fourier-domain correlation between two separate images reconstructed from half of the localization data set. This method, however, has one innate drawback in that it is fundamentally reliant on the generation of an image reconstruction.

Resolution vs. Localization Precision: Conventions

Ultimately, the community has yet to converge on a single measure for quantifying image resolution in single molecule localization microscopy. For clarity, the term "resolution" will be used in this manuscript as the ability to separate two individual molecules in any dimension (spatially, temporally, spectrally, etc.). When a resolution is specified, the Abbe criteria ($d = \frac{\lambda}{2NA}$ (1.3) or FWHM is implied. Otherwise, the localization precision (σ, the standard deviation of the localization cloud associated with a single fluorescent molecule or bead) along will be used as a relative indicator of image resolution without factoring in labeling considerations.

Localization Errors and other Factors Contributing to Resolution

In any imaging system, it is essential to understand the processes behind the contrast mechanism from which the image is generated. The key to this in SMLM is ensuring sparse fluorescence such that each separate fluorescent spot can be considered an ideal point spread function of the imaging system. However, the fluorescence is generated from the electric field emitted from nanometer sized molecules, which can vary greatly in their degrees of spatial freedom; some molecules may be immobilized on the coverslip surface, whereas others may be spinning and diffusing freely. In fact, the dipole orientation of these emitters has been shown to have a great effect on the position of the imaged point spread function relative to the true position of the molecule[37,38], although this bias can be removed optically filtering the emission to contain only azimuthally-polarized light[39,40]. These localization biases are important to consider when analyzing single molecule data or quantitatively comparing conditions.

1.2.5.2 Mechanical Drift Correction

Nanoscale mechanical microscope motion, whether emanating from the microscope system or the sample itself, is essential to consider when imaging single molecules. As imaging typically occurs over several minutes, motion that is invisible in diffraction-limited microscopy becomes detrimental to single molecule imaging, since this mechanical drift can exceed the spatial resolution of the imaging system. The principal source for drift in most SMLM microscopes is thermal; focused high-power laser sources temperature create temperature gradients in the sample that result in a slow sample drift on the order of tens of nanometers to several microns after several minutes of acquisition. Thermal isolation and stabilization are thus commonly employed by the use of local sample heating chambers or plexiglass caging. Furthermore, optical air tables are essential for suppressing short time-scale (faster than an image exposure time) mechanical vibrations. Even with vibrational and thermal isolation, residual sample drift may still occur, and a number of methods have been introduced to correct for these drifts, from mechanical stabilization using optical feedback loops to post-processing using stable fiducial markers in the sample.

Lateral: Fiducial Markers

A straightforward method to compensate for lateral drift is to implant photostable fiducial markers into the sample that do not blink or photobleach over the course of the acquisition.

This is traditionally achieved by implanting polystyrene beads of sub-diffraction limit diameter coated with fluorescent dyes, whose excitation and emission spectra are compatible with the spectra of the individual single molecules to be imaged. Tracking the bead's displacement over the course of acquisition, a frame-by-frame *xy*-displacement trajectory can be generated and applied to correct the single molecule localizations (**Figure 1.11**a).

This approach has served as the gold standard in lateral drift correction since the advent of SMLM for a number of reasons. The large number of fluorophores adhered to each bead results in fairly stable fluorescence emission over time, even when imaging in thiol and oxygen scavenger based imaging media. Furthermore, these polystyrene beads adhere easily to the coverglass and can be coated with multiple colors of fluorescent dyes, making drift correction feasibly even when imaging multiple fluorescent species.

One key drawback to using fluorescent beads as fiducial markers is fundamental to their reliance on fluorescent dyes: they are inherently prone to intensity fluctuations and eventually photobleaching over time. Gold nanoparticles have been used as fiducial markers, however their surface chemistry makes them difficult to adhere to uncoated glass coverslips and their relatively unstable photochemistry induces blinking unsuitable for frame-by-frame localization. Recently, nanodiamonds have been used as photostable fiducial markers for drift compensation[41-43]. Their fluorescence mechanism is based on nitrogen-vacancy point defects in the diamond structure, rendering them ideal fiducial markers with broad excitation and emission spectra[44], and incredibly stable fluorescence emission immune photobleaching.

Fiducial markers allow for lateral drift correction with a slightly higher precision than the localization precision of single molecule detection due to their more abundant photon emission. In order to further improve their localization accuracy, and because the drift is a slow process compared to the acquisition frame-rate, it is common to temporally filter the positions, using e.g. a median filter.

These fiducial markers must be injected into the sample with a sufficient density to be in the field of view of the structure to be imaged, which is not also biologically feasible. For imaging continuous structures such as cytoskeleton filaments, an alternative method is sometimes preferred, based on inferring the drift by generating intermediate images made from temporal subsets of the localizations [45]. By cross-correlating these images, lateral sample drift can be inferred. While this method works well for small, constant drifts in samples with a finite structure and a large localization density, it is less precise than fiducial registration both spatially and temporally.

Axial: Coverslip surface detection using a back-reflected IR LED

Fiducial markers serve an excellent tool for estimating and correcting lateral mechanical drift because the precision with which the *xy*-drift trajectory can be calculated is greater than the average localization precision of the individual blinking fluorophores comprising the SMLM image. However, such drifts can also occur in the axial direction, and *a posteori* axial localization

correction is non-ideal since axial drift shifts the focal plane, quickly resulting in out of focus molecules due the small depth of field of the high NA objectives used in SMLM. Furthermore, axial localization (to be discussed in detail in section 3.1) is several times less precise than the lateral localization precision and can induce further variability in the axial localization instead of the desired stabilization.

Therefore, alternative optical systems based on closed-loop feedback are typically implemented in high-precision SMLM microscopes to provide mechanical real-time axial stabilization. While several implementations are available, the most common solution is to detect the axial position of the surface of the coverglass and mechanically shift the microscope objective axially to stabilize its focal plane. By injecting a near infrared light emitting diode (LED) into the microscope objective such that it is focused on the coverglass, back-reflected, collected by an offset lens and finally imaged onto a line CCD, the imaging system's focal plane is decoupled from the coverslip surface plane, which can be continuously positioned axially using the line CCD. Commercial implementations of this technique offer the ability to stabilize the focal plane with 50nm axial precision.

While this real-time axial repositioning of the objective is simple to implement, it has several key drawbacks. Since the system is based on using a reflection off the top surface of the coverslip, a refractive index difference between the imaging media and the coverslip is essential to proper function, preventing axial correction of samples embedded in high-NA gels like vectashield or glycerol. Furthermore, the use of near-IR diodes for coverslip surface detection limits the spectral selection of dyes for single molecule imaging to a maximum of 800nm.

A new technique introduced by *Bon et al.* uses gold nanoparticles embedded between the coverslip and the biological sample instead of reflection to sense the coverslip surface, allowing for combined lateral and axial active drift correction[46]. While promising, this technique requires significant modifications to the optical path and requires a quantitative phase imaging camera to image the gold nanoparticles, limiting its implementation in current conventional microscopes.

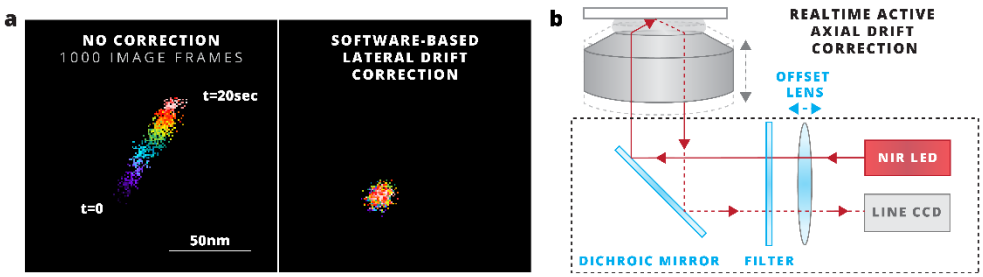

Figure 1.11: Lateral and Axial Drift Correction for SMLM. (a) Lateral drift can be compensated post-acquisition by generating a drift trajectory from a fiducial marker present in every imaging frame. (b) Axial drift is commonly corrected using a system similar to the Nikon Perfect Focus System (PFS) that uses an NIR LED to detect the coverslip surface.

1.2.6 On the Approximation of Single Molecules as Ideal Point Sources

The fundamental assumption underlying single molecule localization methods is that the localized region represents the ideal, diffraction-limited point spread function of only one single emitting molecule. It is critical to consider the implications of this assumption and the consequences of their violation.

An inherent issue when imaging densely labeled stems from the stochastic activation of single molecules exploited in SMLM. Indeed, while it is possible to slightly reduce the activation density by minimizing UV-light power density or modifying the imaging buffer to favor long-lived dark triplet states, there is a non-null probability that multiple fluorescent emitters will be simultaneously activated in a given spatial region at a given time. The fluorescent image of these multiple emitters is segmented and localized, but the resulting localization is biased and can create artifacts in super-resolution reconstructions[47]. These density-based artifacts can be particularly misleading when studying protein clustering, where artefactual localizations could cause the appears of false clusters of spatially-separated proteins, although a recent method based on varying the labeling density can be used to validate true degree of protein clustering[48].

A numerical solution also exists in the form of density-aware fitting algorithms. A logical extension of the single Gaussian fit used in typical localization algorithms is to use a multiple-Gaussian fit[49]. While these multi-emitter techniques are effective, they are much more computationally intensive than simple single Gaussian fits, and are themselves prone to errors, particularly when the point spread function of the microscope differs from an ideal Airy function, as in 3D imaging. Moreover, these methods offer inferior localization precision, and prevent efficient single-molecule tracking experiments, restricting their use to very particular applications with extremely very high fluorescence density.

To ensure accurate and efficient reconstructions, it is imperative that only a single fluorescent molecule emitting in a diffraction-limited area per frame. To achieve this single molecule condition, a combination of the appropriate protein labeling technique and correct imaging conditions must be implemented.

1.3 TARGET PROTEIN LABELING STRATEGIES FOR SINGLE MOLECULE IMAGING

Single molecule imaging is very sensitive to a variety of labeling errors, which are otherwise transparent in traditional fluorescence microscopy. Labeling specificity for the desired structure is of critical importance, as is minimizing the linker error, the distance between the fluorescent marker and the protein it is tagging. This section details the import of these labeling properties for single molecule imaging.

The field of fluorescence microscopy owes its specificity to the ability to specifically tag fluorescent molecules to biomolecules of interest. The first major innovation with this regard occurred in 1941, where *Coons et al*[50] first demonstrated the ability to couple antibodies to organic fluorescent dyes, thereby allowing any antigen of interest to be selectively labeled and imaged. Commonly referred to as **immunostaining** or **immunolabeling** (*immuno* as a reference to the immunological origin of the antibodies), this technique is widely used in the field of biology as a readout for a specific protein. Furthermore, the technique is inherently multiplexible, allowing for several antibody tags with spectrally separate fluorescent dyes to simultaneously tag multiple proteins of interest in a single biological sample. However, the technique is fundamentally limited by the antibody accessibility and antigen specificity; “bad” antibodies result in unspecific binding which manifests itself as background in microscopy images.

It wasn't until 1962 with the discovery of the Green Fluorescent Protein (GFP)[51] and progress in molecular biology that eschewed the use of exogenous markers and allowed for the direct expression of proteins fused directly to various fluorescent proteins. The advent of these **genetically encoded fluorescent proteins** in a wide variety of spectral ranges retained the multiplexibility of antibody-based techniques with an even higher molecular specificity, at the expense of generally dimmer fluorescent proteins in comparison to organic fluorescent dyes. While this technique has been frequently used, it is often criticized in biological studies as they are difficult to express in the same concentration as the original, unmodified protein, and these fused protein complexes possibly change the function or accessibility of the original protein. While it is possible to study these complexes at the native concentration by knocking out the entirety of the original protein and expressing the fused complex with the fluorescent protein at the original concentration, this method cannot function for all proteins and is fundamentally restricted to a single generation of cells, as the supplemental RNA which codes for this protein complex is not incorporated into the organism's genome.

Quite recently, a targeted genome editing system known as CRISPR-Cas9 (Clustered regularly interspersed short palindromic repeats) has addressed this issue by allowing for permanent modification of the genetic code of an organism[52]. These revolutionary advances in molecular biology permit the native expression of fused fluorescent protein complexes in cell lines or even entire organisms, opening fluorescence microscopy to the study of a wide variety of proteins at their native expression level in genetically modified cells.

1.3.1 Strategies for Efficient Single Molecule Labeling

Single molecule super-resolution imaging takes advantage of the unique photophysics of certain fluorescent molecules. When considering probes for single molecule imaging, there are two major components which need to be optimized: The fluorescent molecule and its underlying photophysics, and the ligand or mechanism used to attach the fluorescent molecule to the protein of interest. This section discusses the relevant photophysical properties to consider for ideal single molecule imaging, as well as how to efficiently and specifically label these single fluorescent molecules to biological structures of interest.

1.3.1.1 Fluorescent Probe Photophysics

In terms of photophysics, brightness, total number of photons, and temporal stability of photon emission are essential parameters to consider when evaluating the performance of a fluorophore for single molecule imaging. Together, these quantities define the number of photons per localization event, affecting the localization precision and thus the effective image resolution.

1.3.1.2 Probe-Protein Linker Length

In all single molecule fluorescence imaging, it must not be forgotten that the fluorescent probe is just a proxy for the protein of interest. Its localization is not necessarily identical to the location of the protein of interest. Indeed, a variety of methods exist that link the fluorescent molecule to the protein of interest, and the size of this linker defines the linker length between the fluorescent molecule and the actual protein.

Conventional labeling approaches for bulk widefield and confocal microscopy use the immunolabeling process with antibodies targeted against the protein of interest. These

antibodies can easily be coupled to a wide range of bright organic dyes. While this labeling technique is also used for SMLM, common full-size antibodies are ~15nm in length. The combination of primary and secondary antibodies can therefore easily introduce 20-30nm between the probe and the protein, thereby introducing a linker-induced localization bias larger than the localization precision. Furthermore, the relatively large size of antibodies can prevent them from reaching targets in protein-dense cellular compartments due to steric hindrance. Antibody size can be reduced by using antibody fragments (Fabs) or directly-coupled primary antibodies or nanobodies[53]. However, specific antibodies do not exist for all proteins, and non-specific binding of antibodies can result in a strong background in super-resolution reconstructions or false interpretation of the biological structure.

An alternative to immunolabeling is to couple organic dyes to small biological or synthetic ligands to increase specificity and decrease linker error. Genetically encoding short binding sites like HaloTag [54], Snap-tag[55], or Flag[56] greatly reduce the linker length to just a few nanometers, but background specificity can be difficult to control. A recently introduced technique based on the highly specific biotin-streptavidin coupling scheme combines the small linker length of an genetically expressed tag enzymatically converted to a biotin tag with monomeric streptavidin coupled to organic dyes to perform live- and fixed-cell super-resolution imaging.[57]

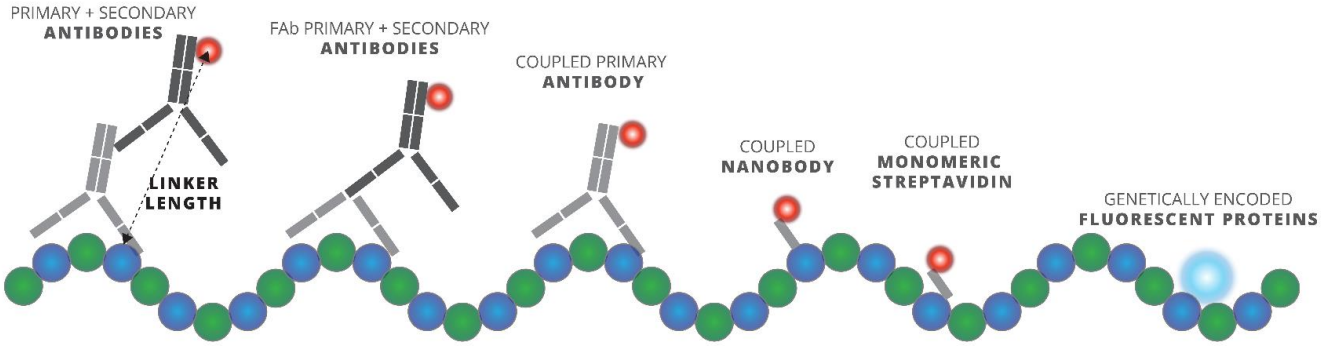

Figure 1.12: Probe-Protein Proximity in SMLM Labeling Strategies. The linker length between the fluorescent probe directly affects the accuracy of the localization. Immunolabeling techniques used in conventional microscopy result in ~20nm of linker error that, while invisible in conventional microscopy, is critical in SMLM. Directly coupled primary antibodies or nanobodies offer the same labeling specificity yet bring the fluorescent molecule much closer to the protein of interest. New labeling strategies like monomeric streptavidin increase labeling specificity and density while minimizing linkage error. Genetically encoded fluorescent proteins like GFP offer the advantage of exact protein position, but are much dimmer than organic dyes.

The final common technique is to genetically express a photoactivable fluorescent protein directly coupled to the protein of interest. These tags, based on the cylindrical structure of GFP, are just ~3-4nm in size, and can be genetically coupled to the protein of interest at very specific molecular sites inaccessible by conventional immunolabeling. However, genetic modification of proteins requires careful control experiments to verify the protein overexpression level. Critically, these fluorescent proteins have a photon budget an order of magnitude smaller than their organic dye counterparts, limiting their localization precision to the 10s of nanometers regime. Furthermore, there is currently no bright photoactivable fluorescent protein in the 650-700nm emission wavelength range, a spectral window especially important for background-free cellular imaging.

1.3.1.3 Considerations for Live Cell Single Molecule Imaging

Compared to electron microscopy, which is generally considered the gold-standard in terms of resolution, single molecule based super-resolution microscopy provides a key advantage: it can be used to image live cells. However, the electromagnetic radiation that is absorbed by the cell must be taken into consideration when selecting the appropriate probe for live single molecule imaging. The previously discussed immunolabeling techniques have the disadvantage that antibodies cannot penetrate the cell membrane, and thus these techniques can only be used to label surface proteins like membrane receptors. To access internal structures with antibodies, the cell must be fixed and the membrane must be permeabilized[58-60]. Perhaps the most common and minimally-invasive technique for live-cell imaging uses the genetically fusion of the target protein with fluorescent protein derivatives of GFP in a wide spectrum of absorption and emission wavelengths .

1.3.2 Low-Density Single Molecule Labeling for Single Particle Tracking

The field of single molecule imaging found its first hallmark biological application in single protein tracking. This was accomplished by subsampling the entire population of the protein of interest with low-density tagging. Functionalization of the fluorescent quantum dots (QDs) enabled the first In-vitro and in-vivo QD-SPT applications[61], and their brightness continues to make them an excellent choice for SPT applications where brightness is preferred to a large number of tracks, recently having been demonstrated for neurotransmitter receptor tracking in brain slices[62,63]. However, their large size, in the tens of nanometers, causes steric hindrance and prevents them from entering tight, dense cellular compartments. While these low-density techniques continue to have their use in certain low-density single particle tracking applications, newer, stochastically-activated probes have enabled nanometer-scale structural imaging with high-density single molecule imaging.

1.3.3 High-Density Single Molecule Labeling: Stochastic Approaches

The recent photochemical advances in fluorescent probes have opened the doors to a new realm of single molecule imaging where the entire population of interest is tagged with stochastically activated fluorescent probes, simultaneously allowing high-density labeling and spatially sparse imaging. A variety of extremely similar techniques named with confusing acronyms make introducing the field of SMLM difficult; here, the techniques are simply separated by their method of illuminating individual single molecules.

1.3.3.1 Genetically Encoding Fluorescent Proteins (PALM)

Photoactivated localization microscopy (**PALM**)[8,64] was the first single molecule localization-based imaging method that allowed for nanometer-scale imaging of individual proteins. This technique was made possible by the advent of photoactivable fluorescent proteins that are genetically expressed adjacent to a protein of interest, offering high density, specific labeling. The stochastic photoactivation process induces a shift in the chemical structure of the protein, red-shifting its excitation and emission wavelength. By photoactivating with microWatts of UV excitation, a sparse subset of these fluorescent proteins are stochastically photo-activated over time, enabling single molecule in the photo-activated channel.

While a wide range of photoactivable molecules exist[65] based on photoactivable-GFP[66], PA-mCherry[67], EosFP[68], and Dendra2[69] are the most commonly used in PALM imaging. The relatively low intensity of light required for their photoactivation (µWs) and imaging (mWs) as well as their relatively good brightness for a FP render them ideal for live-cell single molecule imaging and tracking[10]. These fluorescent proteins, however, are not as bright as common organic fluorophores and have a smaller total emitted photon budget, resulting fewer, less precise localizations. Furthermore, they must be genetically expressed by the cell, causing concerns of overexpression and potential protein modification.

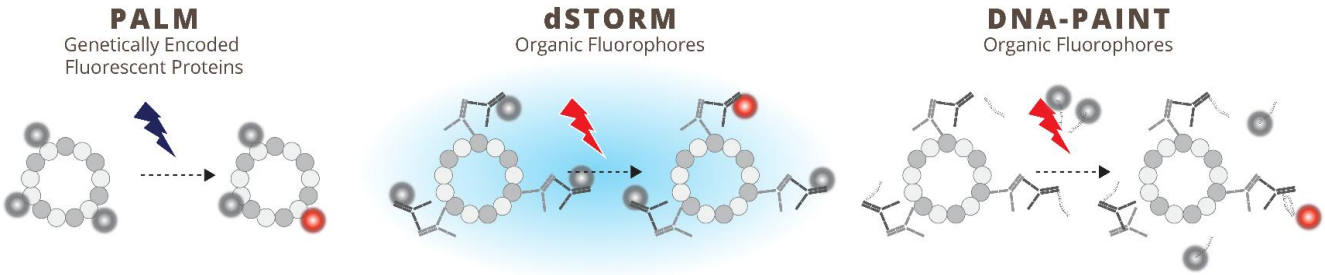

Figure 1.13: High-Density Single Molecule Labeling Approaches. PALM uses fluorescent proteins that photoconvert or photoactivate with application of a low dose of UV light (~µW) to ensure single molecule conditions. In dSTORM, a special imaging buffer enable stochastic blinking of conventional fluorescent probes. The DNA-PAINT technique decouples the protein labeling from the fluorescent tag, linking the two with complementary strands of DNA. This technique allows nearly infinite and potentially quantitative single molecule imaging thanks to the well-understood binding kinetics of DNA.

1.3.3.2 Immunolabeling with Organic Fluorophores (STORM)

Introduced shortly after PALM in 2006, **STORM**[11] allows for single molecule imaging using traditionally immunolabeling techniques by labeling with a pair of fluorescent dyes and weakly activating to induce stochastic blinking of a reporter dye. While this technique was the first to demonstrate stochastic single molecule imaging, immunolabeling with a specific activator-reporter dye pair prevents the technique for general accessibility. In 2008, direct STORM (**dSTORM**)[12] demonstrated stochastic blinking of single conventional organic dyes when placed in a special imaging buffer containing an oxygen-scavenger like *glucose oxidase* and a dark-state favoring thiol, like ßMEA. While many commercially available dyes can be used for dSTORM imaging, Alexa647 is still considered as the gold-standard in terms of brightness and blinking quality[70]. STORM imaging with organic dyes offers extremely high localization precisions, on the 5-10 nanometer scale, at the expense of a high dose of laser power required for efficient blinking, in the kW/cm² range. This intensity of light, plus the toxic imaging buffer, has limited most STORM imaging to the structural study of fixed cells.

1.3.3.3 Transient Protein Labeling: PAINT/uPAINT/DNA-PAINT

Transient labeling approaches exploit the high photon count of organic fluorophores without the requirement of special imaging buffers or high-intensity lasers to enable single molecule conditions. Another way to introduce spatial sparsity is to stochastically label the protein of interest during the imaging process. First proposed in 2006 under the name of Points Accumulation for Imaging in Nanoscale Topography[13], **PAINT** imaged fluorescent molecules which specifically bind to biological structures of interest. This technique was later refined by *Giannone et al*[71] by transiently binding antibodies coupled to organic fluorophores, allowing the tracking of endogenous membrane-based proteins in a variant called **uPAINT** (universal PAINT). **DNA-PAINT**[72] extends dissociates the protein labeling process from fluorescent probe

binding by inserting a pair of complementary DNA-strands coupling the probe to the antibody, thereby rendering photobleaching of individual fluorescent markers negligible by allowing an essentially infinite number of fluorescent probes to be imaged.

1.3.3.4 Multicolor SMLM

One of the hallmark advantages of fluorescence microscopy is its inherent ability to be multiplexed: by using fluorescent markers with spectrally distinct excitation and emission spectra, multiple biological structures can be imaged in the same sample, opening the doors to a suite of analyses to investigate the respective organization and potential interaction of several proteins. In conventional diffraction-limited microscopy, one often refers to spatial overlap, commonly referred to as **colocalization,** as a readout of molecular interaction. However, true molecular spatial colocalization cannot exist, and the measured colocalization is a fundamental artifact of the limited resolution.

SMLM has opened the doors to determining molecular coordinates with nanometer-scale precision and the study of the proximity of several proteins. The first report of multicolor SMLM was an implementation of multicolor STORM by *Bates et al* in 2007 using a shared reporter dye, Cy5, with 3 spectrally separate activation dyes acquired sequentially[73]. For multicolor dSTORM, it is essential to find the correct combination of spectrally separate dyes which retain good blinking properties in a common imaging buffer. Significant research has gone into the choice of fluorophores[70] and imaging buffer[74], but these constraints generally limit dSTORM to two colors. A common and simple solution to 2-color SMLM imaging has been dSTORM of Alexa647 combined with PALM imaging of mEOS, obviating the need for imaging buffer optimization for several organic fluorophores.

Conventional multicolor SMLM imaging using static labeling is hindered by a number of experimental difficulties, from the necessity of special filter sets for each wavelength, to differing localization precision for each wavelength and wavelength-dependent chromatic aberrations. To address this, a number of methods have been proposed to dynamically label and sequentially image several different proteins of interest with the same fluorescent probe. In 2014, *Jungmann et al* introduced an easily multiplexible method, called DNA-PAINT, using orthogonal DNA strands bound to conventional secondary antibodies to tag 4 proteins of interest, and sequentially performing stochastic DNA-PAINT imaging of each structure [72]. This Exchange-PAINT technique has recently been generalized to primary antibodies and other small-molecule binders for sequential DNA-PAINT imaging of 9 proteins[75]. Similarly, *Kiuchi et al* demonstrated the screening and application of several PAINT probes which specifically bind to various biological structures with a sufficiently low affinity such they can be efficiently washed away between acquisitions[76].

Whether concurrently or transiently labelled, multicolor SMLM experiments are frequently performed sequentially, using a specific filter set for each imaging channel to optimize contrast for each fluorescent probe. The result is a linear increase in the acquisition and analysis time, and total volume of acquired data. Commercial systems exist for performing simultaneous multicolor imaging of up to 4 channels, by optically splitting the total fluorescence emission using a set of dichroic mirrors for each fluorophore being imaged and dividing the field of view into wavelength-specific regions on the imaging sensor. While these simultaneous multi-channel imaging methods are critical to live-cell imaging, they limit the temporal resolution and

the field of view by mandating the use of the full imaging sensor. Moreover, they require a set of filters for each specific fluorophore reducing the number of collected photons and therefore the localization accuracy for SMLM. Importantly there is a tradeoff between the number of wavelengths imaged, the spatial and temporal resolutions, and the field of view being imaged.

In SMLM, the localization uncertainty of each individual localization, and thus the effective point spread function, varies as a function of the fluctuating number of photons collected per localization per image frame. Additionally, each distinct fluorescent species exhibits a unique photon emission cycle and total number of photons emitted, resulting in localization precisions that vary between the color channels. Furthermore, nanoscale chromatic aberrations on the order of the localization precision stemming from imperfectly corrected optical components must be carefully characterized and corrected when performing quantitative comparisons between color channels[77].

1.4 SPATIOTEMPORAL SAMPLING OF SINGLE MOLECULE FLUORESCENCE

Once the target protein has been efficiently labeled with fluorescent probes, we must consider how to appropriately excite these fluorophores and efficiently collect their emitted photons. When imaging single molecules with low photon counts, it is essential to maximize the signal to noise ratio. The first single molecule imaging methods were restricted at first to cryogenic temperatures[78] due to the lack of sensitive detection but shortly thereafter, advancements in fluorescent probes and detector photosensivity enabled single molecule imaging applications to expand into live-cell imaging applications.

1.4.1 Optimizing Contrast with a Constrained Photon Budget

While each fluorescent probe has its own unique advantages and disadvantages for imaging use, all fluorescent molecules share one common disadvantage: the number of fluorescence cycles is limited, and after a certain number of excitation-emission events, the molecule's chemical structure will be irreversibly altered in such a way that it can no longer fluoresce. This process, known as photobleaching, essentially limits the total number of photons that a single fluorescent molecule can emit, giving each probe its own unique photon budget. In single molecule imaging, it is essential to optimize the imaging system and parameters to the limited photon budget of the fluorescent molecule being imaged.

1.4.2 Efficient Single Molecule Excitation

There are a number of commonly employed excitation schemes used for single molecule imaging, ranging in complexity of implementation, imaging thickness, penetration depth, and perceived contrast.

Limited contrast: Widefield

The simplest illumination scheme is a classical wide-field or epifluorescence illumination (**Figure 1.14**a). Focusing the excitation laser at the back focal plane of the objective along the optical axis results in the light exiting the objective parallel to the optical axis. While this illumination scheme works effectively in conventional microscopy, the strong background from

out of focus fluorescence above and below the focal plane greatly reduces contrast and makes single molecule imaging quite difficult.

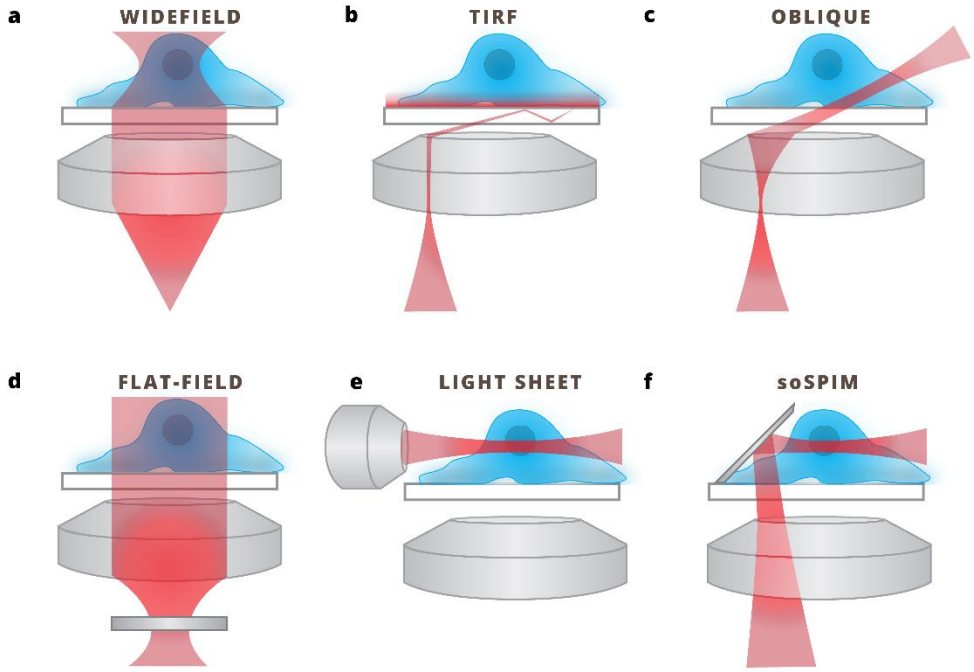

Figure 1.14: Single Molecule Excitation Schemes. (a) Widefield imaging suffers from strong background from excitation of out of focus fluorophores. (b) TIRF imaging exhibits strong optical sectioning within a few hundred nanometers from the coverslip surface. (c) Oblique or HiLo imaging creates thin sheet of light that improves contrast over widefield imaging for a few microns above the coverslip surface. (d) The recently-introduced flat-field imaging uses advanced excitation optics to eliminate the Gaussian spatial profile of the excitation beam and creating a homogeneous, high-power excitation beam. (d) Light sheet imaging decouples the excitation from the detection by the use of two separate objectives, but the geometry is mechanically difficult to implement for single molecule imaging. (f) A single objective light sheet excitation (soSPIM) uses a 45° mirror in the sample to benefit from the excellent optical sectioning of light sheet excitation combined with the collection efficiency of high numerical aperture collection objectives.

High-contrast, low penetration depth: TIRF and HiLo

Total Internal Reflection of Fluorescence (TIRF) [3] addresses the strong background in widefield illumination by exciting only the first few hundred nanometers above the coverslip surface with an evanescent wave (**Figure 1.14**b). It is obtained by including a set of beam steering mirrors in the excitation path and focusing the excitation near the outside of the back focal plane of the objective, adjusting the excitation laser such that it is totally internally reflected in the coverslip due to the difference in refractive index of the sample imaging medium. This provides an excellent signal-to-noise ratio and extremely thin optical sectioning. When imaging true biological samples, however, classical TIRF systems are often marred by interference patterns. One convenient solution is to rotate the excitation beam in the back focal plane of the objective, thereby homogenizing any interference that might result from single angle illumination while retaining the optical sectioning of TIRF.

To image thicker specimens, Highly Inclined Laminated Optical Sheet (HiLo)[4] can be used, where the excitation beam is focused closer to the optical axis of the back focal plane, resulting in a thin sheet of light with an angle oblique to the optical axis (**Figure 1.14**c). This imaging

method can provide excellent optical sectioning and a strong signal to noise ratio at a couple of microns into the sample.

High power: Flat-field illumination

To address the issue of field inhomogeneity due to the Gaussian spatial profile of the excitation lasers, *Douglass et al.*[79] and *Deschamps et al.*[80] recently introduced similar methods for illuminating the sample plane with a homogeneous, flat illumination field (**Figure 1.14**d). This technique trades the optical sectioning of TIRF excitation with a high power, uniform illumination, which is particularly imperative when doing quantitative single molecule photophysics analyses.

High-contrast, deep penetration: Light sheet illumination – soSPIM

Ideally, the excitation and detection paths would be completely decoupled, as in conventional selective plane illumination microscopy (SPIM), also called light sheet microscopy. In SPIM imaging, two separate objectives are mounted orthogonally to each other, sharing a common focus at the sample plane, allowing for strong optical sectioning through the creation of a thin sheet of light perpendicular to the collection objective (**Figure 1.14**e). However, the high NA objectives used in single molecule imaging impose strict mechanical constraints that prevent two commercial microscope objectives to be placed in an orthogonal geometry. Recently, *Legant et al.* [81] demonstrated single molecule lattice light sheet imaging in this orthogonal geometry using a pair of custom-developed low-NA excitation and high-NA detection objectives. Even with these custom designs, the geometry still imposes constraints on the size of samples being imaged.

A new technique has emerged that allows for the creation of this light sheet orthogonal to the collection path was introduced in 2015 by *Galland et al.*[82]. The single objective SPIM (soSPIM) system exploits polymer-based 45° microfabricated mirrors to create a thin sheet of light in the same field of view as the single molecules to be imaged (**Figure 1.14**e). This allows all the benefits of high-NA immersion based detection with the optical sectioning of light sheet systems.

1.4.3 Efficient Single Molecule Fluorescence Collection

Single molecule imaging mandates an extremely efficient collection scheme due to the low photon emission count of common fluorescent molecules. Microscope systems are thus designed to maximally collect fluorescence emission, employing high numerical aperture (NA) objectives. To achieve a NA greater than 1, immersion objectives remove the air gap between the glass objective and coverslip by introducing an “index-matching” intermediate layer of water, glycerin, oil, or other viscous transparent gels that increases the NA aperture of such objectives up to 1.49 with standard glass. These microscope objectives are composed of a complex system of precisely designed and manufactured glass lenses. Most objectives used in single molecule imaging have a magnification of 60x or 100x to effectively spread the point spread function onto several pixels.

1.4.3.1 Spatial Considerations: Single Molecules as Point Sources

Spatial sampling of single molecule fluorescence through a digital imaging system requires discretization of the point spread function onto a digital sensor. A certain compromise is inherent when binning a limited number of collected photons into discrete pixels: smaller pixel size allows for better sampling at the tradeoff of reduced photons per pixel. It is usual, in single-

molecule imaging as in microscopy in general, to use the ideal Shannon-Nyquist sampling criterion defined by a pixel size equal to half the lateral resolution. The magnification of the detection objective and any additional zoom provided by the tube lens are therefore carefully chosen to effectively sample the point spread function onto the camera.

1.4.3.2 Sensitivity Considerations: Separating Signal from Noise with Sensitive Detectors

Most single molecule imaging techniques use a widefield detection scheme, where an entire field of view of the sample is imaged directly onto a grid of photosensitive detectors in a scientific camera. This allows a high degree of spatial multiplexing, imaging fields of view on the order of around 100μm x 100μm.

Conventionally, charge-coupled devices (CCD), and in particular electron multiplying CCDs (EMCCD) have been used for single molecule detection, due to their high quantum efficiency (>95%). In order to efficiently detect single molecules emitting a small number of photons, it is essential to reduce sensor noise. CCDs are generally air- or water-cooled to reduce background "dark current," a thermally-induced Poisson distributed background. Similarly, the electron multiplication stage of EMCCDs renders insignificant the pixel readout noise inherent to CCDs, but itself introduces a new source of stochastic excess noise. The impressive sensitivity of EMMCDs has made them the de facto detector for full-field single molecule imaging in recent years.

While other detector alternatives exist, few technologies are as well suited to single molecule fluorescence imaging as EMCCDs. Complementary Metal Oxide Semiconductors (CMOS) detectors, for example, provide exceptional speed and sensor size, but have traditionally lacked the necessary quantum efficiency for single molecule imaging applications. Recently, however, scientific CMOS (sCMOS) devices have improved their peak quantum efficiency to nearly 80% and dynamic range over conventional CMOS devices, rendering them ideal for high frame rate, large field of view acquisitions. Commercially available sCMOS cameras commonly have 2048 x 2048 pixel grids with 6.5μm x 6.5μm pixels, and can image between 100Hz-1000Hz depending on the size of the region of interest. Typical EMCCDs, however, have a smaller maximum sensor size of 512 x 512 pixels, albeit with larger, 16μm x 16μm pixels and a reduced imaging speed between 20Hz-100Hz. Although they are subject to very strong pixel-dependent readout noise and must be carefully calibrated for accurate localizations[83], sCMOS cameras have been shown to be especially effective for fast imaging of bright molecules and ideal for fast dSTORM imaging[83].

1.4.3.3 Temporal Considerations: Optimizing Exposure for Single Molecule Fluorescence

With extremely fast and sensitive detectors like sCMOS, the limiting factor in the temporal sampling of single molecule fluorescence is not technological, but is rather due to the photophysical process of fluorescence itself. While the fluorescence cycle (absorption of an excitation photon and emission of a fluorescence photon) occurs on the order of nanoseconds, many collected photons are required in order to generate an accurate image of the single molecule. The exposure time is ideally matched to the length of the single molecule fluorescence emission burst. Typical single frame exposure times for single molecule imaging of most conventional fluorescent probes is typically in the range of 1-100 milliseconds.

1.4.3.4 Imperfectly detected molecules and wavefront aberrations

The camera's ability to create an accurate image of the ideal point spread function of the microscope assumes a perfect optical imaging system. Any deviations to this ideal model, known as **wavefront aberrations**, result induce imperfect wavefront focusing, thereby reducing the number of photons in the focal plane. The resulting localization is therefore less precise and possibly skewed with respect to the true position of the molecule. These aberrations emanate from a variety of different sources – both from the sample and the microscope system itself – and aberrations emanating from specific optical misalignments have common names. While this topic will be further discussed in **CHAPTER 3**, some common wavefront aberrations which and their specific implications in SMLM are briefly introduced here.

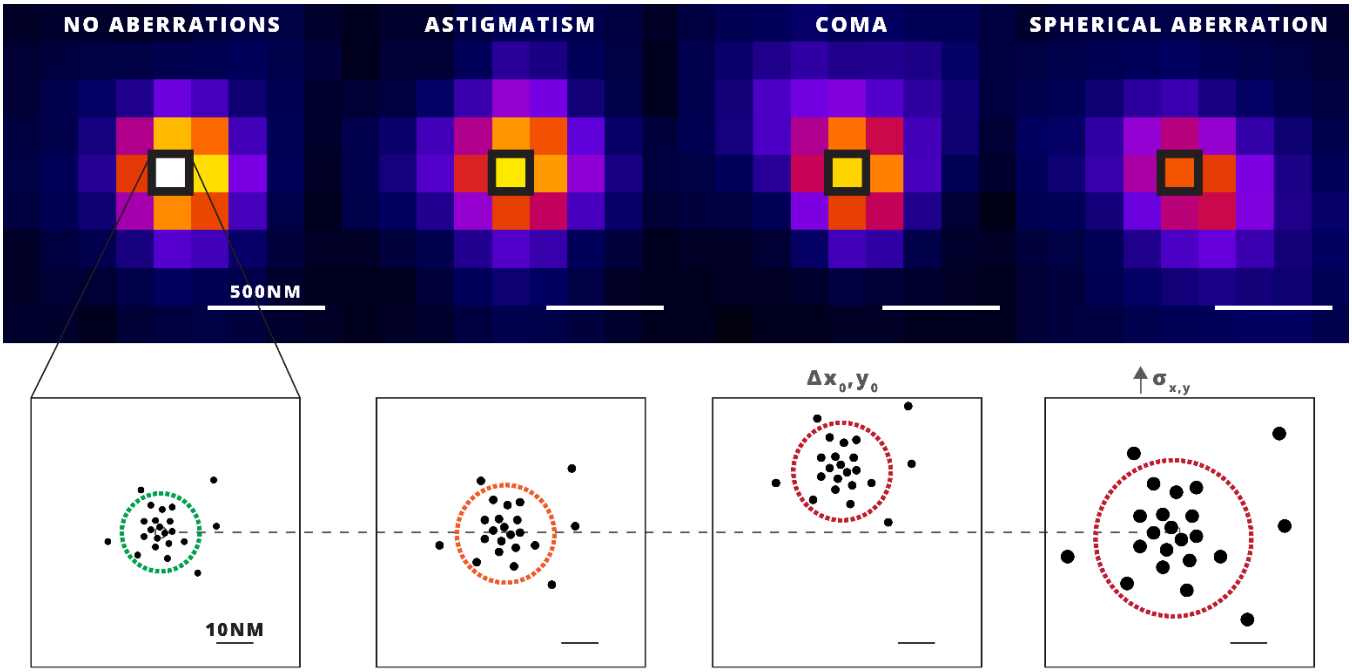

Figure 1.15: The Effect of Common Microscope Aberrations on Localization. The astigmatism aberration results in a cross-shaped PSF in the nominal focal plane, slightly reduces the peak intensity and decreasing localization precision. The coma aberration is detrimental to single molecule localization as it laterally shifts the localization cloud from the true position of the single emitter. Very common in microscopy, spherical aberration reduces the photon count in the nominal focal plane and greatly increases the variance of the localization process.

Spherical Aberrations from Refractive Index Mismatches

Spherical aberration is perhaps the most commonly found optical aberration in microscopy systems, specifically in single molecule imaging systems. The use of high magnification, high NA, oil-immersion microscope objectives to collect a maximal number of photons comes with a tradeoff: most biological samples are submerged in imaging media with a refractive index close to water, and this refractive index mismatch between the sample (containing the single molecules being imaged) and the coverslip/immersion medium axially stretches the PSF: rays closer to the optical axis will focus at a different axial position than those near the extremities. The net effect is a reduction of the photons and a marginally wider PSF in the effective focal plane, which in turn reduces the localization precision and the effective resolution in SMLM images (**Figure 1.15**).

While these spherical aberrations are very common, it is possible to alleviate their impact or modify the optical system to minimize these aberrations. It is common to submerge the sample

in an imaging medium with a refractive index close to that of the immersion medium and coverglass. This is unfortunately incompatible with live-cell experiments. Another alternative is to use a water immersion objective at the cost of a slightly reduced numerical aperture (~1.2 compared to ~1.4 for oil immersion objectives).

Aberrations stemming from optical system misalignment

Two other primary aberrations quite commonly found in single molecule microscopes stem from misalignments in the optical path of the imaging system. Similar to spherical aberration, **astigmatism** is the effect of varying focal length for a set of rays emanating from a common point in the sample plane; however, unlike spherical aberration, there is not radial symmetry to an astigmatic system. An astigmatism occurs when rays from two perpendicular planes converge to two separate foci; simply, horizontal rays will have a separate focus than vertical rays, resulting in a cross-like shape of the PSF at the average focal plane (**Figure 1.15**).

Lastly, and perhaps the simplest to visualize, known as **coma**, which manifests itself as a slightly comet shaped PSF, with a central node and a large tail, is linked to an off-axis optical element in the imaging path. This can be due to an improperly aligned lens (either the microscope objective or the tube lens), or quite commonly due to the coverslip being non-orthogonal to the imaging element. This induces a lateral offset in the localizations, resulting in inaccurate localization of the true position of the fluorescent molecule (**Figure 1.15**).

In widefield microscopy, these optical aberrations may be observed as a slight, nearly imperceptible blurring of the image. In SMLM, however, these aberrations are amplified via the Gaussian fitting process, resulting in biased, sometime false, estimates of the localization of the underlying emitter. The reduction of in focused photons due to these aberrations as well as the contrast needed for single molecule imaging has restricted SMLM applications close to the coverslip surface, making imaging in complex biological imaging environments impossible. It is therefore critical to have an optimally aligned imaging system with minimal aberrations, and advancing SMLM imaging will require correction for any sample-induced aberrations.

1.5 THESIS SUMMARY: OPTIMIZING ATTAINABLE INFORMATION FROM SINGLE EMITTERS

The past few decades have seen swift advances in chemical probes and optical schemes that have enabled single fluorescent molecules to be visualized, localized, and tracked in native cellular environments. A critical, recurring theme found in this introductory chapter on single molecule imaging has been that the resolution gained by localizing single fluorescent molecules is fundamentally limited by the ability of the imaging system to accurately and efficiently collect the limited number of photons emitted by these individual molecules. Due to these low photon counts and the optical aberrations stemming from system imperfections or sample inhomogeneities, SMLM has been traditionally limited to imaging on the surface of glass coverslips.

This thesis aims to address the issues limiting depth, resolution and spectral information in three-dimensional single molecule imaging using a combination of optical, chemical and numerical approaches. Together, these contributions advance SMLM towards quantitative single molecule biology in complex systems.

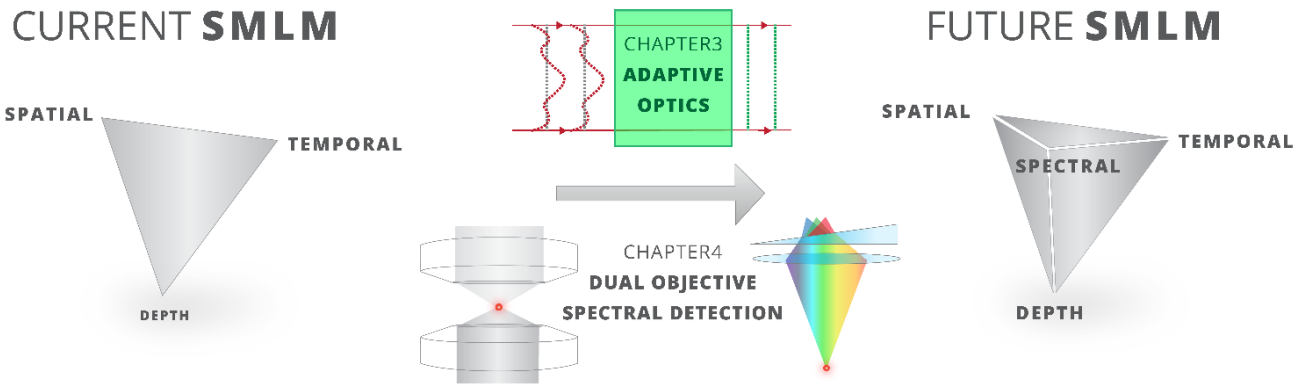

Figure 1.16: Expanding the Resolution Triangle with Advanced SMLM Techniques. This thesis aims to expand the resolution and applicability of conventional single molecule imaging systems through two primary methods: correcting wavefront aberrations using adaptive optics to enable 3D imaging deep in complex biological samples, and adding a second collection objective to enable spectral detection of single molecules.

CHAPTER 2

TOWARDS SINGLE MOLECULE QUANTIFICATION AND IMAGING

Single molecule imaging offers a unique peek into the nanoscale molecular environment that has previously been hidden behind the blur of the diffraction limit. While sub-micrometer scale structural information can be obtained by localizing individual fluorescent molecules and accumulating these nanometer-scale precision localizations over tens of thousands of imaging frames, a wealth of additional quantitative information can be extracted from the localized molecule spatio-temporal pattern. However, the stochastic nature of SMLM renders the localization process susceptible to errors that make quantitative SMLM a non-trivial problem.

In this chapter, I introduce some of the collaborative work we have done to achieve quantitative single molecule biology, focusing on several aspects including protein labeling, fluorescence acquisition and image analysis. Each of these contributions were investigated in the context of separate projects, and are presented here as individual steps towards an ultimate goal: quantitative single molecule biology.

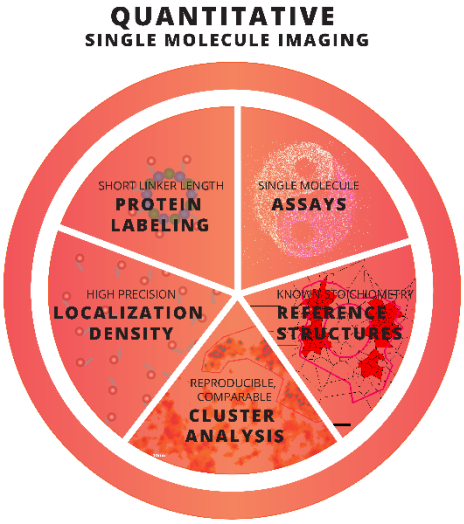

Figure 2.1: Steps Towards Obtaining Quantitative Single Molecule Data. This chapter presents several independent workflows towards enabling quantitative single molecule in biology in the form of protein labeling, characterization of reference structures, and clustering from localized single molecule coordinates.

2.1 QUANTIFYING INDIVIDUAL SINGLE MOLECULE LOCALIZATIONS

A single SMLM experiment typically generates millions of localizations, allowing for statistical analyses unique in the domain of microscopy. Coupling the spatial and temporal localization patterns with supplementary information garnered from the PSF fitting process, a wide array of quantitative vectors can be used to assess acquisition quality or filtered to remove imaging artifacts that help to respond to specific quantitative biological questions.

2.1.1 Quantifiable Single Molecule Parameters from Gaussian Fitting

The Gaussian fit used in the PSF localization process provides a wealth of information beyond the lateral spatial localization of the emitter, including an estimate of the axial position of the molecule (to be discussed further in section 3.1). Furthermore, it can be exploited to give feedback on the quality of the acquisition, including validation of single molecule conditions and estimation of the individual precision of each localization, which can be incorporated into the visualization to visually favor precise localizations and allow more accurate segmentation.

The intensity of the Gaussian fit can, in fact, give a good estimate of the true fluorescence intensity of the emitter since the integrated intensity of the 2D Gaussian curve estimates the total number of photons collected by the imaging system. While special care should be taken to quantitatively measure the number of photons per localization (to be briefly discussed in section 2.1.2), the intensity per localization histogram can contain some information relative to the acquisition conditions, in particular the density of emitting single molecules. **Figure 2.2**b shows several frames of a dSTORM acquisition of the centrosome protein CEP164, a frequently imaged structure in SMLM due to its small but known structure (~300μm diameter). Over the course of imaging, the intensity of the single molecule image fluctuates, and plotting the intensity histogram (**Figure 2.2**c) from all of the localizations shows a bimodal distribution. These first, larger peak can be considered to be the localization of a single emitter; however, since the dSTORM process is stochastic by nature, a small fraction of the localizations might accidentally localize multiple emitting fluorophores, resulting in false centroid localizations[47]. **Figure 2.2**d demonstrates that by filtering the localizations to those only from the single emitter population, inaccurate localizations in the center of the structure are removed and the centrosome image is improved.

This intensity distribution also demonstrates the variability in the precision of each individual localization, which is typically disregarded in the spatial histogram image reconstructions like those found in **Figure 2.2**d. As discussed in detail in 1.2.2.2, the intensity per localization, proportional to the number of photons (N), can be combined with the variance (σ) of the Gaussian fit to estimate its theoretical localization precision (Δx), based on the simplified equation:

$$\langle(\Delta x)\rangle \approx \frac{\sigma}{\sqrt{N}} \quad (2.1)$$

By incorporating the intensity and localization precision into Gaussian reconstructions, more precise localizations can provide more visual weight, helping increase the effective signal to noise of the super-resolution reconstructed images without the need for filtering. This effect is demonstrated in **Figure 2.2**e on the clustering of membrane receptors (detailed further in

section 2.4.4), where the Gaussian visualization clearly helps to visually distinguish individual AMPA receptor clusters by prioritizing regions with high-density, high-precision localizations. It should be noted that this Gaussian visualization distributes a single localization across several pixels according to the calculated localization precision, which requires precise calculation of the number of photons that contribute to that localization.

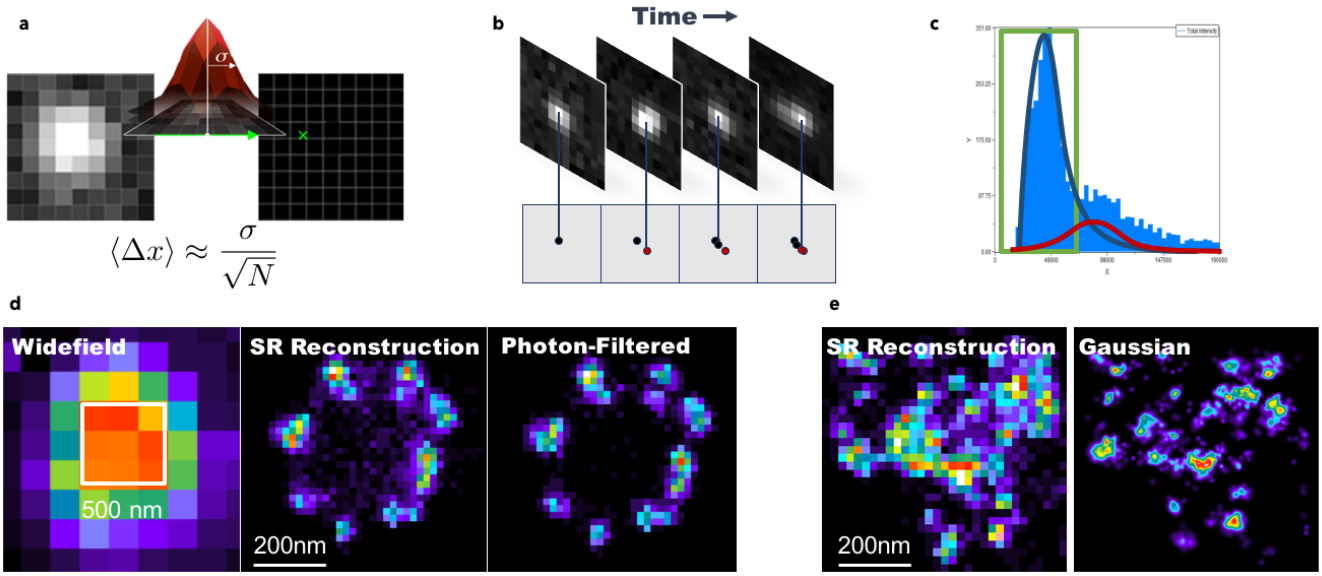

Figure 2.2: Gaussian Fit Provides Quantitative Single Molecule Information. **(a)** The localization precision is inversely proportional to the number of photons acquired, N. **(b)** The stochastic blinking may result in multiple single molecules emitting during a single camera exposure frame, inducing localization errors. **(c)** The localization intensity histogram may reveal these multiple-emitter localizations in the form of a bimodal distribution, with single (green) or double (red) emitters per localization. **(d)** The centrosome structure is a hollow ring, but localization errors due to double emitters result in some localizations appearing in the center of the ring. Filtering these localizations based on the intensity histogram removes these erroneous localizations and clean the superresolution image for better quantification. **(e)** Weighting the localization precision into the visualization prioritizes more accurate localizations and regions of higher localization density, like these neurotransmitter receptor clusters.

(b-d) Cep164-Alexa647 dSTORM. Collaboration with Karine Monier, ENS Lyon
(e) GluA2-Alexa647 dSTORM Collaboration with Benjamin Compans, IINS

2.1.2 Photon Counting with EMCCDs

Beyond its use in localization precision and visualization, the number of photons per localization N is a common quantitative metric frequently used to compare SMLM experiments. With an EMCCD camera, calculating the number of photons per localization is a straightforward conversion from the image intensity:

$$N = \mathrm{I_{ADU}} \times \frac{\text{Stage Gain}}{\text{EM Gain}} \times \frac{1}{\eta(\lambda)} \quad (2.2)$$

where $\mathrm{I_{ADU}}$ is the integrated Gaussian intensity in ADU and $\eta(\lambda)N$=IADU×Stage GainEM Gain×1η(λ) (2.2 2.2 may be used. The importance of this EM gain calibration must not be understated as it is imperative to the proper calculation of photon count and essential when comparing photon counts from different cameras.

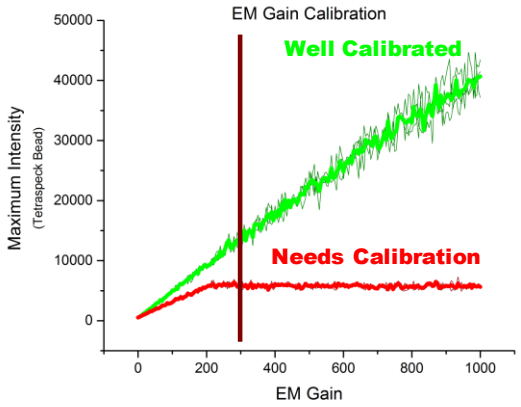

Figure 2.3: Assessing EMCCD's EM-Gain Stage Calibration. The electron multiplication stage of EMCCDs are very sensitive to light exposure and aging. A quantitative conversion from intensity ADU to number of incident photons requires proper calibration, ideally once per week. The maximum image intensity as a function of desired EM gain can be used to differentiate a well calibrated EM gain stage (green curve) from one that needs calibration (red curve).

Photometrics EVOLVE512 EMCCD

2.1.3 Matching Temporal Sampling Speed to Molecular Photophysics

In addition to the number of photons, many other photophysical parameters of fluorescent dyes impact their quality as super-resolution probes. In the stochastic imaging process of single molecule imaging, the time required for the single fluorescent probe to complete an on-off cycle, known as the **duty cycle**, has a drastic effect on acquisition quality. As discussed in detail in section 1.2.5.1, resolution in SMLM is a function of both localization precision as well as the labeling density of fluorescent probes, but ensuring that only a single molecule is emitting fluorescence in a given imaging frame requires that the fluorescent probes have a low duty cycle; that is, the fluorophores are only in their fluorescent electronic configuration for a small fraction of the time compared to a long-lived dark state. More quantitatively, for M fluorescent molecules in a diffraction limited area, the duty cycle of the fluorophores must be at least $1/M$ for accurate single molecule localization[70]. **Figure 2.5** from *Dempsey et al*[70] clearly validates Alexa647 as an ideal dSTORM probe with high but infrequent photon emission bursts, allowing many precise localizations and an accurate reconstruction of the true object.

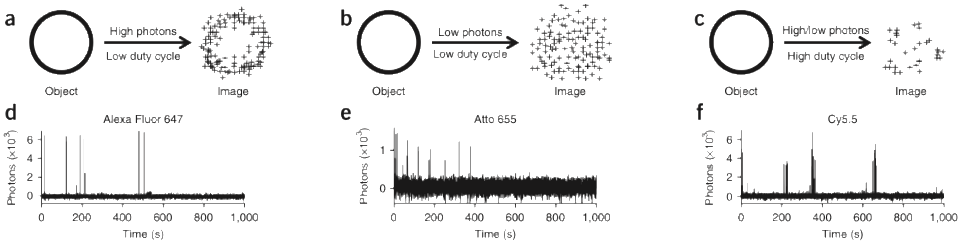

Figure 2.4: Effect of Photon Count and Duty Cycle of the Fluorescent Tag. (a,d) Alexa647 is an ideal dSTORM probe due to its low duty cycle and high photon emission per burst. **(b,e)** Atto655 is rarely used in dSTORM imaging due to its low photon count, which increases localization error. **(c,f)** The high duty cycle of Cy5.5 makes dense dSTORM imaging difficult, but is frequently used in conventional STORM where an activator fluorophore limits the fluorescent emission over time.

From *Dempsey et al*[70]

An ideal image frame would expose for exactly the duration of fluorescence emission, but the stochastic nature of fluorophore blinking combined with the finite exposure times of

commercially available scientific cameras impose a compromise in a fixed exposure time. Until recently, EMCCD cameras were exclusively used for single molecule detection due to their high sensitivity (1.4.3.2), but even the fastest EMCCD cameras are limited to 50Hz imaging across their full field of view. While the blinking kinetics of single molecules can be modified using special imaging buffers and high laser power, dSTORM acquisitions of densely labeled proteins are frequently marred by multiple fluorophores emitting in the same diffraction limited area in a single image frame. Recently, sCMOS cameras capable of millisecond exposure times have been used for high-speed acquisition SMLM imaging[84], accelerating imaging speed and noticeably reducing these artifacts (**Figure 2.5**). Ultimately, the total acquisition time is fundamentally limited by the local dimensionality of the structure being imaged; inherently 3D structures require many more localizations for complete reconstruction than single protein clusters[85].

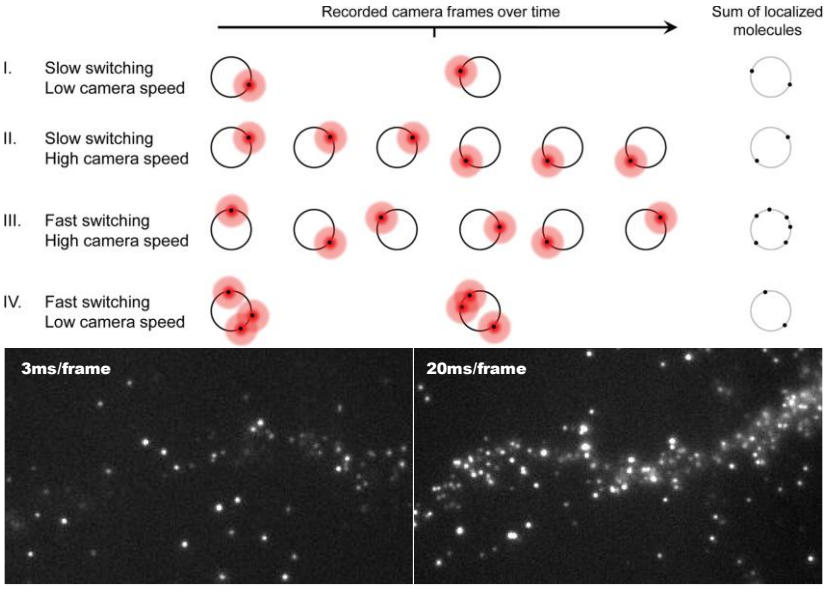

Figure 2.5: Matching exposure time to single molecule blinking rate. **(a)** Increasing image acquisition rate by decreasing frame exposure time is only beneficial if the single molecule switching rate is faster than the exposure time. **(b)** For densely-labeled proteins, a single exposure frame can capture multiple single molecule blinking events, resulting in false localizations and potential image artifacts.

(a) from *Lin et al.* [84]
(b) GluA2-Alexa647 dSTORM | Hippocampal neuron cultures | sCMOS

2.1.4 Limitations of SMLM as a Quantitative Tool

One of the ultimate goals of SMLM as a quantitative tool is to quantify the number of tagged proteins from single molecule localization data. Techniques for measuring protein stoichiometry and oligomerization state using well-characterized fluorescent proteins like mEOS2[86] have been introduced, and newer methods evade the constraints of molecular photophysics such measurements with mEOS[87] and even Alexa647 under dSTORM conditions[88]. However, while the previously described sampling artifacts are undesirable in structural imaging and decrease the effective SNR of the super-resolution image, they are detrimental to these protein counting approaches. Furthermore, undercounting due to fluorophore bleaching, protein folding errors, and fluorescence quenching from densely labeled structures, prevent accurate protein counting [89]. Therefore, tools to quantitatively prepare, acquire and analyze SMLM data are essential to making SMLM truly quantitative.

2.2 QUANTITATIVE SINGLE MOLECULE LABEL CHARACTERIZATION VIA PHOTO-PATTERNING

A wide range of labeling techniques are commonly employed in SMLM, but characterizing the optical properties of these fluorescent probes for particular use cases can be tedious as not all ligands adhere efficiently to the glass surface of a coverslip. A new technique introduced by *Strale et al.*[90] in 2016 named light-induced molecular adsorption (LIMAP), allows for quantitative protein adhesion to a glass coverslip via the use of a digital micro-mirror device (DMD) to spatially pattern UV-light(**Figure 2.6**a). Briefly, a layer of Pll-g-PEG is adsorbed to the surface of a clean coverslip, creating a coating that prevents molecules from adhering to the coverslip surface. By incubating the coverslip in a photoinitiator and illuminating it with spatially patterned UV-light, the PEG layer is selectively removed in the black regions of the pattern. Subsequent incubation of the coverslip with a desired protein allows its selective adhesion to the coverslip only in the patterned, PEG-free regions. Repeating this process for several proteins allows for multi-protein patterning (**Figure 2.6**b).

Notably, the combination of the grayscale patterning abilities of the DMD with a quantitative relationship between the UV dose and the patterned molecular density (**Figure 2.6**c) make it ideal for single molecule studies. The multi-scale technique was demonstrated for various applications, including orthogonal patterning of adhesion proteins to spatially separate cell types, but its performance as a tool for single molecule imaging has yet to be demonstrated. Specifically, we were interested in the technique's ability to create patterns of varying molecular density for quantifying the SMLM performance of various single molecule labels.

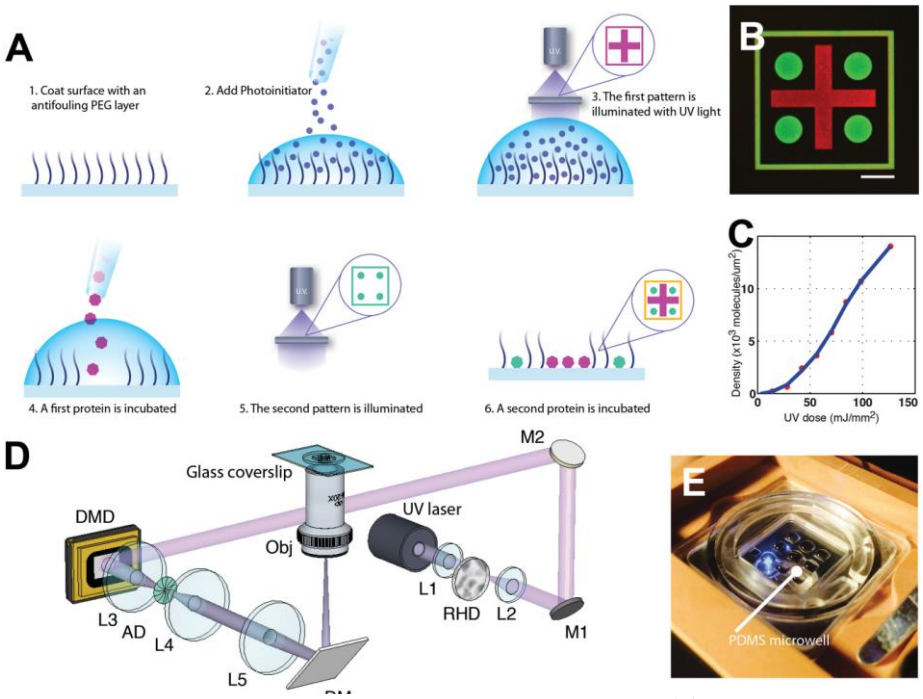

Figure 2.6: Principle of LIMAP Photopatterning Technique. **(a)** Spatially patterned UV light selectively activates a photoinitiator, removing a PEG antifouling surface coating and allowing protein incubation at the coverslip surface. **(b)** The process can be repeated, allowing for multiple proteins to be patterned in different spatial locations. **(c)** Immobilized mEOS2 molecules as a function of UV-dose **(d)** Spatial patterning is achieved by conjugating a digital micromirror device (DMD) to the focal plane of a microscope objective. **(e)** 9 PDMS microwells allow several conditions to be imaged on a single coverslip and minimize the amount of reagents used (5 µL per well).

From Strale et al.[90]

2.2.1 Pattern Resolution and SMLM Illumination Homogeneity Characterizations

While the spatial patterning technique remains diffraction limited with the use of UV light, the exact patterning resolution remained in question. In collaboration with Pierre-Olivier Strale, we patterned single DMD pixel width diagonal lines separated by a single pixel to create a diffraction-limited response to these finite patterns (**Figure 2.7**). To ensure that the lines were maximally filled in the super-resolution reconstructions, we used the DNA-PAINT technique, which affords a nearly infinite number of fluorescent probes and localizations. We patterned the Goat Anti-Rabbit-D2 DNA-PAINT antibody (in a collaboration with the Ultivue company, who commercializes DNA-PAINT oligomers for single molecule localization imaging), and imaged for 80,000 full image frames (512px x 512px @ 50ms/frame) at 4nM I2-550 @ ~5kW/cm² 561nm excitation to ensure single molecule conditions (**Figure 2.7**a). The final reconstruction (**Figure 2.7**b), composed of >25,000,000 localizations, was cross-correlated in ThunderSTORM [91]) for drift correction, as fluorescent beads bleach over the course of such long acquisitions. A line scan of the Gaussian super-resolution reconstruction @ 10nm/pixel shows a distinct sinusoidal pattern with a period of 571nm resulting from the convolution of the patterning microscope PSF with the single-width pixel (**Figure 2.7**d).

This experiment also demonstrates the strong field of view dependence of the single molecule imaging excitation used for DNA-PAINT. The diagonal lines are uniformly patterned, and ideally would have the same intensity in the super-resolution reconstruction; however, we notice a 2D Gaussian profile to the intensity. The higher intensity near the center of the Gaussian profile results in faster single molecule bleaching in this zone at this excitation angle and power, visible as more single-molecule conditions near the center of the FOV (**Figure 2.7**,a,b) than near the edges of the image. This spatial-dependence to the excitation is especially important in dSTORM experiments to ensure high power density for fast blinking and true single molecule conditions. This kind of experiment could be used in conjunction with further analysis of spatially isolated localization clusters for determining the FOV variance of localization precision.

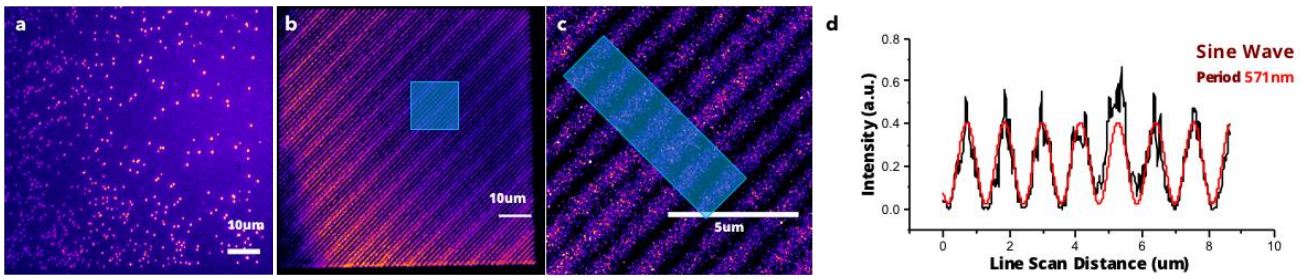

Figure 2.7: Measuring LIMAP Patterning Spatial Resolution and Spatial Dependence of Excitation with DNA-PAINT. Measuring the spatial resolution of LIMAP with a diagonal pattern a single DMD pixel wide followed by DNA-PAINT acquisition of the pattern results in >25,000,000 localizations across the full field of view and a linescan shows a spatial patterning resolution of 571nm. Simultaneously, this puts into evidence the inhomogeneity of the single molecule excitation scheme.

2.2.2 Multicolor Imaging Labeling Orthogonality and Crosstalk

LIMAP's ability to orthogonally pattern various proteins renders it a useful tool for quantifying labeling specificity of new techniques. For example, the DNA-PAINT technique may suffer from nonspecific labeling if the fluorescently tagged DNA-oligomer adheres to any structure other than its antibody-coupled complementary oligomer. To ensure test the cross-talk between two DNA-PAINT probes, we orthogonally patterned rabbit and mouse IgGs and incubated Anti-

Rabbit-D1 and Anti-Mouse-D2 and performed sequential DNA-PAINT imaging of 0.5nM I2-650 @ 105mW 640nm and then 0.25nM I1-550 @ 50mW 561nm. Only 8,000 frames were acquired to demonstrate the orthogonality of the technique (**Figure 2.8**e). The slight crosstalk between the two channels can be attested to the D2 (650nm) antibody adhering to unfilled sites in the first D1 pattern and not to aspecificity of the DNA-PAINT labels themselves, as critically the localizations remain primarily localized in the ying-yang pattern.

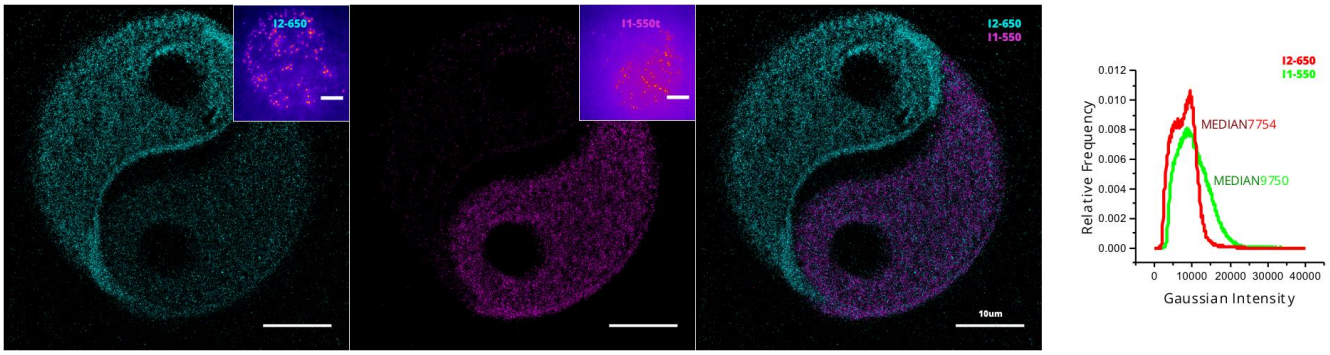

Figure 2.8: Pattern for DNA-PAINT Orthogonality Characterization. Anti-Rabbit D1 and Anti-Mouse-D2 DNA-PAINT secondary antibodies were patterned in the shape of a ying yang. Slight crosstalk in the D2 channel is due to the fact that it was patterned after the D1 antibody, filling some unoccupied sites in the orthogonal pattern. Localization intensity quantifications (**right**) show that the 550nm probe is slightly brighter in our imaging configuration.

In addition to labeling orthogonality, this technique allowed us to separately evaluate each DNA-PAINT probe in terms of brightness as an SMLM label. The intensity per localization histogram (**Figure 2.8**, right) shows that for our illumination and detection scheme, the 550nm probe is ~20% more intense than the 650 probe, and thus was chosen as the optimal probe for further DNA-PAINT imaging.

2.2.3 Anti-GFP:Alexa647 Nanobody Comparisons

In DNA-PAINT imaging, the imager concentration can be varied at the time of imaging to ensure single molecule imaging conditions. This is not the case, however, in fixed dSTORM imaging, where the protein is directly labeled with a fluorescent probe. In this case, the number of fluorescent probes per antibody or ligand, is critical for accurate superresolution imaging.

We used LIMAP to characterize two anti-GFP nanobodies[53] (fabricated and coupled by Matthieu Sainlos), one with a low degree of labeling (DoL) (~0.73 Alexa647 molecules per nanobody) and the other with a high DoL (~2.53 Alexa647 molecules per nanobody) for superresolution imaging. We photopatterned a 3 x 3 grid of varying densities of squares in which the GFP molecule was incubated for 5 minutes at 1μg/mL and then washed 3 times. The nanobodies were incubated for 2-3 minutes at their stock concentration, selectively binding to the GFP pattern (**Figure 2.9**, top left, DoL 2.53). Tetraspeck beads were incubated for 5 minutes at 1:1000 in PBS for post-acquisition drift correction. The coverslip was then submerged in dSTORM buffer solution (Glucose Oxidase + Catalase + 100mM MEA) and dSTORM imaging was performed for 20,000 frames, resulting in >5,000,000 localizations in total.

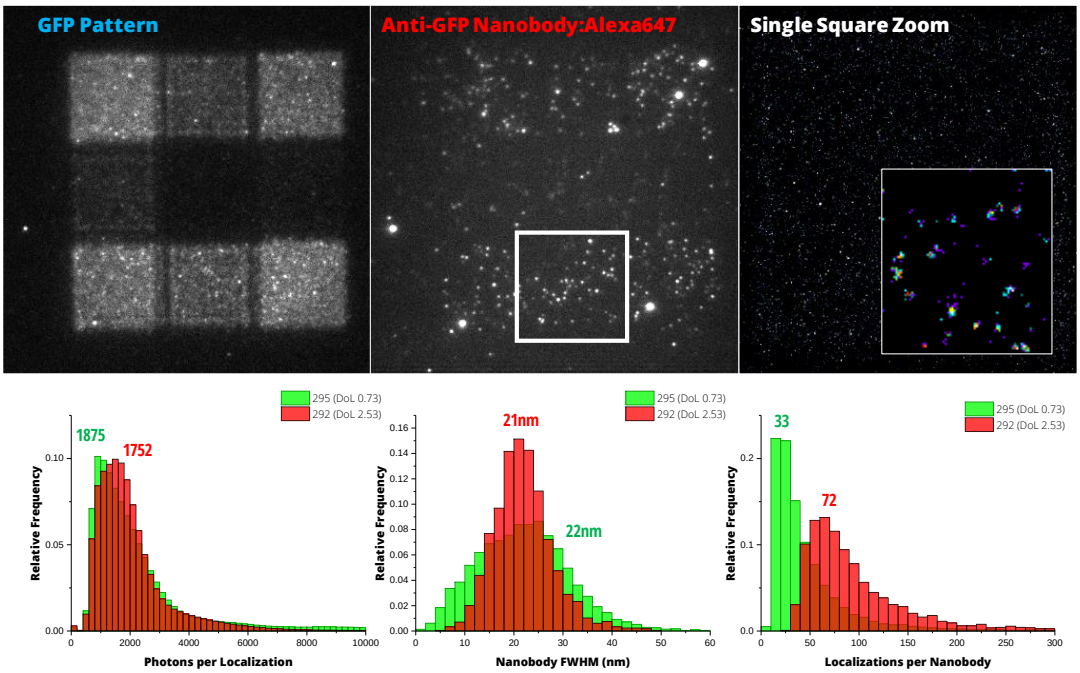

Figure 2.9: Anti-GFP Nanobody Degree of Labeling Comparisons with Photopatterned GFP. The degree of labeling affects the localization density in final superresolution reconstructions. (**top left**) Two anti-GFP nanobodies were fabricated with different degrees of labeling and quantified using GFP patterns of different densities. (**top center**) After dSTORM imaging, a single square was selected for nanobody characterizations. (**bottom**) The two nanobodies were compared, showing negligible difference in photon count per localization (**left**) or localization precision (**center**). The higher degree of labeling nanobody shows 2.2 times the number of localizations (**right**), making it a higher quality label for SMLM.

A single square with single molecule densities in the dSTORM imaging was then selected for nanobody analysis. The resulting clusters of individual nanobodies (**Figure 2.9**, top right, inset) were then quantified for common properties of SMLM labels (**Figure 2.9**, bottom): number of photons per localization (left), lateral localization distribution FWHM (center), and finally number of localizations per nanobody (right). The number of photons per localization is expected to be the same between conditions and was validated as a quality control metric that the photon emission of the Alexa647 fluorophore was consistent between experiments and dSTORM buffers. Similarly, as the number of photons remains the same, the distribution showed a negligible difference in median FWHM around 21nm. However, the higher DoL nanobody showed 2.2 times the number of localizations per nanobody, a critical metric for dSTORM imaging as it allows. Together, these quantifications validate the higher DoL nanobody as the more effective label for dSTORM imaging, particularly of sparsely labeled proteins.

2.3 SCREENING EFFECTIVE RESOLUTION OF SINGLE PROTEIN LABELING WITH SR-HCS

The previously outlined photopatterning technique addresses one issue in quantitative single molecule imaging, namely in the preparation of accurate single molecule assays. Another major hurdle preventing routine single molecule imaging is ensuring consistency between imaging conditions to be able to extract biologically relevant data. SMLM acquisitions are quite slow; imaging a single cell can commonly take 10 minutes of acquisition time, thus acquiring enough data to compare biological conditions can take hours or even days of non-stop imaging, yet the user is required to stay near the microscope to find new cells to image, change coverslips, verify proper blinking characteristics, etc. The large volume of raw image data generated in such

acquisitions complicates matters further, with post-acquisition image and data analysis doubling the required image processing time, not to mention the immense time required to compare all the quantitative single molecule data in a statistical manner.

An automated SMLM acquisition, analysis and data mining pipeline capable of imaging and compare multiple biological conditions would obviate the need for user intervention over the course of the imaging session and prevents user biases in image reconstruction.

2.3.1 SR-HCS Workflow: An automated SMLM Acquisition and Analysis Assay

We sought to address these issues by combining some aspects of high content screening (HCS) with single molecule super-resolution microscopy in a pipeline called SR-HCS. Widely used in cell biology and particularly in drug discovery, HCS massively multiplexes and automates microscopy image acquisitions, using a precise lateral translation stage and multi-well plates (commonly containing 6, 12, or 96 wells), allowing for multiple conditions to be tested in triplicate without user intervention. While HCS has been used extensively for drug discovery and other applications, it has yet to be applied to single molecule super-resolution techniques for a variety of reasons, mostly technical.

The SR-HCS pipeline (**Figure 2.10**a) begins with the automatization of a commercial microscope for multi-well acquisition with an oil-immersion objective. Maintaining oil contact with the coverslip surface over the large size of 96-well plates is challenging, but feasible by painting a thin layer of immersion oil on the bottom of entire 96-well plate surface. Intra- and inter-well displacement is automated via an xy-translation stage, while axial position is maintained using the Nikon Perfect Focus System, ensuring consistent sample illumination across the entire plate.

Random or user-defined positions can be imaged in (spt)PALM, dSTORM or DNA-PAINT configurations. Online Gaussian fit, localization and tracking performed with the WaveTracer module obviate the need to save the raw image stacks, saving only the localization data and a super-resolution reconstruction for each position (**Figure 2.10**b), and most importantly saving time compared to classical SMLM acquisitions (**Figure 2.10**d). Finally, the localization and tracking data from all positions are compiled into a database for easy comparison between positions (**Figure 2.10**c). It is worth noting that while this automated workflow is essential for true high content SMLM, for example in 96-well plates, it is equally applicable to imaging single coverslips.

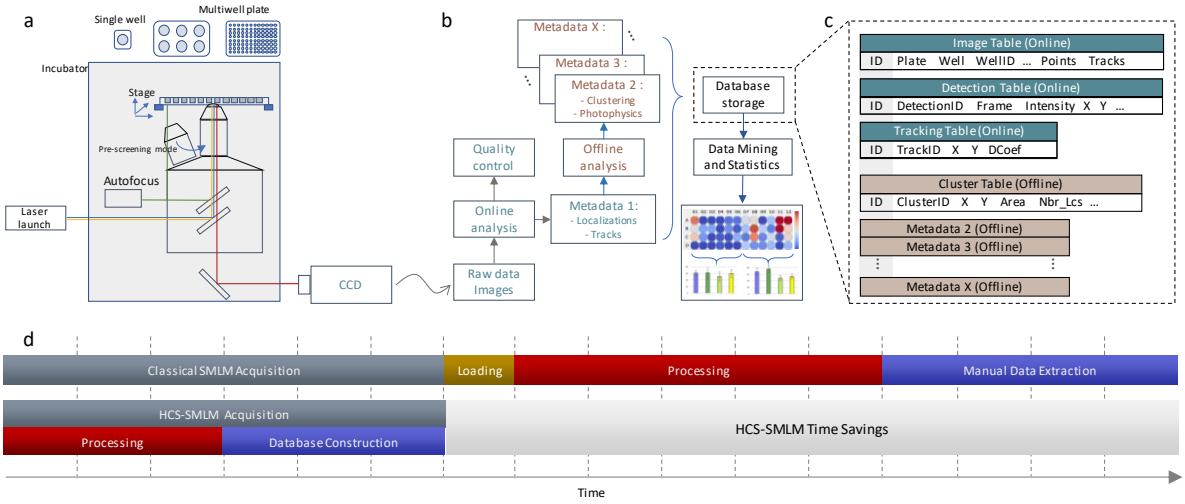

Figure 2.10: SR-HCS Automated SMLM Workflow. **(a)** A conventional SMLM microscope can be automated with a motorized *xy*-stage for imaging multiwell plates. **(b)** Single molecules are localized, fitted to Gaussians, and connected for tracking online, eliminating the need to save the raw data stacks. **(c)** The cumulate data from all positions are pooled into a databased for easy data analysis. **(d)** The automatization and online localization accelerates the single molecule imaging process by nearly 2x and obviates the need for user intervention during the acquisition.

2.3.2 Optimizing Membrane Protein Expression, Fixation and Labeling with SR-HCS

A proof of concept experiment was designed with the goal of assessing the combined effect of label linker length and probe localization precision on the effective resolution of a single tagged membrane receptor. This differs from the nanobody characterizations in section 2.2.3 in that the linker length adds further localization uncertainty, and potentially increases the distribution of localizations around their central point. To be properly labelled, the protein of interest must properly be expressed, fixed and labelled in a biological model such that they are spatially isolated enough for single molecule cluster quantification.

A preliminary version of the SR-HCS pipeline based on the MetaMorph Multi-dimensional Acquisition functionality and manual imaging FOV selection was used to screen HeLa cells for optimal expression, fixation, and labeling of individual membrane receptors. This kind of experiment is typical in cell biology, where the biologist has created several DNA vectors containing genetically modified versions of the protein of interest tagged with different fluorescent proteins or tags, and would like to see which of the genetically-modified proteins are most efficiently and correctly expressed by the cell. The biologist may desire validation of proper cell fixation without inducing artifacts, and for single molecule imaging they must confirm optimal labeling conditions from a variety of possible antibodies. A conventional single molecule imaging approach with a single condition per coverslip would need to limit the number of avenues explored in the interest of time.

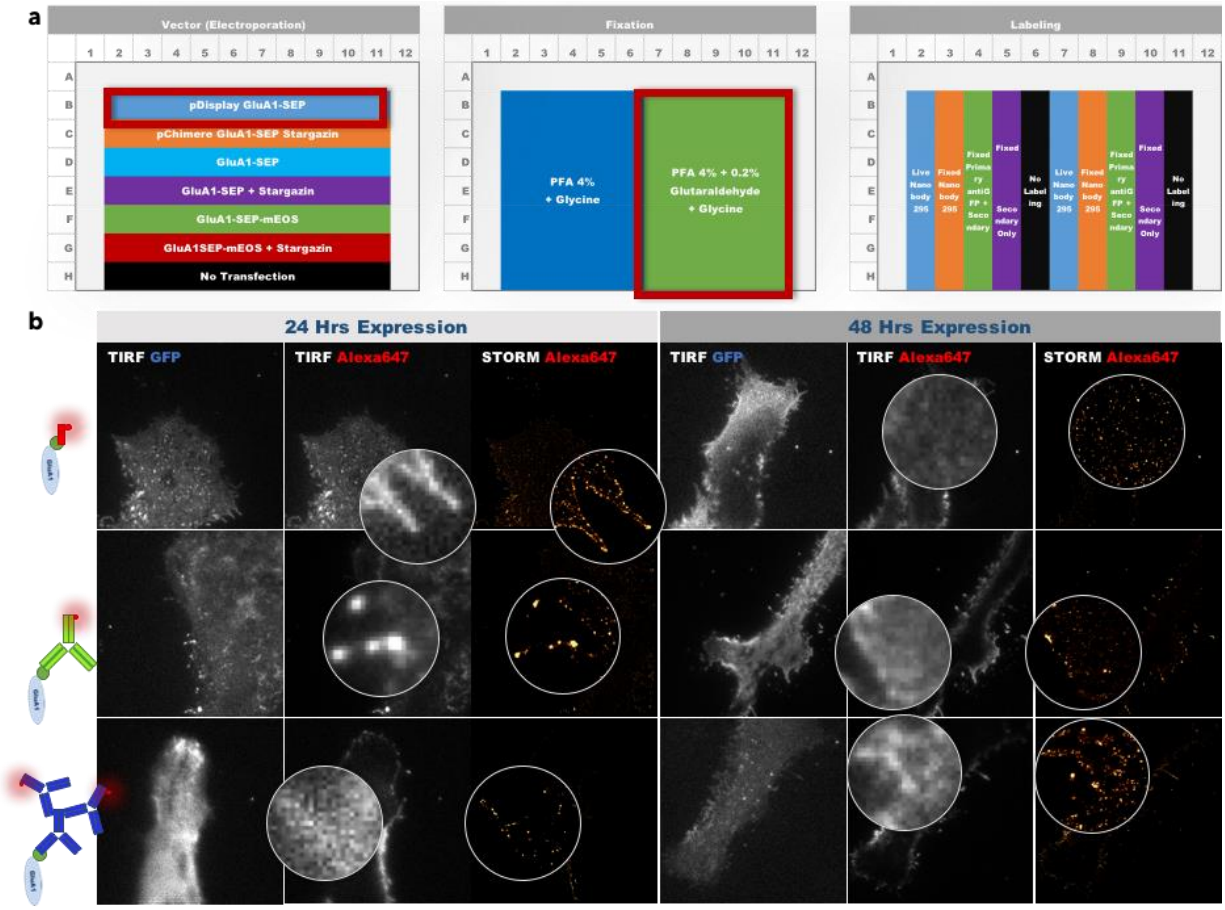

Figure 2.11: SR-HCS Facilitates Protein Expression, Fixation and Labeling Selection. (a) 70 wells of two 96-well plates were plated with HeLa cells and electroporated with 6 different transfection vectors, fixed with 2 different fixation protocols, and labeled with 3 different labeling strategies. The two 96-well plates were allowed to express the electroporated protein for either 24- or 48 hours, culminating in 140 different biological conditions, from which an optimal expression plasmid and fixation protocol were selected. **(b)** Representative images of the three labeling strategies from the two different expression times show similar results in terms of labeling efficiency.

The 96-well plate commonly used in HCS lends itself extremely well to these kind of crossed experiments, and thus we prepared 70 wells of two separate 96 well plates with HeLa Cells, and electroporated one row with one of six DNA vectors, each a genetically tagged variant of the GluA1 subunit (**Figure 2.11**a, left). One plate was allowed to express for 24-hours, whereas the second was fixed after 48-hours to ensure a sufficient density of receptors had expressed to the membrane surface. Half of each row was fixed only with 4% Paraformaldehyde (PFA), while the second half was fixed with 4% PFA + 0.2% Glutaraldehyde (GA) (**Figure 2.11**a, center). After quenching cross-linking induced fluorescence from the PFA and GA and surface blocking with BSA, 3 different labeling strategies were employed in separate columns of each fixation block (**Figure 2.11**a, right). This orthogonal plate layout across two plates creates 140 separate biological conditions, a daunting number for conventional imaging approaches with separate coverslips per condition, but requiring only a single plate change in the SR-HCS approach.

Three of the tested parameters could be assessed based on diffraction-limited imaging. A widefield scan of the plates allowed us to choose, based subjectively on image quality, an optimal transfection vector (pDisplay GluA1-SEP, row B) and fixation method (PFA 4% + 0.2% GA, columns 7-11) expressed for 24-hours.

Once the optimal conditions were selected, wells B8-10 were submerged in conventional dSTORM buffer (Glox + Catalase + 100mM MEA), and superresolution images were acquired. A subset of the results from the labeling strategies are presented in **Figure 2.11**b, showing little visual difference in cluster size between nanobody, primary antibody, and primary + secondary antibody labeling.

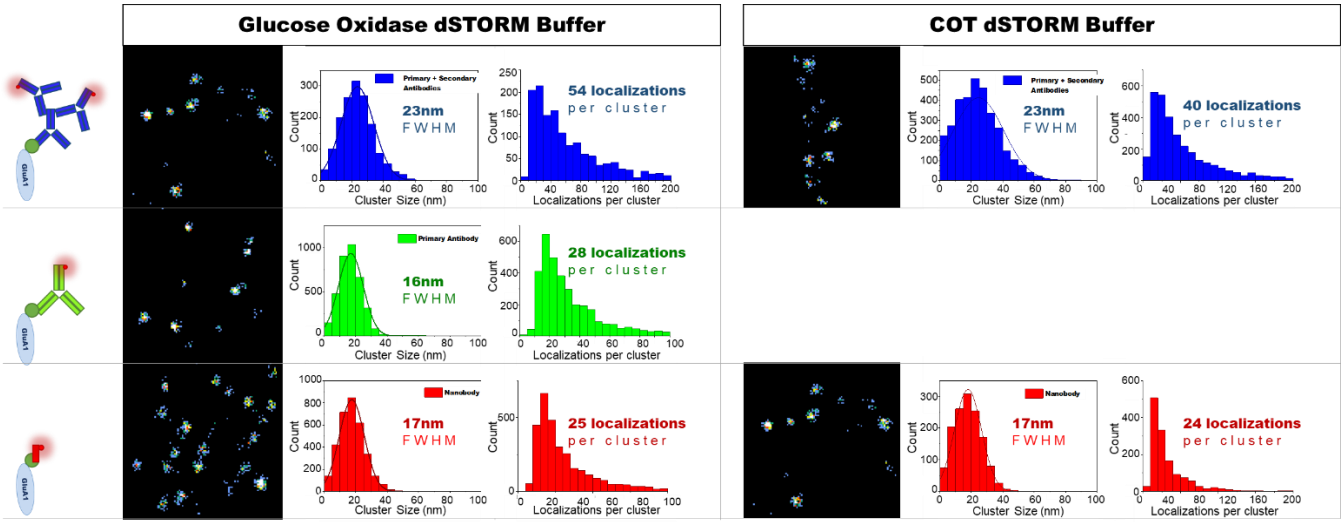

Figure 2.12: SR-HCS Screening Assay for dSTORM Buffer and Labeling Strategy. Two dSTORM solutions and three labeling strategies were used to quantify single receptor labeling efficiency. The COT dSTORM buffer (right), which has previously been shown to increase the number of photons per localization[92], does not noticeably decrease the median size of GluA1 clusters expressed in the HeLa cell membrane when compared to the commonly employed dSTORM buffer (left). However, the use of primary and secondary antibodies (top) does increases the effective cluster size with respect to primary antibodies (middle) or nanobodies (bottom), indicating that the cluster size is governed by the fluorescent probe's linker length.

pDisplay-GluA1-SEP in HeLa cells | Anti-GFP primary antibodies or nanobodies | 20nm/px reconstructions

Cluster analysis was performed (using a cluster analysis method to be discussed in the next section, 2.4) on the three labeling conditions (**Figure 2.12**, left), quantifying the spatial distribution and number of localizations per cluster. Notably, the primary and secondary antibody has a slightly larger spatial spread (23nm FWHM) than the primary antibody (16nm) or nanobody (17nm), and roughly twice the number of localizations per cluster (54 localizations for the primary and secondary antibody vs. 28 and 25 for primary antibody and nanobody, respectively). These results confirm the expected effect of increased linker length due to primary and secondary antibody labeling of a single protein.

We next tested the effect of a different dSTORM buffer that has been shown to increase the brightness of Alexa647 with the addition of cyclooctatetraene (COT)[92]. The Glox buffer was imaged first, the wells were washed 3 times with PBS, and then the COT solution was imaged. Surprisingly, the dSTORM buffer did not effect the size (FWHM) of these localization clusters, indicating that the increased number of photons, and thus better localization precision, of the COT buffer does not have a concrete effect on effective receptor resolution.

In tandem, these results demonstrate that resolution in SMLM is truly a combination of labeling density and localization precision, and an increase in just one of these parameters does individually improve resolution of an individual protein.

2.4 CLUSTER ANALYSIS USING POLYGONS WITH SR-TESSELER

The kinds of cluster analysis presented in section 2.3.2 are common in single molecule biology, where the spatial organization of membrane receptors is frequently imaged. Image-based quantifications of these clusters are heavily dependent on pixel size of the reconstruction and localization density; large pixels may not provide enough accurately sample small clusters, while small pixels are more sensitive to variations in localization density.

To address these potential biases in cluster analysis, we introduced a new segmentation method of single molecule localization super-resolution data using the localization coordinates directly[93]. Based on Voronoï tessellation, the spatial subdivision method creates polygons around each individual localization, giving intrinsic weight to denser molecular regions. While Voronoï tessellation had previously been used in super-resolution imaging, it had been limited to visualization[94].

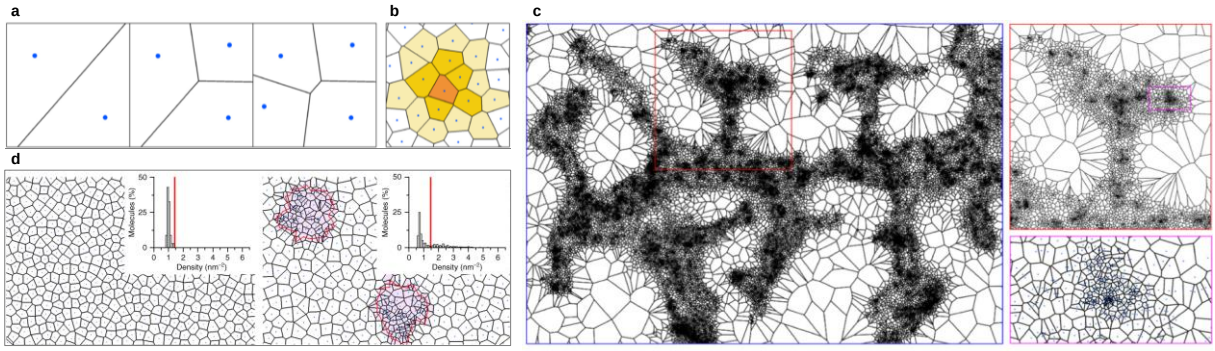

Figure 2.13: Principle of Voronoï Segmentation in SR-Tesseler. (a) Individual localization coordinates are used as seeds at the center of polygons, the edges of which are formed by the perpendicular bisectors between seeds. **(b)** Individual localizations are quantified by their area and number of neighbors. **(c)** Regions of higher localization density exhibit intrinsic contrast, demonstrated here with GluA1-mEOS2. **(d)** A single parameter based on the normalized localization density is used for automatic segmentation.

From *Levet et al.*[93]

The basic principle of our implementation of Voronoï tessellation for single molecule visualization and cluster analysis, called SR-Tesseler, is shown in **Figure 2.13**. Excerpts from our article *Levet et al.*[93] detail the Voronoï diagram creation (section 2.4.1) and automatic segmentation (section 2.4.2).

2.4.1 Voronoï Diagram Creation from Single Molecule Localizations

The Voronoï diagram is built from localized molecule coordinates as the center of the polygon regions, called seeds. As the Voronoï edges are equidistant from the two nearest seeds, the simplest way to generate the diagram is to compute the perpendicular bisectors between the seeds (**Figure 2.13**a). Each polygon P_i of seed s_i has an area A_i and several neighbors (**Figure 2.13**b). First-rank neighboring polygons $P^1_{i,j}$ of s_i are defined by the n^1_i polygons of area $A^1_{i,j}$ sharing edges with P^i, centered on the seeds $s^1_{i,j}$. Similarly, higher rank polygons $P^k_{i,j}$, $k > 1$, are defined as the n^k_i polygons sharing edges with $P^{k-1}_{i,j}$. The neighborhood of s_i at the k^{th} rank is then defined by the $\{n^1_i, \ldots, n^k_i\}$ localized molecules. Each Voronoï polygon has on average six neighbors, making the structure robust to labeling density. For each seed s_i, various parameters can be computed, such as the area A^k_i and density δ^{ki}. These parameters provide quantitative information on the localizations surrounding each seed. Therefore, Voronoï diagrams are a

natural way to characterize and efficiently navigate the molecular neighborhood of each localized molecule at multiple scales, where regions with higher molecular densities are composed of smaller and denser polygons (**Figure 2.13**c).

2.4.2 Normalized Local Density Based Automatic Segmentation

A difficulty in single molecule imaging is the definition of a bias-free threshold for segmentation that can be compared across biological conditions and is insensitive to localization density. In SR-Tesseler, segmentation thresholds can be either manually adjusted or automatically determined to avoid user bias. We defined a general criterion for automatic thresholding, which the user can infer by comparing the localization distribution to a reference distribution that is spatially uniform. The average density δ of such a distribution can be approximated as the number of localizations divided by the image area. With the first-rank density δ^1_i as the main parameter, the automatic segmentation is achieved through selection and merging of all the polygons having $\delta^1_i > \alpha\delta$ (**Figure 2.13**d,right), where α is a positive multiplicative coefficient. As a control, the same threshold applied to a reference distribution did not provide any objects (**Figure 2.13**d, left).

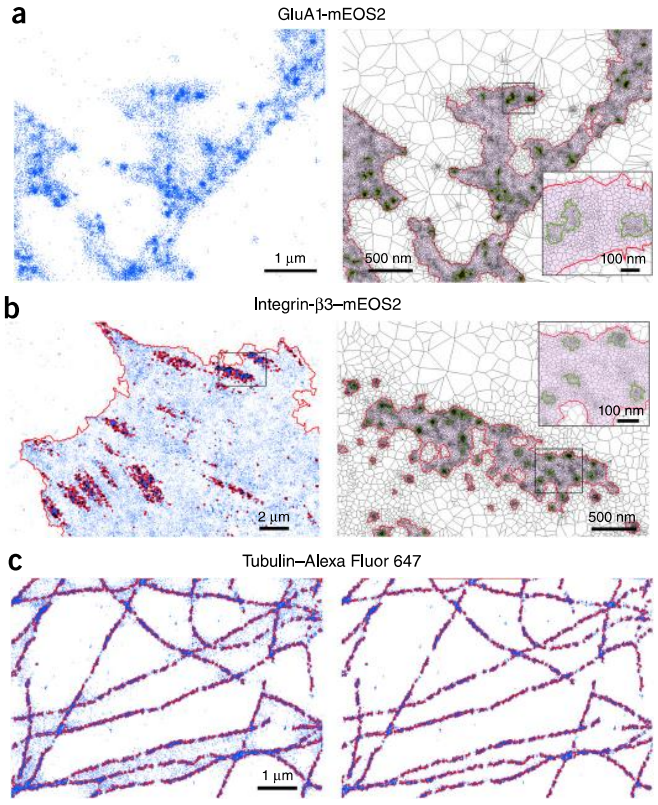

Figure 2.14: Automatic Segmentation in SR-Tesseler based on Normalized Local Density. A unique density parameter, $\delta^1_i > 2\delta$, is used for automatic, multi-scale segmentation of different biological structures. Original SMLM localization data (left) and automatic segmentation (right) for GluA1-mEOS2 (**a**), Integrin-ß3-mEos2 (**b**), and ß-tubulin-Alexa647 (**c**).

From *Levet et al.*[93]

To test the versatility of SR-Tesseler, we automatically segmented multiple levels of organization in different types of biological data and SMLM modalities, using a unique density parameter $\delta^1_i > 2\delta$ (**Figure 2.14a–c**). On neuronal data, we could automatically segment both the neuronal cell body and the molecular clusters of receptors of GluA1 fused to the mEOS2 fluorescent protein

(GluA1-mEOS2; **Figure 2.14a**). Similarly, we could automatically extract the three levels of organization (cell contour, adhesion sites and inter- action clusters) in live PALM data of fibroblasts expressing integrin-β3–mEOS2 (**Figure 2.14b**). Finally, we could identify nonisotropic structures such as microtubules in dSTORM data of COS7 cells labeled with tubulin–Alexa647 (**Figure 2.14c**). Another important feature of SR-Tesseler is its robustness to noise; segmentation of noisy data and cleaned data led to very similar results (**Figure 2.14c**).

2.4.3 DNA Origami for Cluster Analysis and Localization Precision Characterization

Testing SR-Tesseler for cluster analysis required the need for a model with known cluster properties. Biological models are difficult to quantify; genetically encoding fluorescent proteins for PALM imaging requires compensation for fluorophore bleaching and improper protein folding for accurate quantification, and the variability in protein labeling and the stochasticity of fluorescence emission make quantifying dSTORM images difficult. To avoid biological models, we tried single molecule assays using the LIMAP system (section 2.2) to pattern regions of varying antibody densities, but were unable to obtain quality data demonstrating quantitative differences in cluster analyses.

Luckily, a new tool capable of accurately and reproducibly creating nanometer sized structures that can be labeled with a known number of fluorescent markers was recently introduced into the world of single molecule imaging. DNA origamis[95] are ideal structures for quantifying resolution and validating cluster analysis tools for SMLM, due to their small size (in the tens of nanometers) and ability to precisely control the location of fluorescent tags on their structure, as shown in **Figure 2.15** from [96].

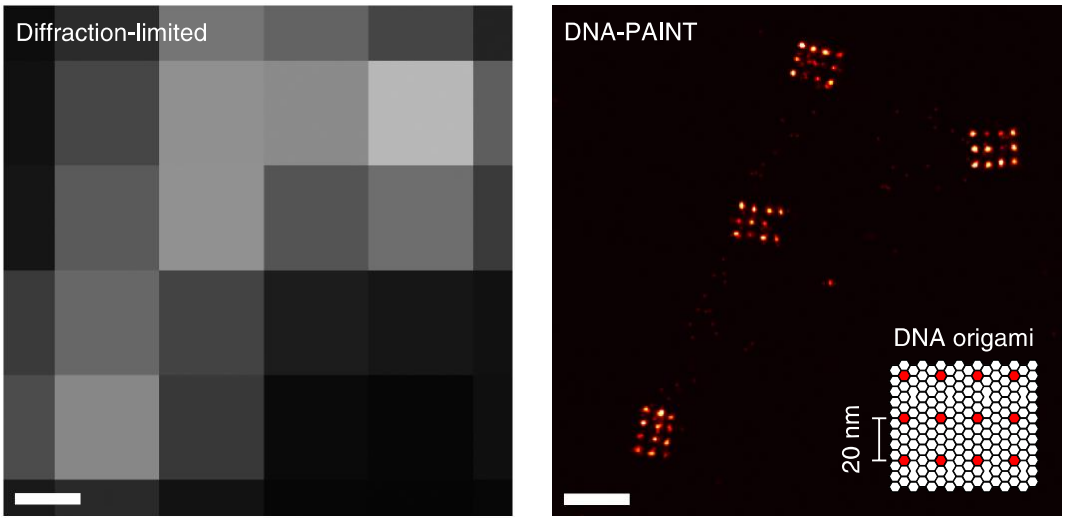

Figure 2.15: 2D DNA-Origami Structures. Individual DNA origamis organized as 4x3 rectangles with 20nm between each DNA docking site. Here, DNA-PAINT is used to label each of the 12 individual docking sites, but individual fluorophores can also be attached to the origami grid for dSTORM imaging.

From *Schnitzbauer et al.* [96]

Briefly, DNA origami are carefully designed strands of DNA that self-assemble into 2D or 3D structures, folding into a pre-designed shaped[97]. By placing fluorescent probes at specific locations along the DNA structure, these DNA origamis have found their place in single molecule super-resolution as tools for metrology[98].

We performed dSTORM imaging of DNA origamis (in a collaboration with Ralf Jungmann, Max Planck Institute) assembled in a 2x2 grid with 40nm horizontal and 60nm vertical spacing between Alexa647 molecules to apply the automatic multiscale segmentation of the SR-Tesseler (**Figure 2.16**). The top row shows the multiscale segmentation; The first level of segmentation separates individual origami (pink) from background localizations, and a second density-based segmentation inside the origamis separates corners (red) inside individual origami. A pair correlation analysis (PCA) of the localizations in each cluster was used to calculate the spatial distribution of the localizations in each cluster (**Figure 2.16**, right). From the PCA analysis of individual origamis (**Figure 2.16**, left middle). shows a calculated size of 64nm x 41nm (for a true structure size of 60nm x 40nm). Furthermore, PCA analysis of the individual corners of the origamis (**Figure 2.16**, left bottom). show an average size of 17nm and represents the localization precision of the setup and confirms the localization precision results seen with Alexa647 anti-GFP nanobodies in section 2.2.3.

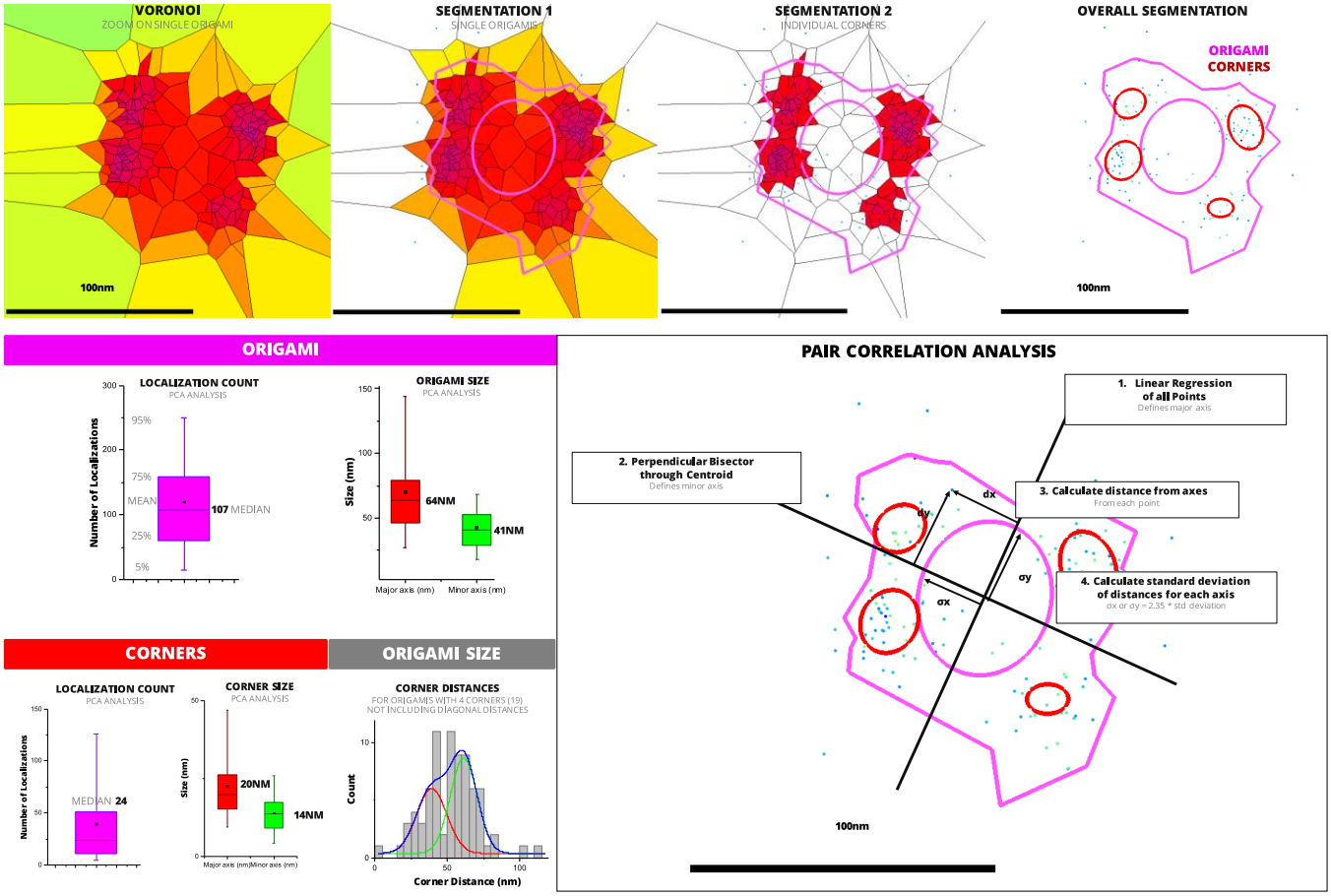

Figure 2.16: Quantifying Size of DNA Origami with SR-Tesseler. Rectangular DNA-Origami with Alexa647 molecules placed in the corners of a 60nm x 40nm rectangle. Sequential automatic segmentation provides access to individual origami (level 1) and individual corner molecules (level 2). A PCA analysis was performed to quantify the size of each segmentation level (bottom), showin a calculated median origami size of 64nm x 41nm and corner size of 20nm x 14nm.

60nm x 40nm Alexa647 Origami | dSTORM | Collaboration with Ralf Jungmann, Max Planck Institute

2.4.4 AMPA Receptor Clustering in Nanodomains

We used SR-Tesseler to analyze in more detail the clustering of AMPA receptors imaged in dSTORM conditions (**Figure 2.17**). *Nair et al*[24] have shown previously that these neurotransmitter receptors organize in ~70nm size synaptic clusters, called nanodomains. This

analysis used image-based cluster quantification to quantify cluster size, and we wanted to validate the cluster analysis tools against these previous analyses.

The density-based automatic thresholding separates isolated AMPARs from AMPA nanodomains and isolated antibodies, opening the door to precise quantifications of the molecular content per object family (**Figure 2.17**b,c). While it is difficult to quantify the number of tagged proteins based on the random spatiotemporal distribution of localizations in dSTORM imaging, an estimate can be made if a reference can be obtained. The isolated fluorophores, sticking non specifically to the glass coverslip outside the neuronal structures, were used as a reference for the average number of localizations per antibody and microscope resolution (**Figure 2.17**e). Normalizing the number of localizations per individual AMPAR allowed for estimation of the number of fluorophores per receptor (**Figure 2.17**e), as well as the average number of receptors per nanodomains and nanodomain size of ~70nm (**Figure 2.17**h), confirming the results presented by *Nair et al*[24].

It should be noted that these classifications were dependent on a manual segmentation step based on a low-resolution widefield Alexa647 image taken prior to dSTORM imaging that allowed separation of neuronal areas (dendritic and synaptic) from nonspecific adsorption of antibodies to the coverslip surface. Recent work in a collaboration with Valentin Nagerl's group on a dual-modality STED-SMLM microscope obtains information about spine morphology that can be used to much more accurately classify spatial organization of AMPA receptors and their nanodomains as being localized principally to the spine neck or the spine head, for example. The nanoscale colocalization needed to extract this kind of quantitative information a highly precise field of view transformation. As part of separate work (4.2.1) in this thesis project, a highly robust and versatile field of view transformation was implemented into our single molecule localization software, PALMTracer. The 2-dimensional third order polynomial transformation (equations 4.1 and 4.2) accounts for scale, rotation, shift, and higher order deformations between the STED detection and the single molecule imaging path with sub-localization precision error. For the STED-SMLM project, this FoV transformation is calibrated for a given imaging configuration (objective, filter sets, etc.) and applied to the single molecule localization data such that it can be accurately overlaid onto STED images for much higher-resolution classification that may help to lead to new physiological discoveries thanks to multimodal STED-SMLM imaging.

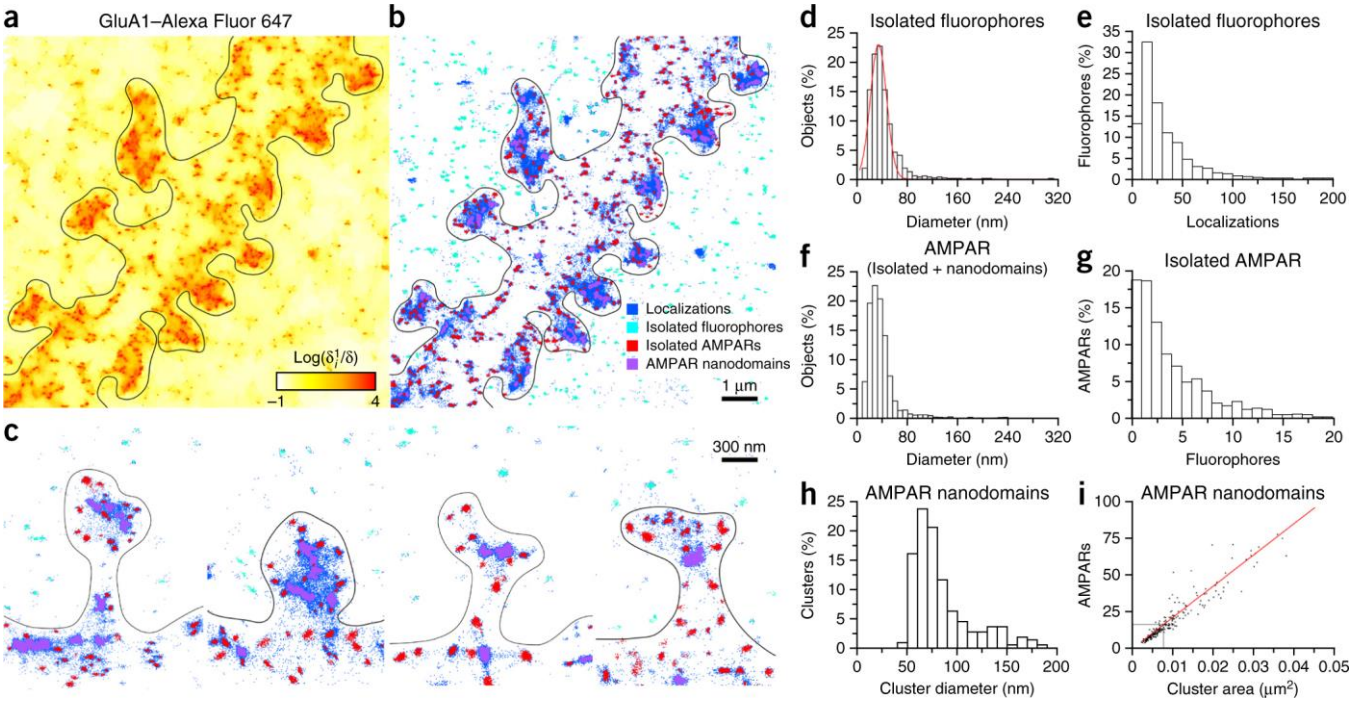

Figure 2.17: SR-Tesseler for AMPAR Nanodomain Quantifications. dSTORM Cluster quantifications with primary and secondary antibodies, validating SR-Tessler's cluster analysis on receptor clustering (**a**). (**b,c**) Localizations are clustered into 3 levels: isolated fluorophores outside of the neuron (light blue), isolated AMPA receptors (red), or regions of high density with several clustered receptors, called nanodomains (purple). (**d-i**) Quantifications match image-based cluster analysis in *Nair et al*[24], notably demonstrating a median cluster diameter of ~70nm that grows linearly with number of receptors.

From *Levet et al* [93], Nature Methods 2015

A keen eye might notice the large number of dark blue localizations in **Figure 2.17**c, corresponding to localizations that are inside the manual neuron segmentation but are below the automatic density threshold for individual receptor segmentation. These localizations are likely multiple emitters artifacts due to the stochastic nature of fluorophore blinking in dSTORM, and the intensity-based filtering workflows detailed in 1 could be beneficial for future quantitative analysis. These kinds of structures are frequently imaged using dSTORM but the variability in local protein density (individual receptors vs clusters of several tens of receptors) make high-quality, artifact-free imaging difficult.

DNA-PAINT offers the unique advantage of being able to control the density of fluorophores independently from the ligand density, allowing an effectively unlimited source of fluorescent tags. Despite the long linker length of commercially available primary and secondary antibody labeling DNA-PAINT kits (UltiVue), we performed DNA-PAINT imaging on endogenous GluA1 receptors (Figure 2.18a) for 80,000 imaging frames as a proof of concept. A super-resolution reconstruction of all 2,234,959 localizations is shown in Figure 2.22a. The SR-Tesseler was used to generate a Voronoï diagram and an individual dendritic spine was selected for nanodomain analysis (Figure 2.18b). The first level of clustering coarsest outlined the dendritic area, and a second level of clustering outlined nanodomains and individual AMPA receptors on the membrane surface (Figure 2.18c). A third level of clustering (Figure 2.18d) inside a single nanodomain (green outline) reveals several areas of high localization density (white ellipses) with FWHM ranging between 24-34nm, similar to the expected resolution limit of primary and secondary antibody labeling (section 2.3.2). While one would like to try to extract more

quantitative information about the spatial organization of individual nanodomains, the labeling strategy prevents further interpretation of the data.

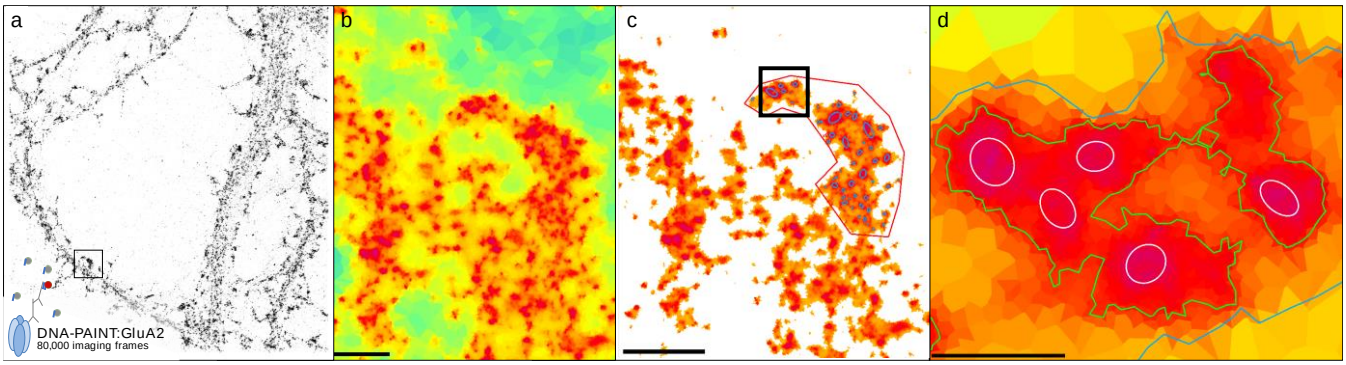

Figure 2.18: GluA2 DNA-PAINT and Nanodomain structure. **(a)** Reconstruction of 2,245,959 localizations from 80,000 DNA-PAINT imaging frames. **(b)** Voronoï diagram of a single dendritic spine. **(c)** Automatic Multi-scale segmentation of individual receptors and nanodomains **(d)** An individual nanodomains (green outline) is segmented into sub-regions of 24-34nm (white ellipses, FWHM), representing the labeling-limited resolution of the experiment.

DNA-PAINT | Endogenous GluA2 | Hippocampal Neuron Culture | Scale bars: (b, c) 500nm, (d) 100nm

Further improvements to protein labeling with DNA-PAINT, for example using primary antibodies, antibody fragments or nanobodies coupled to the DNA oligomer, are required before a quantitative analysis of the internal structure of nanodomains can be obtained. This is an ongoing project in collaboration with Matthieu Sainlos from Daniel Choquet's group.

2.5 ADVANCED QUANTITATIVE SINGLE MOLECULE MICROSCOPY: TOWARDS MOLECULAR COUNTING

Localizing a high density of single molecules provides a vast amount of quantitative information about biological structures and their environments, but the complex sample preparation, image acquisition and data analysis have prevented the mainstreaming of SMLM. In this chapter, tools to facilitate quantitative SMLM have been presented, as well as their application to a complex biological model, AMPA receptor clustering in hippocampal neuron cultures.

An ultimate goal of single molecule quantitative biology is to be able to count individual proteins in their native environment. While statistical step photobleaching approaches[99,100] have been demonstrated for synaptic protein counting[101], and specifically AMPAR subunit composition counting[102], these approaches do not offer the spatial resolution to resolve individual receptors or subunits in their native cellular environment. The localization-based radiometric approach outlined here is effective as an estimate but highly dependent on fluorophore blinking. Furthermore, quantifying individual receptors requires extremely precise and well-known labeling efficiency, and the primary and secondary antibody labeling used the previous work presented in this chapter introduces variability in the stoichiometry of fluorescent labels to receptors. While true protein counting will require further advances in labeling strategies, new tools are becoming available that enable quantitative SMLM label counting independent of fluorophore photophysics.

2.5.1 Molecular Counting with Quantitative DNA-PAINT

Recently, *Jungmann et al.* introduced an exciting new tool expanding on their DNA-PAINT modality that decouples fluorophore counting from the intrinsically variable molecular photophysics in a method called quantitative PAINT (qPAINT)[103]. The basic principle uses the well-known and reliable binding kinetics of the fluorescently tagged DNA-strands to calculate the number of DNA binding sites (**Figure 2.19**). The dark times, τ_d, between fluorescence bursts (**Figure 2.19**b) for a given spatial region are calculated and their cumulative distribution function is plotted (**Figure 2.19**c) and fit to an exponential, from which the average dark time $\tau_d{}^*$ is extracted. The influx rate of imager strands, $\xi = k_{on} \times c_i$, is calibrated using a structure of known stoichiometry (a DNA origami with known number of binding sites, validated by image reconstruction to ensure all binding sites are functional). With this influx rate calibration, the number of DNA binding sites for any given region can be calculated as: $(k_{on} \times c_i \times \tau_{d*})^{-1} = (\xi \times \tau_d^*)^{-1}$. **Figure 2.19**e-g from *Schnitzbauer et al* clearly demonstrates the power of qPAINT in its accurate counting of binding sites even when visual identification is difficult or impossible, is in the 10-nm grid Origami (**Figure 2.19**f).

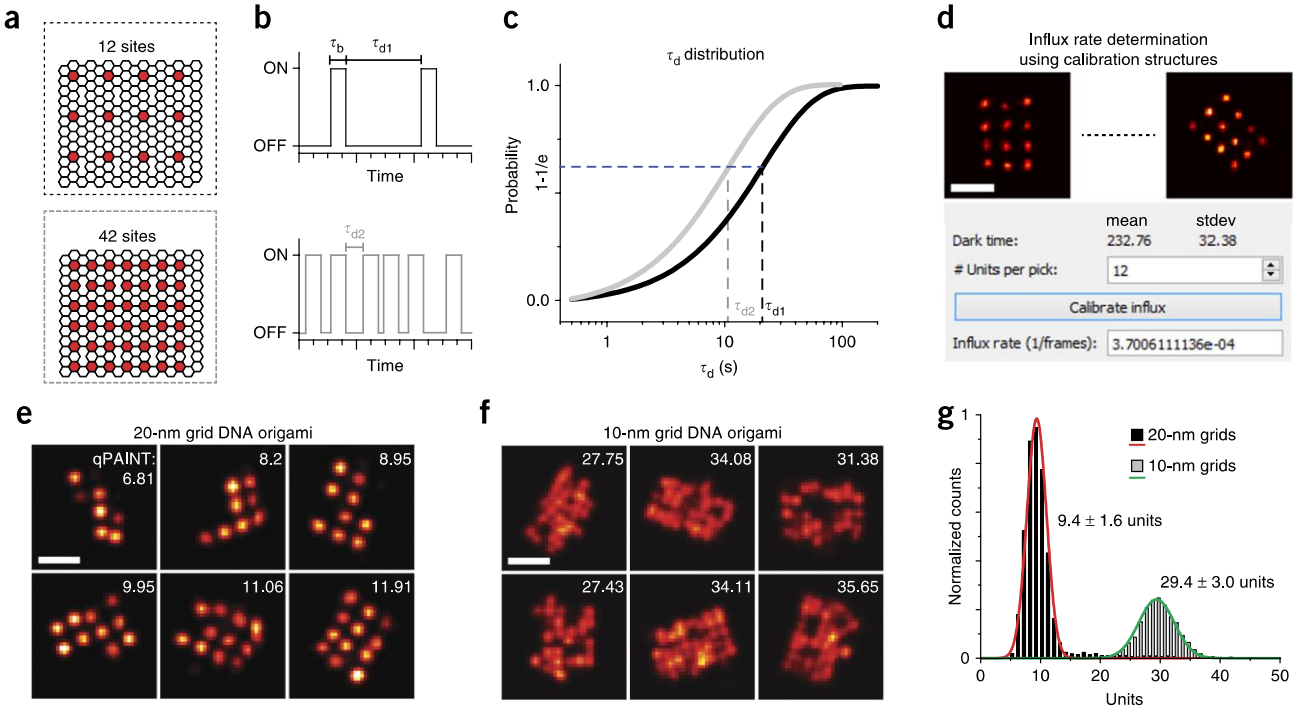

Figure 2.19: Quantitative PAINT (qPAINT). **(a)** DNA origami are used as reference structures with known stoichiometry. **(b)** The dark time, τ_d, between fluorescence bursts decreases with increasing number of binding sites. **(c)** The average dark time, τ_{d*}, can be calculated from an exponential fit of the cumulative distribution function of all dark times. **(d)** The influx rate of imager strands can be calculated based on known numbers of binding sites in a given region, enabling quantitative calculation of number of binding sites in any region based solely on its dark time distribution. **(e)** DNA origamis with variable number of binding sites and their calculated number of binding sites. **(f)** Smaller spacing between DNA origami reduces the ability to visually distinguish binding sites but the qPAINT technique can still accurately extract the number of binding sites based on the dark time distribution. **(g)** Distributions of the number of binding sites (units) per grid origami

from *Schnitzbauer et al* [96]

Like dSTORM counting, qPAINT requires a reference for single binding site to enable relative counting between conditions. Whereas *Jungmann et al.* used DNA origami with a known number of binding sites for this calibration, our commercially available DNA-PAINT kit was not

compatible with our DNA origami, and so we implemented the qPAINT analysis routine to test if we could use a ratiometric approach for counting similar to the previous dSTORM approach. We used LIMAP to spatially pattern a 4x4 grid of various densities (**Figure 2.20**a) and we manually selected spatially isolated binding sites in low-density regions as the reference for a single binding site (**Figure 2.20**b, top). Bright fluorescent spots that contained significant variance in maximum intensity over the course of the 10,000 imaged frames were considered as multiple fluorophores in a diffraction-limited area and ignored for calibration (**Figure 2.20**b,bottom). A MATLAB program was developed to correct for short-term blinking and binarize the fluorescent time traces from these individual regions, and the dark time between blinking events for each time trace was calculated. The dark time cumulative density function of all single binding sites was calculated and fit to an exponential (**Figure 2.20**c, blue line), indicating a mean dark time of 133 seconds between blinking events. As a proof of concept of the method, time traces were compiled from 3 spatially isolated individual single binding sites and analyzed with the same MATLAB routine, revealing a mean dark time of 58.5 seconds for the triple binding sites (**Figure 2.20**c, red line). The ratio between the mean dark times gives an estimate of the number of binding sites calculated by qPAINT as 2.16. While this preliminary qPAINT application did not find the true number of binding sites, 3, this is likely due to improper calibration or limited statistics. The use of DNA origami will enable true binding site calibration, and recent advances in DNA labeling for highly multiplexed imaging and DNA-conjugated primary antibodies [75] could allow for better specificity and labeling quality in biological qPAINT applications.

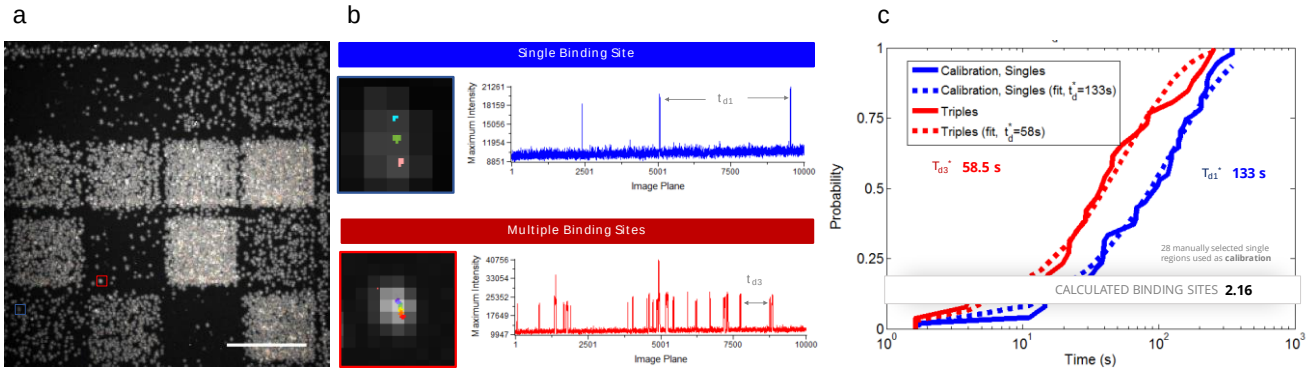

Figure 2.20: Preliminary Quantitative PAINT Tests with UltiVue DNA-PAINT Antibodies (a) Antibodies were patterned in a 9x9 grid of squares with varying densities (b) Time traces of single DNA-binding sites (top) and multiple binding sites (bottom). Localizations are overlayed on maximum projection of 10,000 acquisition frames and color coded for time. The lateral spatial shift due to sample drift helps to visually separate temporally distinct localizations of the same binding site. (c) The qPAINT method was used to calculate the cumulative density function of the fluorescence dark time, that is, the time between DNA binding events. The CDF was fitted to an exponential, and the ratio of the mean dark times is used as a quantitative indicator for the number of binding sites.

Goat Anti-Rabbit D2 Patterned by LIMAP | DNA-PAINT Acquisition for 10,000 frames, 50ms/frame

2.5.2 Improving Labeling Quality with dense, low linker length probes

Further improvements to protein labeling with fluorescent probes will allow for more quantitative SMLM. Small ligands like monomeric Strepatividin[57,104] (**Figure 2.21**) and nanobodies[53] allow for high-density labeling of target proteins, allowing for extremely homogeneous labeling of small molecular compartments. In combination with new methods for cluster analysis, either by software[105,106], varying labeling density[48], or in combination with

quantitative DNA-PAINT, these small probes will help to make cluster quantification in terms of protein counting via single molecule imaging a reality.

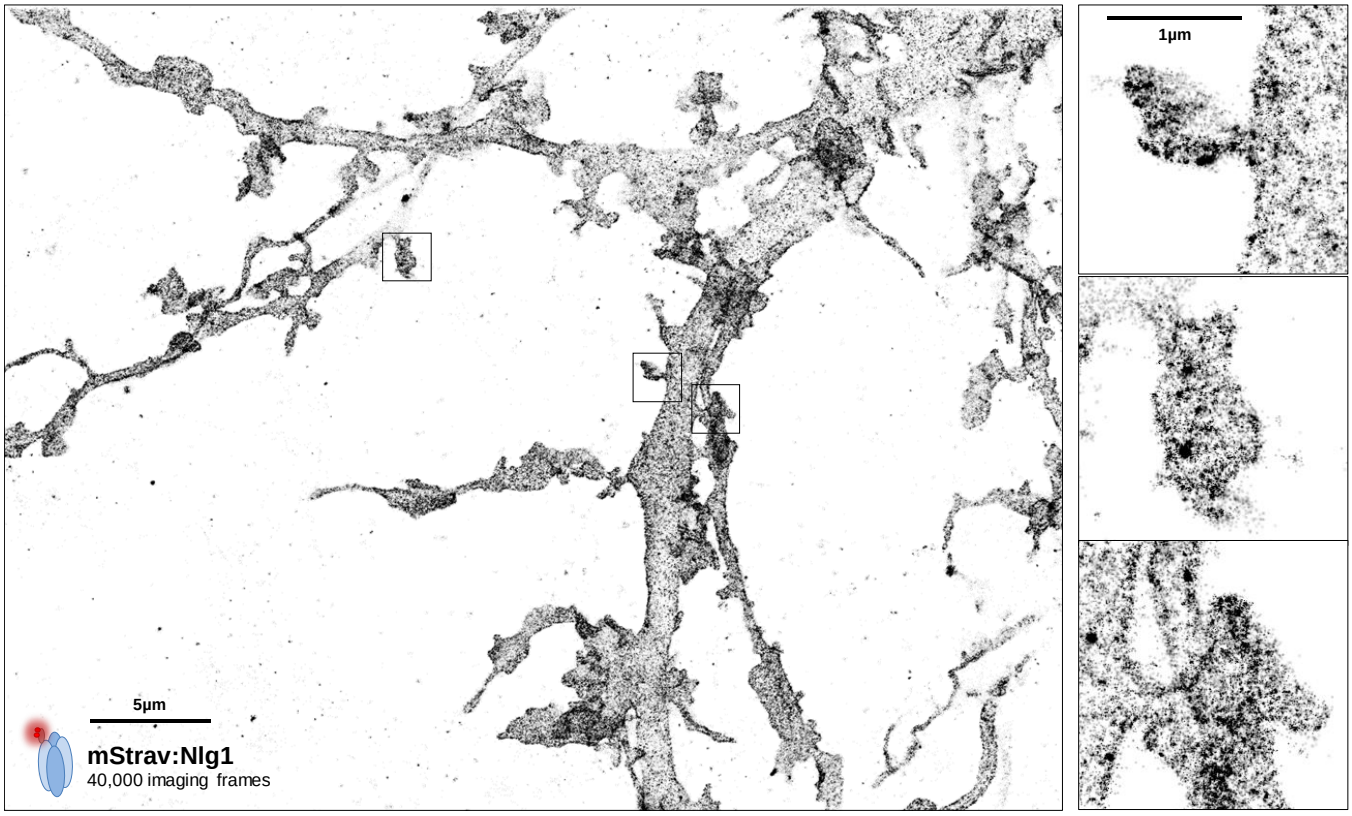

Figure 2.21: High-Density Labeling Techniques for SMLM in Neuron Cultures. Monomeric Strepatividin[57,104] enables extremely high density, low linker-length dSTORM imaging of Neuroligin1 in hippocampal neuron cultures.

Neuroligin1 | mStrav:Alexa647 dSTORM | Rat Hippocampal Neuron Cultures | Collaboration with Ingrid Chamma

2.5.3 Minimizing Reconstruction Artifacts for Accurate Quantification

An important consideration when performing such long-duration experiments like dSTORM or DNA-PAINT is the quality of drift correction with a fiducial marker; the limiting factor in number of frames is typically bleaching of tetraspeck beads after the ~1 hour of imaging time. Using nanodiamonds as stable fiducial markers can allow for imaging over an indefinite amount of time[43]. Furthermore, averaging the drift trajectory of several fiducial markers across the field of view of the acquisition can improve the quality and most notably variance of the drift correction (**Figure 2.22**). However, imaging nanometer structures will require more precise drift correction. Recently, *Dai et al*[107] proposed a method of drift correction using precisely labeled DNA origami for drift correction with residual error less than 1 nanometer, visually resolving fluorophores that were spaced only 5 nm apart. This kind of accurate drift correction will be essential for individual protein visualization in the future, making DNA-origami essential structures for quantitative SMLM for both protein counting and image registration.

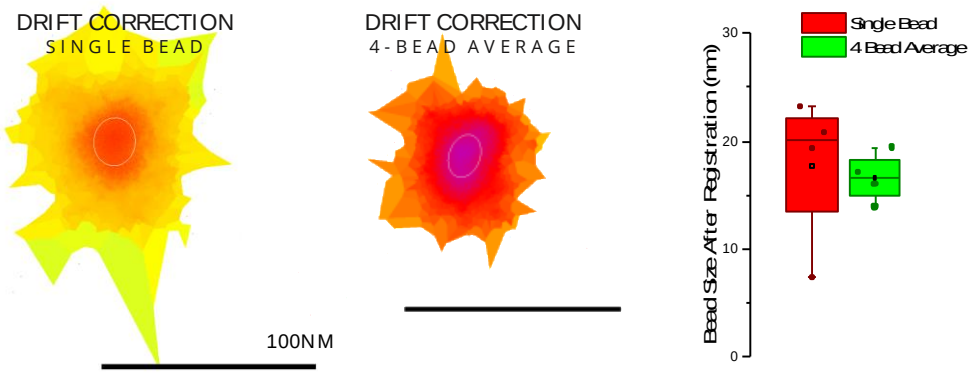

Figure 2.22: Averaging the drift from several fiducial markers improves drift correction. Conventional image registrations are performed using a single bead (left, red), but averaging the trajectories of multiple beads across the imaging field of view provides ~25% more precise drift correction (right, green).

100nm Tetraspeck beads, 640nm Excitation

Finally, when performing the kinds of cluster analyses presented in this chapter, it is critical to consider the biological context being imaged. The AMPA receptor clusters presented in this chapter were imaged on the dendritic surface of hippocampal neuron cultures. While neuron cultures adhered to the glass surface and are considered flat relative to the complex 3D network of a complete brain, they still possess a thickness of several micrometers, which, if neglected, can induce errors in cluster analysis or protein counting and artifacts when imaging structures. An example of these 2D projection artifacts can be seen in **Figure 2.23**, where the 2-D projection of localizations analyzed by the SR-Tesseler combines clusters of localizations with different axial positions, skewing the cluster size and count statistics. Furthermore, 3D cluster analysis is imperative when investigating the spatial relationship between multiple proteins (Figure 2.24)

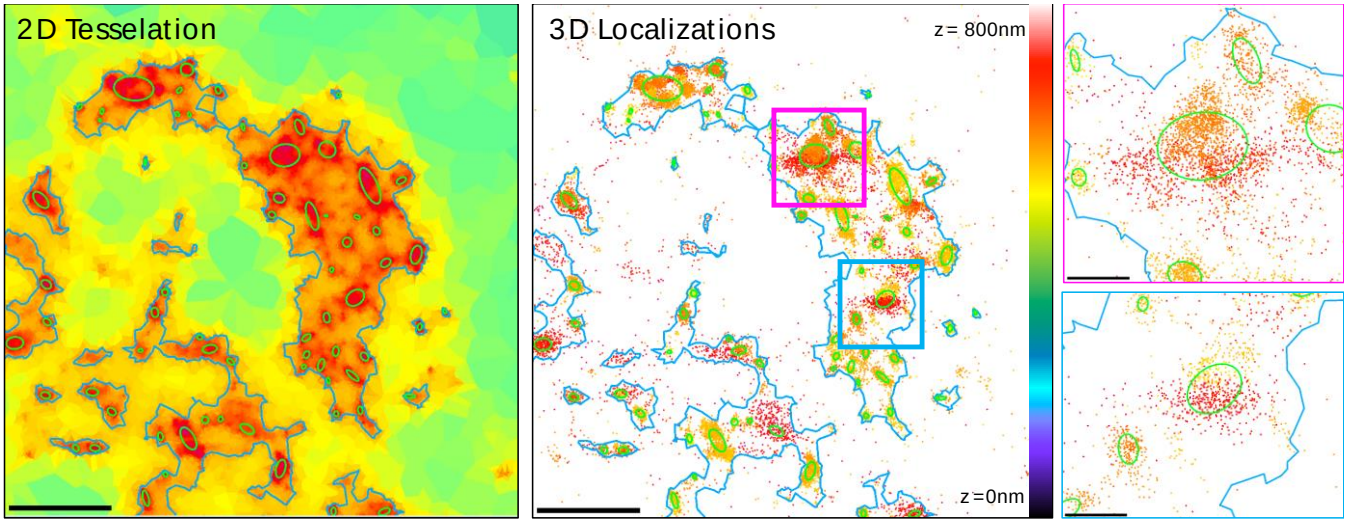

Figure 2.23: 2D Projections of 3D Environments Produce Artifacts in Cluster Analysis. (left) 2D Voronoï Diagram created with SR-Tesseler of GluA1 in a single dendritic spine, automatically segmented for spine (blue region) and AMPAR clusters (green ellipses). Color code: Normalized density. Overlaying individual localizations color-coded for axial position (center) shows that clusters may be artificially identified as a single cluster (right) when they are actually two distinct, axially separated clusters of localizations.

Endogenous GluA1 | DNA-PAINT I1-550 | 3D with Cylindrical Lens

Thus, a clear need exists for precise 3D axial localization, especially for quantitative SMLM imaging. Chapter 3 will introduce conventional approaches for axial localization at the coverslip

surface, as well as a new approach for 3D SMLM imaging in complex biological environments like brain tissue.

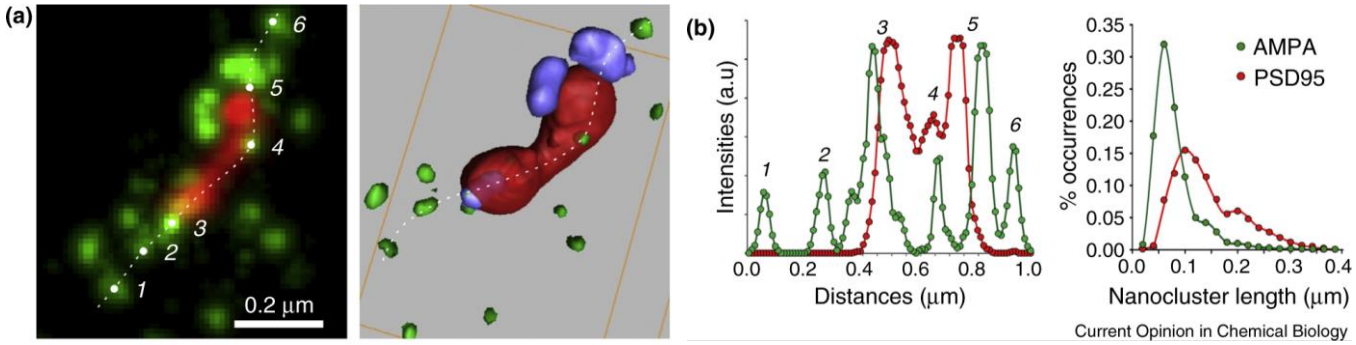

Figure 2.24: 3D Imaging reveals colocalization between clusters of synaptic proteins. AMPA Receptors (green) form nanodomains near the edges of intracellular the PSD95 scaffolding protein (red), showing the importance of axial localization for protein co-organization.

From *Hosy et al*[108]

CHAPTER 3 3D SINGLE MOLECULE IMAGING USING ADAPTIVE OPTICS

Single molecule localization techniques like PALM, STORM, and PAINT offer unique access to the nanometer-scale environment of individual proteins. In a biological context, the study of the spatial organization and dynamics of individual proteins, and especially the co-organization of several proteins, requires a 3D vision of the sample. While PSF fitting methods introduced in Chapter 1 provide greatly improved lateral resolution, the axial resolution with these techniques remains diffraction-limited. Furthermore, imaging into nonhomogeneous samples induces optical aberrations, which reduces the number of collected photons and therefore the localization precision with depth.

The 3D organization of biological structures makes axial localization imperative for single molecule biology, but requires more advanced optical and numeric approaches. Moreover, detecting and correcting these depth-induced aberrations is essential to progressing SMLM away from the coverslip surface and into more complex and physiologically-relevant biological models, such as brain tissue.

In this chapter, I outline several techniques that enable axial localization beyond the diffraction limit by encoding axial position of the molecule into the point spread function, comparing the drawbacks and advantages of each technique in terms of PSF complexity, imaging depth, and resolution. I introduce the notion of adaptive optics for correcting common aberrations, using a deformable optical element to directly compensate for phase variations induced by imperfections in the optical path, and detail our implementation of a commercially available plug-and-play adaptive optics system for single molecule localization microscopy (SMLM). As part of the CIFRE collaboration with Imagine Optic, the software integration I developed within the MetaMorph acquisition environment is employed for depth-dependent aberration correction. Finally, in collaboration with various teams in the IINS, I outline a workflow that enables aberration correction for 3D SMLM in brain slices.

3.1 THREE-DIMENSIONAL SINGLE MOLECULE IMAGING VIA POINT SPREAD FUNCTION ENGINEERING

In order to accurately localize individual molecules, SMLM microscopes impose stringent criteria on the optimization of the excitation and detection that maximize the contrast of single molecule fluorescence by minimizing background. At best, residual background fluorescence reduces the localization precision of the event; at worst, it can make segmenting individual localizations impossible, completely omitting single molecule events. Even when successfully localized, the fitting process discussed in 1.2.2 gives access only to the lateral *xy* coordinates of the single emitter. However, as shown in 2.5.3 **Figure 2.24**, this 2D projection may result in false biological conclusions when imaging 3D structures. Unfortunately, accessing the axial position of the molecule is not as straightforward as the centroid-based techniques used for lateral localization, as the point spread function is laterally symmetric and lacks axial optical discrimination.

3.1.1 Axial Resolution in Optical Microscopy

The Airy pattern created by the diffraction of the point source through the optical system presented in **Figure 1.2** of section 1.1.2.1 is just one transverse slice of the more complete, 3-dimensional diffraction pattern, which extends symmetrically above and below the focal plane previously investigated. This axial Airy diffraction pattern is anisotropic, resulting in the intensity pattern spreading much more axially than laterally. This **axial resolution**, given by:

$$\Delta z_{FWHM} = 2n\frac{\lambda}{NA^2} \qquad (3)$$

is highly dependent on the wavelength and objective numerical aperture and is typically between 600nm-800nm for visible light. While high-NA objectives afford maximal photon collection and maximal lateral and axial resolution, they do so at the expense of limiting the **depth of field**, the thickness of single focal plane, given by the equation:

$$d = n\frac{\lambda}{NA^2} \qquad (4)$$

where *d* is the depth of field, typically limited to ~1μm for SMLM microscopes using conventional optics. The effect of numerical aperture on depth of field and axial resolution is shown in **Figure 3.1** .

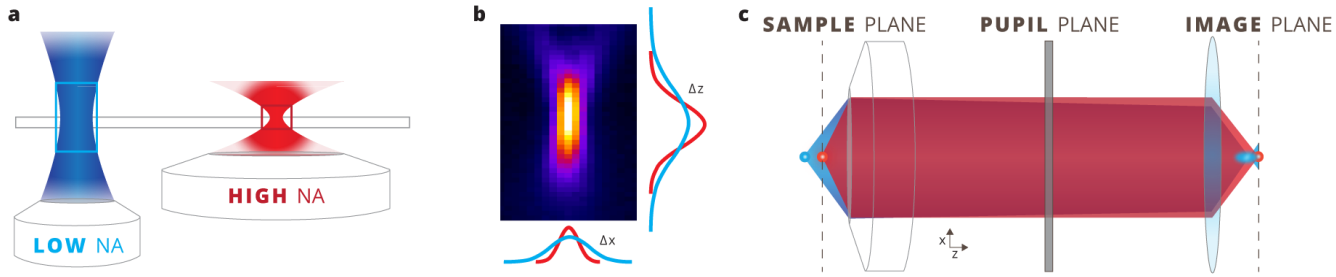

Figure 3.1: Axial Resolution Blurs Images of 3D Objects. (a) Increasing the numerical aperture of the collection objective reduces the thickness of the imaged area, called the depth of field. **(b)** The axial PSF as collected by a high-NA objective displays a much larger spread axially than laterally. **(c)** Out of focus fluorophores (blue) are spread storngly in the axial direciton and cause strong blurring in the image plane.

Combining the axial spread of fluorescence from a single molecule with this concept of depth of field, it can be easily shown that excited fluorophores outside the focal plane can still create a strong signal in the focal plane, blurring features in conventional microscopy and creating a strong background that degrades single molecule imaging. While confocal systems use a pinhole optically conjugate to the focal plane to spatially filter out of focus light, preventing background fluorescence from blurring the image, the widefield detection schemes used in single molecule imaging preclude this kind of confocal filtering. SMLM techniques therefore seek to minimize the out of focus light by ensuring single molecule conditions through weak photoactivation or optimizing imaging buffers.

Once the single molecule has been separated from the background, a single image frame still lacks the information necessary to extract the molecule's axial position. In 2003, *Speidel et al* demonstrated that the axial position of the emitter from the focal plane is actually encoded in the observed intensity pattern as the number and diameter of rings of the Airy function, but this 3D single particle tracking method requires extensive experimental PSF characterization, extremely bright, spatially sparse fluorescent beads and is sensitive to optical aberrations [109] (**Figure 3.2**). Using the lateral shape and size of the PSF to estimate axial localization is marred by two main flaws: the photon count and thus the localization precision of this method decrease with axial position relative to the focal plane, and a perfectly isotropic emitter's PSF is axially symmetric and therefore lacks the discrimination to indicate whether the molecule is above or below the focal plane.

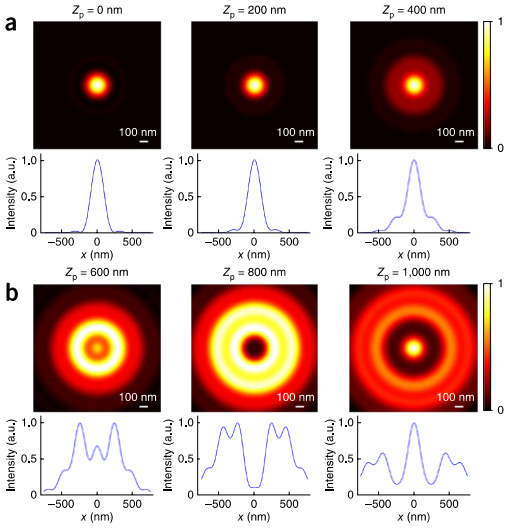

Figure 3.2: Simulated Lateral Profile of Isotropic Emitter at Various Axial Positions. (a) The size of the Gaussian fit can be used as an estimate for the axial position of a single emitter when it is close to the focal plane **(b)** The characteristic ring structure of the PSF exploited in [109] is complex to fit, requiring a strong signal

From *Deshout et al*.[34]

3.1.2 Multi-Image Based Techniques for Axial Imaging

Recently, a variety of techniques have been developed to address the lack of axial discrimination in conventional microscopy, enabling axial localization of single molecules well below the diffraction limit. The experimental setups and effective superresolution PSFs of each technique is summarized in **Figure 3.3**.

The first set of techniques disambiguates the axial position of a single emitter by directly imaging multiple planes. First demonstrated for single particle tracking[110] and shortly thereafter for PALM imaging[111], the bi-plane method separates the fluorescence emission into 2 image paths using a 50/50 dichroic beamsplitter; the first path images creates a conventional single molecule image, whereas the second optical path is slightly longer and creates a concurrent image at focal plane axially shifted by ~500nm-1μm. By simultaneously imaging two focal planes, the molecule's axial position can be unambiguously determined by measuring lateral PSF size. Unfortunately, this method sacrifices axial resolution for lateral localization precision due to the requirement of splitting the detected fluorescence in 2 paths. This technique was expanded upon Dahan's group in 2014 by placing a phase mask in the detection path and simultaneously imaging 9 planes, enabling whole-cell PALM[112]. However, this multiplane technique compromises imaging depth for a greatly reduced field of view. Another very recently introduced technique achieves similar 10μm thick imaging with ~50-100nm axial resolution by using an electrically tunable lens to convert axial displacement into a lateral shift in the PSF over the course of a single image exposure[113].

One slightly different technique uses a unique physical property of high NA objectives to quantitatively assign an axial position to the emitter. Objectives with a numerical aperture great than 1, such as the oil-immersion objectives commonly employed in SMLM, are able to detect fluorescence that is coupled into the coverslip and that propagates as an evanescent wave, known as the super-critical angle fluorescence (SAF). In the detection-analog to total internal reflection excitation, *Bourg et al*[114]and *Deschamps et al*[115] optically calculate the amount of SAF per localization to axially localize single fluorescent molecules with 20-25nm axial localization precision. Because the SAF depends exponentially on the distance of the emitter to the coverslip surface, this technique has the unique ability to determine an absolute axial localization with respect to the coverslip surface and can be used for quantitative comparisons between coverslips without the need for extensive calibration; however, like TIRF, SAF is only valid for several hundred nanometers above the coverslip.

By similarly sacrificing depth of field, interferometric approaches increase experimental complexity for nearly isotropic axial localization precision. The iPALM[116] technique employs an interferometric approach where fluorescence emission is collected by two objectives interfered onto 3 separate cameras. While the axial localization position is extrapolated from the relative intensities with extreme accuracy, resulting in axial localization precision ~10nm even more precise than its ~20nm lateral localization precision, the technique is limited to a thickness of $\lambda/2$. The 4Pi-SMS[117] technique interferes orthogonal polarizations of the emission collected by the two objectives to extend the imaging depth to ~650nm.

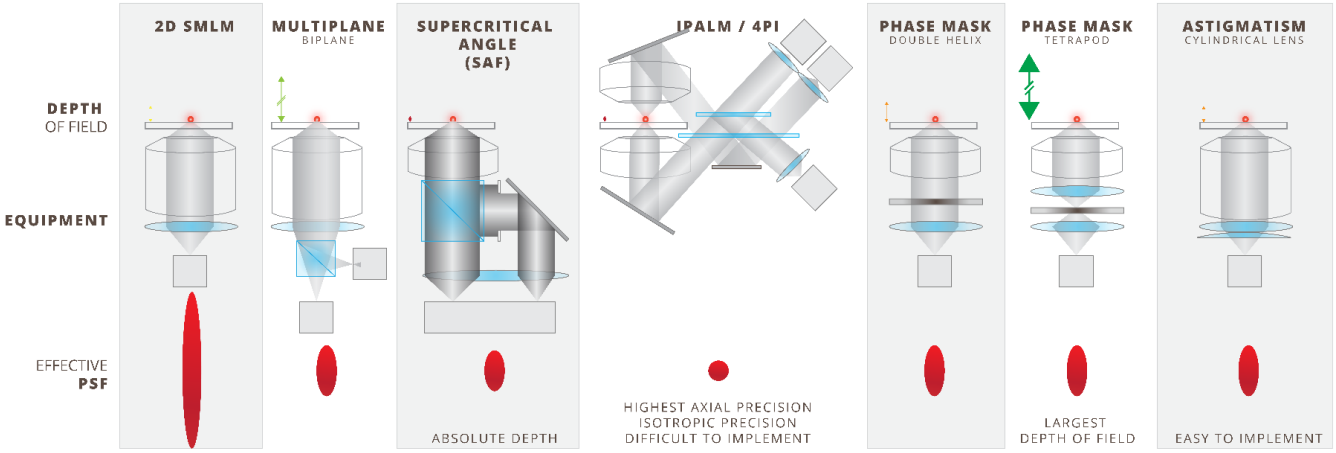

Figure 3.3: Methods for Axial Localization Beyond the Diffraction Limit A non-exhaustive list of common methods for axial localization. Notably, the iPALM technique has the highest axial localization precision at the expense of experimental complexity. The tetrapod phase mask has the largest depth of field of nearly ~20μm for bright molecules, and the SAF technique benefits from a quantitative axial assignment from the coverslip surface. The astigmatism method is very simple to implement optically and numerically, making it the most common axial localization method

Inspired by [34, 118]

3.1.3 3D Single Molecule Imaging via PSF Engineering

These previously mentioned interferometric approaches for axial localization exploit valuable information in the phase of the collected fluorescence, information that is lost through a conventional imaging system. Since traditional imaging cameras are incapable of determining the entire complex light field and image simply the square of the electromagnetic wave's electric field, a set of complementary axial localization techniques seek to modify the phase of the detected light field such that the axial information is encoded in the intensity profile of the point spread function, a technique called **PSF engineering**. By placing a phase modifying element in the **Fourier plane** of the detection path, also known as the **pupil plane** as it is optically conjugate to the back focal plane of the objective (**Figure 3.1**c), it is possible to perform optical spatial frequency transformations that enable the desired phase to intensity conversion.[119]. The exact shape of the point spread function depends on the specific phase profile applied to the detection system. In SMLM, a calibration of the intensity profile of the PSF as a function of axial position is used to generate a lookup table from which axial positions of individual emitters can be assigned.

One of the first implementations of PSF engineering for axial localization was introduced by *Pavani et al* in 2008, where they used a double-helix point spread function to encode axial position as a rotation of two individual points[120]. The centroid of the two localization gives a lateral localization precision of $\sigma_{x,y}$~25nm laterally, and the rotation between them gives an axial localization precision of σ_z~50nm through an imaging depth of ~1.5μm. A key advantage of these PSF engineering techniques is that, by carefully modifying the phase and thus the interference of the collected fluorescence, information that is technically outside of the optical depth of field of the objective can be obtained, enabling sub-diffraction limit spatial information in an axial range larger than optically possible.

W.E. Moerner's group has been instrumental in the optimization of the point spread function for 3D single molecule imaging and tracking. In 2014, *Shechtman et al* introduced a pupil-plane phase pattern that was specifically designed to maximize information content in the low-signal, high-background context of single molecule imaging. Dubbed the Saddle-point PSF[121], this phase pattern produced a point spread function capable of localization with high precision ($\sigma_{x,y}$~15nm and σ_z~20nm) over an extended axial range of 3μm. Just a year later, the same group introduce the Tetrapod PSF family[122], which is currently considered the optimal point spread function for single particle tracking applications as it extends the localizable axial range to 20μm for sufficiently bright fluorescent markers.

These aforementioned phase alteration techniques have several drawbacks that prevent their widespread implementation. In addition to a small 4f optical relay system to perform the optical Fourier transform (**Figure 3.3**), they require specifically designed and fabricated phase masks. While dynamic elements like spatial light modulators (SLM) can be employed, phase modification techniques are inherently wavelength sensitive, making multicolor SMLM difficult. Furthermore, one key tradeoff of the tetrapod PSF is the compromise in spatial spread of the PSF for imaging depth; the tetrapod point spread function is spread over ~10x the spatial extent from the diffraction-limited, aberration-free PSF. This large PSF area restricts the number of concurrent emitters per SMLM frame, and limits the tetrapod PSF primarily to SPT applications.

As in conventional microscopy, the resolution tradeoff becomes apparent in axial single molecule localization: imaging depth cannot be increased while retaining the same temporal resolution in the form of imaging speed.

The most popular method for injecting axial discrimination into the PSF of a SMLM microscope situates itself as a good compromise between imaging depth, spatial and temporal resolution. The method, first employed in 1994 in an SPT application[123], explicitly introduces the common system aberration of **astigmatism** into the detection path, which induces an ellipticity in the PSF that varies based on axial position. Using a cylindrical lens to create this astigmatism, *Huang et al* [124] were the first to apply this for high-density single molecule localization in their STORM application, demonstrating comparable localization precision to bi-plane imaging[125] ($\sigma_{x,y}$~20-30nm, σ_z~60-70nm) over an axial range of ~600nm. They addressed this limited imaging depth shortly thereafter by combining astigmatic detection and axially stepping the focus, enabling whole-cell STORM over a 3μm axial range[126]. Recently, *Legant et al* combined astigmatic single molecule detection with their lattice light sheet excitation to perform multi-color PAINT imaging of entire cells up to 20μm thick[81].

In addition to its relative low cost and optical simplicity to implement into an existing SMLM microscope, astigmatism has the unique advantage over the majority of axial localization techniques in its numeric simplicity. The ellipticity of the PSF can easily be measured by extending the Gaussian fit model to 2-dimensions, an operation which is relatively easy to parallelize and implement into existing SMLM localization pipelines compared to the complicated PSF model fitting required in other techniques.

3.1.4 Improving Axial Localization in Complex Media with Advanced PSF Engineering

Astigmatism, and all phase-modification based axial localization techniques, share a common aberration sensitivity that limit their application to complex biological samples. Combining inherent field-dependent microscope aberrations with a fixed phase element like a phase mask or cylindrical lens induce biases on lateral localization and/or axial lookup[127]. Furthermore, depth-dependent spherical aberrations reduce the PSF's axial discrimination, making uncorrected astigmatic 3D imaging unreliable away from the coverslip's surface[128]. Therefore, having a wavelength-insensitive, dynamic element that can correct for system and sample aberrations is imperative for accurate 3D single molecule imaging in complex biological samples.

3.2 ADAPTIVE OPTICS AND WAVEFRONT CORRECTION FOR 3D SINGLE MOLECULE IMAGING

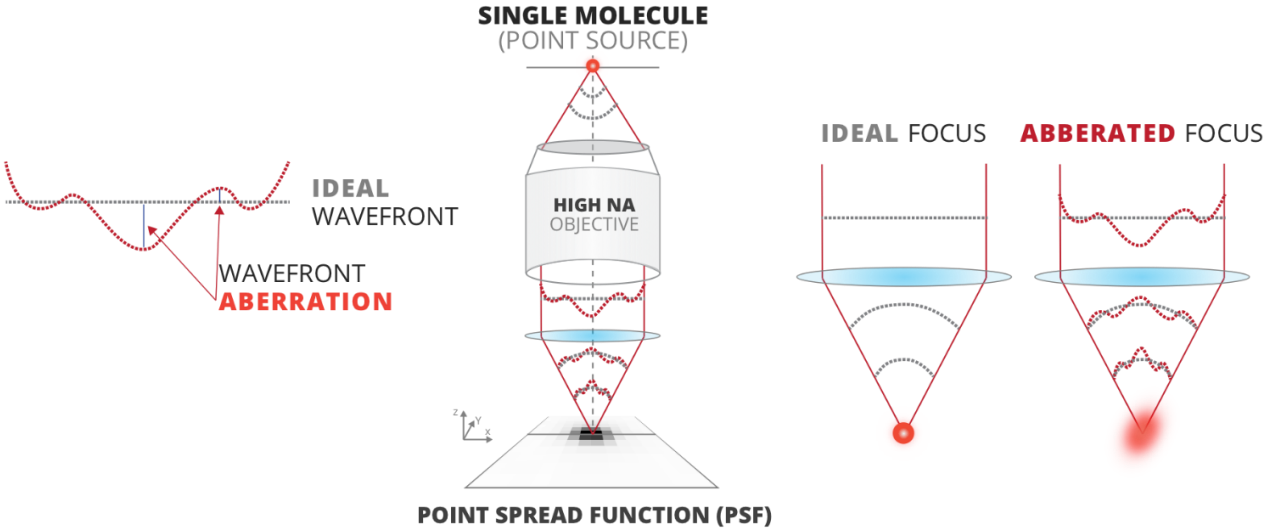

Figure 3.4: High-NA Single Molecule Microscopy and Wavefront Aberrations Wavefront aberrations are deviations from the ideal wavefront caused by imperfections in the optical path either from the sample or the microscope itself. SMLM is especially sensitive to these defects,

Originally developed in astronomy to correct for fluctuations caused by atmospheric turbulence, **adaptive optics (AO)** has become a recently begun to make its way into the domain of ophthalmology[129] and microscopy, where similar distortion correction is desired. The term adaptive optics is generally used to refer to the use of a dynamic optical device capable to correct wavefront aberrations. In microscopy applications of AO, such adaptive correction can be used to correct the excitation or detection path. In confocal, two-photon and STED microscopy, it is common to correct only the excitation path, whereas the widefield detection approaches used in single molecule imaging require only correction of the detection path[130]. Adaptive optics have an essential role in SMLM, where a diffraction-limited PSF is essential for accurate single molecule localization, as aberrations may induce localization errors larger than the localization precision[131]. *Izeddin et al*[132] were the first to use AO in single molecule localization microscopy to correct wavefront aberrations originating from the microscope to perform astigmatic 3D PALM imaging with higher precision than a cylindrical lens. However, SMLM imposes certain constraints that make conventional approaches to adaptive optics difficult to implement, particularly in quantifying aberrations in a low-signal environment.

3.2.1 Adaptive Optics for Microscopy

Understanding this adaptive correction requires a brief introduction to a wave optics perspective of microscopy. A single fluorescent point source emits its fluorescence a spherically radiating electromagnetic wave, of which a portion is collected using a high numerical aperture objective. Physically, the radial difference in thickness of the lens results in longer optical path length (OPL) for rays at the center of the optical axis compared to the extremities:

$$\mathrm{OPL} = \int n(x)dx \qquad (5)$$

where n(x) is the refractive index, which can vary as a function of distance, x. This radially-dependent optical path delay transforms the spherical wavefront of the point source into a planar wavefront. The microscope's tube lens then converges the light onto the imaging device in a similar manner, where a clear image is obtained.

Whereas ideal lenses modify the wavefront in a fixed, controllable manner to focus light, imperfections in the optical system result in a quantifiable local phase delay to the wavefront. These aberrations deviate the local wavefront from its ideal shape by a phase that is dependent on the wavelength of light and the optical path length:

$$\Psi = \frac{2\pi}{\lambda} OPL \qquad (6)$$

The effect of these phase aberrations on image formation can be understood by mathematically considering the frequency-space formalization of the point spread function. The complex **pupil function** describes the transmission of light through an optical system in radial coordinates (r,θ):

$$P(r,\theta) = A(r,\theta)e^{i\Psi(\mathrm{r},\theta)} \quad (7)$$

with the imaginary number i, and the amplitude variation function A(r,θ), which is frequently disregarded unless considering strongly aberrating samples. The image formation in incoherent fluorescence imaging can thus be formalized as a convolution of the sample's fluorescence distribution, f(**x**), with the Fourier Transform of the pupil function:

$$I(\boldsymbol{x}) = f(\boldsymbol{x}) \otimes |FT[P(r,\theta)]|^2 = f(\boldsymbol{x}) \otimes \left|FT[A(r,\theta)e^{i\Psi(\mathrm{r},\theta)}]\right|^2 \qquad (8)$$

This relation directly shows the effect of system and sample-dependent aberrations, Ψ, on the resulting image. The local phase deviations prevent proper focusing (**Figure 3.4**), spreading the focus both laterally and axially and reducing the maximum intensity in the focal plane and elongating the PSF along the optical axis[133].

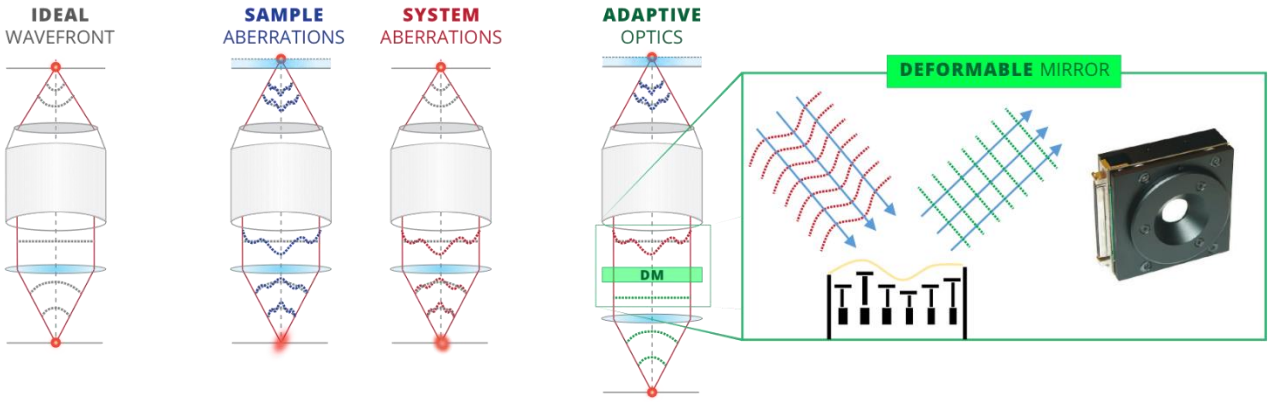

Figure 3.5: Adaptive Optics Corrects Aberrations and Restores Diffraction-Limited Focus Wavefront aberrations can be separated into two classes based on their source of origin: sample aberrations (blue) are induced by inhomogeneities in biological samples or depth-dependent imaging errors, while system aberrations (red) stem from the microscope system itself. A deformable mirror (DM) can be used to correct these wavefront aberrations, restoring a flat wavefront (green) and a diffraction-limited focus.

In this context, the fundamental idea of adaptive optics is simple: directly compensating for these aberration-induced optical path length differences using an adaptive element allows proper focusing of the wavefront and restores the diffraction-limited PSF.

One such adaptive element capable of precisely controlling the wavefront is called a **deformable mirror (DM)**. As the name suggests, DMs are composed of a highly reflective surface whose shape can be locally modified to create a non-conventional but continuous deformation. While several kinds of DMs exist, the most commonly-employed in microscopy adaptive optics consist of a reflective membrane attached to an array of electromagnetically activated actuators, as shown in **Figure 3.5**. The DM is placed in a plane conjugate to the pupil plane such that the deformation of the membrane surface imparts relative changes in the OPL across the beam profile. By applying the proper deformation to exactly compensate for the aberrations in the imaging path, the wavefront can be restored to its pristine flat profile.

Since the complex wavefront containing the instantaneous phase profile cannot be directly imaged using conventional imaging optics, specific optics and algorithms are required for wavefront detection. In **Direct Wavefront Sensing**, a **Shack-Hartmann wavefront sensor (SHWFS)** is placed in a plane conjugate to the pupil plane, in which an array of microlenses placed in front of a CCD camera converts the local phase of the wavefront at each microlens into a spatial displacement that can be measured on the sensor. Combined with a known distance to the microlens array, the angle orthogonal to the wavefront can be calculated at each point in the microlens array, from which a continuous wavefront can be inferred.

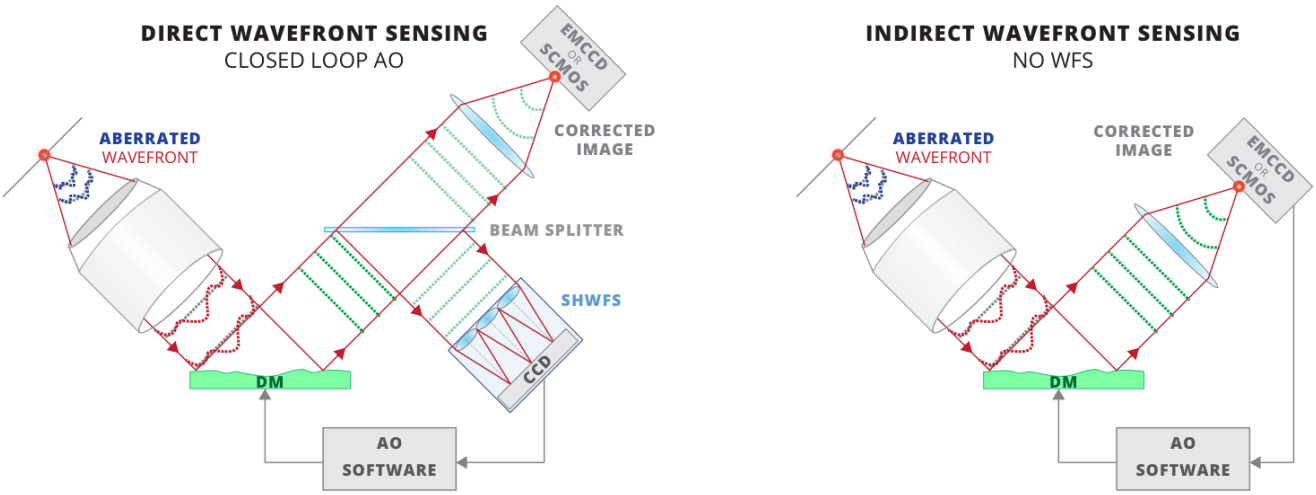

Figure 3.6: AO Modes of Operation (Left) In direct wavefront sensing, a wavefront sensor (for example, a Shack-Hartmann, SHWFS) is placed in a closed feedback loop with the deformable mirror, allowing for fast and precise wavefront correction. (Right) Indirect wavefront sensing optimizes the wavefront based on an image quality metric, requiring iterative image-based aberration detection algorithms to correct the wavefront.

Most conventional adaptive optics techniques combine the use of a WFS for wavefront detection with a DM for wavefront correction in a closed-loop configuration as shown in **Figure 3.6**. A short calibration step performs a push-pull operation sequentially over each actuator while measuring the wavefront deformation from individual actuators. This actuator command matrix is then numerical inverted to obtain an **interaction matrix (IM)** that gives the corresponding actuator changes required to induce a given wavefront modification. After proper calibration, a wavefront optimization routine flattens the wavefront within the mechanical constraints of the deformable mirror.

Once the wavefront is known, it is common practice to represent the wavefront as a linear set of the orthogonal Zernike modes[134]:

$$\phi(x,y) = \sum_{k=1}^{M} a_k z_k(x,y) + \partial\phi(x,y)$$

where M is the total number of Zernike polynomials, $z_k(x,y)$ is the k^{th} Zernike polynomial with a_k being its coefficient, and $\delta\phi(x,y)$ is the error due to the truncation of using only M Zernike polynomials. Defined on a unit circle, these Zernike polynomials represents an excellent base for describing wavefront aberrations through optical systems with circular apertures. Furthermore, common system wavefront aberrations found in many microscope systems like coma, spherical aberration and astigmatism are conveniently related to individual Zernike modes. In fact most microscopy applications can limit their Zernike decomposition into the first 10 polynomials. These primary aberrations and their corresponding Zernike polynomial, can be found in **Figure 3.7**.

Mode k	Order n	Norm. Factor N_k	Polynomial $z_k(\rho, \theta)$	Meaning
0	0	1	1	Piston
1	1	4	$\rho \sin \theta$	Tilt in x direction
2		4	$\rho \cos \theta$	Tilt in y direction
3	2	6	$\rho^2 \sin 2\theta$	Astigmatism (±45°)
4		3	$2\rho^2 - 1$	Defocusing
5		6	$\rho^2 \cos 2\theta$	Astigmatism (0° and 90°)
6	3	8	$\rho^3 \sin 3\theta$	Triangular astigmatism
7		8	$(3\rho^3 - 2\rho)\sin \theta$	Coma
8		8	$(3\rho^3 - 2\rho)\cos \theta$	Coma
9		8	$\rho^3 \cos 3\theta$	Triangular astigmatism
10	4	10	$\rho^4 \sin 4\theta$	Spherical aberration

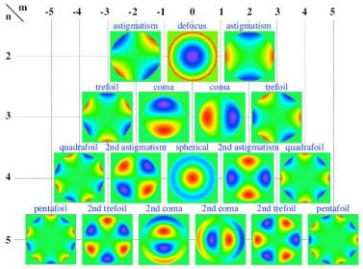

Figure 3.7: Primary Zernike Modes and their Associated Aberrations (Left) The primary Zernike modes, most commonly found in microscopy, are commonly referred to by a common aberration name, for example mode 10 is spherical aberration. (Right) The Zernike modes represented as their phase deformation.

From *Zhu et al.*[135]

However, directly measuring the wavefront in this manner requires the wavefront sensor to image the wavefront from a single focal point. Astronomical adaptive optics applications employ a single, stable, point-like reference source, known as a "guide star". In microscopy, such single bright point-sources are difficult to achieve. The pinhole detection scheme of two-photon microscopy allows for the detected signal to be used as a proxy for a point source[136], but the widefield-detection scheme used in SMLM prevents this method from being functional. While large fluorescent beads can be injected into a sample[137], their size prevent access into biological tissues and their exact position is difficult to control. The large photon count requirement combined with issues of parasitic background fluorescence prevents the adoption of direct wavefront sensing in single molecule microscopy.

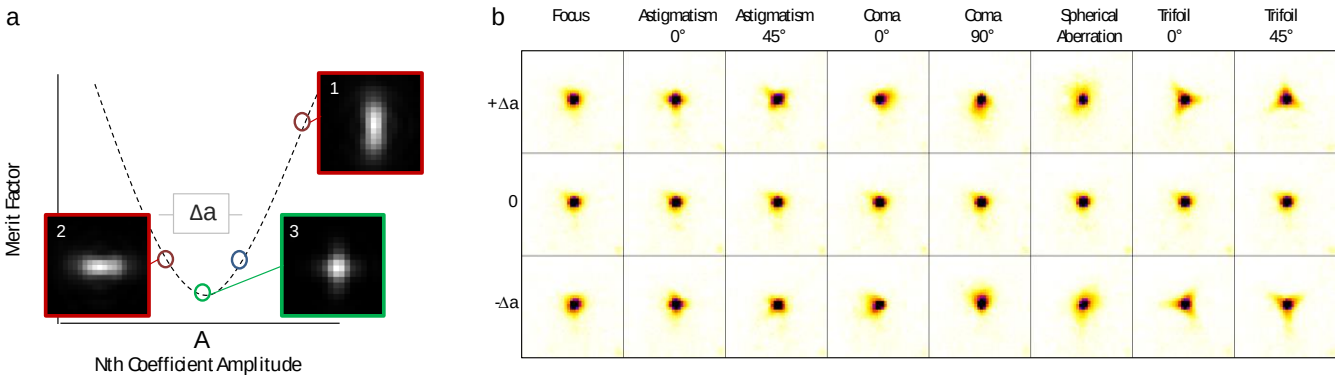

Figure 3.8: 3N Algorithm for Indirect wavefront aberration detection. (a) Indirect wavefront detection involves measuring the point spread function of the microscope as a function of an applied fixed amount of a specified Zernike mode, for example (1)+60nmRMS astigmatism and (2) -60nm RMS astigmatism. An image-based merit factor like the maximum intensity is maximized, and the resulting optimal aberration weight is applied to optimize the PSF (3). (b) This process is repeated for each of a given number of Zernike modes, commonly the primary Zernike modes. The final wavefront correction is a linear weighted combination of the iterated Zernike modes.

100nm Tetraspeck Bead | 640nm Excitation | 100x NA1.49 TIRF Objective | EMCCD @ 160nm/px

Therefore, an alternative method of accessing the wavefront that does not require a wavefront sensor known as **indirect wavefront sensing** is commonly employed in microscopy techniques. The basic principle is founded on the idea that the optimal focus is obtained from an aberration-free wavefront, and thus the maximum intensity of the lateral PSF at the focal plane can be used as a metric for wavefront quality. The same camera used for imaging the sample is then used to image a single fluorescent point source (Figure 3.6) while the deformable mirror iterates over the individual, orthogonal Zernike modes. While a range of optimization algorithms exist, the

commonly-employed $3n$ algorithm iterates over n Zernike modes, taking an image with a quantity of -Δa, 0, +Δa aberration for that particular mode (**Figure 3.8**). From these 3 images, the optimal amount of the particular aberration, ψ_n, is then calculated by maximizing the wavefront quality metric (here, maximum intensity). The resulting optimal wavefront correction is a linear weighted combination of the optimized Zernike polynomials, which are assumed to be orthogonal in the sample plane[138], giving indirect access to the underlying aberrations of the wavefront.

While indirect wavefront sensing simplifies the hardware implementation of adaptive optics due to lack of wavefront sensor, it is accompanied by the tradeoff of more complicated software in the form of wavefront optimization algorithms. Furthermore, proper alignment and calibration of the deformable mirror into conventional microscope systems is difficult and can be daunting for the everyday user.

3.2.2 Adaptive Optics for 3D Single Molecule Localization Using MicAO

To address these implementation difficulties and lower the barrier to entry of adaptive optics into single molecule imaging, a plug-and-play adaptive optics system containing the requisite hardware and ease to use software is desirable. The MicAO 3DSR system from Imagine Optic, a CIFRE collaborator for this PhD project, contains a deformable mirror and all the requisite optical components to conjugate the DM to the pupil plane of any conventional inverted microscope. A Shack-Hartmann wavefront sensor is also included, used only for alignment purposes at the initial installation or if the optical configuration of the microscope is changed, for example the installation of a new objective.

Figure 3.9: The MicAO Plug and Play 3DSR Adaptive Optics Kit from Imagine Optic. The commercially available kit contains a deformable mirror and wavefront sensor as well as the required software for easy implementation of adaptive optics on single molecule localization microscopes.

In addition to the adaptive optics hardware, the MicAO 3DSR also includes a complete software suite that allows detailed control of the entire adaptive optics workflow. The large number of configurable parameters can make the software daunting at first impression. Software integration and ease-of-use are key to widespread adoption of new technologies across a large user base, and most microscopes are operated by biologists who do not need to understand the mathematical description of how aberrations affect the pupil function; they are simply interested in optimizing their image quality in a fast and reliable manner so they can extract their biologically-relevant data quickly. As part of the CIFRE collaboration for this PhD project, a

plugin for the MetaMorph software acquisition environment was developed that was designed to obviate the need for the user to interface directly with the more complicated MicAO software. The interface, architecture and modes of operation of this plugin are detailed in Appendix o

The single molecule adaptive optics workflow using this MetaMorph plugin will be described in detail here and forms the foundation for the subsequent 3D SMLM imaging using AO. It should be noted than initial hardware installation and alignment step is required. The system is considered properly aligned when closed-loop wavefront optimization using the included WFS removes the majority of aberrations such that the residual wavefront error is less than 20nm RMS. At this point, the AO system uses only the DM in conjunction with the interaction matrix to perform wavefront modulation in an indirect wavefront sensing configuration.

3.2.2.1 Wavefront Optimization with MicAO

The first step in the SMLM AO workflow is to optimize the wavefront. An indirect wavefront sensing approach and 3N algorithm are used to optimize the maximum intensity of the PSF established a single fluorescent bead on the coverslip surface. While the advanced user can specify the specific Zernike modes used for the 3N algorithm, a sufficient correction can generally be obtained using Zernike modes 3-10, the primary aberrations commonly known as defocus, astigmatism, coma, trefoil and spherical aberration. In this manner, system aberrations inherent to the microscope are corrected, including the objective, dichroic mirrors, filters and tube lens. In general, these aberrations remain constant as long as the optical system is not perturbed. However, this optimization also accounts for optical path length differences induced by coverslips with varying thickness.

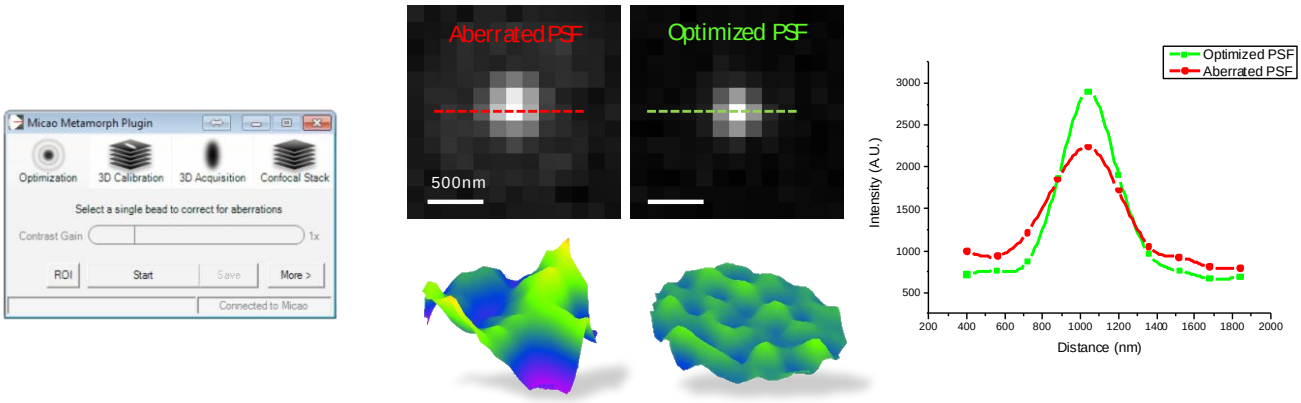

Figure 3.10: PSF Optimization using the developed MetaMorph MicAO Plugin. (a) MetaMorph MicAO plugin interface with one click PSF optimization. (b) PSFs (top) and representative wavefront reconstructions (bottom). 3N Optimization of the primary Zernike modes flattens the wavefront and restores the diffraction-limited, aberration-free PSF. (c) PSF intensity linescan demonstrating enhancements of aberration correction.

Tetraspeck beads | λ_{exc}=640nm

3.2.2.2 3D SMLM with Pure Astigmatism

After the crucial optimization step where residual system aberrations are removed from the wavefront, the deformable mirror is used to selectively add a dynamic amount of the astigmatism aberration that is commonly exploited for giving axial discrimination to the PSF in SMLM imaging as described in 3.1.3.

Compared to the conventional cylindrical lens approach, AO provides several advantages. The cylindrical lenses used for SMLM generally introduce other wavefront aberrations than just astigmatism that can significantly influence the axial localization of single molecules. Most 3D localization techniques do not use the actual PSF of the microscope for axial localization but reduce the complicated 3D diffraction of light into a calibration curve. For astigmatic imaging, this calibration curve is a 2-dimensional fit to axial divergence of the beam waist, w(z), of a Gaussian beam with higher order terms to correct for aberrations.

$$w(z) = w_0 \sqrt{1 + \frac{z - z_0^2}{z_R} + A\frac{z - z_0^3}{z_R} + B\frac{z - z_0^4}{z_R}}$$

where w_o is the beam waist at the focal position, z_o, and z_R is the Rayleigh range. This fit is performed in both lateral dimensions by fitting the PSF width at varying axial positions. An ideal astigmatism will separate the focal positions z_o in the *x*- and *y*- directions while retaining the same beam waist w_o.

Quantifying the quality of this astigmatism can be accomplished by comparing the astigmatic calibration curves that are used as a look-up table for axial localization. Critically, if this fitted curve does not match the experimental PSF, improper axial assignments will occur. **Figure 3.11** demonstrates the effect of the residual system aberrations combined with the additional aberrations induced by the cylindrical lens on these calibration curves. Notably, the astigmatic calibration curves from the cylindrical lens are usually laterally asymmetric, indicated residual aberrations that prevent optimal focusing. Furthermore, calculating the difference between the width and height of the PSF for each plane along the z-axis shows a non-linear dependence of σ_x-σ_y on z, which can be interpreted as an axially-dependent resolution. In contrast, the PSF optimization step in the MicAO workflow corrects these residual aberrations, and the application of a pure 60nm RMS astigmatism results in symmetric calibration curves and a linear relationship of σ_x-σ_y over a larger axial range. With adaptive optics correction and pure astigmatism, the astigmatic 3D SMLM depth of field can be performed up to extended to nearly ~1μm, compared to just 600nm from a fixed cylindrical lens.

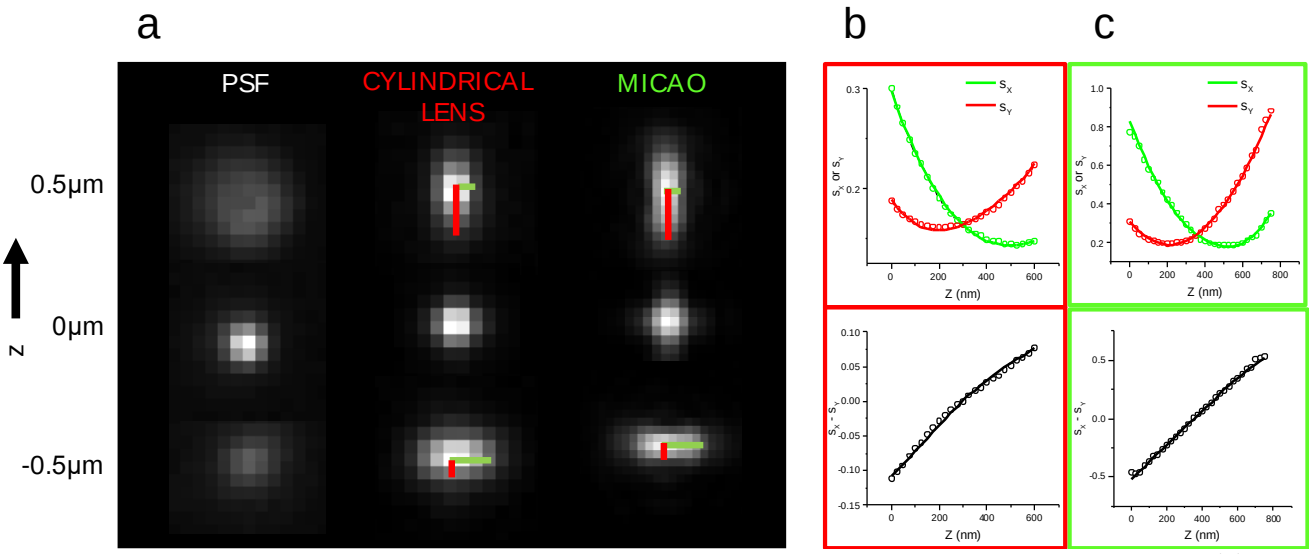

Figure 3.11: Comparison of Cylindrical Lens to Adaptive Optics for Astigmatic 3D Imaging. (a) While the diffraction limited PSF has little axial discrimination, injecting an astigmatism into the detection path via a cylindrical lens (red) or adaptive optics (green) allows for unambiguous axial localization. (b) 3D calibration curves with the cylindrical lens are frequently asymmetric due to residual system or sample aberrations, resulting in a variable resolution ($\propto \sigma_x$-σ_y) (c) Correcting system aberrations with adaptive optics and applying a pure 60nm RMS astigmatism to the wavefront results in a symmetric 3D calibration curve and a constant axial resolution over ~1µm for bright fluorescent markers.

Tetraspeck beads | λ_{exc}=640nm

One advantage of using a wavefront modulator like the deformable mirror is in its capacity to modify the amount of astigmatism based on the application; while 60nm RMS astigmatism gives a comparable astigmatism to the conventional cylindrical lens approach, increasing this astigmatism to 90nm RMS increases the axial discrimination of the PSF and thus axial resolution at the expense of imaging depth as shown in **Figure 3.12**.

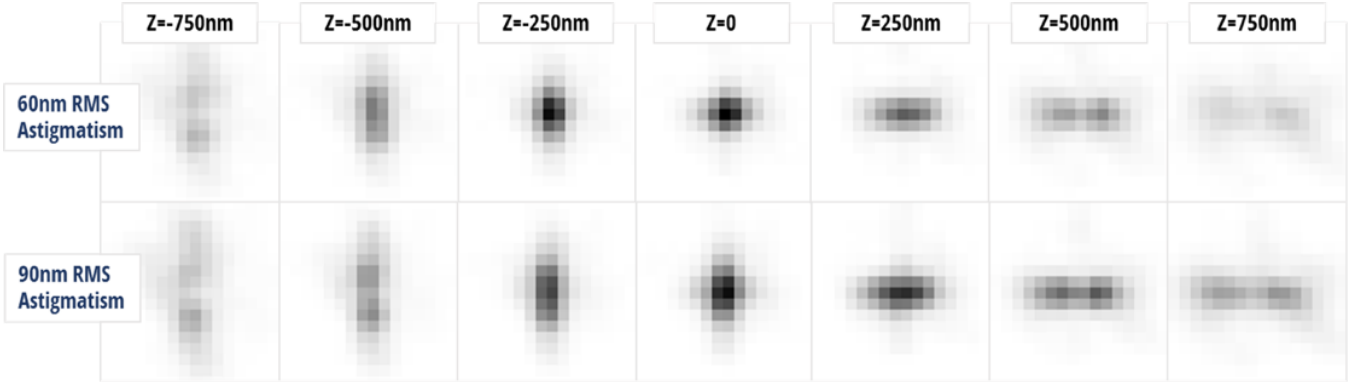

Figure 3.12: Dynamic Astigmatism using Adaptive optics. Using adaptive optics, a customizable astigmatism can be applied to the wavefront for specific applications. 90nm RMS astigmatism provides stronger axial discrimination over a shorter axial range compared to 60nm RMS (comparable to a cylindrical lens)

Tetraspeck beads | λ_{exc}=640nm

It is important to keep in mind the lateral localization precision, which is heavily dependent on the photon count and the PSF size. In the focal plane, the astigmatic PSF has a slightly larger, cross-like shape, which in theory would increase the localization uncertainty. For the case of the cylindrical lens, this is the case; 3D astigmatic SMLM with a cylindrical lens suffers from a slight increase in lateral localization uncertainty. Figure 3.13 demonstrates that interestingly, even 2D

imaging with a cylindrical has an increased localization uncertainty. This can be attested to the fact that the additional relay lenses in the Nikon cylindrical lens kit used for these experiments result in a reduction of the number of photons at the focal plane as well as possibly inducing some small aberrations. In contrast, the adaptive optics system provides the same lateral localization precision while performing astigmatic 3D imaging as the imaging path with no additional optical elements, and we see a slight improvement to the localization precision with 2D imaging due to the correction of system and coverslip-thickness aberrations that increase the photon count in the focal plane.

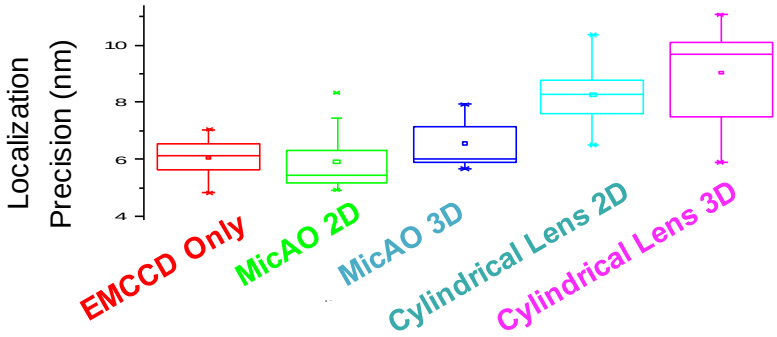

Figure 3.13: Localization precision comparison between conventional 2D SMLM imaging and 2D/3D astigmatic imaging with a cylindrical lens and adaptive optics system. The experimental localization precision, measured by the spatial distribution of individual beads across the field of view, remains constant after PSF optimization using adaptive optics for 2D or 3D imaging. The insertion of a commercial cylindrical lens kit in the detection path (right) makes the localization process less precise for 2D or 3D imaging.

Tetraspeck beads | λ_{exc}=640nm | 100 frames per stack | ~20 beads per field of view

3.2.3 Aberrations in High-NA Microscopy Limit Axial Discrimination in SMLM

While correcting for system aberrations can show an improvement in the PSF quality, the majority of SMLM microscopes are precisely aligned and carefully calibrated, using high-quality optical components intended to minimize aberration sources. Furthermore, many high-NA objective lenses include a correction collar that finely adjusts the internal network of lenses to compensate for thermally induced optical path length differences or variations in coverslip thickness. However, these correction collars are difficult to properly manually adjust, and these static elements cannot dynamically adjust for depth-dependent aberrations.

The major limiting factor preventing SMLM from imaging away from the coverslip surface is the spherical aberration that stems from the refractive index mismatch between the immersion medium and the sample. In more detail, this refractive index difference creates a change in angle at the coverslip surface that deviates the actual focal plane (AFP) from the nominal focal plane (NFP). This change in angle adds a radial dependence to the optical path length, which is commonly known as spherical aberration. These spherical aberrations axially stretch the point spread function, which results in a degradation of axial resolution in conventional microscopy. Furthermore, as the desired focal plane extends further from the coverslip surface, the effect of these spherical aberrations increases linearly with imaging depth[139].

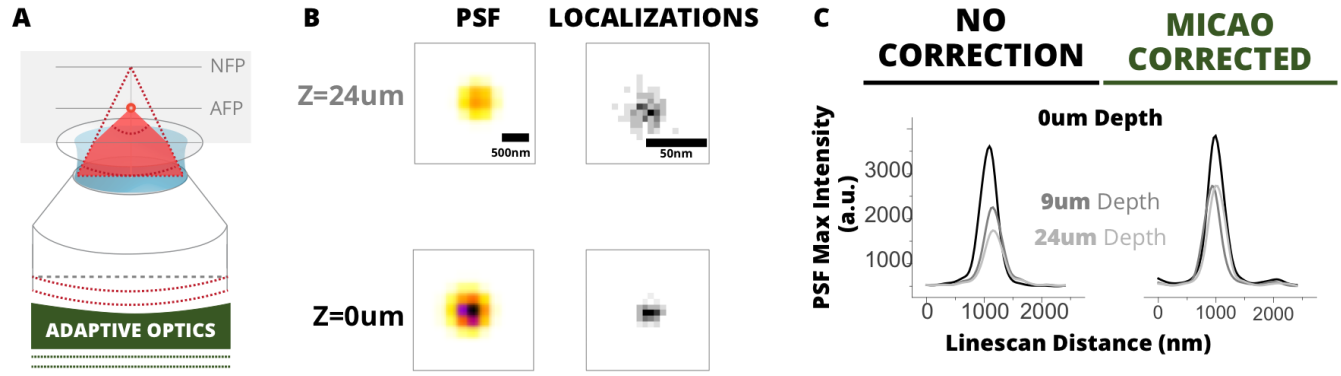

Figure 3.14: Spherical Aberrations Axially Spread the PSF (a) The refractive index mismatch between the immersion and imaging medium shifts the Nominal Focal Plane (NFP) from the Actual Focal Plane (AFP) (b,c) Axial spreading reduces the number of photons in the focal plane, demonstrated as a reduction in the maximum intensity of a PSF linescan and an increased localization uncertainty. Adaptive Optics can correct for spherical aberrations and regain maximum intensity in the focal plane.

100nm Tetraspeck Bead | λ_{exc}=640nm | 100x NA1.49 oil-immersion objective (n=1.515) | EMCCD

The axial stretching of the PSF has a critical effect on localization microscopy in the net reduction of photon count in the focal plane. **Figure 3.14** demonstrates this effect for a Nikon NA1.49 oil-immersion objective imaging fluorescent beads distributed in an agarose gel. The maximum fluorescence intensity is reduced to 50% at just 24μm imaging depth. For SMLM imaging, this intensity reduction greatly decreases the localization precision, resulting in a ~2x larger lateral distribution of the localizations (for 100 localizations at the same focal plane).

The combination of uncorrected spherical aberration and a fixed astigmatism reduces the effective PSF stretching induced by fixed astigmatism. For localization microscopy, the net effect is a reduction in axial discrimination, demonstrated in **Figure 3.15**. At 24μm deep, the axial discrimination, visualized as the slope of the σ_x-σ_y curve as a function of depth, is nearly completely removed compared to at the coverslip surface.

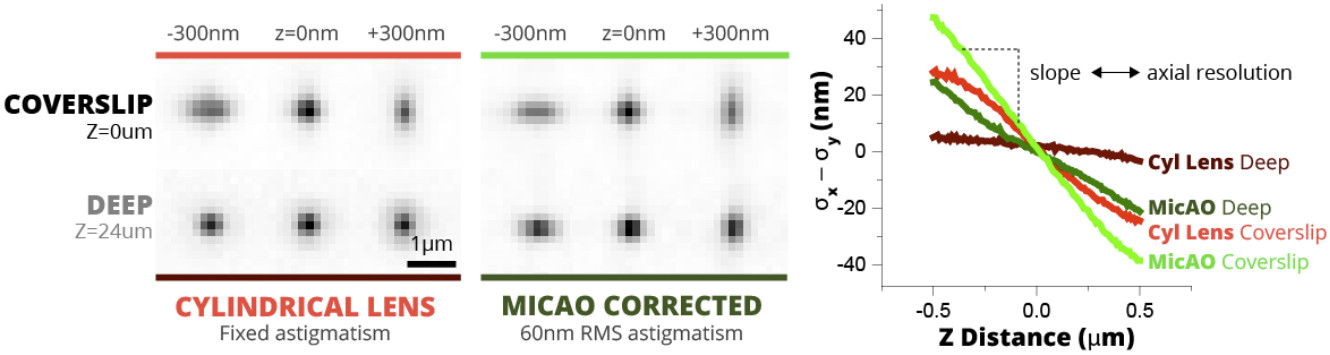

Figure 3.15: Depth-dependent spherical aberrations reduce axial discrimination with a cylindrical lens. Fixed astigmatic elements like a cylindrical lens **(left)** provide sufficient astigmatism at the coverslip surface, but depth dependent spherical aberrations reduce the effect of the astigmatism when imaging away from the coverslip surface. The wavefront modulator in the MicAO adaptive optics system **(center)** can apply a constant astigmatism as well as correction for these depth-dependent spherical aberrations, allowing for sufficient PSF deformation for 3D assignment. **(right)** The slope of the difference between the vertical and horizontal PSF elongation can be used as an indicator for axial discrimination ability. Here, the corrected adaptive optics system with spherical aberration correction has the same axial discrimination as the cylindrical lens at the coverslip surface.

Tetraspeck beads | λ_{exc}=640nm | MicAO with 60nm RMS Astigmatism

Using MicAO to correct for system aberrations at the coverslip surface and apply a pure astigmatism creates a strongly linear relationship of σ_x-σ_y as a function of imaging depth, as expected. At 24μm imaging depth, optimizing the PSF for defocus and spherical aberration using the 3N aberration detection algorithm corrects for the depth-dependent aberrations, and applying a pure 60nm astigmatism at this depth enables astigmatic 3D imaging with the same axial discrimination as the cylindrical lens at the coverslip surface.

3.3 ABERRATION CORRECTION ENABLES 3D SMLM IN COMPLEX BIOLOGICAL ENVIRONMENTS

Adaptive optics provides a large astigmatic depth of field of nearly 1μm, a size of import in cellular neuroscience imaging. In biological applications, these adaptive corrections are assumed to be valid over the entire field of view[140], although this assumption is invalidated when imaging deep into samples[141]. The ability to correct for system and depth-dependent aberrations, particularly spherical aberration, is requisite for enabling 3D SMLM imaging of biological samples away from the coverslip using high NA oil-immersion objectives.

3.3.1 Extending 3D SMLM Imaging at the Coverslip

The first application of adaptive optics for biological single molecule localization microscopy in 2012 by *Izeddin et al.* demonstrated PALM imaging and quantum dot tracking with an axial depth of ~800nm and an axial localization precision of σ_z~15-40nm at the coverslip surface[132]. This pioneering work served as a basis for the adaptive optics for SMLM workflow outlined in 3.2.2, which we employed for several SMLM applications at the coverslip surface, specifically high-photon count applications like dSTORM and QD tracking.

3.3.1.1 3D dSTORM of ß-Tubulin in Cultured Cell Lines

The extended astigmatic depth of field provided by MicAO was first explored using 3D dSTORM to image ß-tubulin in various cultured cell lines. Cell culture methods, including fixation, permeablization, and ß-tubulin labeling using primary and secondary antibodies can be found in Appendix 3. Once the coverslip was prepared and placed onto the microscope, system aberrations were corrected by first optimizing the PSF of a fluorescent bead at the surface of the coverslip using the 3N algorithm. A nearby cell was chosen for dSTORM imaging, and a widefield image was acquired with an aberration-free PSF, after which a pure 60nm RMS astigmatism was applied and dSTORM imaging was performed as detailed in section 3.2.2.2. A representative widefield image, 2D and color-coded 3D reconstructions of the tubulin cytoskeleton in COS-7 cells are demonstrated in **Figure 3.16**, with typical acquisitions ranging from 10,000-80,000 frames for a single reconstruction.

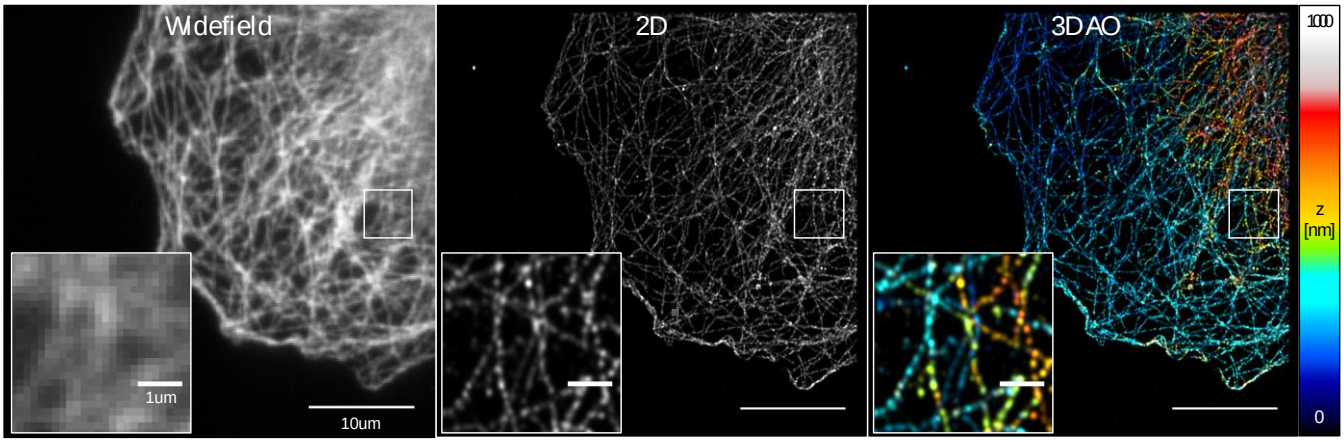

Figure 3.16: Representative 2D and 3D Reconstructions of ß-Tubulin::Alexa-647 dSTORM Imaging in COS-7 Cell. (Left) Widefield image of the tubulin network. **(center)** 2D accumulation of localizations from 20,000 imaging frames shows the clear benefit in resolution of the dSTORM technique. **(right)** Using adaptive optics for astigmatic 3D imaging allows accurate axial assignment over 1 µm depth.

COS-7 Cell | ß-Tubulin::Alexa647 | Primary and Secondary Antibody | Imaged at Coverslip, z=0µm

The benefits of using AO for aberration correction and astigmatism generation were then compared against using a fixed cylindrical lens. 3D dSTORM was first performed using the adaptive optics system for 20,000 frames, then immediately using the cylindrical lens by switching the output port of the microscope. As can be seen in **Figure 3.17**, the microtubules appear more continuous both laterally and axially for the adaptive optics case. This is quantified in an axial localization histogram, demonstrating the adaptive optics imaging not only has more localizations, but it localized over a larger axial range as well. Two different EMCCDs were used for these experiments, each with their own respective EM-Gain curves, and therefore a direct comparison of intensity per single molecule event would be inaccurate. The increased number of localizations can be attested to the photon gain thanks to the PSF optimization process for the adaptive optics system. Another unspoken benefit of using AO for 3D dSTORM is the facility to enable/disable the astigmatism; conventional cylindrical lenses induce a small field of view deformation when inserted into the imaging path, slightly skewing the 2D and 3D images. This makes direct comparison between the widefield image and the super-resolution reconstructions difficult.

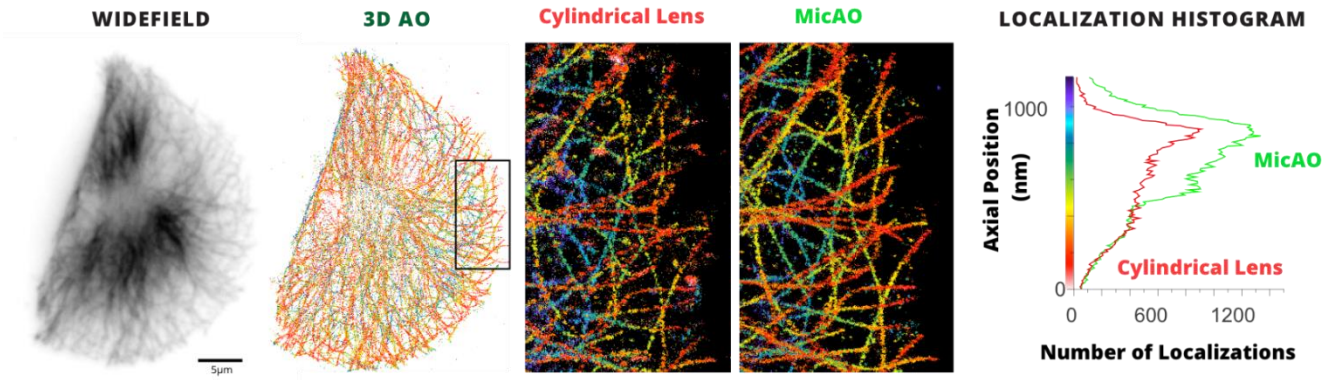

Figure 3.17: Comparison between cylindrical lens and adaptive optics for 3D ß-Tubulin dSTORM imaging in RPE1 Cells. The same field of view was imaged first with MicAO and subsequently with MicAO. The zoom (**center**) demonstrates the visual improvement of 3D reconstructions using the adaptive optics system, notably in the continuity of the microtubule network and the small variation in axial assignment. (**right**) The axial localization histogram shows that the adaptive optics system is able to localize more single emitters over a larger axial range compared to the cylindrical lens.

RPE1 Cell | ß-Tubulin::Alexa647 | Primary and Secondary Antibody | Imaged at Coverslip, z=0µm

3.3.1.2 Live-Cell 3D QD-Tracking over 1.5µm

The adaptive optics workflow for 3D astigmatic imaging the coverslip surface was also performed for tracking quantum dots in fibroblast cells. The quantum dots were tagged to the overexpressed GPI-GFP membrane protein using an anti-GFP antibody. As the bright QDs diffuse across the cell membrane, they outline the 3D contour of the cell over more ~1.5µm.

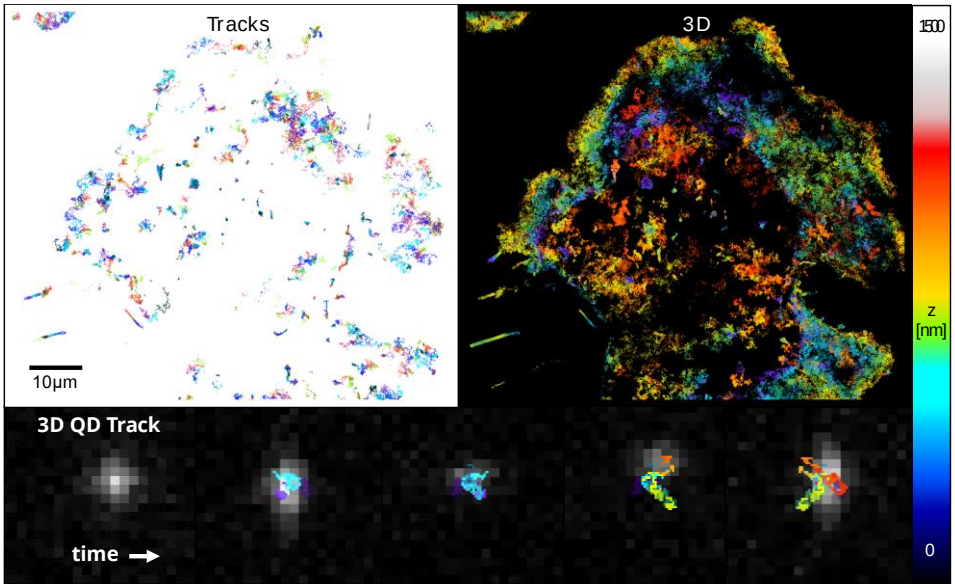

Figure 3.18: 3D Quantum Dot Tracking of a Membrane Protein in Fibroblast cells. Individual Tracks and 3D Projection of quantum dots specifically tagged to freely diffusing overexpressed GPI proteins in the cell membrane. Bottom: The astigmatism of the individual QD changes over time as it displaces vertically, along the optical axis.

Fibroblast Cell | GPI-GFP | α-GFP:QD655 | Imaged at Coverslip, z=0µm | 37°C

3.3.2 Spherical Aberration Correction Enables 3D dSTORM in Organotypic Brain Slices

While system aberration correction using adaptive optics provides some significant improvements compared to conventional techniques, the true power of AO systems for SMLM resides its ability to dynamically modify the wavefront to correct for depth-dependent

aberrations. The high-NA objectives used in single molecule imaging are only well corrected for imaging near the coverslip surface and require aberration correction for proper 3D imaging away from the coverslip surface.

Correcting for the system aberrations, as well as the depth-induced aberrations from imaging away from the coverslip, requires precise knowledge of the aberrations at the desired focal plane. Measuring these aberrations using indirect wavefront sensing methods requires a bright and stable fiducial marker, which are difficult to accurately place in complex 3D biological samples such as brain tissue. In situations where a fiducial marker is not present, an alternative technique outlined here characterizes the depth-dependent spherical aberrations in a model system with a similar refractive index as the biological sample, which is then used as a calibration curve to estimate spherical aberration as a function of imaging depth in the real sample, allowing 3D astigmatic SMLM at the desired focal depth.

This workflow for 3D imaging away from the coverslip surface in complex biological media is outlined in further detail here.

3.3.2.1 Calibration Spherical Aberrations as a function of Imaging Depth.

Correcting spherical aberrations requires precise knowledge of the linear relationship between spherical aberration and imaging depth, which is primarily dependent on the difference of refractive index between the immersion medium and imaging medium; for biological samples, the refractive index of the imaging medium is generally close to n_{water}=1.33. By embedding tetraspeck beads in 2% agarose gel, the beads are distributed in 3-dimensions. Individual beads were chosen in the field of view, their distance from the coverslip surface was measured using the perfect focus system (PFS) of the Nikon microscope, and the PSF optimization routine outlined in 3.2.2.1 was performed only for spherical aberration. Comparing the mirror shape for beads embedded in the gel with a reference bead on the coverslip surface allowed extracting the relative phase aberrations between the two imaging planes in the Zernike bases. This is possible by using the interaction matrix generated when the adaptive optics system was aligned, which converts mirror deformation in the pupil plane into PSF deformation in the image plane. Coma, astigmatism, and spherical aberration were recorded for each of ~20 beads in the sample. A linear interpolation of the RMS value of spherical aberration vs. measured bead position revealed a slope of ~5nm RMS spherical aberration per micrometer imaging depth (**Figure 3.19**a).

3.3.2.2 Correct for System Aberrations

After mounting the coverslip to be imaged on the microscope, aberrations must first be corrected using the PSF optimization routines outlined in 3.2.2.1 on fiducial markers placed on the coverslip surface.

3.3.2.3 Correct for Spherical Aberrations at Imaging Depth

Once the structure of interest has been identified, the imaging distance relative to the coverslip surface was measured using the PFS. Using the calibration curve from step 3.3.2.1, the required amount of spherical aberration is calculated and applied to the wavefront with the MicAO software. This process is outlined in **Figure 3.19**, where the sample is mounted between two coverslips in 30μm of imaging medium and placed upside-down on the microscope to intentionally image at z=30μm.

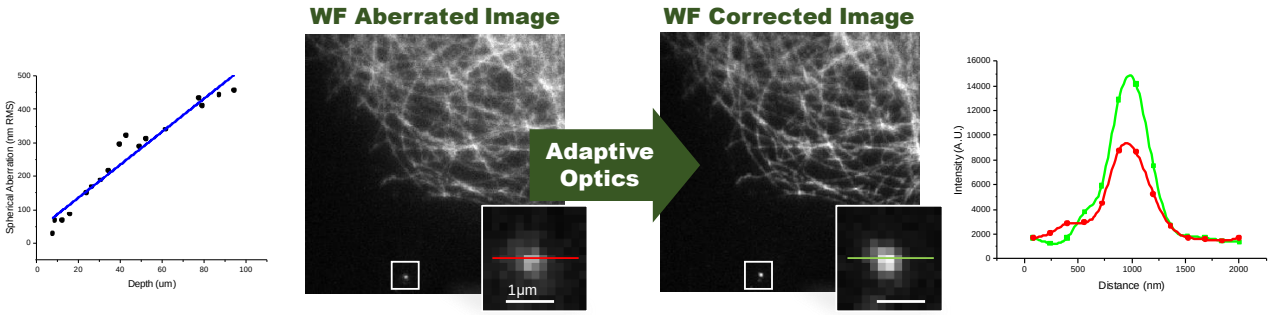

Figure 3.19: Calibration of Spherical Aberration Depth Dependence. (a) Calibration curve of spherical aberration as a function of imaging depth. (b) Applying 150nm of spherical aberration improves PSF and image quality @ z=30µm.

(a) Tetraspeck Beads in 2% Agarose Gel | λexc=640nm. (b) COS-7 | ß-Tubulin::Alexa647 | Imaging depth z=30µm

3.3.2.4 Apply Pure Astigmatism and Acquire 3D SMLM

Once the system and spherical aberrations have been corrected, the final step is to apply 60nm RMS astigmatism and begin 3D SMLM imaging. Figure 3.20 demonstrates the detrimental effect of spherical aberrations on the astigmatic PSF of a tetraspeck bead using the cylindrical lens, whereas correcting these aberrations using MicAO regains the focal separation needed for 3D SMLM.

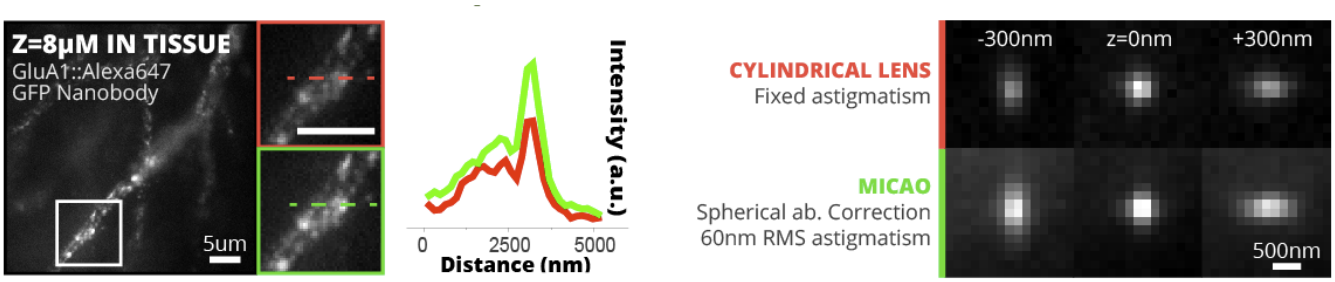

Figure 3.20: Spherical Aberration Correction enables astigmatic 3D imaging at 8µm depth in Brain Tissue. (a) Application of ~40nm RMS spherical aberration improves widefield intensity and image quality. (b) Astigmatic focal separation is regained by correcting spherical aberrations with AO.

GluA1-GFP | Alexa647 Nanobody | Organotypic rat hippocampal brain slice | Oblique Illumination @ λ=640nm | 8µm imaging depth

3.3.2.5 Application: 3D dSTORM in Organotypic Brain Slices

While SMLM has been used extensively in molecular neuroscience, its application has been mostly limited to cells cultured near the coverslip surface. The physiological relevance of studying the molecular distributions and interactions of proteins in such artificial environments has frequently been questioned, but the resolution required to investigate such interactions is lacking in other microscopy modalities. *Dani et al*[142] were the first to report STORM in brain tissue, and recently *Tang et al*[143] also employed multicolor 3D astigmatic PALM-dSTORM imaging to uncover nanoscale columns aligning presynaptic neurotransmitter release with postsynaptic neurotransmitter receptor localization in these complex environments. However, these works are limited very close to the slice surface due to lack of aberration correction.

We applied the previously described AO-3D SMLM to image postsynaptic neurotransmitter receptors in organotypic brain slices from the rat hippocampus. The first attempts proved to be limited not optically, but rather by the labeling of the desired protein in the brain slice. Effective SMLM requires proper labeling techniques that can efficiently label the protein of interest with

a fluorescent tag, and while conventional antibodies can be used for cell culture labeling, small probes must be used for maximum labeling coverage in brain slices. However, bulk labeling of all of the neuronal cells in a brain slice results in an extremely strong background signal that prevent localizing individual blinking molecules in these dense environments. We therefore chose to perform single-cell electroporation of individual neuronal cells to express the desired membrane protein, which was then surface stained using a small fluorescent probe.

As a proof of concept collaboration with Daniel Choquet's group and specifically Eric Hosy and Julia Goncalvez, a single neuron electroporated with soluble GFP and GluA1-SEP and subsequently live labeled with an anti-GFP nanobody coupled to Alexa647 (degree of labeling ~2.3) before PFA fixation and imaging. Anti-GFP nanobodies are an excellent choice for brain slice labeling due to their small size, specific labeling, and easy conjugation to organic fluorophores commonly used in dSTORM imaging. Figure 3.21 shows this specific labeling of the Alexa647 nanobody to the individual neuron expressing GluA1-SEP.

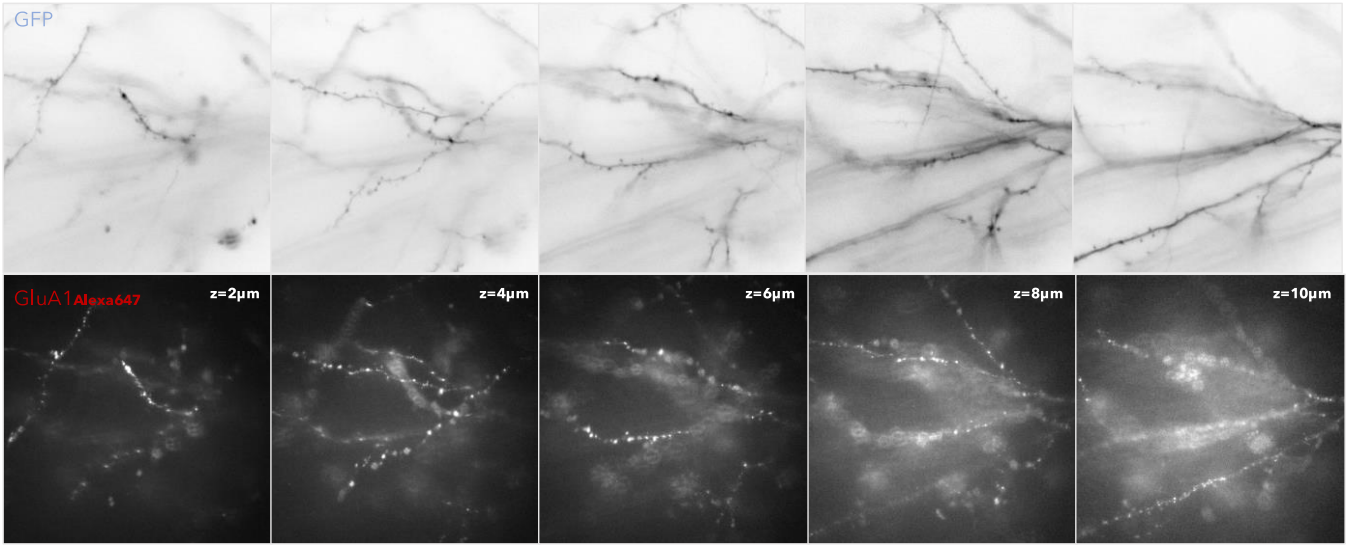

Figure 3.21: Anti-GFP Nanobody Labeling in Organotypic Brain Slices. Z-stacks in the GFP channel (top) and Alexa647 channel (bottom) show the highly specific nanobody labeling to the single electroporated neuron in the brain slice.

Hippocampal Organotypic Brain Slice | Single-cell Electroporation GluA1-SEP | Nanobody Anti-GFP:Alexa647 | Oblique Illumination

Once efficiently labeled with the Alexa647 nanobodies, the AO-3D SMLM workflow was performed, as outlined in Figure 3.22. System aberrations were corrected at the surface of the brain slice by optimizing the PSF for 100nm tetraspeck beads adhered to the slice surface, which unfortunately do not penetrate into the tissue. A z-stack was performed in the GFP channel to select the desired focal plane; here, criteria were primarily good labeling density and number of dendritic spines in a single FOV. The best focal plane was chosen at z=10µm, and 50nm RMS spherical aberration was applied to the wavefront, providing a slightly improvement to the contrast of the widefield Alexa647 image. 60nm RMS astigmatism was added in addition to the system and spherical aberration corrections previously applied, and 3D dSTORM imaging was acquired. 20,000 image frames were acquired. Efficient single molecule blinking was ensured by optimizing the oblique illumination, slightly varying the lateral position of the excitation beam in the back aperture of the 100x NA1.49 TIRF microscope objective to maximize the power density at the focal plane. Once the image was acquired and data analyzed, a nearest neighbor

in adjacent image frame analysis for experimental localization precision was performed,[35] giving an experimental lateral localization precision of $\sigma_{x,y}$~19nm (resolution of ~44nm) at an imaging depth of 10μm.

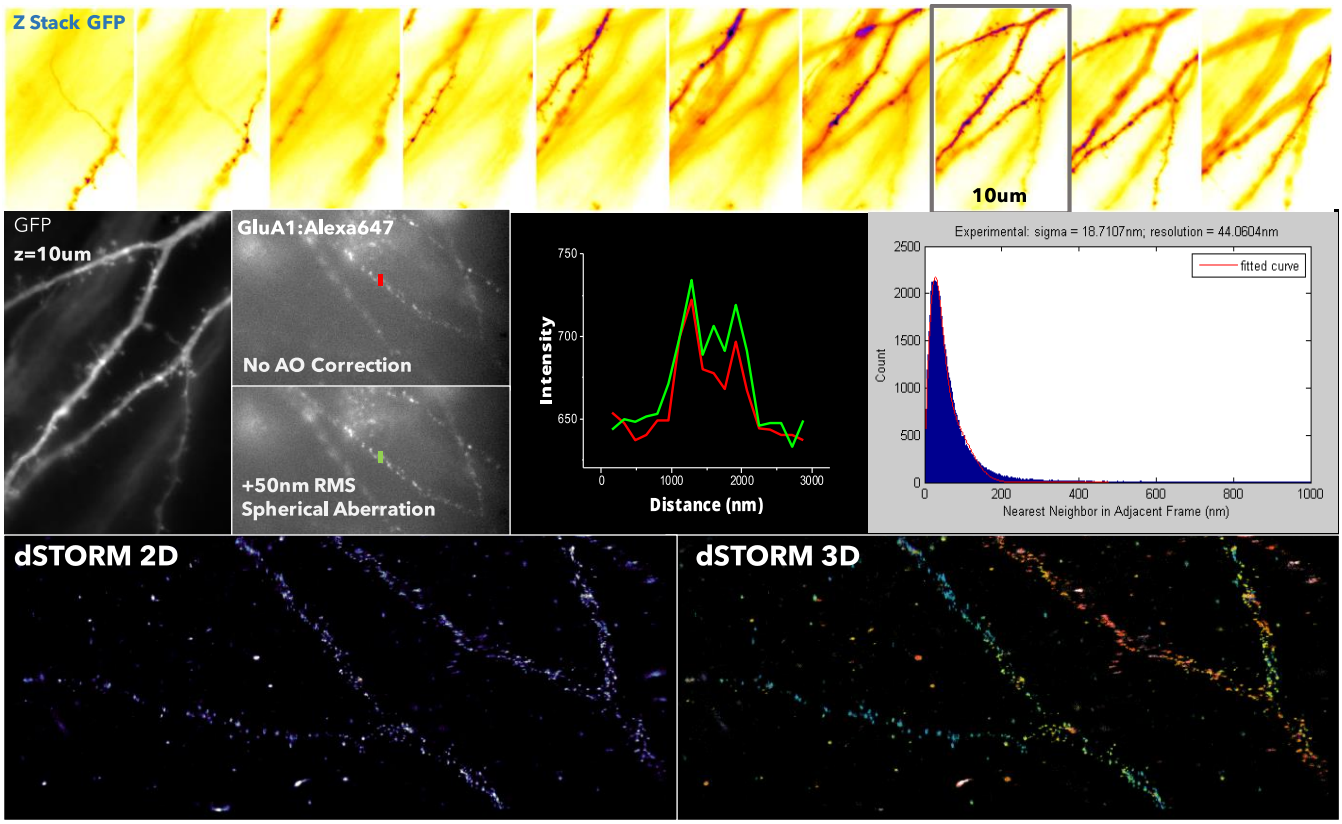

Figure 3.22: AO-3D SMLM Workflow. (a) Z-stack of the solulble GFP fluorescence was obtained to select focal plane for imaging. (b) The focal plane at 10μm was selected, and 50nm RMS spherical aberration applied, improving the widefield image contrast. (c) 60nm RMS astigmatism was applied and 3D dSTORM images were acquired for 20,000 frames @ 50ms/frame. (d) Lateral localization precision of ~19nm was calculated using the nearest neighbor in adjacent frame method from *Endesfelder et al.*[35]

Organotypic Rat Hippocampal Brain Slice| Single-cell Electroporation GluA1-SEP | Nanobody Anti-GFP:Alexa647 Oblique Illumination

The use of the anti-GFP nanobody imposes certain constraints on the molecular biology of the imaged structures, specifically in that the protein must be overexpressed and genetically fused to a GFP tag which may not be possible for all proteins. It was therefore crucial to seek alternative labeling strategies to expand the applications of the AO-3D SMLM workflow in brain slices. Ingrid Chamma in Olivier Thoumine's group had recently developed a monomeric variant of streptavidin (mStrav) for use in single molecule imaging applications. Briefly, a single neuron was electroporated with Neuroligin1-AP (Nlg1-AP) and an enzyme that biotinilates this AP tag when it reaches the cell membrane. mStrav:Alexa647 was then used to selectively and efficiently link Alexa647 fluorophores to Nlg1. More details on surface protein labeling using using monomeric streptavidin can be found in the protocol article by *Chamma et al*[104].Compared to nanobody labeling, mStrav labeling offers a shorter linker length, higher labeling density, and is compatible with any membrane protein which can be fused to the small AP tag. After correcting system aberrations using beads on the slice surface, the focal plane of interest was chosen directly in the Alexa647 channel as the high labeling density provided a very strong SNR for Nlg1-mStrav:Alexa647. Spherical aberration correction was applied as a function of imaging depth, here only a few micrometers, and 60nm RMS astigmatism applied for 3D dSTORM imaging.

dSTORM images were acquired using an oblique illumination with exit angle manually adjusted for maximum Alexa647 blinking in the focal plane at the desired depth.

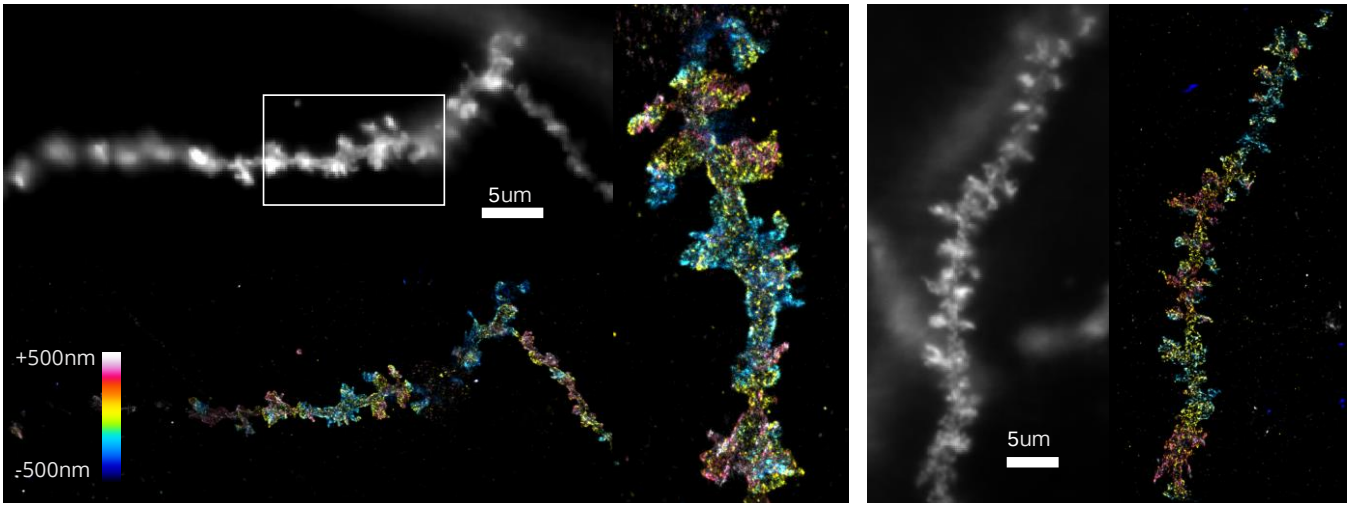

Figure 3.23: Postsynaptic Adhesion Protein 3D dSTORM Imaging in Hippocampal Organotypic Brain Slices. Widefield single-cell electroporated Nlg1:Alexa647 image demonstrating labeling specificity and efficiency of the mStrav tag[57]. AO-3D dSTORM reconstructed images with 60nm RMS astigmatism over 1µm thickness at several micrometers depth.

Rat hippocampal organotypic brain slices | Nlg1:Alexa647 | mStrav labeling | Oblique Illumination
System aberration correction + depth-dependent spherical aberration correction + 60nm RMS astigmatism

A selection of 3D reconstructions of these acquisitions can be found in Figure 3.23, and this collaborative work was published in *Nature Communications* in 2016[57], the full text of which can be found in the Publications at the end of this manuscript.

3.3.3 Deep 3D-AO SMLM with soSPIM + MicAO

While efficient adaptive optics enables 3D single molecule localization in brain tissue and other complex biological media by correction wavefront aberrations in the detection path, the approach as outlined above is fundamentally limited by the ability to efficiently excite the densely labeled fluorescent probes in the sample. The inverted microscope geometry that lends itself very well to conventional 3D SMLM at the coverslip surface necessarily couples the excitation and detection paths through the same high-NA objective, imposing aberrations on the excitation wavefront that are left uncorrected by the adaptive optics system in the detection path. In point-scanning techniques like 2-photon and STED microscope, correcting these excitation aberrations is essential since resolution in these modalities depends on the tight focus of the excitation beam; in widefield imaging geometries found in conventional SMLM, these aberrations induced on the excitation wavefront similarly prevent optimal propagation and limit the power density delivered to the sample. Commonly employed techniques like dSTORM requiring several kW/cm² for efficient fluorophore blinking, most SMLM is thus limited to the first ~10µm micrometers of complex biological tissue.

While decoupling the excitation and detection paths, as is common in light sheet imaging, might seem thus advantageous for deep 3D SMLM, the high-NA detection objectives impose strict mechanical constraints that prevent two commercial objectives from being mounted in a perpendicular geometry. Eric Betzig's group has designed a pair of excitation and detection

objectives specifically for 3D SMLM[81], but their custom optical design is expensive and specific sample mounting procedure limit the applicability of the technique.

The single objective light sheet system soSPIM[82] detailed in section 1.4.2 has the unique advantage of combining light-sheet optical sectioning with high-NA detection on existing inverted microscopes used for conventional SMLM. While *Galland et al* demonstrated 2D dSTORM imaging using the technique, spherical aberrations induce a depth-dependence to the astigmatism that prevented the use of a fixed astigmatic element like a cylindrical lens for encoding axial position into the PSF. 3D acquisitions were acquired by scanning the z-stage every 500nm, acquiring a 2D dSTORM image at each focal plane, and thus while lateral superresolution was achieved, the axial resolution remained diffraction limited.

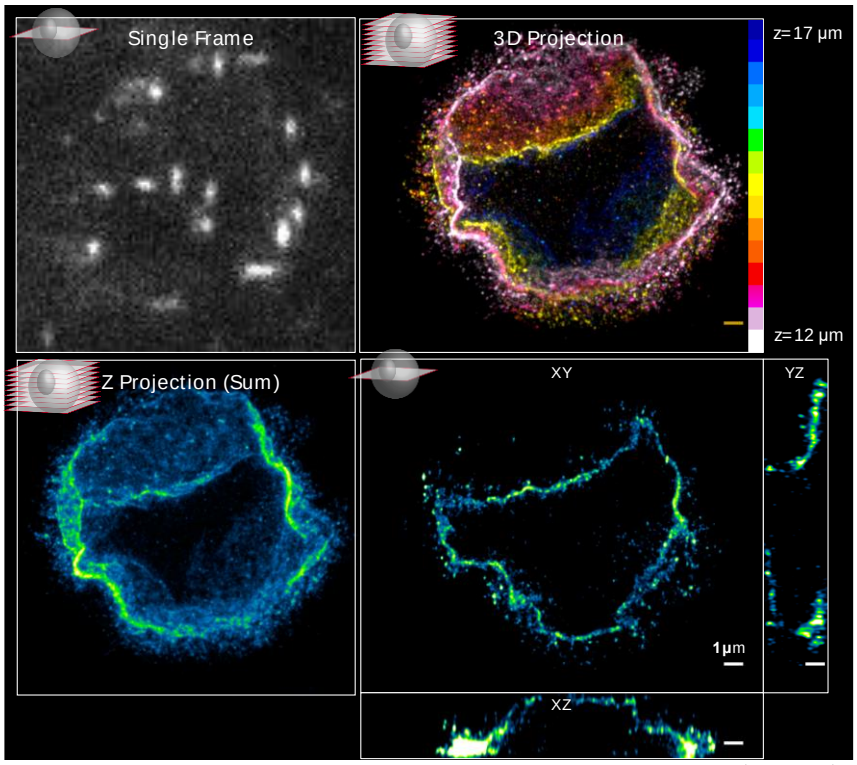

Figure 3.24: Nuclear Membrane Astigmatic 3D DNA-PAINT with soSPIM. (top left) A single imaging frame demonstrating 40nm astigmatism at z=14.3µm. Scanning the objective and taking an SMLM image every 500nm allows 5µm thick reconstructions. (top, right) Axially coded reconstruction of 3D projection over 5µm. (bottom, left) 2D Projection of same data. (bottom, right) Orthogonal projections showing the 3D morphology of the nuclear membrane that necessitates SR imaging over several microns.

S180 Cells | LaminB1 DNA-PAINT | soSPIM excitation @ λ=561nm| Imaging depth z = [12µm, 17µm]
System + depth-dependent spherical aberration correction + 40nm RMS astigmatism

To address this, we implemented a MicAO adaptive optics system onto a Nikon Ti inverted microscope with Remi Galland's soSPIM excitation system. The same AO-3D SMLM workflow outlined in 3.3.2 was applied, first compensating for system aberrations by optimizing the wavefront for a nanodiamond at the coverslip surface and then performing a second system and depth-dependent aberration correction via 3N optimization of a fluorescent nanodiamond embedded in the polymer surrounding the imaging ROI at z=15µm. For this configuration, 40nm RMS astigmatism was found to be optimal for 3D astigmatic imaging. **Figure 3.24** shows a single frame from DNA-PAINT imaging of the nuclear membrane in S180 cells at a depth of z=14.3µm from the coverslip surface, visibly demonstrating the appropriate astigmatism for 3D DNA-PAINT imaging, as well as a reconstruction from a single imaging plane at this focal depth of

1μm thickness. To extend the effective depth of field, 3D DNA-PAINT images were acquired every 500nm between 12μm and 17μm, resulting in a total SMLM reconstruction with a thickness of 5 micrometers up to 17 micrometers imaging depth.

The primary factor limiting the AO-3D soSPIM SMLM acquisitions is image registration; the Nikon PFS system stabilizes the system axially, while localizations from each z-plane are laterally drift compensated post-acquisition using beads embedded in the polymer surrounding the imaging ROI. However, the individual beads are only localized in a single imaging plane, preventing 3D stack alignment using the beads.

3.4 ILLUMINATING NEW BIOLOGY WITH SINGLE MOLECULE ADAPTIVE OPTICS

The developments in adaptive optics for single molecule localization microscopy detailed in this chapter provide a workflow, as well as proof of concept applications, for 3D single molecule imaging in heterogeneous, physiologically relevant biological environments. Despite optimizing hardware design and software plugins, the pipeline remains complicated for the average user, requiring a number of calibration steps and manual aberration correction.

3.4.1 Towards Simplifying Adaptive Optics for General SMLM Adoption

Like spherical aberration, the majority of biological sample-induced aberrations in are depth-dependent[144], requiring a dynamic phase modulating device for effective wavefront correction. One of the largest challenges in single molecule adaptive optics is accurately detecting these sample aberrations via indirect wavefront sensing methods, which can have significant consequences on spatial measurements[145] and single molecule localization.

While bright fluorescent beads are commonly used as a reference to measure sample-induced aberrations[137], new work by several groups optimize wavefront correction using the blinking of individual single molecules as proxies for PSFs. [128] used a phase retrieval algorithm to numerically compensate for the depth-dependent PSF, extending astigmatic 3D imaging up to 2.5μm deep without the need for wavefront compensation. *Burke et al* were the first to demonstrate sample aberration correction for astigmatic 3D dSTORM imaging[146] by initially correcting for system aberrations at the coverslip surface and optimizing the correction using a phase retrieval algorithm for sample aberration detection directly on the dSTORM blinking events. Using this technique, they were able to image microtubules through ~6μm of cell (Figure 3.25). Similarly, using a robust genetic algorithm to detect sample aberrations, *Tehrani et al*[147] saw a 4x improvement in localization precision ~50μm in tissue by using genetic algorithm to detect and correct sample aberrations directly on SMLM. Even more recently, *Huang et al* demonstrated 4Pi AO SMLM using two objectives, with deformable mirrors in each arm of the 4Pi-interferometric cavity to correct for system and sample aberrations[148], enabling astigmatic superresolution up to 10μm deep with 10- to 20-nm localization precision.

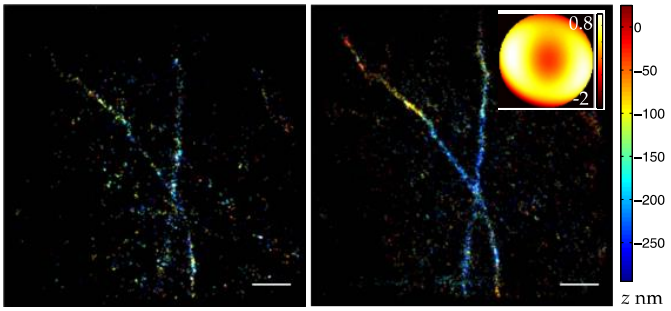

(a) Instrumental correction only. **(b)** Specimen correction.

Figure 3.25: Sample Aberration Correction for improving SMLM. (a) Image reconstructions of microtubules at the top of the protein-dense cell display few localizations and many image artifacts due to the optical aberrations of the nonhomogeneous cellular structure. **(b)** Correcting these sample aberrations allows for correct dSTORM imaging through the cell.

From *Burke et al* [146]

Further integration between AO hardware and acquisition software will facilitate the user experience, with the ultimate goal of obviating the need for manual aberration calibrations. A phase diversity algorithm in the MicAO software will soon allow parameter-free wavefront correction that requires fewer images for wavefront optimization. Used in combination with real-time single molecule localization tools like WaveTracer, the effect of the adaptive optics correction on the PSF will be able to be analyzed and modified directly on the acquisition system, opening up many opportunities for real-time wavefront modification.

At the same time, commercial development in response to customer needs will increase ease of use and broaden adoption. Deformable mirrors are extremely sensitive to ambient temperature, and small temperate variations can induce a strong and undesired astigmatism on the system. To address this, new MicAO systems are beginning to be shipped with automatic mirror temperature correction. Additionally, it may be desirable to perform certain kinds of imaging without wavefront correction; for this, a DM bypass mode has been integrated, allowing direct imaging onto the camera sensor.

3.4.2 Conclusion: Adaptive Optics Optimizes Collected Photons

With its first applications appearing only a decade ago, single molecule localization microscopy is still in its infancy. The first applications have been limited to optically and physiologically simple environments, imaging cells cultured directly on the coverslip surface. Expanding the biological applicability of the technique requires being able to accurately spatially localize a few hundreds of photons traversing through tens of micrometers of aberration-inducing tissue, and wavefront correction can compensate for these optical path deviations if they can be well characterized. Thus, it is not difficult to envision a future where adaptive optics become essential for single molecule imaging, and this work hopes to be the first steps towards an integrated adaptive optics hardware and software SMLM workflow.

CHAPTER 4 5-DIMENSIONAL SINGLE MOLECULE LOCALIZATION & TRACKING

Single particle tracking techniques such as sptPALM, uPAINT and QD tracking have given unprecedented insight into molecular dynamics in living cells. These modalities, detailed in section 1.3.2, allow monitoring the behavior of plasma membranes proteins at millisecond temporal resolution and nanometer-scale spatial resolution via centroid localization and subsequent temporal reconnection. While these SPT methods have been extensively used to study the temporal dynamics and co-organization of multiple proteins, conventional setups are usually limited to two simultaneous wavelengths. Increasing the number of simultaneously imaged wavelengths requires specific filtering optics for each fluorescent species being imaged and frequently compromises resolution and field of view for spectral and temporal resolution, limiting the minimum and maximum diffusion coefficients that can be measured and differentiability of different molecular diffusion behaviors.

In this chapter I detail the development of a single particle tracking technique that includes spectral detection without compromising the spatiotemporal resolution or imaging field of view. I demonstrate how we achieved 5-dimensional single particle tracking (x,y,z,t,λ) of several membrane proteins using "commercially available" microscopes by exploiting photons unused in conventional SMLM imaging. Unfortunately, the project took more time than expected due to technical difficulties in setting up this geometry, requiring the scope to be disassembled and reassembled several times for Perfect Focus system modifications, addition of adaptive optics supports, caging for thermal isolation, and culminating in a final move to a new heavy load optical table capable of supporting the additional weight of all these components. Since this kind of dual-microscope geometry is unique, each of these modifications required case studies to ultimately achieve the mechanical stability necessary for routine use. Thanks to these microscope overhauls, the dual-microscope system outlined here is now functional, with trained neurobiologist collaborators able to independently perform multicolor SPT experiments.

4.1 INCREASING DIMENSIONALITY IN SINGLE MOLECULE LOCALIZATION MICROSCOPY

In conventional microscopy systems, the overall dimensionality of the acquisition is often reduced to improve the resolution in a certain dimension. Typically, SMLM acquisitions gain an

order of magnitude increase in spatial resolution, both laterally and axially, at the expense of temporal resolution. Similarly, field of view is often compromised with temporal resolution, as the readout time of imaging sensors increases with increasing field of view. Furthermore, the spectral bandwidth of the imaging system is entirely compressed, and spectral discrimination is optically performed using specific filter sets for the desired fluorescent probe.

The limited number of photons emitted from a single fluorescent molecule requires a choice to be made in how to efficiently use the photons to gain information in the desired dimension (**Figure 4.1**). To avoid compromising spatiotemporal resolution and field of view, increasing the number of usable photons collected by the imaging system is desirable.

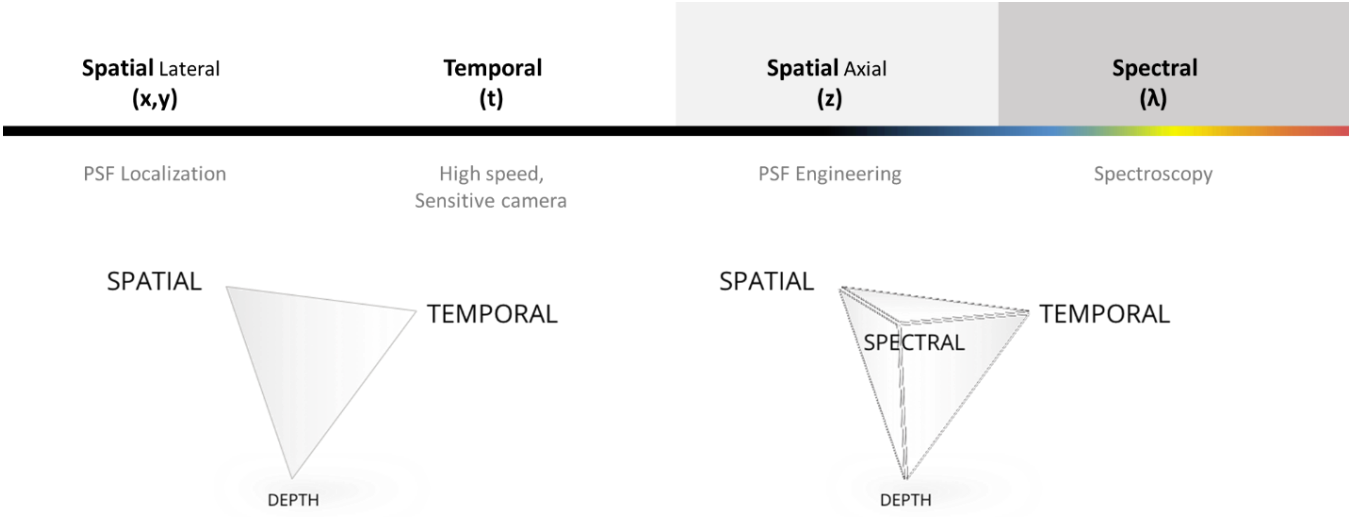

Figure 4.1: The Resolution Compromise. Photons in SMLM are allocated to one of several dimensions of resolution, typically favoring spatial resolution at the expense of imaging time, limited depth, and spectral discrimination.

4.1.1 Dual-Objective SMLM Increases Collection Efficiency

Conventional single molecule imaging approaches collect fluorophore emission in an epifluorescence geometry. Increasing the numerical aperture of the collection objective allows acquiring more photons, but a practical limit is reached at NA~1.5, after which nonconventional materials must be used for the objective and coverslip. The effective NA even decreases to about 1.3 when imaging living samples away from the coverslip due to the refractive index of the living material. However, a large portion of the fluorescence is emitted away from the coverslip, and is not collected by the microscope's objective.

Another way to effectively increase the numerical aperture of the imaging system is to place a second, high NA microscope objective in the transmission geometry. *Ram et al.* first implemented a bi-plane (section 3.1.2) dual-objective collection for single molecule imaging to improve axial localization, with each objective imaging a slightly offset focal plane[149]. Later, *Xu et al* were the demonstrated a dual-objective collection for SMLM imaging of the actin cytoskeleton network by STORM[150], combining the spatial information from each camera to increase lateral and astigmatic axial localization precision (**Figure 4.2**). Their application to 3D imaging of the actin cytoskeleton remains certainly one of the most impressing SMLM images to date, demonstrating the quantitative benefits of dual-objective collection for increasing the number of photons per localization.

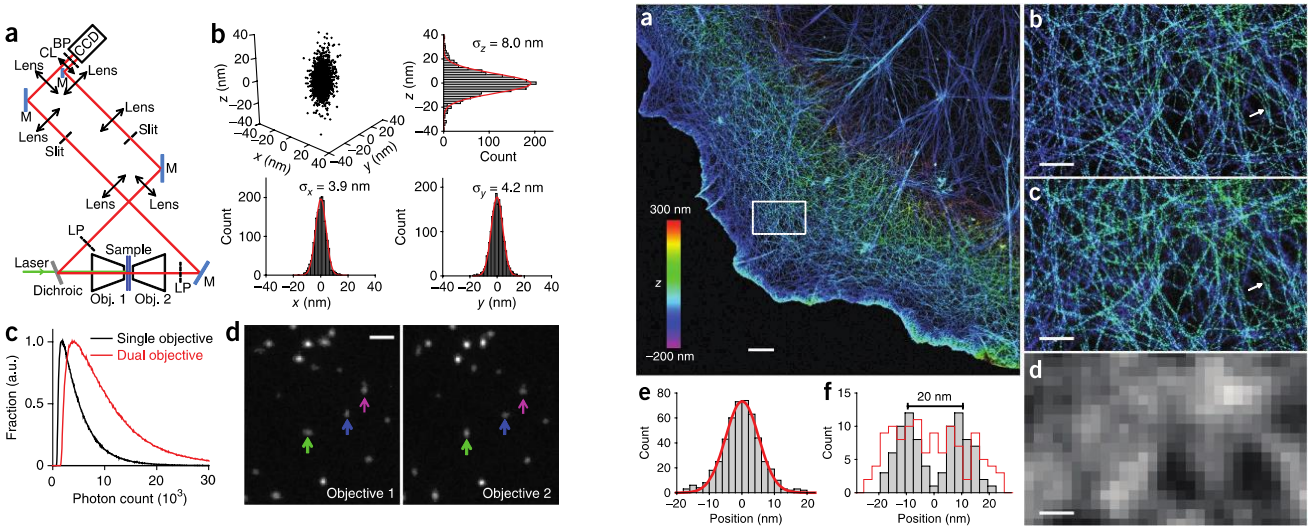

Figure 4.2: Dual-Objective Collection for SMLM. The first implementation of a dual-collection objective configuration for SMLM merged lateral and axial localization information from both imaging paths to increase the (x,y,z) localization precision for actin cytoskeleton imaging.

Adapted from *Xu et al*[150]

4.1.2 Mechanical Considerations for Dual-Objective SMLM

We chose an implementation based on two commercially available inverted microscope bodies to maximize mechanical stability and ease of use for imaging live biological samples. Two Nikon Ti inverted microscope bodies were used, one (bottom) in a conventional geometry for SMLM imaging and the second (top) mechanically inverted, acting as an extra photon collector, and mounted such that the two high-NA objectives can physically touch when at their maximum extent. Both the upper and lower optical paths terminate in separate Photometrics EVOLVE EMCCDs. The laser illumination electronically triggers the bottom and top cameras, ensuring simultaneous exposure between the two sensors. Unsynchronized dual camera acquisitions are automatically annotated in image metadata and compensated post-acquisition.

A few key criteria motivated the creation of this microscope, summarized below together with several technical details on the implementation (**Figure 4.3**)

- **Live-cell compatibility**. The coverslip is placed horizontally, sandwiched between two conventional inverted microscopes, both compatible with the observation of living sample holders. The entire microscope system is caged in plexiglass and heated to 37°C for live cell experiments. A specially fabricated sample chamber was designed to allow for 30µm thickness between the top of a 170µm thick, 18mm-diameter coverslip on which cells were cultured to the bottom of a second 170µm thick 22mm-diameter coverslip. The larger upper coverslip allows the majority of the bottom coverslip area to be imaged without mechanically limitation, and liquid reservoirs allow for >100µL of imaging medium to be used while limiting the distance between coverslips to ~30µm.
- **Dual Perfect Focus System Compatibility**. Axial stability is extremely important for maintaining the desired focal planes for each imaging path, especially for SMLM. The Nikon Ti microscope bodies used here support the Nikon Perfect Focus System (PFS) (detailed in section o) for realtime axial drift compensation based on LED reflection at the coverslip surface. To

ensure that two PFS systems can be used simultaneously without interfering, special filters were ordered and installed in the microscope bodies (Figure4.4b)

- **Objective Flexibility.** Previous dual-objective systems use matching objectives to minimize field of view errors between the two detection paths. Our system accepts matched objectives, but also supports mismatched objectives, notably allowing a 60x water immersion objective to be used on the upper optical path with a 100x oil immersion objective on the lower path. The advantages of such a configuration are an increased depth of field with the lower NA water immersion objective and the reduction of spherical aberrations induced from imaging through 30μm of imaging medium. The differences in field of view are compensated numerically directly on the localizations (more information in Section 4.2.1).
- **Fluorophore Selection, High Density Acquisitions and Camera Sensitivity.** Being able to take full advantage of the sensitivity of the dual EMCCD configuration allows this microscope to track bright quantum dots as well as dimmer organic fluorophores and fluorescent proteins across the entire field of view of the EMCCDs, nearly 80μm x 80μm @ 30Hz, using conventional filter sets and dichroic mirrors.
- **Ease of use and reproducibility.** A primary goal for this microscope is to render it as user friendly as possible for biologists. By basing the construction on commercial microscope bodies, the system gains mechanical stability, reducing the necessary alignment and rendering the system slightly more accessible to users than conventional two-objective systems. Each microscope body contains multiple input and output ports, making the system flexible and easy to upgrade using commercially available optical components.

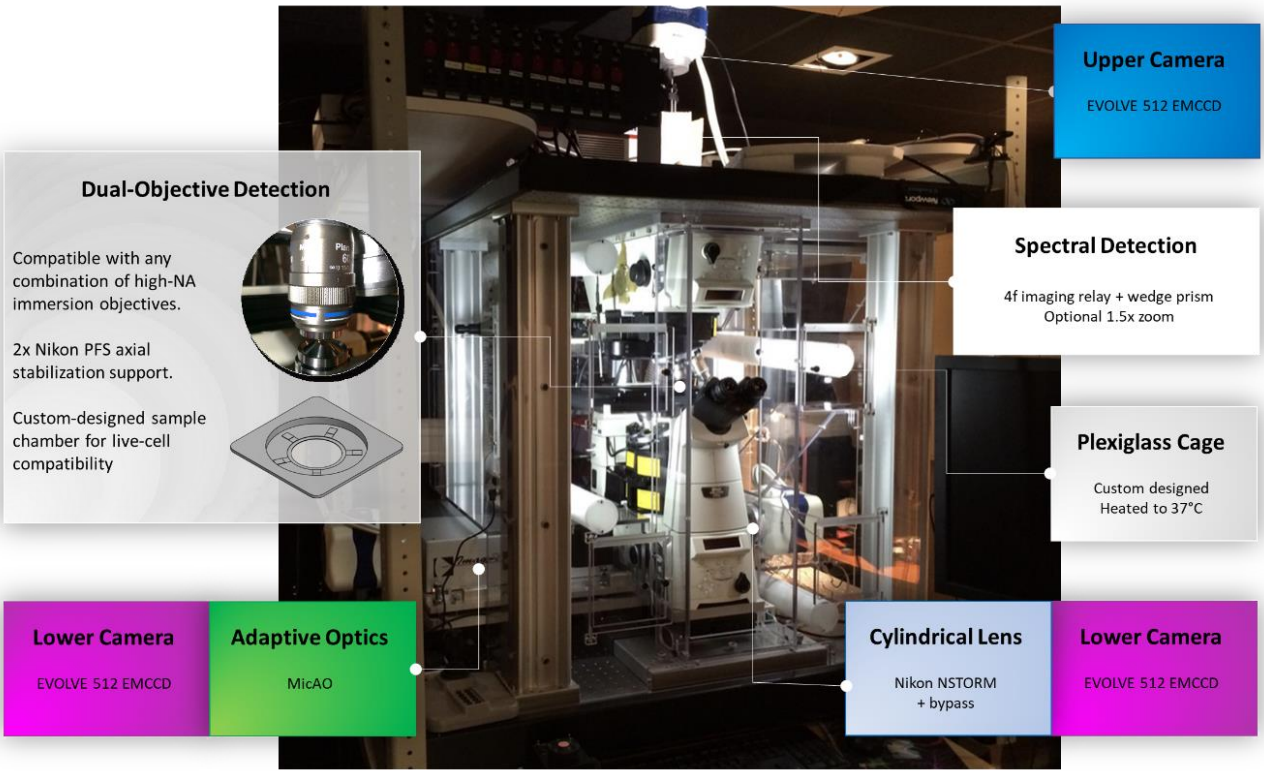

Figure 4.3: Dual-Microscope SMLM with 2 commercial inverted Nikon Ti Microscopes. Two inverted microscopes were mounted such that they could share a common focal plane. By using commercial microscopes provides mechanical stability, use of use to image live biological samples, as well as versatility in objective choice and the use of accessories such as MicAO and cylindrical lenses. The geometrical constraints imposed by using two high-NA microscope objectives required the design and fabrication of a unique sample chamber that is compatible with the complex geometry yet retains compatibility with Ludin chamber support mounts, 18mm diameter glass coverslips and live-cell imaging.

Stringent constraints of live-cell imaging require the top objective to image through ~30μm of imaging medium, inducing strong spherical aberrations on the upper wavefront when imaging with an oil immersion objective, as shown in Figure 4.4. The PSF peak intensity is reduced to ~50% on the upper detection path, with a ~2x reduction in localization precision. While a water immersion objective can be used to minimize these spherical aberrations, we sought to use the extra photons provided by the second objective to seek imaging improvements beyond spatial resolution.

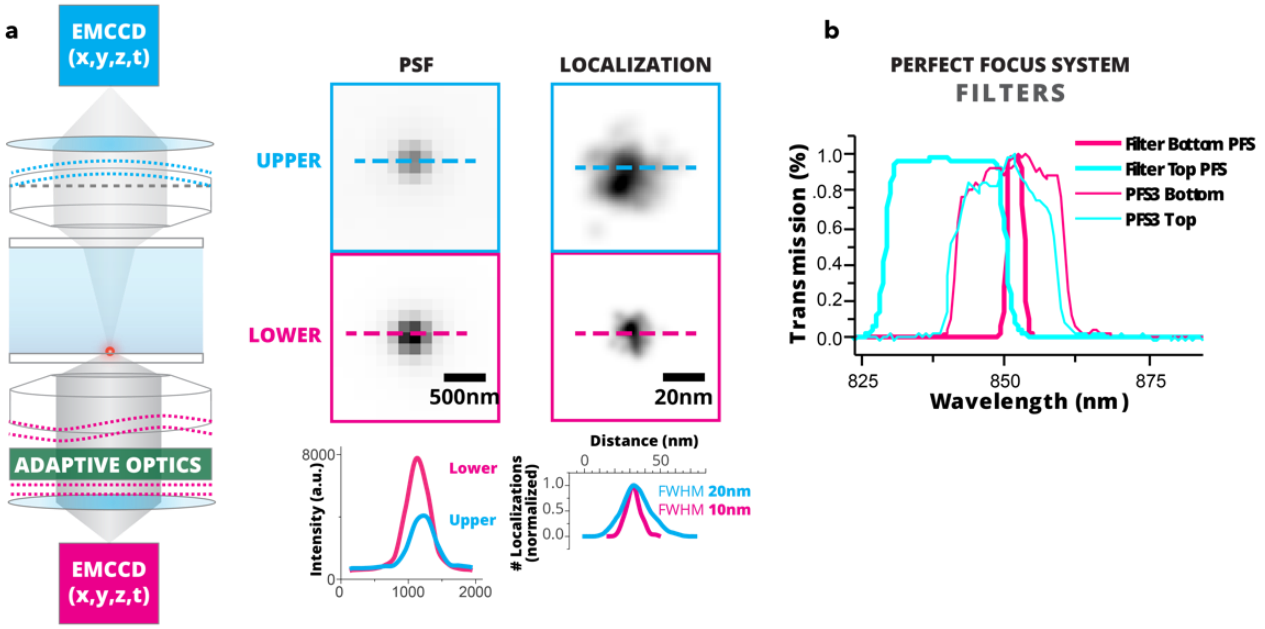

Figure 4.4: Dual-Objective Single Molecule Localization in a Live-Cell Compatible Geometry. (a) Strong spherical aberrations deteriorate the PSF intensity and localization precision when imaging through the several tens of microns of imaging medium necessary for live cell imaging. (b) Perfect Focus System spectra and custom-designed filters required for dual-PFS compatibility.

4.1.3 Exploring New Dimensions with a Second Detection Objective

Indeed, not all applications require more precise localization, instead preferring to use the extra acquired photons to improve the dimensionality of the acquisition in the form of, for example, expanding the spectral bandwidth of the system. In 2015, *Zhang et al* expanded upon the dual-collection objective model implemented by *Xu et al*[150] to perform spectrometry at the single molecule level[151]. By inserting a prism in the second objective's detection path, this optical path is transformed into a single-molecule spectrometer capable of imaging the spectrum of each individual single emitter event. Due to the strong deviation angle of the prism, simultaneously excited fluorescent species were able to be separated with as little as 10nm spectral difference, while retaining the high localization precision from the lower objective.

However, their implementation is incompatible with live cell imaging due to the tight mechanical constraints that their dual-collection objective configuration imposes on the sample. While single objective solutions for spectral imaging have been demonstrated, techniques based on conventional spectrometry approaches[152] require very bright probes, whereas another technique employing a bragg tunable filter for wavelength discrimination sacrifices temporal resolution by requiring 3-4 seconds to acquire a single frame[153]. Recently, *Schechtman et al* proposed a PSF-engineering based solution that unambiguously encodes spectral information as

well axial position into the point spread function using a tetrapod PSF for 3D QD tracking over 20μm depth, and a minimally-aberrating multicolor PSF that encodes emitter wavelength directly into the PSF for simultaneous PALM/dSTORM imaging[154]. This PSF engineering technique provides excellent localization precision and a relatively simple optical configuration, but the complicated tetrapod PSF distribution requires many signal photons, and the lower-signal multicolor PSF for SMLM imaging does not simultaneously encode axial position.

Thus, there exists the need for a spectrally-discriminant single molecule localization and tracking microscope that supports live-cell imaging, without compromising spatiotemporal resolution or the large field of view of conventional SMLM techniques.

4.2 5-D SPT WITH SPECTRALLY DISPLACED LOCALIZATION

To address the need for such a spectrally discriminant high resolution microscope, we developed a robust yet flexible dual-microscope SMLM system capable of live-cell spectral single molecule imaging. The approach takes advantage of the transmitted fluorescence to obtain a spectral mean of each individual emitter, while simultaneously retaining the high spatiotemporal resolution of a traditional SMLM system with no compromises.

4.2.1 Introduction to Spectrally Displaced Localization

The system is an elaboration of a conventional semi-commercial dSTORM microscope based around a Nikon Ti inverted microscope body. **Figure 4.5**a demonstrates a schematic representation of the dual detection paths. This lower microscope is responsible for the spatiotemporal coordinates of the single emitters, using either a cylindrical lens (section 3.1.3) or adaptive optics system (section 3.2.2.2) for 3D localization. A second Nikon Ti inverted microscope body is mounted onto a small optical breadboard, the combination of which is inverted and supported by 4 support legs at the corners of the breadboard, such that the objectives of this upper objective can image the same focal plane as those of the lower microscope. A dispersive element placed in the upper detection path converts emitter wavelength into a spatial displacement, laterally shifting the localization of the single emitter linearly with respect to its spectral mean. This spectral displacement can be measured by referencing the lower (x,y) localization, thereby adding spectral (λ) information to the spatial localization. Tracking fluorescent probes over time using this dual-microscope approach enables 5-dimensional single molecule localization and tracking (x,y,z,t,λ).

Obtaining spectral information from the upper detection path requires the combination of several specific optical and software elements, described in detail here:

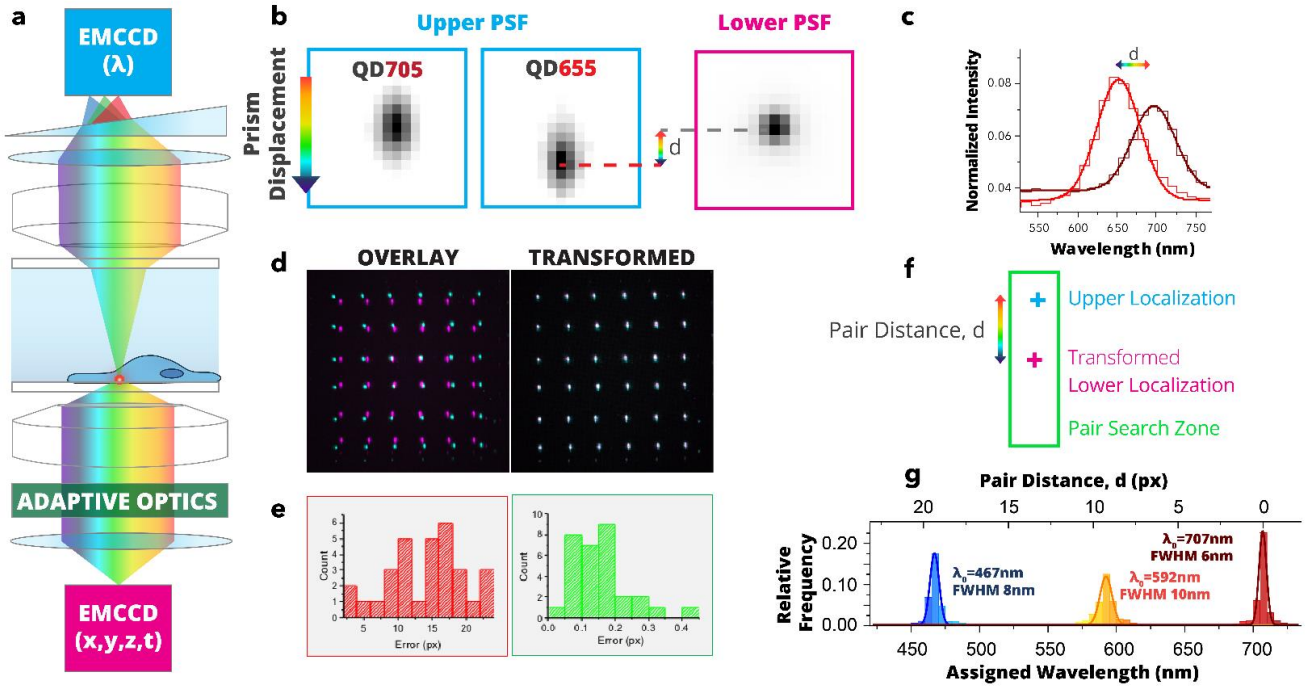

Figure 4.5: Dual-Objective Spectrally Displaced Localization Concept. **(a)** A second detection path collects fluorescence emission in the transmission geometry. **(b)** The weakly dispersing prism linearly shifts the PSF with the emission spectrum of the single fluorescent molecule. **(c)** A 2D Gaussian fit localizes the emitter's position separately on both detection paths. The prism does not significantly vertically stretch the PSF to prevent the validity of a Gaussian fit. **(d)** Localizations from the lower camera are transformed into the upper camera's field of view, with sub-pixel post-transformation pair-distance errors **(e)**. **(f)** The transformed lower localizations are then paired with a single localization from the upper camera. **(g)** Multiple fluorescent species can be separated using a histogram of pair distances, $d = \Delta y = y_{upper} - y'_{lower}$. The ratio between the spectral displacement and wavelength can be calibrated using known fluorescent species, here tetraspeck beads excited at λ=488nm (blue), λ=561nm (orange), and λ=640nm (red).

1. **Dispersive Element for Spectral Detection.** A weakly-dispersing (8°) wedge prism placed in the Fourier plane of a 1.5x zoom 4f-image relay in the upper detection path, inducing a linear displacement proportional to the emission wavelength. Unlike in spectrometry or previous work[151] that spread the spectrum across several tens of pixels, we use a small angle of deviation prism in conjunction with fluorescent probes like quantum dots to shift the lateral position of the PSF without significantly enlarging it, in order to tradeoff localization precision and spectral displacement (give the ratio λnm/dnm). **Figure 4.5**b shows this displacement effect for 2 spectrally neighboring quantum dots, QD705 and QD655.
2. **2-Dimensional Gaussian Fitting.** Unlike previously described spectral detection methods, our approach does not require special PSF fitting algorithms[154] and is designed to work with the standard 2D Gaussian fitting localization. Since the prism only weakly spreads the emission spectrum, the spectral image is spatially confined to several pixels, the Gaussian approximation for localization is still valid on the spectral detection path and in particular in the direction of spectral displacement. (**Figure 4.5**c).
3. **Field of View Transformation.** To compensate for differences in magnification, rotation, or other field of view distortions between the lower and upper cameras, the field of view transformation is calibrated. The two fields of view are spatially sampled by raster scanning a fiducial marker in a 7x7 grid. The corresponding 49 centroids positions are first localized in each channel and paired by nearest neighbor search. A 2-

dimensional 3rd order polynomial transformation is computed from the paired coordinates by least-squares Levenberg-Marquardt minimization algorithm:

$$x' = a_{x,1}x^3 + a_{x.2}y^3 + a_{x,3}x^2y + a_{x,4}xy^2 + a_{x,5}x^2 + a_{x,5}y^2 + a_{x,6}xy + a_{x,7}x + a_{x,8}y + a_{x,9} \quad (4.1)$$

$$y' = a_{y,1}x^3 + a_{y.2}y^3 + a_{y,3}x^2y + a_{y,4}xy^2 + a_{y,5}x^2 + a_{y,5}y^2 + a_{y,6}xy + a_{y,7}x + a_{y,8}y + a_{y,9} \quad (4.2)$$

where x' and y' are the transformed coordinates of x and y, respectively with coefficients $a_{x,n}$ and $a_{y,n}$. This 3rd order polynomial transformation requiring 10 coefficients per spatial dimension is used to render the system as versatile as possible and correct for any non-linear field of view deformations imparted by the spectral optics or the cylindrical lens. Once calibration, this transformation is applied to the lower localizations to match the field of view of the upper camera (**Figure 4.5**d), resulting in a field-dependent error after transformation typically ranging from 0 to ~60nm, with median values around ε=25nm (**Figure 4.5**e). Due to the prism in the spectral detection path, this field of view transformation is wavelength dependent, and this alignment process creates a transformation centered at the spectral mean wavelength of the emission of the fiducial marker.

4. **Dual-FOV Localization Pairing**. Once the lower coordinates are transformed to match the upper field of view, a linear search around the transformed lower localization is performed to find its paired upper localization (**Figure 4.5**f). The displacement angle of the prism, fixed at ~0°, induces a vertical displacement of the localization as a function of wavelength, allowing minimize the pair search zone to reduced a linear zone. Minimizing the size of this pair search zone is critical as it limits the maximum density of simultaneously fluorescing single molecules in a single image frame, minimizing missed pairing. The width and height of the search zone are both user-definable based on *a priori* knowledge of the fluorescent species being imaged. Once the localizations are matched, their pair distance, d, is calculated as $d = y_{upper} - y'_{lower}$ and retained as a proxy for the spectral mean of the emitter.
5. **Quantitative Spectral Displacement and Spectral Separation.** **Figure 4.5**g shows a histogram of these pair distances, clearly demonstrating distinction between spectral species between three of the fluorescent dyes on a tetraspeck bead, obtained by exciting at λ_{exc}=488nm (blue), λ_{exc} =561nm (orange), and λ_{exc} =640nm (red). The system was aligned for the red fluorophore and shows a ~20 pixel = 3.2μm vertical shift for the blue fluorophore. Calculating the spectral means for each of the three fluorescent dyes allows a quantitative calibration of the spectral shift to wavelength of ~12.3 nm / pixel. Fitting the individual wavelength distributions to Gaussian functions gives a spectral $FWHM_\lambda$ of between 6nm – 10nm, which is related to the true spectral resolution of the system.

It is important to note that this spectral displacement localization pipeline does not alter the spatial localizations from the lower detection path and merely provides supplementary spectral information for each localization, if the localization pairing is successful, and when used for 3D single particle tracking applications, enables 5-dimensional SMLM (x,y,z,t,λ).

4.2.2 Spectrally Displaced Localization: The Benchmarks

To quantify the spatial and spectral capabilities of the system, a calibration coverslip of nanodiamonds was created. 100µLs of 1:100 stock nanodiamond solution (REF) was incubated on a #1.5H 18mm coverslip for 5 minutes, adhering a good density of nanodiamonds to the coverslip surface for imaging. To mount the coverslip for dual-objective imaging, the 18mm coverslip was placed inside the particularly designed sample support (**Figure 4.3**), onto which 8µL of ultra pure water was closed with a second #1.5 18mm coverslip. The volume of liquid and the carefully designed sample mount ensure that the coverslip-to-coverslip distance is ~30µm, within the range the perfect focus system's range of ~60µm for the two objectives used.

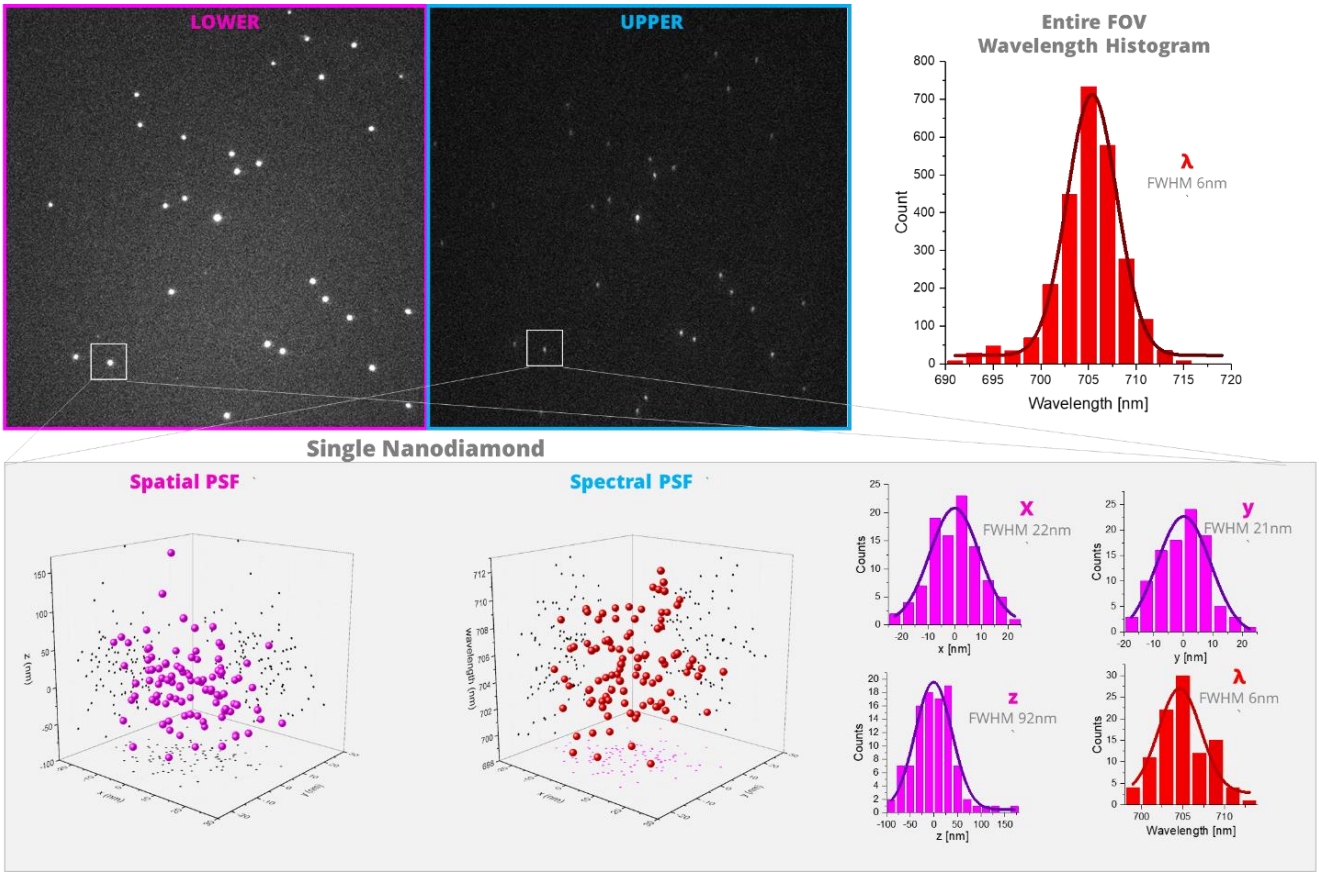

Figure 4.6: Spectrally Displaced Localization: Spatial and Spectral Super Resolution Point Spread Functions. Nanodiamonds covering the full field of view (80µm x 80µm) serve as both the reference for field of view transformation between the two optical paths as well as stable fiducial markers for spatial and spectral localization precision calculations. A single bead near the edge of the field of view was chosen for spatial and spectral localization precision quantifications. The spatial (x,y,z) localizations from 100 consecutive imaging frames from the lower camera are plotted (magenta), demonstrating typical values of astigmatic localization precision. Note the values here are FWHM = 2.3σ. The spectral PSF (red), here the wavelength as a function of (x,y), is calculated as proportional to the pair distance via a linear calibration. It is homogenous over the field of view with a FWHM of 6nm.

100x Oil Immersion NA1.49 on lower path + cylindrical lens for astigmatism (left)
60x water immersion NA1.2 on upper path + 1.5x zoom incorporated in spectral detection system (right)

Experimentally, the desired focal plane was initially found using the bottom microscope and the bottom PFS was locked to retain the objective's axial position. The second objective was then lowered until immersed its immersion medium (water), at which point care was taken to continue to lower the objective slowly to the focal plane of the lower objective to prevent the two objectives from touching or the coverslips from breaking. The PFS system locks the upper objective at the surface of the upper coverslip, and the PFS offset mechanism was used to find

the bottom coverslip surface. The mechanical stability of the system allows the use of the objective retraction mechanisms of the Nikon Ti microscopes to quickly change coverslips without losing the focal plane.

4.2.2.1 Spatial Resolution

The dual-objective system was then used to image nanodiamonds at the surface of the bottom coverslip. 100 frames were acquired for the benchmarking experiments. The lower (x,y,z) localizations for a single bead over the 100 frames are plotted in **Figure 4.6**, as well as the distributions across the individual spatial dimensions. The FWHM of these distributions are typical of astigmatic 3D SMLM with a cylindrical lens.

4.2.2.2 Spectral Resolution

For the spectral characterizations, the field of view transformation between the upper and lower detection paths, detailed in the previous section, must first be calibrated. The nanodiamonds covering the entire field of view of the cameras were used to create this field of view calibration. The localizations from the bottom and top field of view were then paired, and the pair distance was converted into wavelength using the calibration outlined in the previous section. **Figure 4.6** shows the spectral point spread function of a single nanodiamond, demonstrating that this pair-distance based method can quantitatively assign a wavelength to a single emitter with a FWHM of $\Delta\lambda_{FWHM}$=6nm. Furthermore, when plotting the wavelength distribution for all of the nanodiamonds across the field of view (**Figure 4.6**), this value remains constant, demonstrating the accuracy of the field of view transformation.

Spectral Characterization of Quantum Dots

To better characterize the spectral discrimination capabilities of the system in more realistic signal intensity and blinking situations, 5 quantum dot species were adhered to the surface of an 18mm coverslip and excited with a single 488nm laser. 2,000 image frames of the both full cameras sensor at 512 x 512 pixels at 50ms/frame were acquired and analyzed with the spectral pairing process. The **Figure 4.7**a shows a single image frame from the acquisition, with the raw data from the upper spectral image and the color-coded assigned wavelengths on the lower image. **Figure 4.7**b shows representative super-resolution 10nm per pixel reconstructions of each of the individual quantum dot species imaged, again color coded for wavelength, demonstrating the homogeneity of the wavelength distributions for individual quantum dots. Localizations from the entire lower field of view are able to be matched to a spectral localization, as the 90x effective zoom (60x objective x 1.5x zoom) of the upper detection path images a slightly larger field of view than the lower objective.

Spectral Ambiguity Zone Limits Spatial Density

There are, however, spatial constraints on the ability to accurately pair a lower localization with a spectral localization from the upper camera. Specifically, the spectral shift on the upper path imposes a limit on the spatial density of emitting fluorescent molecules. This effect is shown in **Figure 4.7**c, where two quantum dots are separated by only ~1μm on the lower camera, resulting in multiple possible matches in their pair search zones on the upper channel. The analysis software has multiple user-selectable modes of operation for these ambiguous cases, but the most robust and straightforward option retains the spatial localization of such ambiguous events without assigning a wavelength (**Figure 4.7**d, left, black points), tagging them as “special” since

they may contain interesting information about potential colocalization events. If desired, these ambiguous localizations can be removed from the reconstruction (**Figure 4.7**d, center), at the risk of spectral misassignment. Filtering the ambiguous localizations results in clear spectral distinction of the QD605 and QD525 species, although several QD525 localizations are misassigned as ~700nm (**Figure 4.7**d, right).

The size of this spectral ambiguity zone is primarily dependent on the spectral displacement vector created by the orientation and angle of the prism, determining the pair search zone in the upper localization space. As shown in **Figure 4.7**c, this ambiguity is primarily vertical due to the orientation of the prism, and the large spectral spread of ~300nm between QD800 and QD525 requires an 8px x 40px (1.28µm x 6.4µm) pair search zone, representing the effective maximum of the spectral ambiguity zone. Since the pair search zone can be modified with *a priori* knowledge of the spectral variation of the fluorescent markers used in each experiment, this spectral ambiguity zone varies on a per-experiment basis.

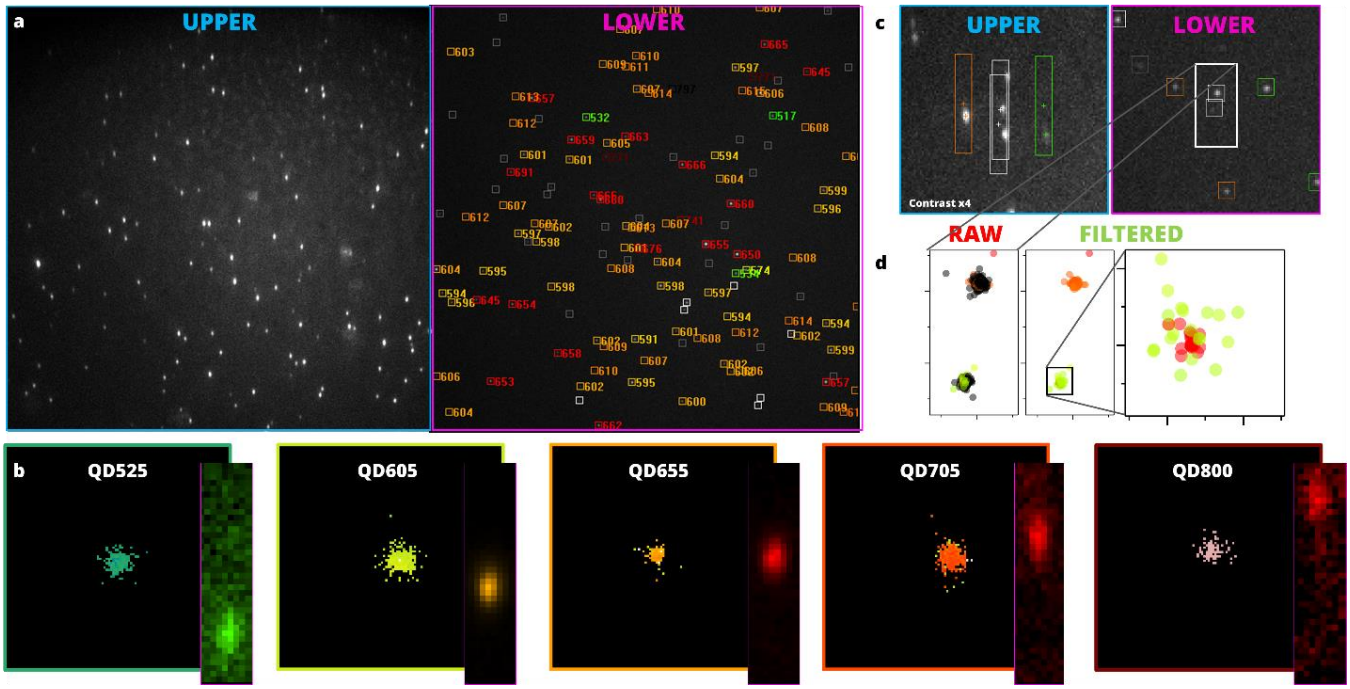

Figure 4.7: Spectral Characterization with 5 Quantum Dot Species. (a) Raw spectral image (left) and assigned wavelength (right) of five quantum dot species adhered to a glass coverslip and imaged for 2,000 imaging frames**. (b)** Individual wavelength-coded reconstructions @10nm/px of individual quantum dot species, demonstrating spectral homogeneity of wavelength assignment despite QD blinking. Representative raw spectral images are inset. **(c)** In dense regions, individual emitters may have multiple matches in the spectral channel (white outlines), causing ambiguities in wavelength assignment. **(d)** Localizations with multiple spectral matches are tagged as ambiguous (black circles), and can be filtered from reconstructions if desired (center). However, this may result in false localization pairing (right).

QD800, QD705, QD655, QD605, QD525 Steptavidin Conjugates
Excitation 488nm | 2,000 frames @ 50ms/frame, 512x512px

In SPT experiments, these ambiguous localizations can be eventually ignored or even used to obtain supplemental spatial information. A spectral smoothing option allows correcting for wavelength misassignment of individual localizations in a given trajectory, including the unassigned localizations. However, these ambiguous localizations can also be an indication of high molecular density and potential zones of protein interaction. These “special” localization

events could, for example, be analyzed using multiple fitting algorithms and taking into account the spectral information in the minimization process.

Lateral Drift Correction

Lateral drift in either the lower or upper detection path affects the pair distance between matched localizations, changing the spectral resolution over the course of the acquisition. To avoid time-dependence in the spectral assignment, it is necessary to numerically compensate for the drift separately on each path post-acquisition. **Figure 4.8** shows the distinct lateral drift incurred on each detection path, and the compensation via separate drift trajectories.

To ensure the spectral shift remains constant over time, tetraspeck beads were used here to monitor several fluorescent species simultaneous; by exciting the bead at 488nm, three fluorescent species were clearly distinguishable on the upper camera (**Figure 4.8**b). Next, two distinct time domains were investigated.

(i) A short-duration time domain simulated the fast stream acquisition speed of SMLM experiments. Here, 200 frames at 100ms/frame were acquired, and localizations from the lower and upper paths were paired. **Figure 4.8**c shows the 2-dimensional pair distance, demonstrating the primarily vertical spectral displacement due to the prism and clear separation of the fluorescent species. The pair distance over time remains constant over ~20 seconds under constant laser illumination (**Figure 4.8**d).

(ii) A long time-domain timelapse was performed, imaging every 15 seconds for 30 minutes, mimicking the fact that SMLM acquisitions range between hundreds to tens of thousands of frames. This duration is typical for dSTORM or SPT experiments. A stream acquisition was not performed over 30 minutes to avoid bleaching of the tetraspeck beads with constant laser illumination, thereby reducing the localization precision and spectral assignment precision. **Figure 4.8**e shows the several micrometer drift of the upper localizations over the course of the acquisition and the detrimental effect of this lateral drift on the localization pairing process (**Figure 4.8**f). Notably, the blue fluorescent dye is only localizable in the first few minutes, after which it extends out of the pair search range. However, once the drift trajectory is incorporated into the localizations, the pair distance remains constant over the 30 minute time duration (**Figure 4.8**g).

The localization drift-correction routine updates the zero-order coefficients of the field of view transformation (equations 4.1 and 4.2) correcting micrometer-scale lateral displacements between the two objectives incurred after the field of view calibration procedure. This automatic correction of the FOV transformation ensures that the two channels are aligned (pair distance = 0) at a fixed wavelength as long as the same fiducial markers and filter sets are used.

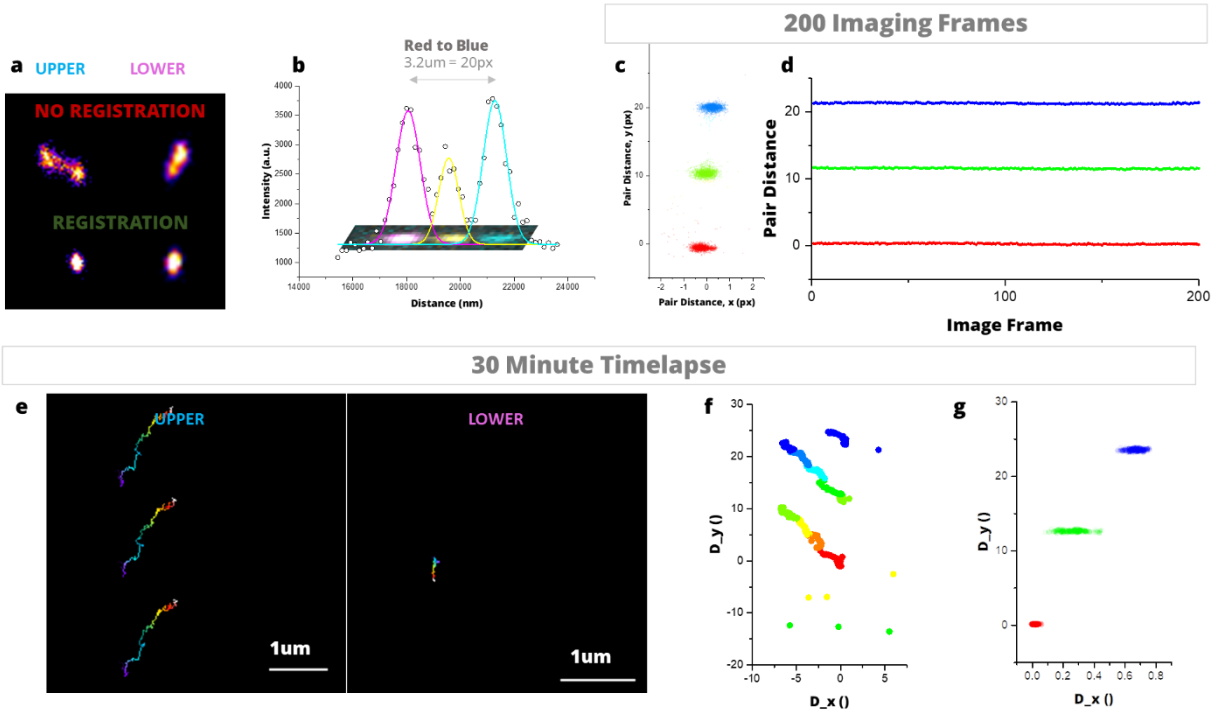

Figure 4.8: Lateral Drift Correction essential for long-duration spectral imaging. (a) The lateral drift over the course of 200 imaging frames is distinct for the upper and lower detection paths. (b) Linescan of three different fluorphores on a single tetraspeck bead, demonstration a spectral shift of ~3.2µm from red to blue. (c) 2D pair distance plot of 3 fluorescent species of a tetraspeck bead over 200 imaging frames @ 100ms /frame. (d) The vertical pair distance remains constant over the course of the 20 seconds. (e) Trajectories from a single tetraspeck bead over the course of a 30 minute timelapse, demonstrating a significantly larger drift that significantly affects the pair distance and results in false wavelength assignment (f). (g)Post-acquisition software drift correction restores proper pairing between the upper and lower localizations.

100nm Tetraspeck Bead | Excitation 488nm

Optimizing Optical Filters

The use of lasers as excitation sources affords precise illumination and extremely narrow excitation bandwidth, allowing several fluorescent dyes to be imaged simultaneously by combining excitation powers. However, their use also requires specific emission filters to be placed in the detection paths that remove a small spectral range around the laser wavelength. For most experiments, a quad-band filter is used, which allows excitation from 405nm, 488nm 561, and 640nm laser sources, and therefore a small spectral range of ~20-40nm around these center wavelengths are removed from the emission spectrum on the upper detection path. **Figure 4.9**a demonstrates this for a green fluorescent bead; the spectrum with the quad-band filter set (composed of a dichroic mirror as well as an emission filter, both with relatively similar spectral filtering capacities) appears as two distinct spots, whereas if a LP488 filter is used, all wavelengths greater than the cutoff wavelength of 488nm are imaged on the upper camera. **Figure 4.9**b shows the same effect on three fluorescent species of the tetraspeck beads, which incidentally fall nicely within the quad-band filter passband. The versatility of the system allows for simple replacement of the emission filters in the spectral path, allowing for quick rotation between a quad-band filter set (quad), a single quad-band emission filter (notch), a long-pass filter at 488nm, and a long-pass filter at 561nm, the latter of which is implemented in most of the live-cell experiments as it removes a large portion of cellular autofluorescence.

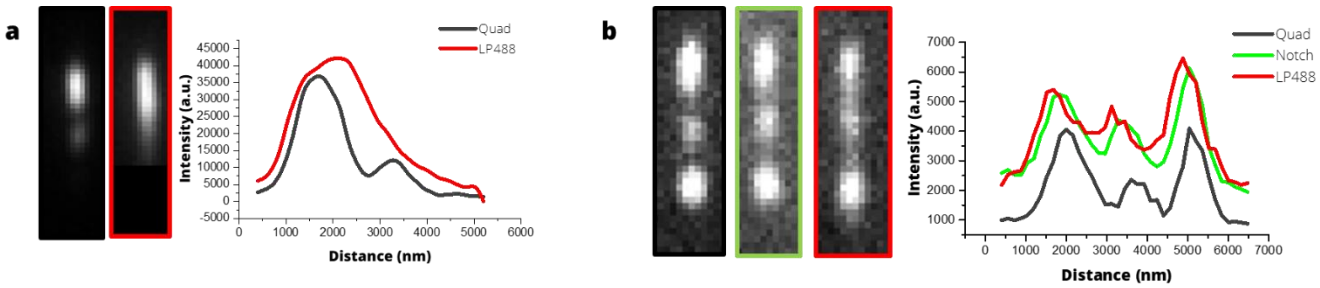

Figure 4.9: Filter Selection in Spectral Path. (a) A portion of the spectrum of a green fluorescent bead is filtered when using the quand-band filter set, resulting in two separate intensity spots on the upper camera. Using a long pass filter (LP488) allows its entire spectrum to be imaged. **(b)** A tetraspeck bead excited at 488nm has three distinct spectral species, which match well with the pass-band of the quad-band filter set. Using just the quad band emission filter without the quad-band dichroic mirror (green) decreases the spectral cutting effect of the filter. Finally, using a long pass filter with cutoff wavelength at 488nm (red) allows the full spectra of the three fluorescent species to be image, notably resulting in a small overlap

(a) Green Fluorescent Bead, EXC@488nm (b) 100nm Tetraspeck Bead, EXC@488nm

4.2.3 Spectral Single Molecule Imaging in Live Biological Samples

After characterizing its spatial and spectral capacities, we wanted to use the system to perform an array of simultaneous multicolor 3D single particle tracking experiments, ranging from quantum dot tracking of membrane proteins in neuron cultures to live DNA-PAINT imaging in cell cultures. Before performing live cell experiments, the optimal fluorescent probes needed to be chosen.

4.2.3.1 Fluorescent Species Selection for Live Cell Imaging

For the initial tracking experiments, quantum dots were chosen due to their brightness and resistance to photobleaching as well as their broad absorption spectra. **Figure 4.10** shows the emission spectra of a wide variety of commercially available quantum dots in relation to the bottom microscope's emission filter, with dual pass-bands for red and far red imaging (Semrock FF01-594/730-25), denoted the Alexa647 Filter. This filter is used frequently in dSTORM imaging as it transmits the majority of the Alexa647 dye's emission spectrum, maximizing collection efficiency. QD705, QD655, and QD605 were chosen as the optimal 3-color solution, providing sufficient spectral separation and compatibility with the filter set. It should be noted that, for simplicity, we opted here to make the probe choice based on our available filters; the filter cube can easily be changed between images without modifying the mechanical alignment of the two-microscope system.

An advantage of using quantum dots in simultaneous multicolor imaging is that multiple species can be excited with a single laser wavelength, reducing the total energy delivered to the sample and therefore the potential photodamage that might alter cellular behavior.

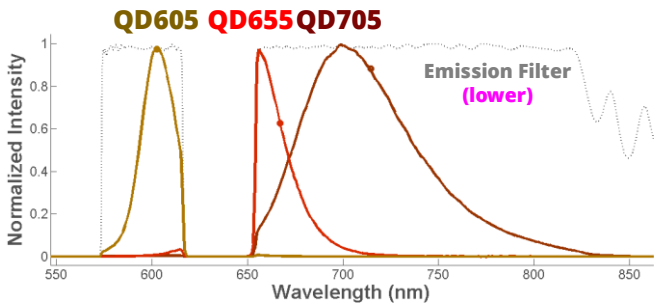

Figure 4.10: Quantum Dot Selection for Live-Cell Tracking Experiments. Commercially available quantum dots in relation to the dual-emission filter (gray). QD705, QD655, and QD605 were chosen as the optimal probes.

4.2.3.2 Simultaneous 3-QD 3D Tracking of Membrane Receptors in Live COS-7 cells

Once the optimal filters were selected, we performed proof of concept live-cell quantum dot tracking on the membrane protein NCAM in COS7 cell cultures. The NCAM protein was overexpressed with the genetically fused AP tag and coexpressed with *Escherichia coli* biotin ligase, $BirA^{ER}$, an enzyme which biotinylates the AP tag during protein maturation[57].A single quantum dot tag, QD705, was initially used to ensure live-cell compatibility of the dual-microscope system and spectral detection capabilities in the live-cell environment. Then, a second quantum dot tag, QD655, was added in conjunction with QD705. A new coverslip was incubated with this premix and spectrally imaged. Finally, 3 quantum dot species (QD705, QD655, QD605) were simultaneously excited with a single 561nm laser at ~500W/cm² for 3-color 3D membrane protein tracking in live cells.

Post-acquisition, the analysis workflow outlined in section 4.2.1 was followed. Briefly, each detection channel was analyzed independently for (x,y) localizations, fit to a 2D Gaussian, and drift-corrected. Localizations from the lower channel were assigned an axial (z) position based on their astigmatism, transformed into the coordinate space of the upper field of view, and paired with a single upper channel localization in the pair search zone, here 4px x 20px (corresponding to a 0.64µm x 3.2µm search area). This spectral pair distance was used to assign a wavelength to each localization. The full set of (x,y,z,t,λ) localizations were then spatially reconnected and 3D trajectories were created.

The large field of view of our spectral detection system allowed us to image entire COS7 cells at 20Hz (50ms/frame) for 1500 frames (**Figure 4.11**b). The wavelength histogram demonstrates the strong spectral discrimination, even with sub-exposure time motion-induced distortion of the spatial and spectral localizations due to QD movements during the exposure time.

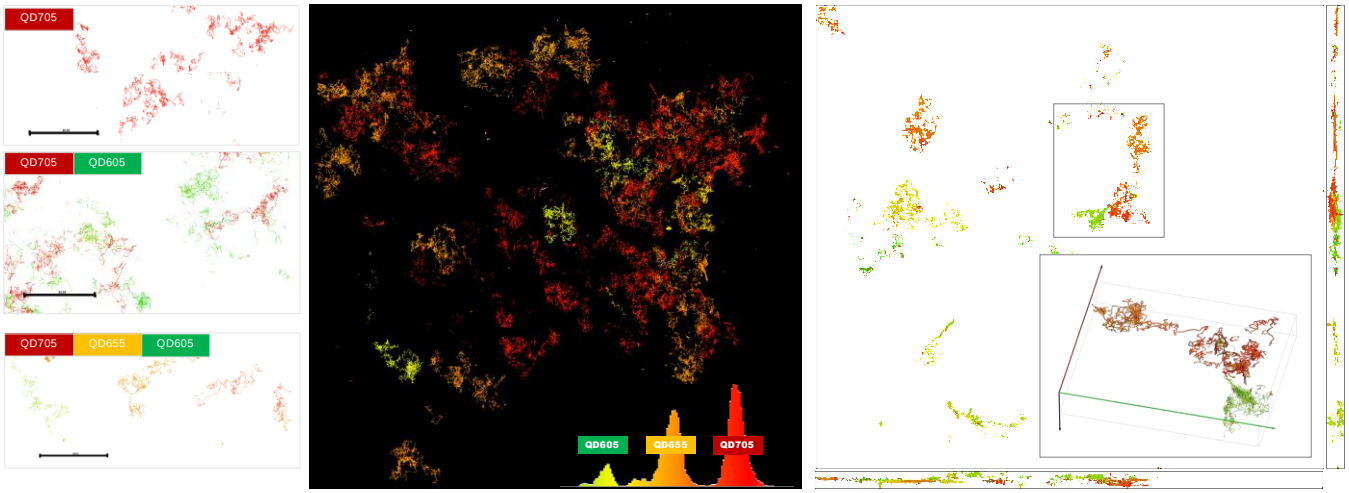

Figure 4.11: Simultaneous 1- 2- and 3-Color 3D QD Tracking in Live COS7 Cells. (left) Individual trajectories 1-, 2-, and 3-Color QD705, QD655, anad QD605 Tracking of NCAM-AP in COS7 cell, demonstrating significant spectral separation. **(center)** A large field of view wavelength-coded trajectory reconstruction of the COS7 cell, showing homogeneous distribution of the different fluorescent species. The wavelength histogram shows clearly separable spectral species. **(right)** A subset of longer (>50 frame duration) trajectories were imported into AMIRA for 3D representation.

COS7 NCAM-AP | QD705, QD655, QD605 Streptavidin Conjugates @ 1:10,000 | 561nm Excitation @ 20Hz

4.2.3.3 Live-Cell Tracking Temporal Resolution: Up to 100Hz Spectral Imaging

Conventional multicolor SPT approaches that use a single objective and separate individual wavelengths onto separate regions of a single image sensor generally require the use of the entire image sensor to image small fields of view, limiting the acquisition speed to ~20Hz for common EMCCDs. At the same imaging speed, our dual-microscope approach allows for a larger field of view, independently of the number of colors imaged (up to 512px x 512px @ 20Hz). However, by reducing the imaging region to 128px x 128px, we can image at 100Hz with the same spectral resolution using the dual-EMCCD setup. Additionally, smaller regions have a more precise field of view transformation, and usually see improved spectral assignment as a result. **Figure 4.12** demonstrates multiple quantum dot discrimination at various exposure times, with a strong signal-to-noise ratio even at 10ms exposure time (100Hz).

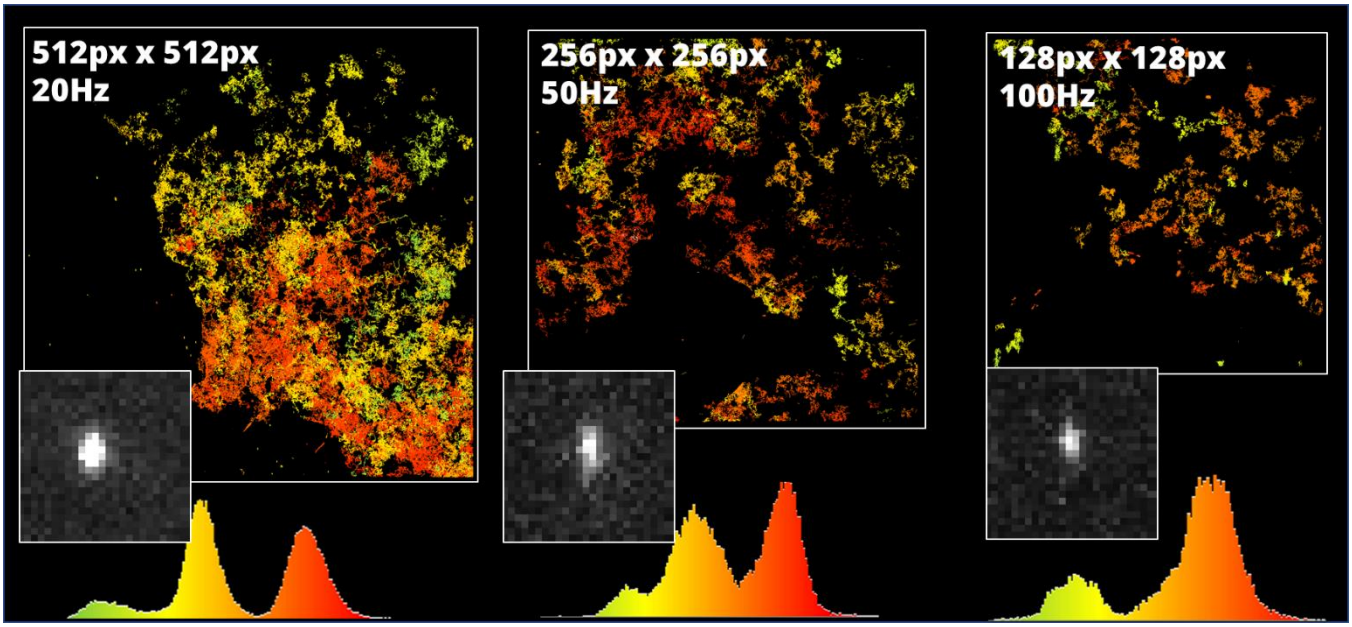

Figure 4.12: Temporal Resolution up to 100Hz. (top) Simultaneous multicolor spectral QD tracking at varying temporal resolutions and fields of view, from full-chip at 20Hz to 100Hz at 128x128px. 40nm/px wavelength-coded track reconstructions. **(Inset)** Normalized single QD spectral image from upper detection. **(Bottom)** Wavelength histograms for all localizations in each image.

COS NCAM-AP | QD705, QD655, QD605 Streptavidin Conjugates | Astigmatism with cylindrical lens

4.2.3.4 Organic Fluorophore Sensitivity: 2-Color Live DNA-PAINT Tracking of Membrane Receptors

An important criterion that was considered when developing this spectrally discriminant microscope was its sensitivity to photon detection, a key parameter for single-molecule experiments. While previous spectrally-resolved single molecule tracking experiments used bright fluorescent probes like QDs thanks to their high photon output, many SMLM experiments are performed in a signal starved environment. One of the benefits of the dual-objective geometry is the retention of all the sensitivity of a conventional SMLM microscope, with supplemental spectral information if the single molecule can be detected on the upper detection path. Furthermore, thanks to the minimally dispersive prism, the single molecule's spectrum is still confined to relatively few pixels, thus maximizing the photons per pixel and thus the chances of single molecule localization. However, traditional single molecule tracking modalities like uPAINT require live injection of a fluorescently tagged ligand while the sample is on the microscope, and the two-objective geometry used here prevents such accessibility.

To circumvent this accessibility issue, an alternative single particle tracking technique based on the DNA-PAINT modality was used (section 1.3.3.3). In collaboration with the company Ultivue, a pair of a secondary antibody (1:400) coupled to a specific DNA oligomer and its fluorescently-labelled complementary oligomer were used in conjunction with a primary anti-GFP antibody (1:200) to follow the GPI membrane receptor overexpressed with a fused GFP molecule and co-expressed with soluble GFP, enabling visualization of electroporated cells and their morphology. The DNA-PAINT "live" oligomers have a stronger binding affinity than the oligomers used for fixed imaging, ensuring the fluorescent probes stay linked to the protein of interest for several imaging frames.

Figure 4.13 shows a dual-color 3D DNA-PAINT GPI-GFP tracking experiment. **Figure 4.13**a shows a single frame from the dual-color DNA-PAINT acquisition, with regions overlaid by the spectral localization software showing two distinct populations of organic fluorophores as well as

nanodiamonds used as fiducial markers. The two organic fluorophores coupled to complementary DNA oligomers at 0.1nM imaging concentration were individually excited such that they were detectable on both channels ($\lambda_{exc,1}$=561nm @ ~500W/cm² and $\lambda_{exc,2}$=640nm @ ~500W/cm²). 2,000 frames were acquired at 20Hz, localized (x,y,z,λ), and their trajectories computed. The wavelength-coded track reconstruction in **Figure 4.13**b shows the specificity of the DNA-PAINT technique for live-cell dual-objective spectral imaging. The wavelength histogram also demonstrates that the reduced signal from using organic fluorophores does not significantly affect the wavelength distribution. Similarly, the 3D position of the fluorophore can be extracted using the astigmatism encoded into the lower PSF, even in the lower signal environment (**Figure 4.13**c).

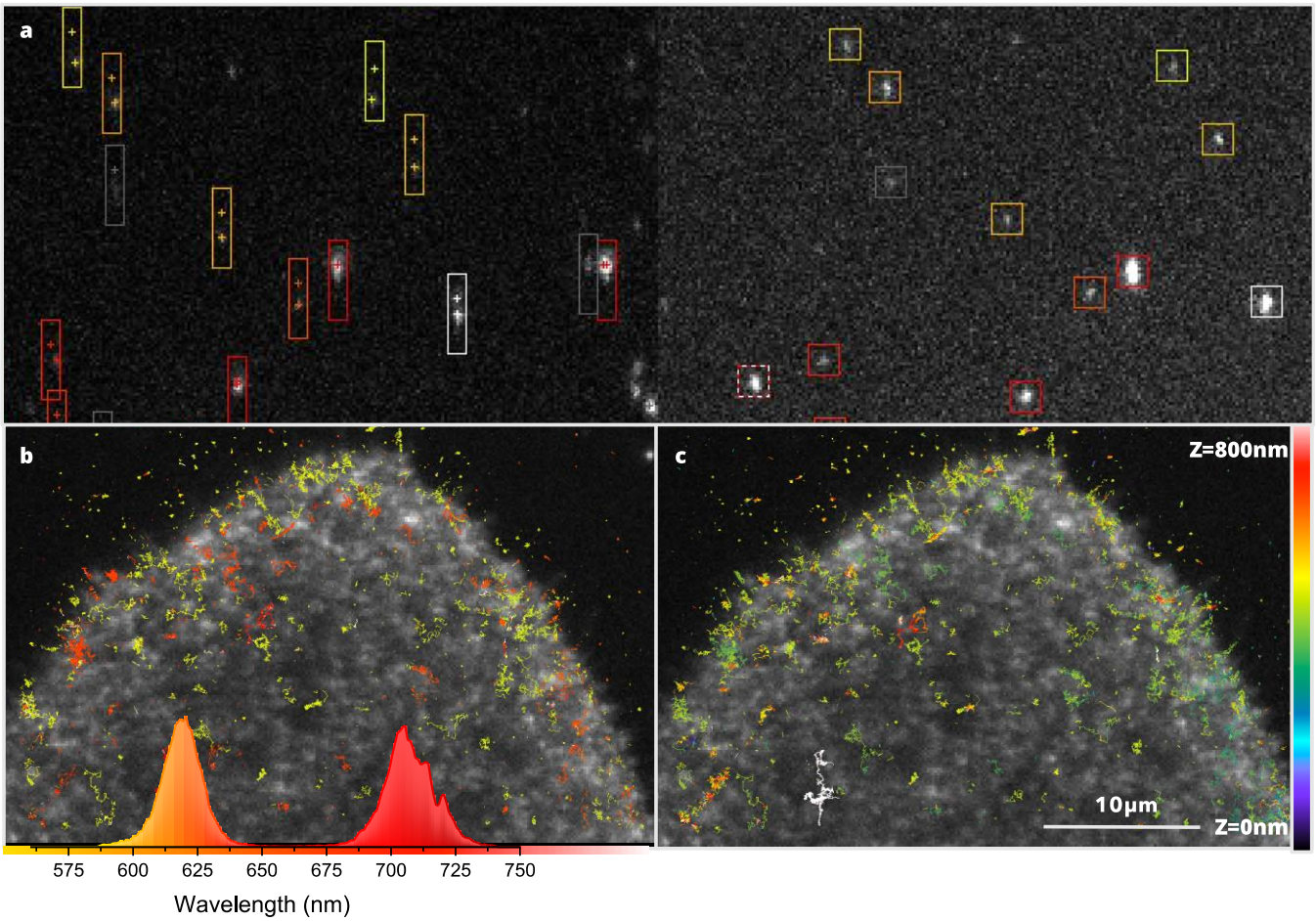

Figure 4.13: Simultaneous 2-Color Live 3D DNA-PAINT Tracking of GPI-GFP in COS7 Cells. (a) A single frame from acquisition demonstrating localization pairing. (Right) Lower channel (Left) Upper channel, crosses indicate trasnforemd lower and upper localizations. The assigned wavelength is linearly proportional to the spectrally-induced displacement between the two localizations. **(b)** Wavelength-coded tracks image overlayed on GFP image. The two spectral species are easily differntiable using the wavelength histogram (bottom). **(c)** Z-coded tracks, simultaenously tracked using the astigmatism encoded in the lower PSF.

COS7 Cell | GPI-GFP | Anti-GFP (Mouse) + Anti-Mouse-D1 | 0.1nM D1-550-Live + 0.1nM D1-650-Live
Excitation 561nm and 640nm | Astigmatism with cylindrical lens

4.2.3.5 2-Color Mixed-Modality DNA-PAINT + QD Tracking of GPI-GFP in COS Cells

The ability to combine labeling and imaging strategies is essential to a versatile SMLM microscope, and the sensitivity of the spectral detection path allows for multimodal single particle tracking using a variety of fluorescent probes. As a proof of concept, simultaneous DNA-PAINT (550nm) and Quantum Dot (705nm) tracking was performed on the same protein, GPI-

GFP expressed in COS7 cells. Despite the difference in fluorescence intensity, both species are detected in the spectral detection channel (averaged spectra in **Figure 4.14**a) and easily separated in the wavelength histogram in **Figure 4.14**b. Wavelength (**Figure 4.14**c) and axial position (**Figure 4.14**d) coded reconstructions demonstrate the specificity of both labeling schemes to the transfected cell.

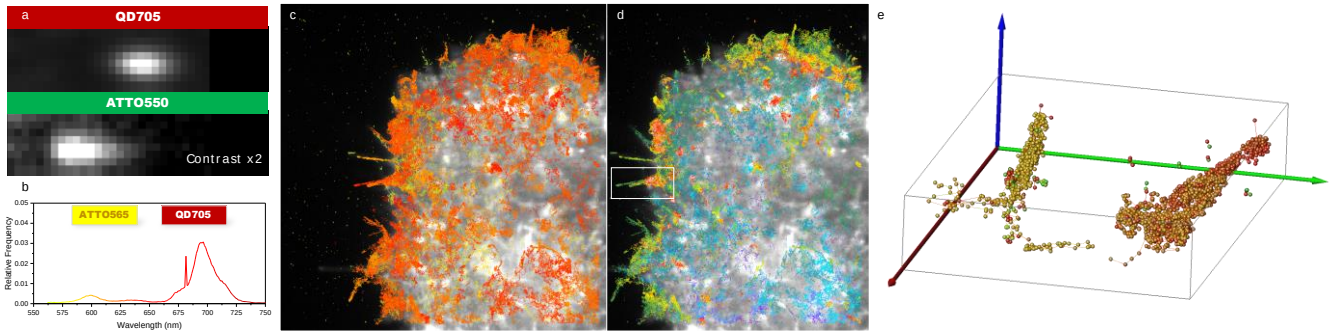

Figure 4.14: Multimodal Spectral SPT: DNA-PAINT + QD-Tracking. **(a)** Averages of ~200 individual single molecule spectra for QD705 (top) and ATTO550 (bottom, contrast x2). Prism displacement direction shown in arrow in top-left. Notably, the tail of the emission spectrum of organic fluorophore, ATTO550, is visible. **(b)** The long track length of the QDs dominates the wavelength localization histrogram, but both spectral species are easily distringuishable. **(c)** Wavelength-coded tracks reconstruction of DNA-PAINT 550 and QD705 Tracking, overlayed on GFP imagie of cell volume. **(d)** Axial position-coded reconstruction of the same tracks. **(e)** 3D reconstruction (Amira) of 2-color multimodal single particle tracking.

COS7 Cell | GPI-GFP | Anti-GFP Antibody + DNA-PAINT or QD Secondary Antibody
561nm Excitation | Astigmatism with cylindrical lens

This proof of concept DNA-PAINT + QD experiment tracks the same protein with two separate fluorescent species, which, while interesting from an optical perspective, has limited biological applications. However, this kind of mixed modality imaging could be useful for combining structural imaging with tracking; for example, using the DNA-PAINT labeling against a diffuse membrane protein like GPI, shown above in **Figure 4.14**, combined with QD-tracking of a protein with specific cellular compartmentalization, or potentially intracellular protein tracking with genetically encoded fluorescent proteins.

4.2.3.6 Fluorescent Protein Sensitivity: Talin-mEOS3.2 sptPALM

Most single particle tracking techniques, like the previously discussed quantum dot and DNA-PAINT based approaches, require the use of antibodies or other non-cell membrane permeable ligands to couple a fluorescent marker to the protein of interest and are therefore restricted to the tracking of membrane surface proteins. SptPALM[10], however, allows tracking of intracellular proteins via the expression of a genetically modified variant of the protein coupled with a photoactivable fluorescent protein, like mEOS. Unfortunately, these proteins emit much fewer photons than quantum dots or organic fluorophores, requiring extremely sensitive detection schemes to accurately track their movement. Our dual-objective spectrally resolved single particle tracking system affords the unique possibility of tracking fluorescent proteins, opening the doors to a wide array of intracellular protein tracking.

As a proof of concept, we expressed a genetically modified variant of the cytoskeletal protein Talin with mEOS3.2 fused to its c-terminal. **Figure 4.15**a shows a single image from the acquisition at 50ms per frame, and a single mEOS protein (inset) in the spatial (magenta) and spectral (cyan, 4x contrast) channel. Here, we used oblique illumination to allow for 3D single

particle tracking, which has the downside of increased background, especially near the center of the cell. Averaging ~400 individual spectral images gave a good representation of the mean spectrum of mEOS3.2 (**Figure 4.15**b). Reconnecting sequential localizations results in a homogeneous wavelength tracking reconstruction (**Figure 4.15**c), and a wavelength distribution centered at ~610nm with a variance of 16.5nm (**Figure 4.15**d). This slightly larger distribution can be attributed primarily to the reduced localization precision because of the low photon count of mEOS. A representative 3D trajectory can be found in **Figure 4.15**e with a temporal color code.

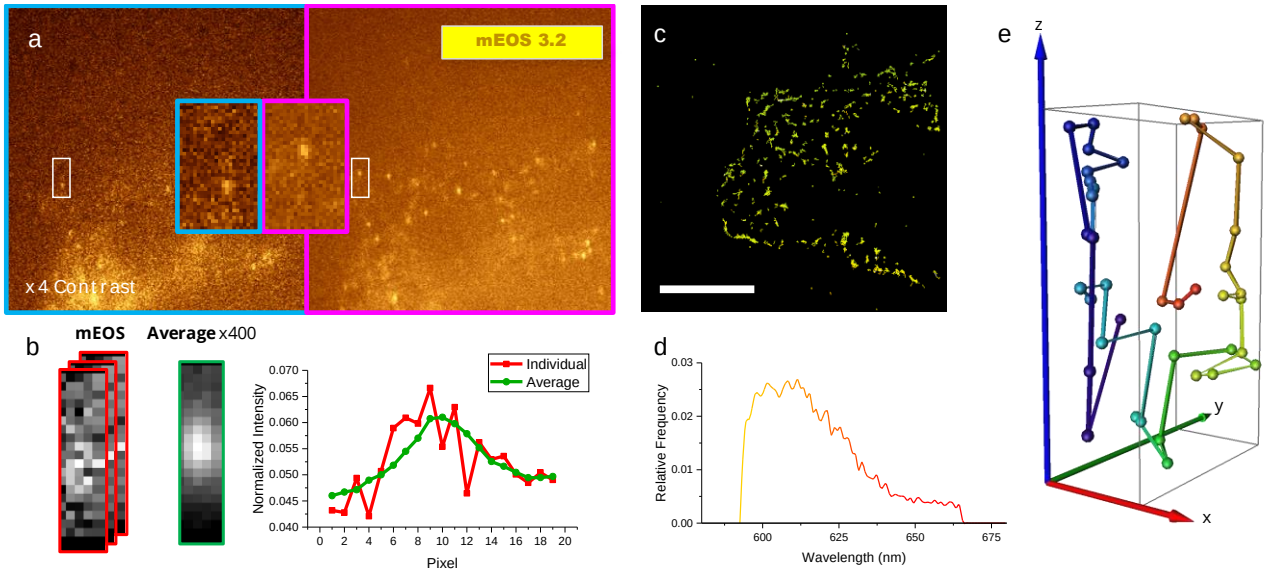

Figure 4.15: Talin-mEOS3.2 Tracking with Spectral Detection. (a) Individual activated mEOS molecules are detectable on the spectral channel (left, x4 contrast). **(b)** Averaging several hundred individual localizations enables fluorescent protein spectral imaging. **(c)** Wavelength-coded tracks reconstruction. Note the track homogeneity. **(d)** Wavelength histogram of localizations shows a peak spectral mean of 610nm with a variance of 16.5nm. **(e)** 3D reconstruction (Amira) of a single mEOS 3.2 trajectory color coded for time.

Talin-CTer-mEOS3.2 | Fibroblast Cells | 256px x 256px @ 50ms/frame

4.2.3.7 Dual-Color 2-Protein Simultaneous Tracking of Neurotransmitter Receptors in Live Neurons

While the previous proof of principle experiments in cultured cell lines provided validation the spectral tracking capabilities of the system, studying the diffusion of membrane-bound proteins in these simple systems is not always biologically relevant. In neuroscience, however, many questions about the functional roles and interactions of membrane proteins, in particular neurotransmitter receptors, remain unanswered. A primary goal when designing this spectrally resolved tracking system was compatibility with imaging of neuron cultures, which are much more sensitive to photodamage, imaging medium and temperate variations than cell line cultures like COS7 and HeLa.

In collaboration with Laurent Groc's team, we first verified the compatibility with embryonic rat cultured neurons by tagging two spectrally distinct quantum dots (QD655 and QD705) to the overexpressed Dopamine D1 receptor genetically tagged with CFP, a structurally similar GFP variant. The wavelength-coded reconstruction in **Figure 4.16**a shows the signal specificity to the transfected neurons, as well as the clear separation between spectral species.

Whereas in previous experiments a single protein type was tagged with several fluorescent species, we then applied our spectral single particle tracking system to track two different proteins in these hippocampal neuron cultures. The genetically-tagged NMDA glutamate receptor GluN1-Flag was co-expressed with D1-CFP, and each tagged with a spectrally distinct QD. **Figure 4.16**b shows a 3D reconstruction of a small region, color-coded for wavelength, demonstrating the necessity for 3D imaging when performing dual-color imaging.

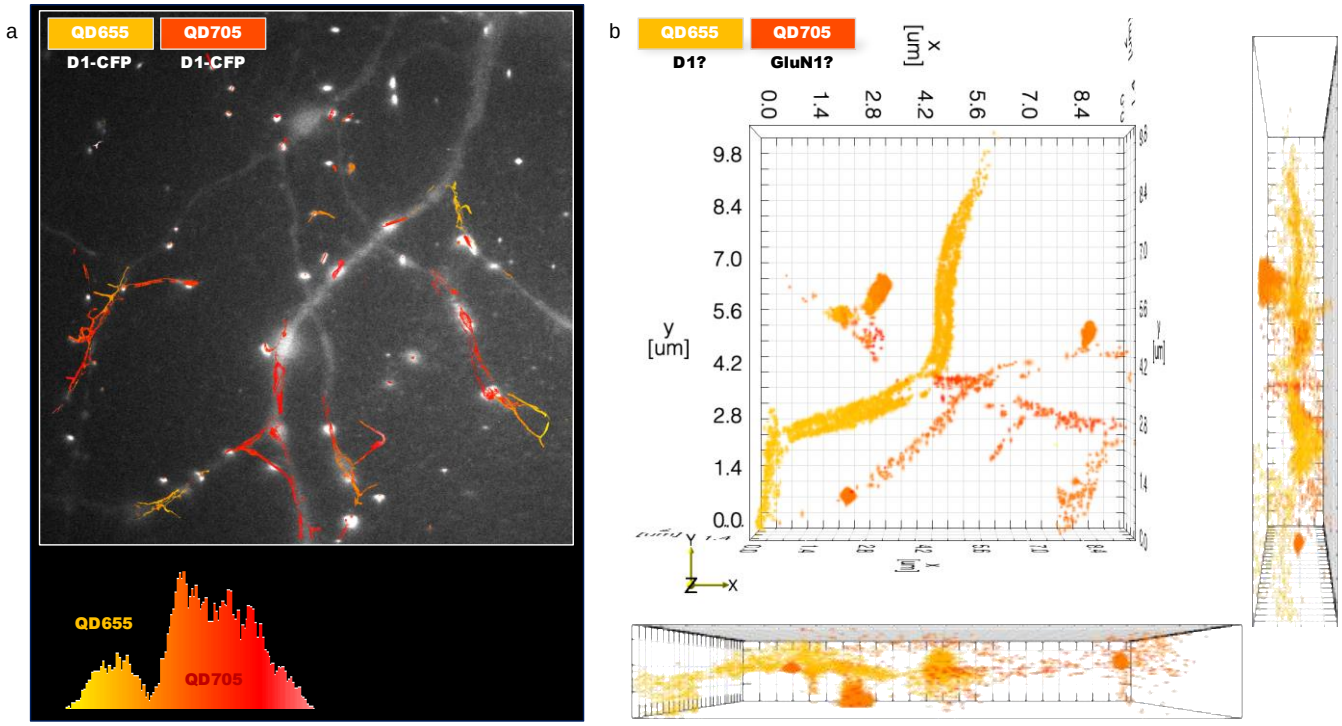

Figure 4.16 Simultaneous Dual-Color and Dual-Protein Tracking of Neurotransmitter Receptors in Live Neurons.(a) Wavelength-coded trajectory reconstruction of overexpressed dopamine receptor D1-CFP tagged with QD655 and QD705, demonstrating feasibility of the dual-objective technique for hippocampal neuron cultures. **(b)** 3D localization reconstruction (VISP)[94] of simultaneous imaging of D1-CFP and GluN1-Flag in hippocampal neuron cultures. The combination of 3D spatial information with multicolor imaging is essential for understanding molecular interaction.

Dopamine receptor D1 and NMDA glutamate receptor GluN1 in hippocampal neuron cultures. D1-CFP + Anti-GFP:QD705 and GluN1-Flag + Anti-Flag:QD655. 256x256 @ 50ms

Further 2-and 3-color 3D QD-SPT experiments in neuron cultures are ongoing. The primary difficulty in such experiments is specifically tagging 3 separate proteins of interest using conventional antibodies, as not all proteins have good quality commercially available antibodies. In the future, combining QD single particle tracking with concurrent structural SMLM imaging could provide interesting information regarding the cellular environment in which the proteins are diffusing.

Methods: Quantum Dot Immunolabeling for Dual-Color Neuron Tracking

Mixed neuron and microglia cell cultures were incubated with the primary antibody (anti-flag-mouse @ 1/1000 and anti-GFP-rabbit @ 1/1000) diluted in neurobasal medium from the dish for 10 min at 37°C (100 µl per coverslip). Cells were washed 4 times with warm, fresh neurobasal medium, incubated with quantum dots QD705 anti-mouse @1/50,000 and QD655 anti-rabbit @ 1/50,000 or QD705 anti-rabbit @1/50,000 and QD655 anti-mouse @1/50,000 for 10 minutes at 37°C (100 µl per coverslip), and washed 4 times. The samples were mounted in 50 µl of neurobasal

imaging media in the custom-designed dual-objective ludin mount described in section 4.2.1, and covered with a 22mm coverslip before being placed onto the microscope.

4.2.3.8 Other Applications: Photon Specificity

Single molecule localization microscopy, and fluorescence microscopy as a whole, benefits from the use of the photophysical process of fluorescence as a specific marker for the protein of interest. However, the cellular environment and imaging process induce noise that can result in false localizations that can be difficult to eliminate in conventional SMLM experiments. The dual-objective spectral imaging system proposed here can also help ensure that acquired photons are emitted from the specific fluorescent probe(s) desired.

A wide array of natively expressed cellular proteins are also capable of fluorescing, and localizing these autofluorescent proteins can cause specificity errors in super-resolution reconstructions. Thanks to spectral imaging, their very large autofluorescence emission spectrum can be filtered out from reconstructions. Furthermore, the ability to visualize this directly on the acquisition system allows verification of proper labeling.

When imaging fluorescent proteins or other low-signal fluorescent markers, a low segmentation threshold is used to separate the signal from sensor noise. A deleterious side effect of this low threshold is the possibility to accidentally localize just sensor noise. By requiring that the single molecule be detected on both cameras, this method can reject false localizations caused by low threshold or sensor noise.

4.3 SUMMARY AND PERSPECTIVES

Most conventional multicolor SMLM experiments are performed sequentially, requiring at least twice the imaging time and preventing the imaging of potentially interesting molecular interactions. While simultaneous imaging approaches do exist, they typically involve specific filtering optics for each fluorescent species being imaged, separating the detection path for each color onto a portion of a single imaging sensor, compromising the field of view and/or temporal resolution of imaging as well as the number of photons (hence the localization accuracy). The method presented in this chapter enables simultaneous multicolor SMLM imaging and tracking without spatiotemporal compromises by assigning a mean wavelength to each localized single molecule.

4.3.1 Expanding the Photon Budget with Spectral Dual-Objective Collection

By using a dual-objective configuration with concurrent imaging of a single focal plane on two separate detection paths, the wavelength is encoded as a relative lateral displacement by a dispersive prism in the spectral detection path. The use of two detection objectives ensures no compromises in spatial localization precision, sensitivity, temporal resolution, and field of view. We have demonstrated the proof of principle of the technique, its characterization with 5 spectrally separate quantum dot species, its application for 3-color simultaneous quantum dot tracking and 2-color simultaneous DNA-PAINT tracking, as well as the sensitivity for detection the wavelength of single fluorescent proteins.

4.3.2 Limitations of method

An important aspect to the development of a microscopy method with the goal to address important biological questions in routine, is a good understanding of its limitations and applicability. A few of these limitations, together with some potential solutions, are addressed here:

Biological Compatibility. While the spectral detection method is extensible to any dual-objective configuration and does not explicitly require the use of two microscopes, the mechanical implementation of our dual microscope configuration itself imposes some restrictions, notably requiring that the sample be sandwiched between two coverslips. The desire to use the Perfect Focus System for axial stabilization prevents the use of water dipping objectives, which could remove this restriction and allow for more complicated biological studies than simple cells grown on the coverslip surface.

Photodamage. Another strong concern for biological studies is the light dose delivered to the sample over the course of the imaging session. Using bright fluorescent probes with a broad excitation spectrum like quantum dots allows the use of a single laser wavelength at relatively low intensity for multicolor imaging. However, as previously noted, quantum dots are not accessible to all cellular compartments, and some SPT experiments opt for organic fluorophores or genetically encoded fluorescent proteins, both of which suffer from a much narrower excitation spectrum and require individual laser lines for excitation and increasing the overall power delivered to the biological sample.

Optical. The fundamental optical limits of the method reside in the ability of the spectral detection path to accurately localize single molecule fluorescence. Any optical aberrations in the spectral detection path quickly prevent single molecule localization. The first implementations used matching oil-immersion objectives on the spatial and spectral detection paths, but the spherical aberrations incurred from imaging through 30μm of water-based imaging medium quickly degraded the spectral signal. Using an index-matched water-immersion objective that reduces spherical aberrations, we have demonstrated the sensitivity to localize fluorescent proteins, but spectral imaging in complex media, like brain tissue slices, will require the implementation of adaptive optics in the spectral detection path (as outlined in section 3.3). Our dual-microscope system is capable of such a configuration, with mechanical mounts already in place for using the MicAO adaptive optics system on the upper microscope, but alignment of the adaptive optics path is extremely difficult in the inverted geometry. Further emphasis on optimizing this alignment procedure will greatly expand the biological applicability of the technique.

Software. The spectral displacement system presented here is fundamentally based on localizing the emission spectrum of singe molecules, which, unlike diffraction-limited point spread functions, are generally not radially symmetric and do not fit perfectly to a Gaussian model. Our approach uses a minimally dispersive prism to reduce the elongation of the spectrum across several pixels, but a more precise fitting method would take into account all of the spectral information acquired from the spectral detection path, and not simply a spectral mean given by the intensity centroid. Additionally, a precise field of view calibration is essential to accurate spectral detection and must be performed for each coverslip, ideally for each cell imaged. A more

advanced algorithm could theoretically refine the field of view transformation on a per-frame basis and eliminate the need for the additional FOV calibration step. Currently, lateral FOV displacements over the course of the image acquisition are compensated via fiducial marker tracking separately on each channel, however a per-frame FOV transform would be able to account for rotation and higher-order deformations that and enable more precise wavelength assignment.

4.3.3 Extending the Use of Spectrally Resolved Dual-Objective SMLM

The method presented here uses a prism to encode the emission spectrum of each individual molecule as a relative spatial displacement, which is calculated based on localization from two separate optical paths. However, the spectral information obtained is not fully exploited. For example, the current tracking algorithm temporally reconnects localizations strictly based on their spatial localizations, incorporating wavelength into the tracking algorithm could help disambiguate reconnection in certain applications, particularly in dense molecular environments. Integrating localization wavelength into the SR-Tesseler quantification software (section 2.4) could allow for direct multi-color cluster analysis, separating species based on the wavelength histogram.

Furthermore, the spectral detection path is currently only used to assign a single mean wavelength to each single molecule emission, but one could imagine encoding additional information into the spectral point spread function via PSF engineering. For example, once the wavelength has been assigned, it could be possible to deconvolve the spectral image with the known emission spectrum of the molecule, at which point the spatial information from the localization could be used as well. This additional PSF engineering on the spectral detection path could be used to encode 3D information in the spectral PSF with an astigmatic optical element and improve axial resolution, similar to the first dual-objective SMLM application [150].

In terms of biological applicability, a wealth of unique studies can benefit from this highly sensitive spectral detection. Chemical sensing using ratiometric or photoconvertible dyes allow sensing local pH[155] or other biological environmental factors as a function of the emitted wavelength, and this system's ability to accurately assign a continuum of wavelengths is ideally suited for these kinds of sensors. Additionally, single molecule FRET could be imaged concurrently and directly. Combining the spectral detection with our SR-HCS high content SMLM acquisition workflow may facilitate the discovery of new photoconvertible fluorescent proteins for single molecule imaging. Finally, using soSPIM for light sheet illumination on the lower microscope, could allow for spectrally resolved SMLM in complex biological environments, which is possible and straightforward thanks to the design of our 2-objective spectral microscope based on conventional microscopes.

Conclusion and Perspectives

Optical single molecule imaging has quickly revolutionized biology by allowing the characterization of the nanometer scale motion of proteins in their live environment. Still in its infancy, most SMLM is performed under the vestigial conditions of conventional fluorescence microscopy, without particular attention to details which can affect the nanometer scale localization of the fluorescent probe, namely labeling linker length and optical aberrations.

The work presented in this thesis addresses many of these limitations in an effort to expand single molecule localization microscopy towards quantitative nanoscale biology. One main idea recurred throughout my work: accurate protein labeling is a main factor preventing quantitative analysis. We tested new tools such as DNA-PAINT as a means of decoupling protein labeling density from fluorescence density in an effort to maximize the number accurate localizations. Unfortunately, current commercially available DNA-PAINT labeling kits are based on secondary antibodies that induce a large distance between the fluorescent probes and the protein of interest, making quantitative nanometer scale analysis difficult. Future advances to DNA-PAINT probes combined with small linker length ligands like anti-GFP nanobodies or monomeric streptavidin will allow for much more accurate protein localization, potentially allowing membrane-receptor resolution in dense proteins clusters. Furthermore, decoupling these labeling strategies from the single molecule imager concentration with DNA-PAINT may help to facilitate routine SMLM in protein dense environments like brain slices. Similarly, efficient fluorophore excitation is essential for accurate single molecule localization, and new promising tools like the single objective light sheet (soSPIM) allow for deep single molecule imaging, while new a technique based on using STED excitation called MINFLUX greatly reduces the amount of photons needed for localization by performing a triangulation process instead of directly fitting the PSF and allows for nanometer scale localization precision with only a few tens to hundred photons[156].

We demonstrated the application of an adaptive optics system for 3D imaging in such protein dense environments by correcting for depth-dependent optical aberrations. While the adaptive optics system implemented over the course of this thesis project was used to extend astigmatic imaging depth of field at the coverslip and enable 3D imaging up to 10 micrometers from the coverslip surface in brain tissue, difficulties in embedding fiducial markers in tissue prevented accurate wavefront correction. Software advances in the form of more robust and parameter-

free aberration correction algorithms based on phase diversity will simply the routine use of adaptive optics systems for SMLM, potentially obviating the need for fiducial markers by correcting aberrations based on individual blinking fluorophores. These steps towards simplifying adaptive optics are essential to its general adoption in routine SMLM imaging in complex biological environments like brain slices.

As discussed several times throughout this manuscript, resolution in single molecule localization imaging is critically linked to two main factors: the ability to densely label a given protein with a fluorescent molecule, and the precision with which this fluorescent proxy can be localized through the optical system. I would also propose that a third criteria limits SMLM resolution: accurate analysis of the acquired localization data. Improper localization analysis can lead to image artifacts that bias quantitative biological data and potentially prevent resolving the desired structure. I presented a tool we developed for analyzing single molecule localization data based on tessellation. The software package makes quantitative comparison between different biological conditions possible thanks to a segmentation threshold based on normalized localization density, making it robust to the variations in localization density prevalent in SMLM acquisitions. In its current form, however, this segmentation takes into account only the lateral position of the localization. Currently under development, 3D visualization and cluster analysis will help avoid projection artifacts. Incorporating qPAINT analysis could give access to true quantitative counting, as long as appropriate reference structures exist in the data set. Finally, colocalization tools based on overlapping Voronoi polygons will simplify the co-analysis of various proteins, which is currently a tedious task.

The most major contribution of this thesis is the development of a versatile microscope capable of simultaneously tracking multiple proteins in living cells. The system was designed to prevent compromises in spatiotemporal resolution and imaging field of view by adding a second detection objective capable of determining the wavelength of a single emitter with ~10-20nm resolution. It was constructed around two inverted microscope bodies to maximize mechanical stability and routine ease of use. The results presented in this manuscript represent the first proof of concept experiments of the technique and its application to multiple protein tracking in cell line and neuron cultures. We are continuing to use the system on a routine basis, collaborating with neurobiologists to exploit the systems spectral tracking capabilities and help uncover new protein interactions.

It is my hope that, in combination with future development in accurate and proximate protein labeling techniques, each of the steps detailed in this thesis may help in enabling routine quantitative single molecule imaging in complex biological samples.

APPENDIX 1 DEVELOPED SOFTWARE

ADAPTIVE OPTICS: MICAO METAMORPH PLUGIN

A primary deliverable of this thesis as part of the CIFRE collaboration with Imagine Optic was the development of a MicAO plugin for the MetaMorph acquisition environment that simplifies the user experience of using the adaptive optics system for routine imaging. The software was developed in Visual Basic .NET and C#, as required by the MetaMorph plugin environment.

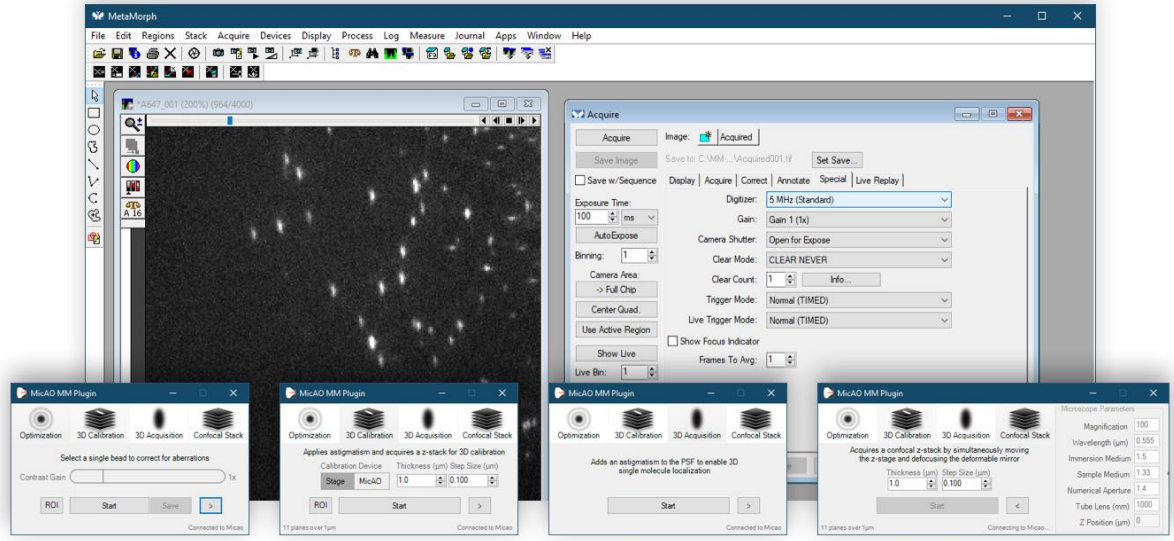

Figure A0.1: MetaMorph MicAO Plugin Modes of Function. Designed for operation in the MetaMorph acquisition environment, the MicAO Plugin for MetaMorph facilitates the user experience of adaptive optics for single molecule imaging. **Optimization** mode (left) allows for 1-click PSF optimization of common system aberrations using a 3N algorithm. **3D Calibration** mode (center left) allows the user to create an astigmatic Z-stack for calibration of axial assignment routines. The user may choose to perform the scan using a motorized z-stage, if available from MetaMorph, or by applying gradual defocus to the deformable mirror. The thickeness and stepsize can be directly modified by the user. **3D Acquisition** mode (center right) applies a constant astigmatism (defined in the MicAO software, typically 60nm RMS) for 3D imaging. Finally, the **Confocal Stack** mode (right) performs a Z-stack, applies aberrations as a function of depth according to a user-modifiable text file.

The plugin has 4 main modes of operation to facilitate common user AO functions organized into separate tabs: (1) PSF Optimization, (2) Astigmatic 3D Calibration, (3) Astigmatic 3D

Acquisition, and (4) Confocal Stack. The left-to-right workflow and minimal user-visible options are designed to optimize the user experience, prevent confusion, and allow non-specialists to operate the software once trained. Briefly, the Optimization mode performs a PSF optimization routine using the algorithm chosen in the MicAO software (3N algorithm by default), performing indirect wavefront sensing by iterating over a fixed number of Zernike modes (focus, spherical aberration, astigmatism, coma and trefoil by default) and optimizing based on an image quality metric (maximum intensity, by default). A contrast gain indicator directly in the plugin user interface visually indicates the success of the PSF optimization routine. This optimization routine takes ~10-15 seconds to complete, depending on image exposure time, and should be performed using a stable monochromatic fiducial marker at the coverslip surface. Ideally, the PSF optimization routine should only need to be performed once when the coverslip is mounted onto the microscope; however, thermal drift of the mirror membrane may cause variation in the PSF, so it is recommended to perform before each SMLM image acquisition.

For 3D imaging, a lookup table must be generated to associate astigmatic PSF deformation with axial position. The 3D calibration mode facilitates this by applying a fixed astigmatism and performing a Z-stack of desired thickness and step size centered around the current focal plane (typically, the optimal focus after PSF optimization). If the user has a motorized z-stage, they may choose to use it; otherwise, defocus will be applied gradually over the course of the acquisition to change the effective image focal plane. Once the 3D calibration stack has been generated and possibly verified using online localization tools (i.e. WaveTracer), the 3D acquisition mode can be initiated. This mode applies a constant astigmatism (60nm by default, but user configurable in the MicAO software) for 3D imaging.

Last, confocal stack mode creates an stack that applies depth-dependent aberrations based on a user-modifiable file. For example, depth-dependent focus can be added to compensate for the axial displacement of a mechanical stage, or depth-dependent spherical aberrations can be added based on a calibration curve.

It should be noted that the development of this software was a bit delayed due to some software complications. The large data sets generated in SMLM acquisition (~1-10 GB per SR image) mandate the use of a 64-bit acquisition environment, but the MicAO communication plugin was 32-bit only. A 32-bit intermediate interface layer was implemented (**Figure A0.2**) that can make DLL calls to the 32-bit DLL while simultaneously communicating with the 64-bit MicAO plugin via InterProcess Communication (IPC). Debugging this interface layer was complicated and time-consuming, as it necessitated exact type matching across 3 programming languages (VB.NET for the plugin, C# for the interface layer, and C++ for the MicAO DLL) in 32-bit and 64-bit environemnts.

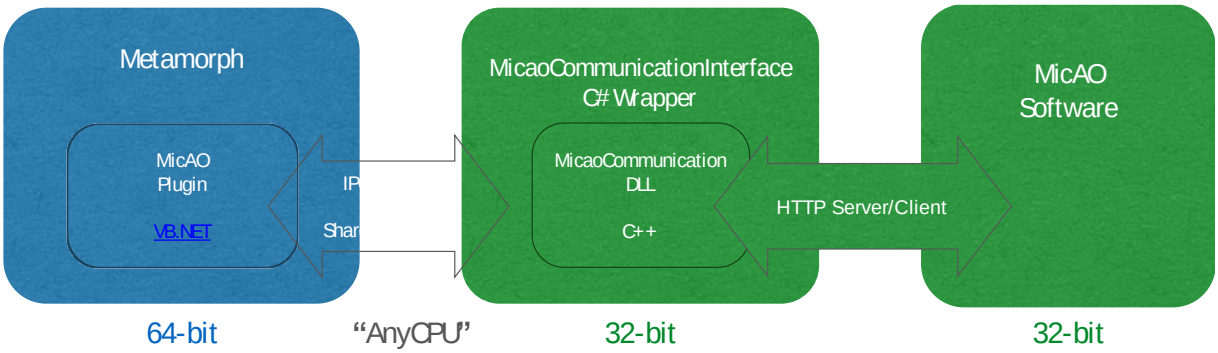

Figure Ao.2: MetaMorph MicAO Plugin Architecture. The large data sets in SMLM require the use of a 64-bit acquisition environment, preventing direct communication with the 32-bit DLLs of the MicAO interface. After quite a bit of research and development, a 32-bit interface layer was implemented that allows communication between with the 64-bit MetaMorph plugin via Inter Process Communication (IPC).

SPECTRAL LOCALIZATION: PALMTRACER METAMORPH PLUGIN

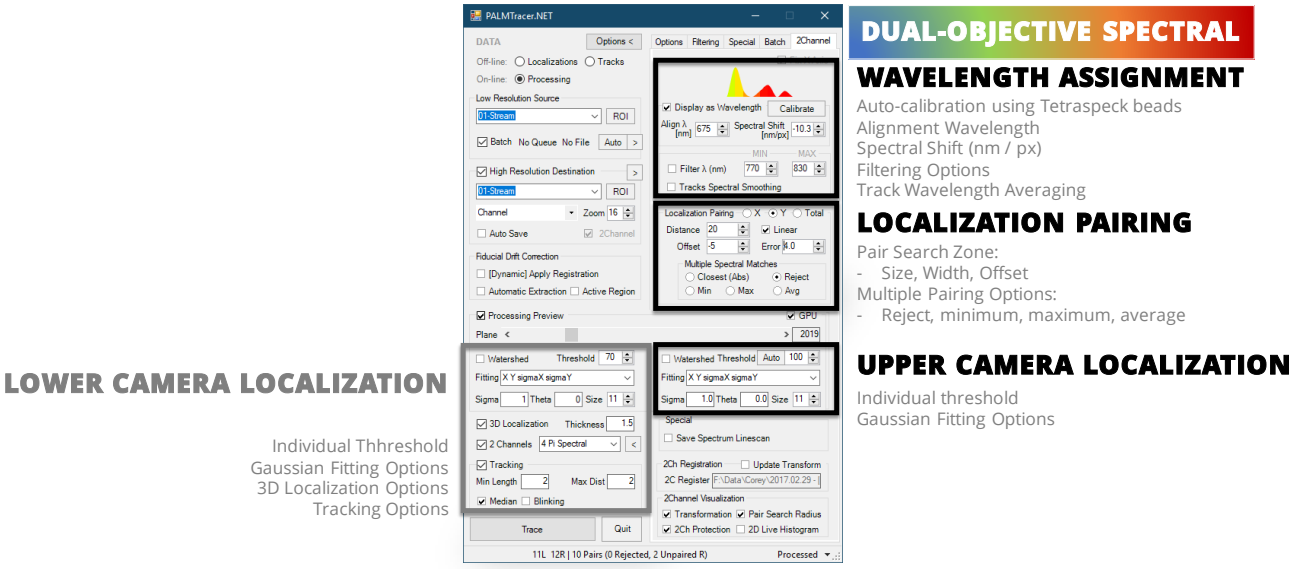

Figure A0.3 PALMTRACER.NET Software Interface for Dual-Objective Spectral Analysis. Our localization software was updated with a separate dual-channel localization pairing and spectral assignment module, designed as part of this thesis.

The analysis software used for localizing, pairing, and assigning wavelengths to single molecule images is an extension of the PALMTracer localization software initially developed by Jean-Baptiste Sibarita and runs in the MetaMorph software environment. Each of the imaging channels are independently analyzed with its own unique threshold, watershed, and Gaussian fit options, allowing efficient single molecule localization. Localization pairing options allow for radial or linear search options, the prior ideal for single-color imaging, while the linear search option is essential for high-density multicolor imaging. The pair distance to wavelength calibration allows for direct visualization of the assigned wavelength of each localization. A wealth of filtering options exists, the most relevant of which is a wavelength gating option that allows generation of a wide variety of visual representations (axial position, track number, plane, etc) for a specific wavelength gate or channel in conventional imaging terms. Finally, exports to common file formats like ThunderSTORM, VISP, and Amira facilitate the use of external software for more advance visualizations.

Wavelength to RGB Conversion

For wavelength-coded reconstructions, the pixel intensity is the wavelength of the localization in that pixel. True-color images, where the wavelength value is mapped to its perceived color, are 16-bit grayscale images where the pseudocolor lookup table is fixed to scale precisely over the range λ=[380nm, 780nm].

For visualization purposes while analyzing the SMLM stacks, it is useful to have a similar true-color wavelength coding for the region areas surrounding individual localizations. In this way, a quick glance at the current image being analyzed gives far more useful information than a wavelength histogram from a single frame. MetaMorph's regions support RGB color coding, thus

the wavelength value was converted to RGB values for region color-coding using the following algorithm:

```
If ((Wavelength >= 380) And (Wavelength < 440)) Then
Red = -(Wavelength - 440) / (440 - 380)
Green = 0.0
Blue = 1.0
ElseIf ((Wavelength >= 440) And (Wavelength < 490)) Then
Red = 0.0
Green = (Wavelength - 440) / (490 - 440)
Blue = 1.0
ElseIf ((Wavelength >= 490) And (Wavelength < 510)) Then
Red = 0.0
Green = 1.0
Blue = -(Wavelength - 510) / (510 - 490)
ElseIf ((Wavelength >= 510) And (Wavelength < 580)) Then
Red = (Wavelength - 510) / (580 - 510)
Green = 1.0
Blue = 0.0
ElseIf ((Wavelength >= 580) And (Wavelength < 645)) Then
Red = 1.0
Green = -(Wavelength - 645) / (645 - 580)
Blue = 0.0
ElseIf ((Wavelength >= 645) And (Wavelength < 781)) Then
Red = 1.0
Green = 0.0
Blue = 0.0
Else
Red = 0.0
Green = 0.0
Blue = 0.0
End If

If ((Wavelength >= 380) And (Wavelength < 420)) Then
factor = 0.3 + 0.7 * (Wavelength - 380) / (420 - 380)
ElseIf ((Wavelength >= 420) And (Wavelength < 701)) Then
factor = 1.0
ElseIf ((Wavelength >= 701) And (Wavelength < 781)) Then
factor = 0.3 + 0.7 * (780 - Wavelength) / (780 - 700)
Else
factor = 0.0
End If

R = Red * factor * 255
G =  Green * factor * 255
B =  Blue * factor * 255
```

CODE SNIPPET 1: Wavelength to RGB Conversion

Visual Basic .NET

APPENDIX 2 INTRODUCTION TO AMPA RECEPTOR NEUROBIOLOGY

Communication in the brain occurs between a vast array of interconnected neurons. Signal transmission occurs at the connection between two neurons, called a synapse, where a presynaptic neuron releases glutamate or other neurotransmitters that bind to their partner neurotransmitter receptors on the membrane of the postsynaptic neuron (Figure 0.). This binding process induces a conformational change in the receptor that opens an ion channel, depolarizing the membrane and initiating the propagation of the signal to the next neuron.

The spatial organization and dynamics of these postsynaptic neurotransmitters are essential to proper signal transmission between neurons. One such neurotransmitter receptor is the AMPA receptor (α-amino-3-hydroxy-5-methyl-4-isoxazolepropionic acid receptor), which is composed of 4 individual subunits (GluA1, GluA2, GluA4, etc) assembled to form a channel ~15nm in size. Combining a variety of super-resolution imaging techniques, *Nair et al*[24] with others demonstrated that these receptors assemble in clusters, called nanodomains, which are essential to proper synaptic transmission.

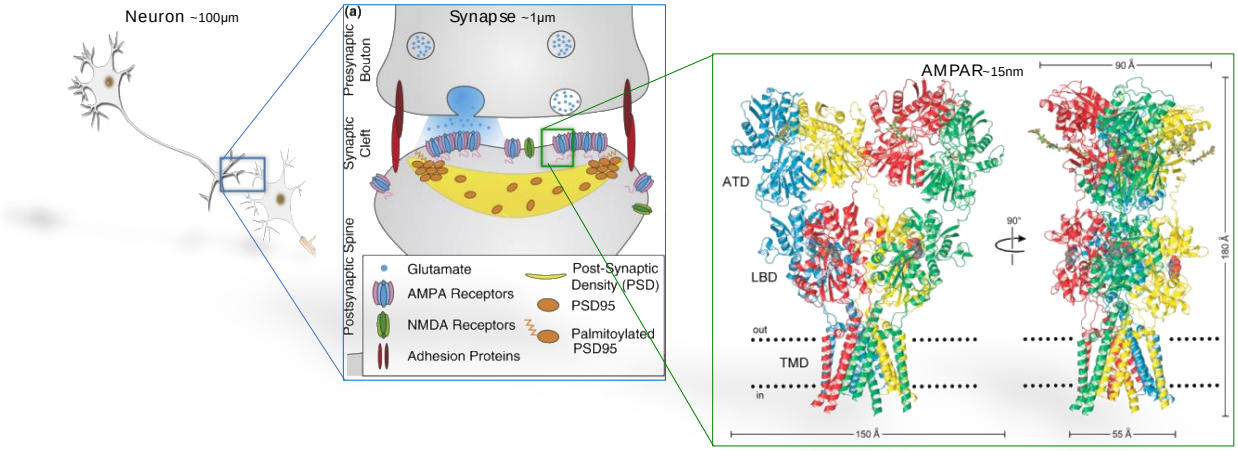

Figure 0.4: Nanometer-sized Post-synaptic AMPA Receptors serve as an inter-neuronal signal transduction mechanism. Communication between neurons occurs at the molecular level as the binding of presynaptically released glutamate to postsynaptic glutamate receptors, like AMPA or NMDA, through a process called synaptic transmission. While a host of synaptic proteins are involved in this process, the spatial distribution of the glutamate receptors and their alignment in the synaptic cleft are critical to proper signal transduction.

(b) Adapted from *Hosy et al*[108]

APPENDIX 3 dSTORM SAMPLE MOUNTING AND IMAGING BUFFERS

Fiducial Markers

Tetraspeck beads beads (1:1000 in 1X PBS) or nanodiamonds (1:100 in ultrapure water) Fiducial markers were incubated on coverslips prior to imaging. A drop of 100-150 µL of the diluted fiducial markers were placed on parafilm onto which the coverslip was flipped (cells face down), incubated for 5 minutes, and washed 3 times in PBS or ultrapure water.

Coverslip Mounting for dSTORM Imaing

Unless otherwise stated, 18mm diameter Ludin chambers were used for sample imaging. The coverslip was placed into the Ludin chamber and 1 mL of imaging buffer was added. A 22mm coverslip was placed on top of the chamber and parafilm was used to close the perfusion holes to minimize gas exchange during imaging.

Conventional Glox Buffer

The Glucose Oxidase buffer used for the majority of dSTORM experiments (unless otherwise noted) was aliquoted into c separate solutions. Before dSTORM imaging, aliquots were allowed to thaw and the final imaging buffer was mixed (1mL G, 125µL E, 125µL M). The pH was verified to be ~7.4-7.6 prior to imaging using pH paper.

(G) Glucose base solution (4°C)

- 45 mL of distilled water
- 5 mL Glycerine (Sigma)
- 5g Glucose (Sigma)

(E) Enzyme solution

- 100 µL Catalase (Sigma C100-0,1% w/v)
- 200 µL TCEP (1 mol/L) (Sigma C4706)
- 25 mL Glycerine
- 22.5 mL distilled water

- 1.25 mL KCl (1 M)
- 1 mL Tris-HCl pH 7.5 (1 mol/L)
- 50 mg Glucose oxidase

(M) MEA solution [1 M] stock solution

- 1,136 g of MEA-HCL (Sigma M6500) in 10 mL distilled water

Pyranose Oxidase Buffer

The Pyranose Oxidase buffer is identical to the GlOx buffer, replacing the enzyme Glucose Oxidase with Pyranose Oxidase that stabilizes the pH for several hours longer than GlOx.

COT Buffer

The COT buffer is identical to the buffer found in *Olivier et al.*[92] The solutions were prepared individually before imaging, as aliquoting seemed to decrease the benefits of the COT-based solution. The final solution was composed of 100 mM MEA, 2mM COT, 2.5 mM PCA and 50 nM PCD in a 75% glucerol-25%Tris-PBS solution.

BIBLIOGRAPHY

1. Abbe, E. Beiträge zur Theorie des Mikroskops und der mikroskopischen Wahrnehmung. *Archiv für mikroskopische Anatomie* **9,** 469–480 (1873).
2. S, L. R. F. R. XXXI. Investigations in optics, with special reference to the spectroscope. *The London, Edinburgh, and Dublin Philosophical Magazine and Journal of Science* **8,** 261–274 (2009).
3. Axelrod, D. & Burghardt, T. P. Total internal reflection fluorescence. *Annual review of ...* **13,** 247–268 (1984).
4. Tokunaga, M., Imamoto, N. & Sakata-Sogawa, K. Highly inclined thin illumination enables clear single-molecule imaging in cells. *Nature Methods* **5,** 159–161 (2008).
5. Denk, W., Strickler, J. H. & Webb, W. W. Two-photon laser scanning fluorescence microscopy. *Science* (1990).
6. Gustafsson, M. G. Surpassing the lateral resolution limit by a factor of two using structured illumination microscopy. *J Microsc* **198,** 82–87 (2000).
7. Hell, S. W. S. & Wichmann, J. J. Breaking the diffraction resolution limit by stimulated emission: stimulated-emission-depletion fluorescence microscopy. *Opt. Lett.* **19,** 780–782 (1994).
8. Betzig, E. *et al.* Imaging Intracellular Fluorescent Proteins at Nanometer Resolution. *Science* **313,** 1642–1645 (2006).
9. Rust, M., Bates, M. & Zhuang, X. Sub-diffraction-limit imaging by stochastic optical reconstruction microscopy (STORM). *Nature Methods* (2006).
10. Manley, S., Gillette, J., Patterson, G. & Shroff, H. High-density mapping of single-molecule trajectories with photoactivated localization microscopy. *Nature* (2008).
11. Rust, M. J., Bates, M. & Zhuang, X. Sub-diffraction-limit imaging by stochastic optical reconstruction microscopy (STORM). *Nature Methods* **3,** 793–796 (2006).
12. Heilemann, M. *et al.* Subdiffraction-resolution fluorescence imaging with conventional fluorescent probes. *Angewandte Chemie International Edition* **47,** 6172–6176 (2008).
13. Sharonov, A. & Hochstrasser, R. M. Wide-field subdiffraction imaging by accumulated binding of diffusing probes. **103,** 18911–18916 (2006).
14. Giannone, G. *et al.* Dynamic Superresolution Imaging of Endogenous Proteins on Living Cells at Ultra-High Density. *Biophysj* **99,** 1303–1310 (2010).
15. Fölling, J. *et al.* Fluorescence nanoscopy by ground-state depletion and single-molecule return. *Nature Methods* **5,** 943–945 (2008).
16. Lee, A., Tsekouras, K., Calderon, C., Bustamante, C. & Pressé, S. Unraveling the Thousand Word Picture: An Introduction to Super-Resolution Data Analysis. *Chemical Reviews* 1–55 (2017). doi:10.1021/acs.chemrev.6b00729
17. Ober, R. J., Ram, S. & Ward, E. S. Localization Accuracy in Single-Molecule Microscopy. *Biophysj* **86,** 1185–1200 (2004).
18. Thompson, R. E. *et al.* Precise nanometer localization analysis for individual fluorescent probes. *Biophysical Journal* **82,** 2775–2783 (2002).

19. Mortensen, K. I., Churchman, L. S., Spudich, J. A. & Flyvbjerg, H. Optimized localization analysis for single-molecule tracking and super-resolution microscopy. *Nature Methods* **7,** 377–381 (2010).
20. Barak, L. S. & Webb, W. W. Diffusion of low density lipoprotein-receptor complex on human fibroblasts. *The Journal of Cell Biology* **95,** 846–852 (1982).
21. Gelles, J., Schnapp, B. & Sheetz, M. Tracking kinesin-driven movements with nanometre-scale precision. *Nature* (1988).
22. Yildiz, A., Forkey, J. N., McKinney, S. A. & Ha, T. Myosin V walks hand-over-hand: single fluorophore imaging with 1.5-nm localization. *Science* (2003). doi:10.1126/science.1080885
23. Rossier, O. *et al.* Integrins β1 and β3 exhibit distinct dynamic nanoscale organizations inside focal adhesions. *Nature Cell Biology* **14,** 1057–1067 (2012).
24. Nair, D. *et al.* Super-Resolution Imaging Reveals That AMPA Receptors Inside Synapses Are Dynamically Organized in Nanodomains Regulated by PSD95. *J Neurosci* **33,** 13204–13224 (2013).
25. Constals, A. *et al.* Glutamate-Induced AMPA Receptor Desensitization Increases Their Mobility and Modulates Short-Term Plasticity through Unbinding from Stargazin. *NEURON* 1–18 (2015). doi:10.1016/j.neuron.2015.01.012
26. Cognet, L., Leduc, C. & Lounis, B. Advances in live-cell single-particle tracking and dynamic super-resolution imaging. *Current Opinion in Chemical Biology* (2014).
27. Sibarita, J.-B. High-density single-particle tracking: quantifying molecule organization and dynamics at the nanoscale. *Histochem Cell Biol* (2014). doi:10.1007/s00418-014-1214-1
28. Chenouard, N. *et al.* Objective comparison of particle tracking methods. *Nature Methods* **11,** 281–289 (2014).
29. Kusumi, A., Sako, Y. & Yamamoto, M. Confined lateral diffusion of membrane receptors as studied by single particle tracking (nanovid microscopy). Effects of calcium-induced differentiation in .... *Biophysical Journal* **65,** 2021–2040 (1993).
30. Deschout, H., Neyts, K. & Braeckmans, K. The influence of movement on the localization precision of sub-resolution particles in fluorescence microscopy. *J. Biophoton.* **5,** 97–109 (2011).
31. Izeddin, I. *et al.* Wavelet analysis for single molecule localization microscopy. **20,** 2081–2095 (2012).
32. Kechkar, A., Nair, D., Heilemann, M., Choquet, D. & Sibarita, J.-B. Real-Time Analysis and Visualization for Single-Molecule Based Super-Resolution Microscopy. **8,** e62918 (2013).
33. Li, D. *et al.* Extended-resolution structured illumination imaging of endocytic and cytoskeletal dynamics. *Science* **349,** aab3500–aab3500 (2015).
34. Deschout, H. *et al.* Precisely and accurately localizing single emitters in fluorescence microscopy. *Nature Methods* **11,** 253–266 (2014).
35. Endesfelder, U., Malkusch, S., Fricke, F. & Heilemann, M. A simple method to estimate the average localization precision of a single-molecule localization microscopy experiment. *Histochem Cell Biol* (2014). doi:10.1007/s00418-014-1192-3
36. Nieuwenhuizen, R., Lidke, K. A., Bates, M. & Puig, D. L. Measuring image resolution in optical nanoscopy. *Nature Methods* (2013).
37. Enderlein, J., Toprak, E. & Selvin, P. R. Polarization effect on position accuracy of fluorophore localization. *Opt. Express* **14,** 8111–8120 (2006).
38. Lew, M. D., Backlund, M. P. & Moerner, W. E. Rotational mobility of single molecules affects localization accuracy in super-resolution fluorescence microscopy. *Nano Lett* **13,** 3967–3972 (2013).
39. Lew, M. D. & Moerner, W. E. Azimuthal Polarization Filtering for Accurate, Precise, and Robust Single-Molecule Localization Microscopy. *Nano Lett* **14,** 6407–6413 (2014).
40. Backlund, M. P. *et al.* Removing orientation-induced localization biases in single-molecule microscopy using a broadband metasurface mask. (2016). doi:10.1038/nphoton.2016.93
41. COLOMB, W., CZERSKI, J., SAU, J. D. & SARKAR, S. K. Estimation of microscope drift using fluorescent nanodiamonds as fiducial markers. *J Microsc* **210,** 131–9 (2017).
42. Fu, C.-C. *et al.* Characterization and application of single fluorescent nanodiamonds as cellular biomarkers. *Proc Natl Acad Sci U S A* **104,** 727–732 (2007).
43. Yi, J. *et al.* madSTORM: a superresolution technique for large-scale multiplexing at single-molecule accuracy. *Mol. Biol. Cell* **27,** 3591–3600 (2016).

44. Bradac, C. *et al.* Observation and control of blinking nitrogen-vacancy centres in discrete nanodiamonds. *Nature Nanotech* **5,** 345–349 (2010).
45. Wang, Y. *et al.* Localization events-based sample drift correction for localization microscopy with redundant cross-correlation algorithm. *Opt. Express* **22,** 15982–15991 (2014).
46. Bon, P. *et al.* Three-dimensional nanometre localization of nanoparticles to enhance super-resolution microscopy. *Nature Communications* **6,** 7764 (2015).
47. Burgert, A., Letschert, S., Doose, S. & Sauer, M. Artifacts in single-molecule localization microscopy. *Histochem Cell Biol* (2015). doi:10.1007/s00418-015-1340-4
48. Baumgart, F. *et al.* Varying label density allows artifact-free analysis of membrane-protein nanoclusters. *Nature Methods* (2016). doi:10.1038/nmeth.3897
49. Huang, F. F., Schwartz, S. L. S., Byars, J. M. J. & Lidke, K. A. K. Simultaneous multiple-emitter fitting for single molecule super-resolution imaging. *Biomed. Opt. Express* **2,** 1377–1393 (2010).
50. Coons, A. Immunological Properties of an Antibody Containing a Fluorescent Group. *Proceedings of the Society for Experimental Biology and Medicine* **47,** 200–202 (1941).
51. Shimomura, O. & Johnson, F. H. Extraction, purification and properties of aequorin, a bioluminescent protein from the luminous hydromedusan, Aequorea. *Journal of cellular and …* (1962).
52. Ishino, Y., Shinagawa, H., Makino, K., Amemura, M. & Nakata, A. Nucleotide sequence of the iap gene, responsible for alkaline phosphatase isozyme conversion in Escherichia coli, and identification of the gene product. *J. Bacteriol.* **169,** 5429–5433 (1987).
53. Ries, J., Kaplan, C., Platonova, E., Eghlidi, H. & Ewers, H. A simple, versatile method for GFP-based super-resolution microscopy via nanobodies. *Nature Methods* (2012).
54. Los, G. V. *et al.* HaloTag: A Novel Protein Labeling Technology for Cell Imaging and Protein Analysis. *ACS chemical biology* **3,** 373–382 (2008).
55. Keppler, A. *et al.* A general method for the covalent labeling of fusion proteins with small molecules in vivo. *Nat Biotechnol* **21,** 86–89 (2002).
56. Hopp, T. P., Prickett, K. S., Price, V. L. & Libby, R. T. A short polypeptide marker sequence useful for recombinant protein identification and purification. *BIOTECHNOLOGY* **6,** 1204–1210 (1988).
57. Chamma, I. *et al.* Mapping the dynamics and nanoscale organization of synaptic adhesion proteins using monomeric streptavidin. *Nature Communications* **7,** 10773 (2016).
58. Whelan, D. R., Whelan, D. R., Bell, T. D. M. & Bell, T. Image artifacts in Single Molecule Localization Microscopy: why optimization of sample preparation protocols matters. *Sci Rep* **5,** 7924 (2015).
59. Benyair, R. & Lederkremer, G. Z. Common fixation–permeabilization methods cause artifactual localization of a type II transmembrane protein. *Microscopy* (2016). doi:10.1093/jmicro/dfw035
60. Leyton-Puig, D. *et al.* PFA fixation enables artifact-free super-resolution imaging of the actin cytoskeleton and associated proteins. *Biology Open* bio.019570 (2016). doi:10.1242/bio.019570
61. Dubertret, B., Skourides, P., Norris, D. J. & Noireaux, V. In vivo imaging of quantum dots encapsulated in phospholipid micelles. *Science* **298,** 1759–1762 (2002).
62. Biermann, B. *et al.* Imaging of molecular surface dynamics in brain slices using single-particle tracking. **5,** 1–10 (2014).
63. Varela, J. A. *et al.* Targeting neurotransmitter receptors with nanoparticles in vivo allows single-molecule tracking in acute brain slices. *Nature Communications* **7,** 1–10 (2016).
64. Hess, S. T., Girirajan, T. P. K. & Mason, M. D. Ultra-High Resolution Imaging by Fluorescence Photoactivation Localization Microscopy. *Biophysical Journal* **91,** 4258–4272 (2006).
65. Lippincott-Schwartz, J. & Patterson, G. H. Photoactivatable fluorescent proteins for diffraction-limited and super-resolution imaging. *Trends in Cell Biology* **19,** 555–565 (2009).
66. Patterson, G. H. A Photoactivatable GFP for Selective Photolabeling of Proteins and Cells. *Science* **297,** 1873–1877 (2002).
67. Subach, F. V. *et al.* Photoactivatable mCherry for high-resolution two-color fluorescence microscopy. *Nature Methods* **6,** 153–159 (2009).
68. Wiedenmann, J. *et al.* EosFP, a fluorescent marker protein with UV-inducible green-to-red fluorescence conversion. *Proc Natl Acad Sci U S A* **101,** 15905–15910 (2004).
69. Gurskaya, N. G. *et al.* Engineering of a monomeric green-to-red photoactivatable fluorescent

protein induced by blue light. *Nat Biotechnol* **24,** 461–465 (2006).
70. Dempsey, G. T. G., Vaughan, J. C. J., Chen, K. H. K., Bates, M. M. & Zhuang, X. X. Evaluation of fluorophores for optimal performance in localization-based super-resolution imaging. *Nature Methods* **8,** 1027–1036 (2011).
71. Giannone, G. *et al.* High-content super-resolution imaging of live cell by uPAINT. *Methods Mol Biol* **950,** 95–110 (2013).
72. Jungmann, R. *et al.* Multiplexed 3D cellular super-resolution imaging with DNA-PAINT and Exchange-PAINT. *Nature Methods* 1–9 (2014). doi:10.1038/nmeth.2835
73. Bates, M., Huang, B., Dempsey, G. T. & Zhuang, X. Multicolor Super-Resolution Imaging with Photo-Switchable Fluorescent Probes. *Science* **317,** 1749–1753 (2007).
74. Nahidiazar, L., Agronskaia, A. V., Broertjes, J., van den Broek, B. & Jalink, K. Optimizing Imaging Conditions for Demanding Multi-Color Super Resolution Localization Microscopy. *PLoS ONE* **11,** e0158884 (2016).
75. Agasti, S. S. *et al.* DNA-barcoded labeling probes for highly multiplexed Exchange-PAINT imaging. *Chemical Science* **8,** 3080–3091 (2017).
76. Kiuchi, T., Higuchi, M., Takamura, A., Maruoka, M. & Watanabe, N. Multitarget super-resolution microscopy with high-density labeling by exchangeable probes. *Nature Methods* **12,** 743–746 (2015).
77. Erdelyi, M. *et al.* Correcting chromatic offset in multicolor super-resolution localization microscopy. *Opt. Express* **21,** 10978 (2013).
78. Moerner, W. E. & Orrit, M. Illuminating single molecules in condensed matter. *Science* **283,** 1670–1676 (1999).
79. Douglass, K. M. *et al.* Super-resolution imaging of multiple cells by optimized flat-field epi-illumination. (2016). doi:10.1038/nphoton.2016.200
80. Deschamps, J., Rowald, A. & Ries, J. Efficient homogeneous illumination and optical sectioning for quantitative single-molecule localization microscopy. *Opt. Express* **24,** 28080 (2016).
81. Legant, W. R. *et al.* High-density three-dimensional localization microscopy across large volumes. *Nature Methods* (2016). doi:10.1038/nmeth.3797
82. Galland, R. *et al.* 3D high- and super-resolution imaging using single-objective SPIM. *Nature Methods* **12,** 641–644 (2015).
83. Huang, F., Hartwich, T., Rivera-Molina, F. & Lin, Y. Video-rate nanoscopy using sCMOS camera-specific single-molecule localization algorithms. *Nature Methods* (2013).
84. Lin, Y. *et al.* Quantifying and Optimizing Single-Molecule Switching Nanoscopy at High Speeds. *PLoS ONE* **10,** e0128135–20 (2015).
85. Fox-Roberts, P. *et al.* Local dimensionality determines imaging speed in localization microscopy. *Nature Communications* **8,** 1–10 (2017).
86. Fricke, F., Beaudouin, J., Eils, R. & Heilemann, M. One, two or three? Probing the stoichiometry of membrane proteins by single-molecule localization microscopy. *Sci Rep* **5,** 14072 (2015).
87. Hummer, G., Fricke, F. & Heilemann, M. Model-independent counting of molecules in single-molecule localization microscopy. *Mol. Biol. Cell* (2016). doi:10.1091/mbc.E16-07-0525
88. Heilemann, M., Fricke, F., Karathanasis, C. & Hummer, G. Molecule counts in localization microscopy with organic fluorophores. *ChemPhysChem* 1–19 (2017). doi:10.1002/cphc.201601425
89. Nicovich, P. R., Owen, D. M. & Gaus, K. Turning single-molecule localization microscopy into a quantitative bioanalytical tool. *Nat Protoc* **12,** 453–460 (2017).
90. Strale, P.-O. *et al.* Multiprotein Printing by Light-Induced Molecular Adsorption. *Adv. Mater. Weinheim* **28,** 2024–2029 (2016).
91. Ovesný, M., Křížek, P., Borkovec, J., Svindrych, Z. & Hagen, G. M. ThunderSTORM: a comprehensive ImageJ plug-in for PALM and STORM data analysis and super-resolution imaging. *Bioinformatics* **30,** 2389–2390 (2014).
92. Olivier, N., Keller, D., Gönczy, P. & Manley, S. Resolution Doubling in 3D-STORM Imaging through Improved Buffers. *PLoS ONE* **8,** e69004 (2013).
93. Levet, F. *et al.* SR-Tesseler: a method to segment and quantify localization-based super-resolution microscopy data. *Nature Methods* **12,** 1065–1071 (2015).
94. Beheiry, el, M. E., Beheiry, el, M. & Dahan, M. ViSP: representing single-particle localizations in

three dimensions. *Nature Methods* **10,** 689–690 (2013).
95. Steinhauer, C., Jungmann, R., Sobey, T. L., Simmel, F. C. & Tinnefeld, P. DNA origami as a nanoscopic ruler for super-resolution microscopy. *Angewandte Chemie International Edition* **48,** 8870–8873 (2009).
96. Schnitzbauer, J., Strauss, M. T., Schlichthaerle, T., Schueder, F. & Jungmann, R. Super-resolution microscopy with DNA-PAINT. *Nat Protoc* **12,** 1198–1228 (2017).
97. Schlichthaerle, T., Strauss, M. T., Schueder, F., Woehrstein, J. B. & Jungmann, R. DNA nanotechnology and fluorescence applications. *Current Opinion in Biotechnology* **39,** 41–47 (2016).
98. Schmied, J. J. *et al.* DNA Origami Nanopillars as Standards for Three-Dimensional Superresolution Microscopy. *Nano Lett* **13,** 781–785 (2013).
99. Arant, R. J. & Ulbrich, M. H. Deciphering the Subunit Composition of Multimeric Proteins by Counting Photobleaching Steps. *ChemPhysChem* **15,** 600–605 (2014).
100. Ulbrich, M. H. & Isacoff, E. Y. Subunit counting in membrane-bound proteins. *Nature Methods* (2007). doi:10.1038/nmeth1024
101. Patrizio, A. & Specht, C. G. Counting numbers of synaptic proteins: absolute quantification and single molecule imaging techniques. *Neurophotonics* **3,** 041805 (2016).
102. Hastie, P. *et al.* AMPA receptor/TARP stoichiometry visualized by single-molecule subunit counting. *Proc Natl Acad Sci U S A* – (2013). doi:10.1073/pnas.1218765110
103. Jungmann, R. *et al.* Quantitative super- resolution imaging with qPaint. *Nature Methods* 1–8 (2016). doi:10.1038/nmeth.3804
104. Chamma, I., Rossier, O., Giannone, G., Thoumine, O. & Sainlos, M. Optimized labeling of membrane proteins for applications to super-resolution imaging in confined cellular environments using monomeric streptavidin. *Nat Protoc* **12,** 748–763 (2017).
105. Andronov, L., Orlov, I., Lutz, Y., Vonesch, J.-L. & Klaholz, B. P. ClusterViSu, a method for clustering of protein complexes by Voronoi tessellation in super- resolution microscopy. *Sci Rep* **6,** 1–9 (2016).
106. Pageon, S. V., Nicovich, P. R., Mollazade, M., Tabarin, T. & Gaus, K. Clus-DoC: A combined cluster detection and colocalization analysis for single-molecule localization microscopy data. *Mol. Biol. Cell* (2016). doi:10.1091/mbc.E16-07-0478
107. Dai, M., Jungmann, R. & Yin, P. Optical imaging of individual biomolecules in densely packed clusters. *Nature Nanotech* (2016). doi:10.1038/nnano.2016.95
108. Hosy, E., Butler, C. & Sibarita, J.-B. Organization and dynamics of AMPA receptors inside synapses—nano-organization of AMPA receptors and main synaptic scaffolding proteins revealed by super-resolution imaging. *Current Opinion in Chemical Biology* **20,** 120–126 (2014).
109. Speidel, M., Jonáš, A. & Florin, E. L. Three-dimensional tracking of fluorescent nanoparticles with subnanometer precision by use of off-focus imaging. *Opt. Lett.* **28,** 69 (2003).
110. Toprak, E., Balci, H., Blehm, B. H. & Selvin, P. R. Three-Dimensional Particle Tracking via Bifocal Imaging. *Nano Lett* **7,** 2043–2045 (2007).
111. Juette, M. F. *et al.* Three-dimensional sub–100 nm resolution fluorescence microscopy of thick samples. *Nature Methods* **5,** 527–529 (2008).
112. Hajj, B. *et al.* Whole-cell, multicolor superresolution imaging using volumetric multifocus microscopy. *Proc Natl Acad Sci U S A* 201412396 (2014). doi:10.1073/pnas.1412396111
113. Sancataldo, G. *et al.* Three-dimensional multiple-particle tracking with nanometric precision over tunable axial ranges. *Optica* **4,** 367–7 (2017).
114. Bourg, N. *et al.* Direct optical nanoscopy with axially localized detection. *Nature Photonics* (2015). doi:10.1038/nphoton.2015.132
115. Deschamps, J., Mund, M. & Ries, J. 3D superresolution microscopy by supercritical angle detection. *Opt. Express* **22,** 29081–29091 (2014).
116. Shtengel, G. & Galbraith, J. Interferometric fluorescent super-resolution microscopy resolves 3D cellular ultrastructure. in 1–6 (2009).
117. Aquino, D. *et al.* Two-color nanoscopy of three-dimensional volumes by 4Pi detection of stochastically switched fluorophores. *Nature Methods* **8,** 353–359 (2011).
118. Beheiry, M. E. *et al.* Accessing the third dimension in localization-based super-resolution

microscopy. *Phys. Chem. Chem. Phys.* **16,** 16340–16348 (2014).
119. Backer, A. S. & Moerner, W. E. Extending Single-Molecule Microscopy Using Optical Fourier Processing. *J Phys Chem B* **118,** 8313–8329 (2014).
120. Pavani, S. & Piestun, R. Three dimensional tracking of fluorescent microparticles using a photon-limited double-helix response system. *Opt. Express* **16,** 22048–22057 (2008).
121. Shechtman, Y., Sahl, S. J., Backer, A. S. & Moerner, W. E. Optimal Point Spread Function Design for 3D Imaging. *Phys Rev Lett* (2014).
122. Shechtman, Y., Weiss, L. E., Backer, A. S. & Sahl, S. J. Precise Three-Dimensional Scan-Free Multiple-Particle Tracking over Large Axial Ranges with Tetrapod Point Spread Functions. *Nano Lett* **15,** 4194–4199 (2015).
123. Kao, H. P. & Verkman, A. S. Tracking of single fluorescent particles in three dimensions: use of cylindrical optics to encode particle position. *Biophysical Journal* **67,** 1291–1300 (1994).
124. Huang, B., Wang, W., Bates, M. & Zhuang, X. Three-Dimensional Super-Resolution Imaging by Stochastic Optical Reconstruction Microscopy. *Science* **319,** 810–813 (2008).
125. Mlodzianoski, M. J., Juette, M. F. & Beane, G. L. Experimental characterization of 3D localization techniques for particle-tracking and super-resolution microscopy. *Opt. Express* **17,** 8264–8277 (2009).
126. Huang, B., Jones, S. A., Brandenburg, B. & Zhuang, X. Whole-cell 3D STORM reveals interactions between cellular structures with nanometer-scale resolution. *Nature Methods* (2008).
127. Diezmann, A. V., Lee, M. Y., Lew, M. D. & Moerner, W. E. Correcting field-dependent aberrations with nanoscale accuracy in three-dimensional single-molecule localization microscopy. *Optica* **2,** 985–9 (2015).
128. McGorty, R., Schnitzbauer, J., Zhang, W. & Huang, B. Correction of depth-dependent aberrations in 3D single-molecule localization and super-resolution microscopy. *Opt. Lett.* **39,** 275–278 (2014).
129. Fernandez, E. J. *et al.* Adaptive optics with a magnetic deformable mirror: applications in the human eye. *Opt. Express* **14,** 8900–8917 (2006).
130. Booth, M., Andrade, D., Burke, D., Patton, B. & Zurauskas, M. Aberrations and adaptive optics in super-resolution microscopy. *Microscopy* **64,** 251–261 (2015).
131. Coles, B. C., Webb, S. & Schwartz, N. Characterisation of the effects of optical aberrations in single molecule techniques. *Biomedical Optics …* (2016). doi:10.1364/BOE.7.001755
132. Izeddin, I. *et al.* PSF shaping using adaptive optics for three-dimensional single-molecule super-resolution imaging and tracking. *Opt. Express* **20,** 4957–4967 (2012).
133. Booth, M. J. Adaptive optics in microscopy. *Philosophical Transactions of the Royal Society A: Mathematical, Physical and Engineering Sciences* **365,** 2829–2843 (2007).
134. F ZERNIKE, von. Beugungstheorie des schneidenver-fahrens und seiner verbesserten form, der phasenkontrastmethode. *Physica* **1,** 689–704 (1934).
135. Zhu, L., Sun, P. C., Bartsch, D. U. & Freeman, W. R. Wave-front generation of Zernike polynomial modes with a micromachined membrane deformable mirror. *Appl. Opt.* **38,** 6019–6026 (1999).
136. Cha, J. W., Ballesta, J. & So, P. T. C. Shack-Hartmann wavefront-sensor-based adaptive optics system for multiphoton microscopy. *J. Biomed. Opt.* **15,** 046022 (2010).
137. Azucena, O., Crest, J., Cao, J., Sullivan, W. & Kner, P. Wavefront aberration measurements and corrections through thick tissue using fluorescent microsphere reference beacons. *Opt. Express* **18,** 17521–17532 (2010).
138. Thayil, A. & Booth, M. J. Self calibration of sensorless adaptive optical microscopes. *JEOS:RP* **6,** 11045–8 (2011).
139. Booth, M. J. & Wilson, T. Refractive-index-mismatch induced aberrations in single-photon and two-photon microscopy and the use of aberration correction. *J. Biomed. Opt.* **6,** 266 (2001).
140. Kam, Z., Kner, P., Agard, D. & Sedat, J. W. Modelling the application of adaptive optics to wide-field microscope live imaging. *J Microsc* (2007).
141. Booth, M. J. Adaptive optical microscopy: the ongoing quest for a perfect image. *Light Sci Appl* **3,** e165–7 (2014).
142. Dani, A., Huang, B., Bergan, J., Dulac, C. & Zhuang, X. Superresolution Imaging of Chemical Synapses in the Brain. *NEURON* **68,** 843–856 (2010).

143. Tang, A.-H. *et al.* A trans-synaptic nanocolumn aligns neurotransmitter release to receptors. (2016). doi:10.1038/nature19058
144. Schwertner, M. Measurement of specimen-induced aberrations of biological samples using phase stepping interferometry. *J Microsc* **213,** 11–19 (2004).
145. Schwertner, M., Booth, M. J. & Wilson, T. Specimen-induced distortions in light microscopy. *J Microsc* **228,** 97–102 (2007).
146. Burke, D. *et al.* Adaptive optics correction of specimen-induced aberrations in single-molecule switching microscopy. *Optica* **2,** 177–185 (2015).
147. Tehrani, K. F., Xu, J., Zhang, Y., Shen, P. & Kner, P. Adaptive optics stochastic optical reconstruction microscopy (AO-STORM) using a genetic algorithm. *Opt. Express* **23,** 13677–16 (2015).
148. Huang, F. *et al.* Ultra-High Resolution 3D Imaging of Whole Cells. *Cell* (2016). doi:10.1016/j.cell.2016.06.016
149. Ram, S., Prabhat, P., Ward, E. S. & Ober, R. J. Improved single particle localization accuracy with dual objective multifocal plane microscopy. *Opt. Express* **17,** 6881 (2009).
150. Xu, K., Babcock, H. P. & Zhuang, X. Dual-objective STORM reveals three-dimensional filament organization in the actin cytoskeleton. *Nature Methods* **9,** 185–188 (2012).
151. Zhang, Z. *et al.* Ultrahigh-throughput single-molecule spectroscopy and spectrally resolved super-resolution microscopy. *Nature Methods* **12,** 935–938 (2015).
152. Cutler, P. J. *et al.* Multi-Color Quantum Dot Tracking Using a High-Speed Hyperspectral Line-Scanning Microscope. *PLoS ONE* **8,** e64320–14 (2013).
153. Labrecque, S. *et al.* Hyperspectral multiplex single-particle tracking of different receptor subtypes labeled with quantum dots in live neurons. *J. Biomed. Opt.* **21,** 46008 (2016).
154. Shechtman, Y., Weiss, L. E., Backer, A. S., Lee, M. Y. & Moerner, W. E. Multicolour localization microscopy by point-spread-function engineering. (2016). doi:10.1038/nphoton.2016.137
155. Shi, X., Lim, J. & Ha, T. Acidification of the Oxygen Scavenging System in Single-Molecule Fluorescence Studies: In Situ Sensing with a Ratiometric Dual-Emission Probe. *Anal. Chem.* **82,** 6132–6138 (2010).
156. Balzarotti, F. *et al.* Nanometer resolution imaging and tracking of fluorescent molecules with minimal photon fluxes. *Science* (2016).

Table of Figures

Publications

2014

Organization and dynamics of AMPA receptors inside synapses—nano-organization of AMPA receptors and main synaptic scaffolding proteins revealed by super-resolution imaging
E Hosy, C Butler, JB Sibarita
Current opinion in chemical biology 20, 120-126

2015

SR-Tesseler: a method to segment and quantify localization-based super-resolution microscopy data
F Levet, E Hosy, A Kechkar, C Butler, A Beghin, D Choquet, JB Sibarita
Nature methods 12 (11), 1065-1071

2016

Mapping the dynamics and nanoscale organization of synaptic adhesion proteins using monomeric streptavidin
Ingrid Chamma, Mathieu Letellier, Corey Butler, Béatrice Tessier, Kok-Hong Lim, Isabel Gauthereau, Daniel Choquet, Jean-Baptiste Sibarita, Sheldon Park, Matthieu Sainlos, Olivier Thoumine
Nature communications 7

Available online at www.sciencedirect.com

ScienceDirect

Current Opinion in Chemical Biology

Organization and dynamics of AMPA receptors inside synapses—nano-organization of AMPA receptors and main synaptic scaffolding proteins revealed by super-resolution imaging

Eric Hosy[1,2], Corey Butler[1,2,3] and Jean-Baptiste Sibarita[1,2]

Progresses in microscopy have often led to major discoveries in neuroscience, and the recent advent of super-resolution microscopy is no exception. In this review, we will show how imaging has advanced our modern vision of synaptic function. More particularly, we will emphasize how novel nanoscopy techniques have helped in deciphering the organization of post-synaptic proteins, offering new insight into the mechanism of synaptic transmission.

Addresses
[1] University of Bordeaux, Interdisciplinary Institute for Neuroscience, UMR 5297, F-33000 Bordeaux, France
[2] CNRS, UMR 5297, F-33000 Bordeaux, France
[3] Imagine Optic, 18 rue Charles de Gaulle, 91400 Orsay, France

Corresponding author: Sibarita, Jean-Baptiste (jean-baptiste.sibarita@u-bordeaux2.fr)

Current Opinion in Chemical Biology 2014, **20**:120–126

This review comes from a themed issue on **Molecular imaging**

Edited by **Christian Eggeling** and **Mike Heilemann**

1367-5931/$ – see front matter,

http://dx.doi.org/10.1016/j.cbpa.2014.05.017

Introduction

Historically, new developments in microscopy have triggered novel concepts in biology. This is particularly evident in the field of neuroscience, where neuronal cells are composed of thin and dense structures ranging from micrometers to tens of nanometers in size.

This relationship between imaging techniques and neuroscience started in the early 20th century with the controversy between Ramon y Cajal and Golgi over the structure of the neuronal network. Only new silver-based cellular labeling developed by Golgi allowed Cajal to demonstrate with microscopy (i) that neurons are independent and delimitated cells and (ii) that the junctions between neurons, called synapses, are physically separated. In the 1950s, the intimate details of synaptic structure were finally revealed by applying electron microscopy to neurons [1]. Subsequently, the discovery of the electrical component of synaptic transmission by patch and voltage clamp techniques and the development of molecular biology completed the current vision of the electrochemical synapse: the pre-synaptic element triggers fast calcium dependent release of neurotransmitter vesicles, and the post-synapse accumulates ionic and metabotropic receptors of these neurotransmitters. This static vision of the synapse with neurotransmitter receptors anchored at the post-synapse was sufficient to sketch a functional model of the synapse.

In the 1970s, new imaging techniques capable of capturing live cell dynamics, such as fluorescence recovery after photobleaching (FRAP) and single particle tracking (SPT), added the idea that these membrane proteins are not static at the surface but show a fast diffusive behavior [2•]. The principle of the SPT technique relies on sparse labeling of individual proteins and follows their movement in real-time. Analysis of this motion allows determining protein behavior in different subcellular environments, reflecting interactions with various molecular complexes. In the 1990s, improvements to imaging setups, charge-coupled device (CCD) cameras, image analysis and engineering of smaller and photostable fluorescent probes like quantum dots (QD), allowed more efficient particle detection [3]. While traditional bulk microscopy techniques were limited in resolution to about 250 nm due to diffraction, SPT imaging enabled monitoring protein motion with nanometric localization using dedicated image analysis [4–7].

The application of SPT techniques to neuroscience gave access to a better understanding of the role of various proteins in synaptic transmission. The first studies focused particularly on the family of glutamate receptors, which are most notably composed of the NMDA receptors responsible for calcium entry inside the synapse and the AMPA receptors responsible for fast synaptic transmission [8]. These experiments revealed that AMPA receptors present two different motions, alternating between states of transient immobility and high mobility. The main conclusions were that (i) AMPA receptors containing the GluA2 subunit stop reversibly at the synaptic site, (ii) during neuronal maturation, the stationary periods of these receptors increase in frequency and length and (iii) a rise in calcium favors local receptor immobilization.

These *princeps* single particle tracking experiments paved way to neurotransmitter receptor mobility characterization, ushering in a new vision of the synapse by identifying components of molecular complexes and unpredicted roles of receptor motion. Nonexhaustively, applications of the SPT technique demonstrated that (i) AMPARs are attached to the postsynaptic density (PSD), and more particularly to a primary scaffolding protein PSD95, through their main associated protein named stargazin [9], (ii) the postsynaptic adhesion protein neuroligin tends to aggregate AMPARs through PSD95 scaffolding protein recruitment [10,11], and (iii) Ncadherin, a pre-synaptic adhesion protein, can trans-synaptically interact with the extracellular domain of AMPARs to limit their diffusion [12] (Fig. 1a). Additional QD-based SPT experiments coupled with electrophysiology explained why synapses can sustain a stimulation frequency higher than predicted by showing that synaptic receptors exchange rapidly within tens of milliseconds [10].

More generally, the incorporation of membrane receptor motion into the synaptic paradigm further tuned the understanding of synaptic transmission. These QD-based SPT experiments have now been extended to a large spectrum of studies, demonstrating various relationships between protein motion and physiology [13–16].

Super-resolution microscopy and first applications to studying postsynaptic molecule organization

Traditional single particle techniques, based on non-renewed low probe concentration, provided between ten and several hundred trajectories per cell. This is insufficient to gather enough temporal and spatial information to map the entire protein organization, which is essential to deciphering its exact physiological role. During the last 15 years, new super-resolution light microscopy techniques have been developed to circumvent the diffraction limit.

Figure 1

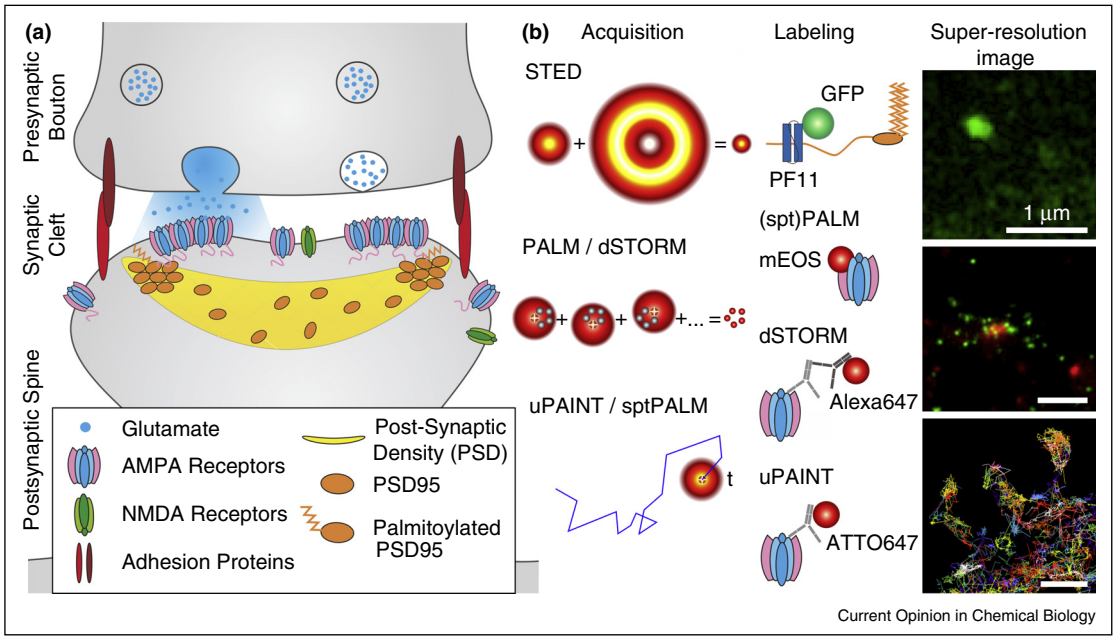

Synaptic transmission, post-synaptic molecule organization and super-resolution imaging techniques. **(a)** The current view of the glutamatergic synapse. Neurotransmitters such as glutamate (blue) are released from pre-synaptic vesicles and diffuse freely across the synaptic cleft, creating a concentration gradient bathing the post-synapse. Specific receptors to neurotransmitter (here the glutamatergic AMPA type receptor) accumulate in postsynaptic subsynaptic domains in the vicinity of the release site. Binding of glutamate to AMPA receptors activate them and trigger the synaptic current. The palmitoylated form of the postsynaptic scaffolding protein PSD-95 analogously groups in nanoclusters inside the postsynaptic density and are a key organizer of AMPA receptors. **(b)** Super-resolution imaging methodologies. (Top) STED imaging [17,18] combines two lasers of different wavelengths to engineer a sub-diffraction-limited effective excitation point spread function (PSF), which is then scanned cross the sample of interest. Proteins of interest can be labeled by intrabodies fused with fluorescent proteins, for example PF11-GFP targeting palmitoylated PSD95 in the dendritic spine. (Center) Localization based techniques rely on the activation of a sparse subset of densely labeled fluorescent markers to provide precise localizations of single molecules. In PALM [22,23], a 405 nm laser is used to activate genetically encoded photoactivatable fluorescent proteins like mEOS. In dSTORM [24–26,27••], the sample is imaged in a specific medium that promotes the stochastic blinking of organic fluorophores coupled to antibody labels. Using spectrally separated fluorophores, nanometer level protein co-organization can be visualized, for example that AMPARs (red) colocalize with PSD95 (green) only at the extremities of PSD95 nanoclusters. (Bottom) High-density single particle tracking methods following the localization of single particles over time, making it possible to quantify live protein dynamics. sptPALM [32] uses genetically encoded fluorescent proteins with excitation light being adjusted to obtain trajectories before photobleaching, whereas uPAINT [34] allows tracking of endogenous proteins via stochastic live antibody labeling. Super-resolution images on the right column represent PSD95 (top), GluA1/PSD95 (middle) and GluA1 (bottom) acquired with STED, 2 color dSTORM and sptPALM respectively; extracted from [45•,46•].

Amongst them, stimulated emission depletion (STED) microscopy [17,18], structured illumination microscopy (SIM), [19–21] and single-molecule localization techniques, such as PALM [22,23] and STORM [24–26,27••], allow the observation of biological samples with 10–100 nm spatial resolution, providing unprecedented insight into molecular organization. Single molecule-based super-resolution techniques are certainly the most widely used ones; initially developed for 2D imaging of fixed samples they have been rapidly extended to 3D [28–31] and to living cells. They have been combined with tracking of genetically encoded fluorescent proteins (sptPALM) [32,33••] as well as organic fluorophores targeted to endogenous proteins (uPAINT) [34,35], increasing the labeling density by three orders of magnitude compared to traditional SPT techniques. Except for the uPAINT method, which monitors the stochastic binding of a freely diffusible fluorescent probe to a protein of interest, PALM-based method and STORM-based method use laser-induced stochastic photoactivation or photoswitching of fluorescent probes between the on and an off states to isolate single molecules. They allow locating, tracking and counting a substantial portion of the protein of interest in its native cellular environment [36–38], making it possible to decipher the composition, structure and organization of molecular complexes with a spatial resolution of a few nanometers and a temporal resolution down to the millisecond. This opens a window into the understanding of complex molecular organization that, until now, could not be addressed by the techniques of classical biology, biochemistry and microscopy.

Concomitantly to the development of these new microscopy techniques, the application of improved electron microscopy (freeze-fracture replica, pre-embedding) and synaptic modeling alluded to a potential sub-compartmentalization of the synapse [39,40]. Glutamate diffusion modeling revealed that glutamate does not encompass the entire post-synapse after its release but covers only a 200 nm diameter extent [41]. Recent mathematical analysis of live high-density single protein tracking data have demonstrated that AMPARs in hippocampal dendrites move to attracting interaction potential wells smaller than the diffraction limit [42]. These models sustained the assumption that receptor clustering and relative position inside the post-synapse with respect to the glutamate release site determines the synaptic strength.

While diffraction limited microscopy techniques do not provide sufficient resolution to decipher such protein organization, the emergence of super-resolution techniques has rendered the protein distribution inside sub-synaptic compartments accessible. The first nanometer scale study of post-synaptic molecular organization was performed using STORM on fixed brain slices [43]. In this work, Dani *et al.* classified various pre-synaptic scaffolding protein and post-synaptic scaffolding protein as well as the two main neurotransmitter receptors (AMPA and NMDA) as a function of depth relative to the synaptic cleft with 50 nm resolution. This study mainly focused on protein position across the synaptic cleft and provided few details on sub-compartment organization in the membrane. In 2013, three papers employed different complementary super-resolution techniques to tackle the nano-organization of AMPAR and postsynaptic scaffolding proteins (Fig. 1b). MacGillavry *et al.* used fixed and live PALM on mEOS2 fused to PSD95, Homer and other scaffolding proteins [44]. Fukata *et al.* [45•] applied STED microscopy to study the localization of a particular form of PSD95 presenting a membrane-anchoring palmitoyl. Finally, Nair *et al.* [46•] mainly focused on AMPAR nano-organization and relative alignment with PSD95 by utilizing uPAINT, sptPALM, dSTORM and STED nanoscopy techniques, in addition to electron microscopy. Each technique presents advantages and potential limits. For example, uPAINT allows long lasting trajectories recordings, but the relatively low labeling density is insufficient to map all receptors, while sptPALM delivers a dense AMPAR map, but the necessity of overexpression can affect endogenous organization. In the following, these three papers are discussed in detail.

AMPAR are organized in nanodomains

The various different imaging methodologies used in these three studies converged to the common conclusion that AMPARs are organized in clusters much smaller than the PSD (Fig. 2a). These AMPAR nanodomains were visible with all used super-resolution techniques as well as with electron microscopy, exhibiting a homogeneous size distribution sharply centered around a 80 nm half-maximum. Such a well-defined size could reflect a specific molecular organization of a subarea of the post-synaptic density. Each synapse presented between 0 and 4 AMPAR nanodomains, showing a linear relationship with the PSD size. Electron microscopy images revealed that poly-nanodomain synapses could arise from either the presence of multiple independent PSDs each facing individual presynapses, or separate nanodomains on a larger PSD. The average center-to-center distance between two nanodomains was measured to be 500 nm, with only 12% closer than 250 nm, suggesting that a single glutamate release cannot affect multiple nanodomains.

Nair *et al.* also investigated nanodomain composition from dSTORM data, estimating around 20–25 individual AMPA receptors per nanodomain. The characterization of the various AMPAR dynamic behaviors inside the synapse using sptPALM and uPAINT demonstrated that AMPA receptors containing GluA2 or overexpressed GluA1 subunits are mainly immobile inside nanodomains but diffuse freely between them (Fig. 2b and c). These results revealed a strong and unexpected heterogeneity of AMPAR distribution and motion inside a single synapse, which could be explained by a previously unobserved scaffolding protein sub-organization.

Figure 2

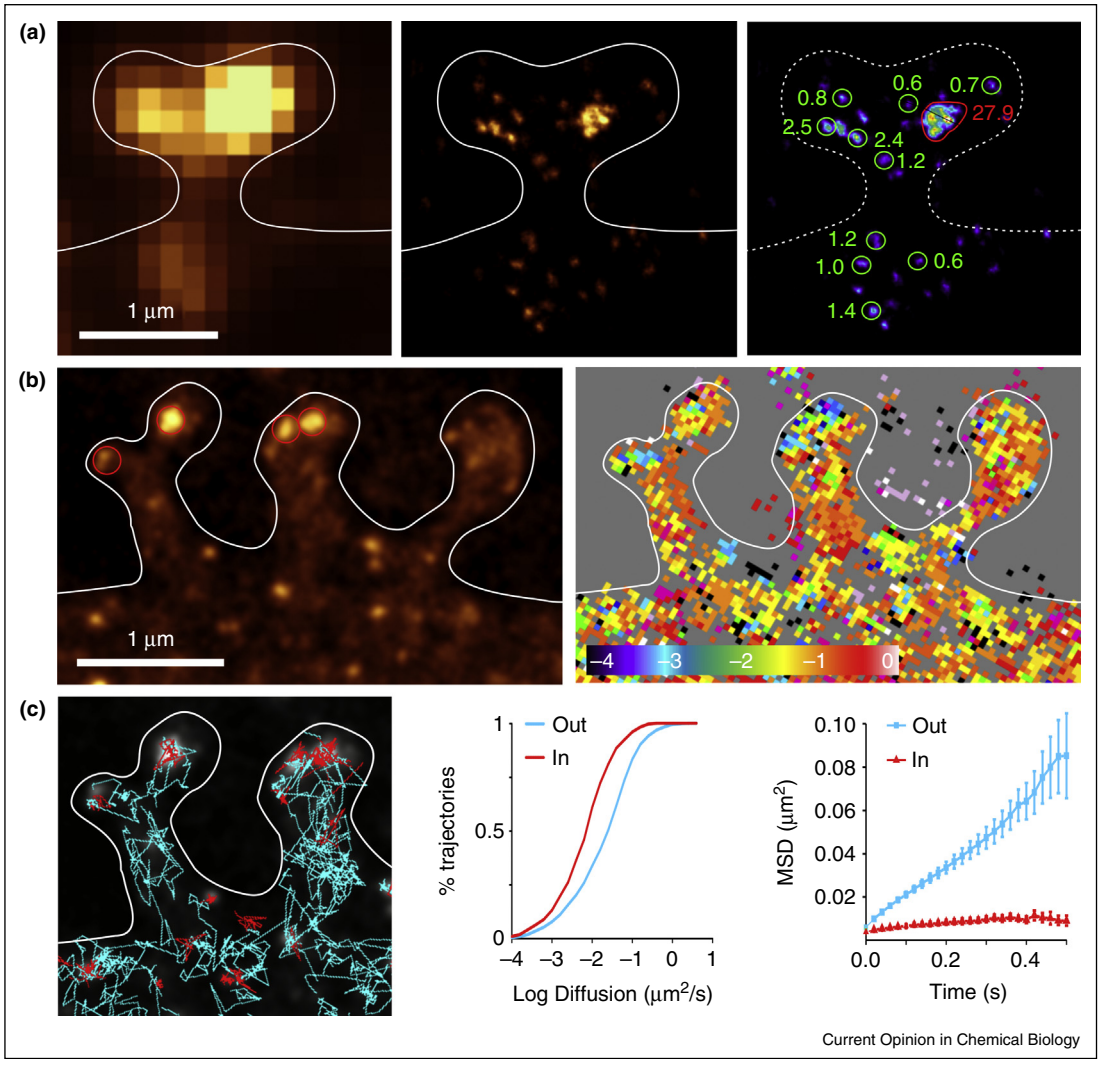

Nanometric organization and dynamics of AMPA receptors. **(a)** AMPARs are organized in nanoclusters. Left: diffraction limited image of AMPARs (GluA2 subunit) labeled with primary antibody coupled to Alexa647 in a dendritic spine. Middle: Super-resolution image of GluA2-containing AMPARs inhomogeneously distributed at the surface of the post-synapse, showing both individual receptors and nanodomains concentrating a large number of receptors. Right: Quantitative estimation of the average number of receptors per individual objects. Values have been normalized based on the intensity distribution of single receptors. Green circles, with a ratio close to one, show single receptors, while the red surface shows a nanodomain composed of about 30 receptors. **(b)** Non-homogeneous spatial and dynamic distribution of AMPAR revealed by sptPALM. Left: Intensity super-resolution image showing nanodomains located at spine heads. Right: Map of diffusion coefficient computed from high-density sptPALM data, showing the non-homogeneous dynamic behavior of receptors that correlated with nanodomain location. Color bar units are in Log(D(µm^2/s)). **(c)** AMPARs move slower inside nanodomains and faster in between them. Left: Red trajectories ($D < 10^{-3}$ µm^2/s) colocalize with nanodomain locations, while cyan ones ($D > 10^{-2}$ µm^2/s) show AMPARs moving faster outside nanodomains. Middle: Cumulative distribution of AMPAR diffusion coefficients inside (red) and outside (cyan) nanodomains, illustrating that AMPARs move slower inside nanodomains and faster outside. Right: Mean square displacement of molecules inside (red) and outside (cyan) nanodomains, showing that AMPARs are confined within nanodomains while they move freely outside.

PSD95 is assembled in nanoclusters

To explore such local potentiation of a PSD subarea, various groups investigated the organization of PSD95, one of the main scaffolding proteins, either in its ensemble [44,46•] or exclusively its palmitoylated form [45•]. They all led to the similar conclusion that PSD95 covers the entire postsynaptic density but, similarly to AMPARs, is over-concentrated in subdomains measuring around 150 nm in diameter (Fig. 3). PSD95 organization, observed with either sptPALM, dSTORM or STED techniques, presented a heterogeneous distribution, with a low concentration encompassing the entire PSD and smaller areas of overaccumulation (around 100 nm in size and with an enrichment factor of 1.8). While the presence of these

Figure 3

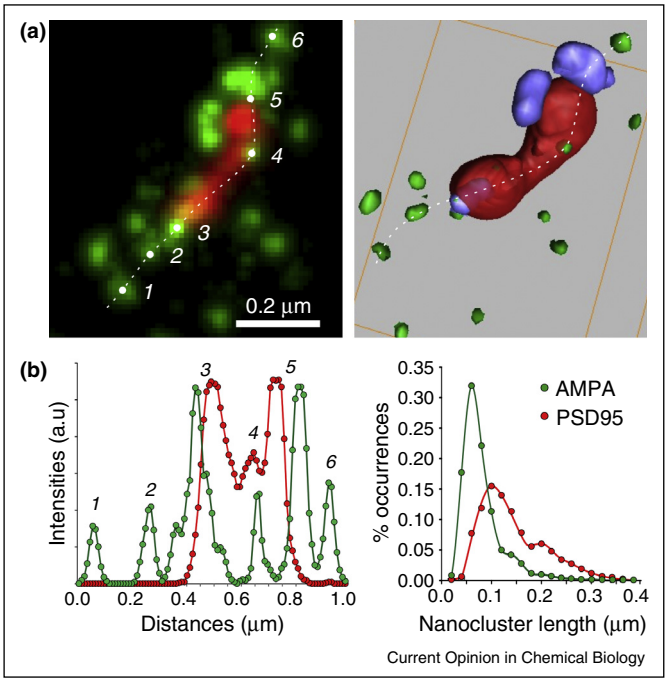

PSD95/AMPARs organization. **(a)** PSD95 and AMPAR partially colocalize. Left: Two-color dSTORM super-resolution image of PSD95-RhodRed (red) and AMPARs-Alexa647 (green) showing partial overlap of nanodomains at the tip of the PSD. Right: 3D surface rendering of two color super-resolution data acquired with astigmatism based 3D dSTORM. PSD95 (in red), GluA1 containing AMPARs (green) and nanodomains (violet). Nanodomains are either appose or colocalized with the PSD95 tip. **(b)** Colocalization and organization of PSD95 vs AMPARs. Left: intensity profiles performed on images in A, illustrating (i) that PSD95 is organized in coarser domains compared to AMPARs, and (ii) that PSD95 and AMPA are partially colocalized. Numbers show different levels of organization and colocalization: (1, 2, 4, 6) show single AMPARs; (3, 5) represent nanodomains either overlapping (3) or apposed (5) with the PSD. When colocalized with PSD95, the presence of AMPARs is in general accompanied by an increase in PSD95 intensity (3, 4, 5). Right: Nanocluster diameter distribution of PSD95 (red) and AMPARs (green) showing that PSD95 is organized in coarser domains compared to AMPARs.

PSD95 nanoclusters is widely accepted, the number of clusters per synapse remains controversial. Concurring with the results on AMPARs demonstrated by Nair *et al.*, Fukata *et al.* counted between one and four nanoclusters of PSD95 per synapse, where MacGillavry *et al.* detected mainly one single PSD95 cluster per synapse (at more than 70%). Interestingly, a correlation between synaptic size and cluster number is reported. Larger synapses contained more PSD95 nanoclusters, and the increase of PSD95 palmitoylation mediated by DHHC2 overexpression tended to increase PSD95 cluster number and enlarge the synapse.

Both the presence of PSD95 subclusters and the previous identification of AMPAR nanodomains suggest a stable local potentiation within the PSD. To validate this hypothesis, all three groups performed time lapse studies. FRAP experiments by Fukata *et al.* showed a constant recycling of palmitoylated PSD95, but a conservation of overall nanocluster structure over the course of at least one hour. This stability is consistent with time-lapse sptPALM experiments realized by Nair *et al.*, demonstrating the immobility of more than 30% of AMPAR nanodomains for at least 45 min. However, sptPALM experiments performed by MacGillavry *et al.* on PSD95 described a more dynamic behavior, with clusters varying in their number, shape and position between 5-min intervals.

PSD95/AMPAR nanoscale colocalization and implications to neurophysiology

The nanoscale colocalization of PSD95 and AMPAR was investigated in basal conditions and as a function of synaptic activity by multicolor super-resolution microscopy. Interestingly, the expected PSD95/AMPAR nanocluster colocalization was not conclusively demonstrated. While Nair *et al.* and Fukata *et al.* could not demonstrate a full colocalization between nanodomains of endogenous AMPARs and endogenous PSD95 clusters (Fig. 3), MacGillavry *et al.* observed a strong overlap between AMPAR clusters and overexpressed PSD95. This discrepancy was potentially explained by Nair *et al.* through the demonstration that overexpressing PSD95 tends to increase the size of AMPAR nanodomains, which could have favored the colocalization between the two proteins. By modulating synaptic activity, Fukata *et al.* showed that the silencing of neuronal activity triggered an increase in PSD95 cluster size, while an increase in activity transiently decreased

their size and disassociated AMPARs from palmitoylated PSD95 clusters. Meanwhile, PSD95 cluster size remained unaffected by activity in MacGillavry *et al.*, a discrepancy potentially explained by the high treatment strength in Fukata *et al.* (KCl depolarization) compared to the softer one in MacGillavry *et al.* (biccuculine).

The synaptic activity dependent modulation of PSD95/AMPAR colocalization reveals the importance of AMPAR organization in the control of synaptic transmission. Indeed, the intensity of the mEPSC, the electrical response attributed to a single synaptic vesicle release, was previously considered to be proportional to the quantity of glutamate in the vesicle. The discovery of the inhomogeneous organization of postsynaptic AMPARs introduces two new postsynaptic factors: (i) the quantity of AMPARs per nanodomain and (ii) their precise position with respect to the release site.

Nair *et al.* established that the AMPAR content inside a nanodomain could be sufficient to mediate the current with an intensity similar to a mEPSC (~17 pA in cell cultures). This correlation between nanodomain composition and synaptic current is strengthened by the fact that decreasing the number of AMPARs per nanodomain via expression of PSD95 shRNA triggers a proportional decrease in the current intensity. This nanodomain AMPAR content could represent the postsynaptic quantum of synaptic response.

The other important parameter could be the physical correlation between release site and postsynaptic nanoclusters. This question was investigated both in Nair *et al.* and MacGillavry *et al.*, who modeled the variation of synaptic current intensity as a function of the distance between release site and AMPAR nanodomains. Direct release site and nanodomain opposition was not required to trigger maximum synaptic response, but a shift greater than 100 nm rapidly decreased the current intensity, validating the hypothesis that both the precise localization and receptor density of nanodomains are essential to synaptic transmission efficiency.

Conclusion

In this review, we demonstrated that advances in microscopy have imparted new conceptual steps to the understanding of synaptic function. Application of super-resolution microscopy techniques has revealed that PSD95 accumulates in sub-PSD clusters, which reorganize and resize during synaptic activity and strongly concentrate AMPARs. AMPARs also concentrate inside the synapse in nanodomains of about 80 nm in diameter, partially colocalized with PSD nanoclusters. This unexpected nanoscale organization brings to light that synaptic transmission regulation does not depend exclusively on presynaptic vesicle content, but additionally on AMPAR nanodomain composition and alignment with the release site.

To decipher the exact physiological role of such AMPAR organization, it seems important to study the variability between various synapses in the brain. Electron microscopy experiments have already reported variation of molecular organization as a function of neuron type [47], and recent publications have demonstrated the feasibility of single-molecule experiments in brain slices [43,48•]. The ultimate step to understanding the intrinsic functioning of the synapse will be correlating the presynaptic organization and post-synaptic organization with electrophysiological recording at the single synapse level.

References and recommended reading

Papers of particular interest, published within the period of review, have been highlighted as:

- • of special interest
- •• of outstanding interest

1. Palade GE, Palay SL: **Electron microscope observations of interneuronal and neuromuscular synapses**. *Anatomical Record* 1954, **118**:335-336.

2. • Miyawaki A: **Proteins on the move: insights gained from fluorescent protein technologies**. *Nat Rev Mol Cell Biol* 2011, **12**:656-668.

Review of fluorescent imaging techniques for monitoring protein dynamics in living cells.

3. Michalet X, Pinaud FF, Bentolila LA, Tsay JM, Doose S, Li JJ, Sundaresan G, Wu AM, Gambhir SS, Weiss S: **Quantum dots for live cells, in vivo imaging, and diagnostics**. *Science* 2005, **307**:538-544.

4. Thompson RE, Larson DR, Webb WW: **Precise nanometer localization analysis for individual fluorescent probes**. *Biophys J* 2002, **82**:2775-2783.

5. Saxton MJ, Jacobson K: **Single-particle tracking: applications to membrane dynamics**. *Annu Rev Biophys Biomol Struct* 1997, **26**:373-399.

6. Ober RJ, Ram S, Ward ES: **Localization accuracy in single-molecule microscopy**. *Biophys J* 2004, **86**:1185-1200.

7. Persson F, Barkefors I, Elf J: **Single molecule methods with applications in living cells**. *Curr Opin Biotechnol* 2013, **24**:737-744.

8. Borgdorff AJ, Choquet D: **Regulation of AMPA receptor lateral movements**. *Nature* 2002, **417**:649-653.

9. Bats C, Groc L, Choquet D: **The interaction between Stargazin and PSD-95 regulates AMPA receptor surface trafficking**. *Neuron* 2007, **53**:719-734.

10. Heine M, Groc L, Frischknecht R, Beique JC, Lounis B, Rumbaugh G, Huganir RL, Cognet L, Choquet D: **Surface mobility of postsynaptic AMPARs tunes synaptic transmission**. *Science* 2008, **320**:201-205.

11. Mondin M, Labrousse V, Hosy E, Heine M, Tessier B, Levet F, Poujol C, Blanchet C, Choquet D, Thoumine O: **Neurexin-neuroligin adhesions capture surface-diffusing AMPA receptors through PSD-95 scaffolds**. *J Neurosci* 2011, **31**:13500-13515.

12. Saglietti L, Dequidt C, Kamieniarz K, Rousset MC, Valnegri P, Thoumine O, Beretta F, Fagni L, Choquet D, Sala C *et al.*: **Extracellular interactions between GluR2 and N-cadherin in spine regulation**. *Neuron* 2007, **54**:461-477.

13. Ehlers MD, Heine M, Groc L, Lee MC, Choquet D: **Diffusional trapping of GluR1 AMPA receptors by input-specific synaptic activity**. *Neuron* 2007, **54**:447-460.

14. Zhang H, Etherington LA, Hafner AS, Belelli D, Coussen F, Delagrange P, Chaouloff F, Spedding M, Lambert JJ, Choquet D *et al.*: **Regulation of AMPA receptor surface trafficking and**

synaptic plasticity by a cognitive enhancer and antidepressant molecule. *Mol Psychiatry* 2013, **18**:471-484.

15. Ladepeche L, Dupuis JP, Bouchet D, Doudnikoff E, Yang L, Campagne Y, Bezard E, Hosy E, Groc L: **Single-molecule imaging of the functional crosstalk between surface NMDA and dopamine D1 receptors**. *Proc Natl Acad Sci USA* 2013, **110**:18005-18010.

16. Dupuis JP, Feyder M, Miguelez C, Garcia L, Morin S, Choquet D, Hosy E, Bezard E, Fisone G, Bioulac BH *et al.*: **Dopamine-dependent long-term depression at subthalamo-nigral synapses is lost in experimental parkinsonism**. *J Neurosci* 2013, **33**:14331-14341.

17. Hell SW, Wichmann J: **Breaking the diffraction resolution limit by stimulated emission: stimulated-emission-depletion fluorescence microscopy**. *Opt Lett* 1994, **19**:780-782.

18. Klar TA, Jakobs S, Dyba M, Egner A, Hell SW: **Fluorescence microscopy with diffraction resolution barrier broken by stimulated emission**. *Proc Natl Acad Sci USA* 2000, **97**:8206-8210.

19. Gustafsson MG, Agard DA, Sedat JW: **I5M: 3D widefield light microscopy with better than 100 nm axial resolution**. *J Microsc* 1999, **195**:10-16.

20. Heintzmann R, Jovin TM, Cremer C: **Saturated patterned excitation microscopy—a concept for optical resolution improvement**. *J Opt Soc Am A Opt Image Sci Vis* 2002, **19**:1599-1609.

21. Gustafsson MG: **Nonlinear structured-illumination microscopy: wide-field fluorescence imaging with theoretically unlimited resolution**. *Proc Natl Acad Sci USA* 2005, **102**:13081-13086.

22. Betzig E, Patterson GH, Sougrat R, Lindwasser OW, Olenych S, Bonifacino JS, Davidson MW, Lippincott-Schwartz J, Hess HF: **Imaging intracellular fluorescent proteins at nanometer resolution**. *Science* 2006, **313**:1642-1645.

23. Hess ST, Girirajan TP, Mason MD: **Ultra-high resolution imaging by fluorescence photoactivation localization microscopy**. *Biophys J* 2006, **91**:4258-4272.

24. Rust MJ, Bates M, Zhuang X: **Sub-diffraction-limit imaging by stochastic optical reconstruction microscopy (STORM)**. *Nat Methods* 2006, **3**:793-795.

25. Heilemann M, van de Linde S, Schuttpelz M, Kasper R, Seefeldt B, Mukherjee A, Tinnefeld P, Sauer M: **Subdiffraction-resolution fluorescence imaging with conventional fluorescent probes**. *Angew Chem Int Ed Engl* 2008, **47**:6172-6176.

26. Folling J, Bossi M, Bock H, Medda R, Wurm CA, Hein B, Jakobs S, Eggeling C, Hell SW: **Fluorescence nanoscopy by ground-state depletion and single-molecule return**. *Nat Methods* 2008, **5**:943-945.

27. •• van de Linde S, Loschberger A, Klein T, Heidbreder M, Wolter S, Heilemann M, Sauer M: **Direct stochastic optical reconstruction microscopy with standard fluorescent probes**. *Nat Protoc* 2011, **6**:991-1009.
Detailed protocol for direct stochastic optical reconstruction microscopy with standard fluorescent probes in fixed and living cells.

28. Huang B, Wang W, Bates M, Zhuang X: **Three-dimensional super-resolution imaging by stochastic optical reconstruction microscopy**. *Science* 2008, **319**:810-813.

29. Juette MF, Gould TJ, Lessard MD, Mlodzianoski MJ, Nagpure BS, Bennett BT, Hess ST, Bewersdorf J: **Three-dimensional sub-100 nm resolution fluorescence microscopy of thick samples**. *Nat Methods* 2008, **5**:527-529.

30. Pavani SR, Thompson MA, Biteen JS, Lord SJ, Liu N, Twieg RJ, Piestun R, Moerner WE: **Three-dimensional, single-molecule fluorescence imaging beyond the diffraction limit by using a double-helix point spread function**. *Proc Natl Acad Sci USA* 2009, **106**:2995-2999.

31. Abrahamsson S, Chen J, Hajj B, Stallinga S, Katsov AY, Wisniewski J, Mizuguchi G, Soule P, Mueller F, Dugast Darzacq C *et al.*: **Fast multicolor 3D imaging using aberration-corrected multifocus microscopy**. *Nat Methods* 2013, **10**:60-63.

32. Manley S, Gillette JM, Patterson GH, Shroff H, Hess HF, Betzig E, Lippincott-Schwartz J: **High-density mapping of single-molecule trajectories with photoactivated localization microscopy**. *Nat Methods* 2008, **5**:155-157.

33. •• Rossier O, Octeau V, Sibarita JB, Leduc C, Tessier B, Nair D, Gatterdam V, Destaing O, Albiges-Rizo C, Tampe R *et al.*: **Integrins beta(1) and beta(3) exhibit distinct dynamic nanoscale organizations inside focal adhesions**. *Nat Cell Biol* 2012, **14**:1057-1067.
New insight into the dynamic nano-organization of integrins and talin adhesion proteins revealed by sptPALM.

34. Giannone G, Hosy E, Levet F, Constals A, Schulze K, Sobolevsky AI, Rosconi MP, Gouaux E, Tampe R, Choquet D *et al.*: **Dynamic superresolution imaging of endogenous proteins on living cells at ultra-high density**. *Biophys J* 2010, **99**:1303-1310.

35. Giannone G, Hosy E, Sibarita JB, Choquet D, Cognet L: **High-content super-resolution imaging of live cell by uPAINT**. *Methods Mol Biol* 2013, **950**:95-110.

36. Huang B, Bates M, Zhuang X: **Super-resolution fluorescence microscopy**. *Annu Rev Biochem* 2009, **78**:993-1016.

37. Lord SJ, Lee HL, Moerner WE: **Single-molecule spectroscopy and imaging of biomolecules in living cells**. *Anal Chem* 2010, **82**:2192-2203.

38. Sengupta P, Van Engelenburg S, Lippincott-Schwartz J: **Visualizing cell structure and function with point-localization superresolution imaging**. *Dev Cell* 2012, **23**:1092-1102.

39. Fukazawa Y, Shigemoto R: **Intra-synapse-type and inter-synapse-type relationships between synaptic size and AMPAR expression**. *Curr Opin Neurobiol* 2012, **22**:446-452.

40. Franks KM, Stevens CF, Sejnowski TJ: **Independent sources of quantal variability at single glutamatergic synapses**. *J Neurosci* 2003, **23**:3186-3195.

41. Lisman JE, Raghavachari S, Tsien RW: **The sequence of events that underlie quantal transmission at central glutamatergic synapses**. *Nat Rev Neurosci* 2007, **8**:597-609.

42. Hoze N, Nair D, Hosy E, Sieben C, Manley S, Herrmann A, Sibarita JB, Choquet D, Holcman D: **Heterogeneity of AMPA receptor trafficking and molecular interactions revealed by superresolution analysis of live cell imaging**. *Proc Natl Acad Sci USA* 2012, **109**:17052-17057.

43. Dani A, Huang B, Bergan J, Dulac C, Zhuang X: **Superresolution imaging of chemical synapses in the brain**. *Neuron* 2010, **68**:843-856.

44. Macgillavry HD, Song Y, Raghavachari S, Blanpied TA: **Nanoscale scaffolding domains within the postsynaptic density concentrate synaptic AMPA receptors**. *Neuron* 2013, **78**:615-622.

45. • Fukata Y, Dimitrov A, Boncompain G, Vielemeyer O, Perez F, Fukata M: **Local palmitoylation cycles define activity-regulated postsynaptic subdomains**. *J Cell Biol* 2013, **202**:145-161.
Nanometric organization of postsynaptic density molecules revealed by live-cell super-resolution microscopy.

46. • Nair D, Hosy E, Petersen JD, Constals A, Giannone G, Choquet D, Sibarita JB: **Super-resolution imaging reveals that AMPA receptors inside synapses are dynamically organized in nanodomains regulated by PSD95**. *J Neurosci* 2013, **33**:13204-13224.
Nano-organization of the post-synaptic receptors in live and fixed neurons deciphered using four super-resolution imaging techniques and electron microscopy.

47. Tarusawa E, Matsui K, Budisantoso T, Molnar E, Watanabe M, Matsui M, Fukazawa Y, Shigemoto R: **Input-specific intrasynaptic arrangements of ionotropic glutamate receptors and their impact on postsynaptic responses**. *J Neurosci* 2009, **29**:12896-12908.

48. • Biermann B, Sokoll S, Klueva J, Missler M, Wiegert JS, Sibarita JB, Heine M: **Imaging of molecular surface dynamics in brain slices using single-particle tracking**. *Nat Commun* 2014, **5**:3024.
First single particle tracking experiments performed in brain slices.

SR-Tesseler: a method to segment and quantify localization-based super-resolution microscopy data

Florian Levet[1–5], Eric Hosy[1,2], Adel Kechkar[1,2,6], Corey Butler[1,2,7], Anne Beghin[1,2], Daniel Choquet[1–5] & Jean-Baptiste Sibarita[1,2]

Localization-based super-resolution techniques open the door to unprecedented analysis of molecular organization. This task often involves complex image processing adapted to the specific topology and quality of the image to be analyzed. Here we present a segmentation framework based on Voronoï tessellation constructed from the coordinates of localized molecules, implemented in freely available and open-source SR-Tesseler software. This method allows precise, robust and automatic quantification of protein organization at different scales, from the cellular level down to clusters of a few fluorescent markers. We validated our method on simulated data and on various biological experimental data of proteins labeled with genetically encoded fluorescent proteins or organic fluorophores. In addition to providing insight into complex protein organization, this polygon-based method should serve as a reference for the development of new types of quantifications, as well as for the optimization of existing ones.

The recent development of optical super-resolution techniques represents a fundamental step toward understanding biological organization. Single-molecule localization microscopy (SMLM) techniques, such as photoactivated localization microscopy (PALM)[1,2] and stochastic optical reconstruction microscopy (STORM)[3–5], rely on the cumulative spatial localization of fluorescently tagged markers[6,7]. Historically, image analysis has had an important role in microscopy, revealing mechanisms underlying biological processes. It requires automatic segmentation for statistical, nonbiased descriptions of protein organization. Unfortunately, segmentation usually requires the implementation of complex techniques adapted to image topology and quality, and few studies have taken into consideration the pointillist nature of localization-based super-resolution data.

Recently, solutions such as K-Ripley[8] functions have been proposed to quantify clusters directly from molecule positions and have been applied to quantify protein organization in SMLM data[9,10]. Similarly, the pair-correlation method[11] identifies molecular interactions inside clusters by analyzing the distance correlation functions between localizations. All these methods, however, are restricted to the analysis of small clusters of relatively homogeneous size. Moreover, they do not provide precise information about the number, position and morphology of clusters. Density-based spatial clustering analysis with noise (DBSCAN) allows the classification of particles in an image into clusters[12]. It has been recently applied to SMLM data[13–15] but is known to be sensitive to background noise and difficult to parametrize experimentally, and therefore difficult to generalize[14,16]. One can also analyze complex molecular organization by summing all localizations into small pixels and applying dedicated intensity-dependent analysis strategies. These quantifications usually combine advanced filtering and analysis methods, which can be difficult to reproduce. Additionally, intensity-based image reconstructions of localization data are known to affect image resolution[17], and segmentation performed directly from the localization coordinates is preferred.

To overcome these limitations, we introduce a framework named SR-Tesseler, based on Voronoï diagrams, for the precise and automatic segmentation and quantification of protein organization at different scales from the same set of molecular coordinates, using a local density parameter. We demonstrate its capability to robustly segment different types of biological data and to precisely quantify small molecular complexes as well as more heterogeneous protein organization. SR-Tesseler software has a graphical user interface that provides direct visual feedback of the results, and the software is freely available under a GPLv3 license.

RESULTS

Voronoï diagram reconstruction from molecule localizations

Voronoï tessellation[18] is a method of subdividing space into a number of polygonal regions centered on a set of points, called seeds. These polygonal regions are defined in terms of Euclidean distances and provide information on the neighborhood surrounding the seeds. Considering S as a set of seeds in $\mathbb{R}^2$, where $\mathbb{R}^2$ is the real-space operator, each seed $s_i \in S$, $i = 1, 2, \ldots, n$, defines a region of space containing all points closer to s_i than any other seed of S. The regions determined by all seeds s_i, called polygons, form the mosaic of tiles that defines the Voronoï diagram. Voronoï diagrams are traditionally used in domains

[1]Interdisciplinary Institute for Neuroscience, University of Bordeaux, Bordeaux, France. [2]Interdisciplinary Institute for Neuroscience, Centre National de la Recherche Scientifique (CNRS) UMR 5297, Bordeaux, France. [3]Bordeaux Imaging Center, University of Bordeaux, Bordeaux, France. [4]Bordeaux Imaging Center, CNRS UMS 3420, Bordeaux, France. [5]Bordeaux Imaging Center, INSERM US04, Bordeaux, France. [6]Ecole Nationale Supérieure de Biotechnologie, Constantine, Algeria. [7]Imagine Optic, Orsay, France. Correspondence should be addressed to J.-B.S. (jean-baptiste.sibarita@u-bordeaux2.fr).

RECEIVED 11 DECEMBER 2014; ACCEPTED 3 JULY 2015; PUBLISHED ONLINE 7 SEPTEMBER 2015; DOI:10.1038/NMETH.3579

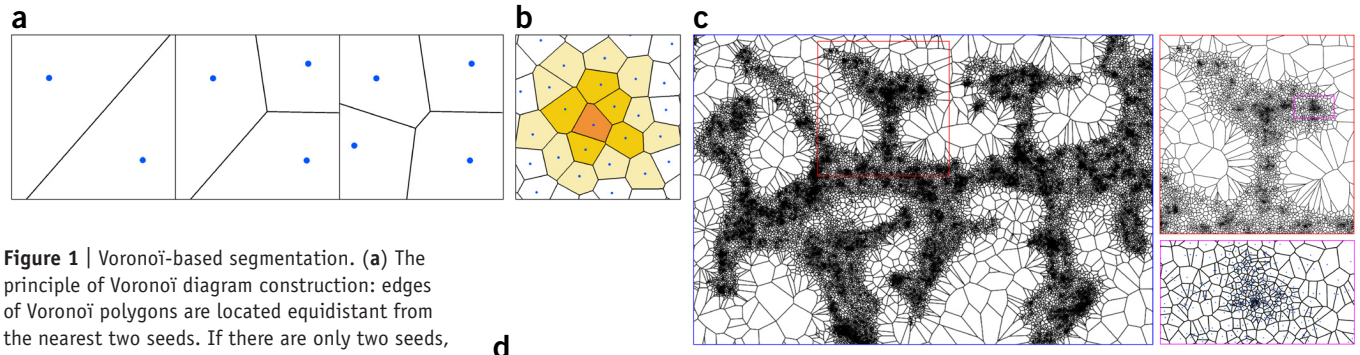

Figure 1 | Voronoï-based segmentation. (**a**) The principle of Voronoï diagram construction: edges of Voronoï polygons are located equidistant from the nearest two seeds. If there are only two seeds, their Voronoï polygons are delimited by their perpendicular bisector. When a new seed is added, this bisector is cut by the bisectors computed between the old seeds and the new one. This process is repeated for each new seed to compute the Voronoï diagram. (**b**) Each seed has a polygon (dark orange) defined by its neighboring seeds. The 5 medium-orange and 11 light-orange polygons are defined as the first-rank and second-rank neighboring polygons of the original seed and the first-rank seeds, respectively, because they share a common edge with those seeds. (**c**) Three different magnification views of a Voronoï diagram built from an experimental GluA1-mEOS2 PALM data set, showing a dendrite (blue outline), a spine (red outline) and a cluster (magenta outline). (**d**) Automatic segmentation of the Voronoï diagram on the basis of the first-rank density, with a spatially uniform distribution to which a threshold of twice the average localization density in the image was applied (red threshold in inset) (left) and a nonuniform data set analyzed with the same threshold, where selected polygons were merged (right).

as different as three-dimensional modeling, path planning[19] and remeshing[20]. Their use in the field of localization-based microscopy data has been mostly dedicated to visualization purposes[17,21]. Delaunay triangulation, which is the dual of the Voronoï diagram, has been previously applied for cluster analysis of dSTORM (direct stochastic optical-reconstruction microscopy) data to characterize cardiac receptor organization in mouse myocytes[22], but there is no existing general analysis framework for single-molecule data using tessellation.

In the case of SMLM data, the diagram is built from molecule coordinates as the seeds. As the Voronoï edges are equidistant from the two nearest seeds, the simplest way of generating the diagram is to compute the perpendicular bisectors between the seeds (**Fig. 1a**). A Voronoï edge is a portion of its corresponding bisector. It is defined such that a point q of the bisector is part of the Voronoï edge between seeds s_i and s_j if q is closer to s_i and s_j than to any other seed. This ensures that there is no intersection between any Voronoï polygons. Each polygon can be considered as the influence region of its corresponding seed, and geometric characteristics such as polygon area or shape can be used to describe the neighborhood of the seeds. In contrast to Delaunay triangles, which are shared by three molecules, Voronoï polygons are centered on individual localizations, making Voronoï tessellation better suited to describe single-molecule properties and neighborhoods. Moreover, each Voronoï polygon has on average six neighbors, making the structure more robust to labeling density and data organization.

Because of the large number of localizations provided by SMLM, performance of the diagram-generation algorithm is a critical issue. We used the sweep line algorithm[23], implemented in the Computational Geometry Algorithms library (http://www.cgal.org/), with which a Voronoï diagram of hundreds of thousands of localizations can be generated in a few seconds on a standard computer.

Multiscale segmentation using a Voronoï diagram

A Voronoï diagram subdivides a super-resolution image into polygons centered on localized molecules. Each polygon P_i of seed s_i has an area A_i and neighbors (**Fig. 1b**). First-rank neighboring polygons ${P^1}_{i,j}$ of s_i are defined by the ${n^1}_i$ polygons of area ${A^1}_{i,j}$ sharing edges with P_i, centered on the seeds ${s^1}_{i,j}$. Similarly, higher rank polygons ${P^k}_{i,j}$, $k > 1$, are defined as the ${n^k}_i$ polygons sharing edges with ${P^{k-1}}_{i,j}$. The neighborhood of s_i at the kth rank is then defined by the $\{{n^1}_i, \ldots, {n^k}_i\}$ localized molecules. For each seed s_i, various parameters can be computed, such as the area ${A^k}_i$, the density ${\delta^k}_i$, the mean distance ${d^k}_i$, the shortest distance (i.e., distance to the closest seed) ${\Delta^k}_i$ and the shape index ${\rho^k}_i$ (Online Methods). These parameters provide quantitative information on the localizations surrounding each seed. Therefore, Voronoï diagrams are a natural way to characterize and efficiently navigate the molecular neighborhood of each localized molecule at multiple scales, where regions with higher molecular densities are composed of smaller and denser polygons (**Fig. 1c**).

Once the Voronoï diagram has been reconstructed and the parameters have been computed, the object segmentation process is computed in three steps. First, the histogram and statistics (average and s.d.) of each parameter are computed from all the polygons. Second, one or several parameters of interest are thresholded on the basis of their histograms and statistics, and polygons with parameters of interest in the defined thresholds are selected. Third, the software computes objects by merging all selected polygons that are touching each other and defines object outlines by connecting all localizations belonging to the borders of the objects.

Thresholds can be either manually adjusted or automatically determined to avoid user bias. We defined a general criterion for automatic thresholding, which the user can infer by comparing

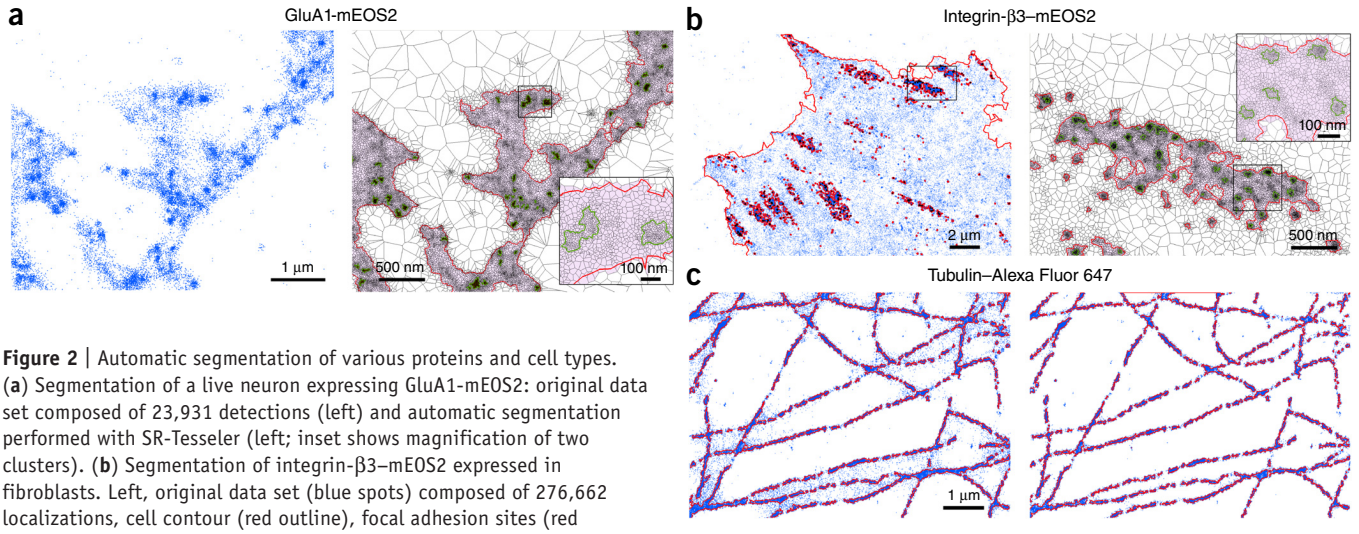

Figure 2 | Automatic segmentation of various proteins and cell types. (**a**) Segmentation of a live neuron expressing GluA1-mEOS2: original data set composed of 23,931 detections (left) and automatic segmentation performed with SR-Tesseler (left; inset shows magnification of two clusters). (**b**) Segmentation of integrin-β3–mEOS2 expressed in fibroblasts. Left, original data set (blue spots) composed of 276,662 localizations, cell contour (red outline), focal adhesion sites (red intracellular contours) and nanoclusters (black). Right, magnification of an adhesion site showing the Voronoï tessellation (black), adhesion site (red) and nanoclusters (green). (**c**) Segmentation of dSTORM tubulin–Alexa Fluor 647 data. Left, original data set composed of 130,493 localizations (blue spots) and the segmentation obtained with SR-Tesseler (red outlines). Right, filtered data set based on the quality of the fit and axial coordinates, composed of 110,438 localizations (blue spots), and the corresponding segmentation obtained with SR-Tesseler (red outlines). We performed all segmentations (except the fibroblast outline) by thresholding the first-rank density by twice the average localization density in the image.

the localization distribution to a reference distribution that is spatially uniform. The average density δ of such a distribution can be approximated as the number of localizations divided by the image area. With the first-rank density $\delta^1{}_i$ as the main parameter, the automatic segmentation is achieved through selection and merging of all the polygons having $\delta^1{}_i > \alpha\delta$ (**Fig. 1d**), where α is a positive multiplicative coefficient. As a control, the same threshold applied to a reference distribution did not provide any objects (**Fig. 1d**).

Automatic segmentation of various biological data

To test the versatility of SR-Tesseler, we automatically segmented multiple levels of organization in different types of biological data, using a unique density parameter $\delta^1{}_i > 2\delta$ (**Fig. 2a–c**). On neuronal data, we could automatically segment both the neuronal cell body and the molecular clusters of receptors of GluA1 fused to the mEOS2 fluorescent protein[24] (GluA1-mEOS2; **Fig. 2a**). Similarly, we could automatically extract the three levels of organization (cell contour, adhesion sites and interaction clusters) in live PALM data of fibroblasts expressing integrin-β3–mEOS2 (ref. 25) (**Fig. 2b**). Finally, we could identify nonisotropic structures such as microtubules in dSTORM data of COS7 cells labeled with tubulin–Alexa Fluor 647 (**Fig. 2c**). Another important feature of SR-Tesseler is its robustness to noise; segmentation of noisy data and cleaned data led to very similar results (**Fig. 2c**). As a comparison, the analysis of the same data with different popular automatic thresholding methods implemented in ImageJ software[26] provided very different and arbitrary results that were strongly dependent on image topology (**Supplementary Fig. 1**).

It is important to note that even if in most cases we used the same automatic threshold based on twice the average molecule density δ, the optimal threshold may vary slightly depending on the difference in molecular densities inside and outside the structure of interest. Similarly, we chose the first-rank density $\delta^1{}_i$ as the main parameter for segmentation, but many other parameters or combinations of parameters could be used, broadening the possible range of biological applications.

Validation on simulations and ground truth data

To validate the capability of SR-Tesseler to identify and quantify clusters of single molecules, we compared it to the K-Ripley clustering method[9,10,27,28] using simulated data. We simulated single-molecule data of 50-nm-radius clusters with various molecular densities ϕ and enrichment factors R (**Fig. 3a–c**). For all conditions, we successfully identified all the clusters using the Voronoï method. We could precisely compute the cluster dimensions, as well as their position in the super-resolution image and their morphological properties (circularity, shape index and orientation). It was also possible to retrieve the number of localizations per cluster and the enrichment factor R. In the special situation where there is very low background, which is unlikely in experimental data, the density criterion underestimates the cluster size. In such cases, using a shortest distance parameter based on the localization accuracy, such as $\Delta^k{}_i < 30$ nm, allows precise retrieval of cluster size (**Fig. 3b–d**). This criterion works only when clusters are well separated from each other and when the background is very low (**Supplementary Fig. 2a**).

For each condition, we compared the results obtained with the two methods by computing the ratio between the simulated and measured cluster sizes. Although our method performed robustly with respect to all the parameters of the simulation, the K-Ripley method was more sensitive to the R ratio. When the background increased (i.e., when R decreased), the efficiency of the K-Ripley function dropped, whereas the Voronoï-based method still performed robustly (**Fig. 3d**). We also analyzed simulated data with different R ratios using the DBSCAN method[12]. Although we were able to define a set of parameters that allowed successful segmentation of the clusters, none of these parameters allowed precise identification of clusters with a different background, illustrating the sensitivity of DBSCAN with respect to molecular density and background

(**Supplementary Fig. 2b**). Localization precision also did not have much influence on the segmentation efficiency of SR-Tesseler (**Supplementary Fig. 3a**).

Ripley's functions provide the radius of maximum aggregation and are therefore not well suited for distinguishing clusters with heterogeneous shapes and sizes. SR-Tesseler has no such restriction; we were able to identify two different populations of 200 and 100 clusters with distinct segmented areas (**Fig. 3b,c,e**) with surface accuracy of 95.51% ± 5.8% and 87.51% ± 5.82%, respectively.

We then validated the capability of SR-Tesseler to perform precise molecular counting on data obtained from a nanotemplate with known stoichiometry. To this end, we analyzed a subset of the PALM data of human glycine receptor (GlyR) expressed in *Xenopus laevis* oocytes described in ref. 29. GlyR is a pentameric structure composed, when the subunits are coexpressed, of three α and two β subunits, such that expression of α or β subunits fused to mEOS2 or PAmCherry, respectively, can serve as a reference stoichiometry. Using a density criterion $\delta^1_i > \delta$ and a shortest distance parameter $\Delta^k_i > 50$ nm, we were able to identify most isolated clusters (**Fig. 3f–h**) and determine the dimeric or trimeric stoichiometry after blinking correction[30]. We computed the photoactivation efficiency of the two proteins by binomial fit of the measured number of α-GlyR and β-GlyR subunits (**Fig. 3i**). β-GlyR–mEOS2 had a photoactivation efficiency of 70%, whereas β-GlyR–PAmCherry and α-GlyR–PAmCherry had equivalent photoactivation efficiencies of 50% and 53.5%, respectively ($\chi^2 = 0.9573$). These results were similar to those previously published for these particular data sets[29].

Analysis of glutamate-receptor organization in neurons

We applied SR-Tesseler to the analysis of PALM and dSTORM data of GluA1 subunits (one of the four glutamate acid–receptor subunits) in neuronal cell cultures (**Figs. 4** and **5**). These AMPARs (α-amino-3-hydroxy-5-methyl-4-isoxazolepropionic acid receptors) have been reported to be densely concentrated at the post-synapse in clusters less than 100 nm in diameter called nanodomains[24,31–33]. As a negative control, we also analyzed a GPI-anchored protein that shows no clear organization[34].

We obtained the neuron contours of both GluA1 and GPI live PALM data by thresholding the localizations, with $\delta^1_i > 2\delta_I$, where δ_I is the average localization density in the whole image (**Fig. 4a–d**). This first segmentation yielded a well-defined neuronal

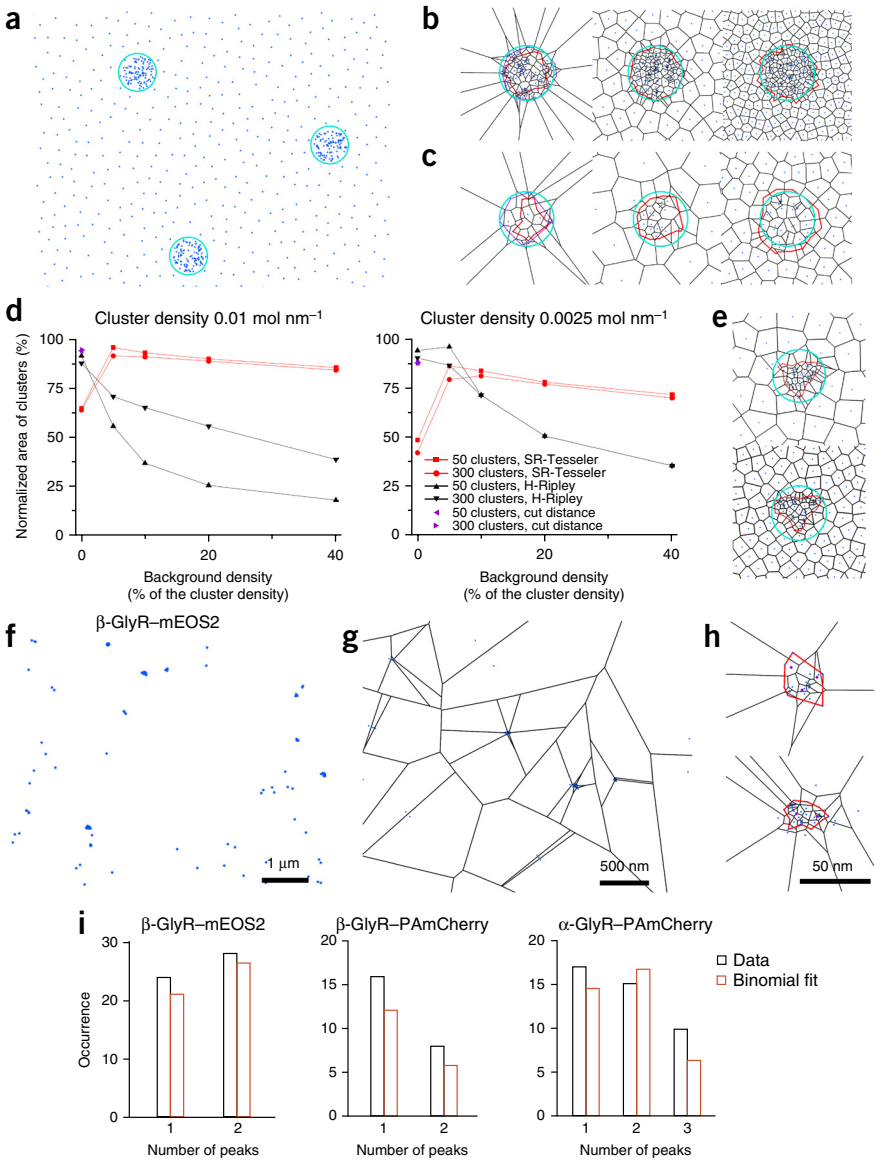

Figure 3 | Segmentation and quantification of simulations and well-characterized nanotemplates. (**a**) Simulated clusters with a density of 0.01 mol nm^{-2} and an enrichment ratio of 20. (**b**,**c**) Segmentations of individual clusters with densities of 0.01 mol nm^{-2} (**b**) or 0.0025 mol nm^{-2} (**c**) and enrichment ratios of ∞, 10 and 2.5 (from left to right in both panels). We obtained outlines by thresholding the first-rank density by twice the average localization density (red) and a shortest distance parameter of 30 nm (magenta); the theoretical outline is in cyan. (**d**) Comparison between segmentation by SR-Tesseler and segmentation by the K-Ripley function (black) for clusters of different densities, different numbers of clusters (50 and 300) and different ratios of background to cluster density (0, 5%, 10%, 20% and 40%). (**e**) Segmentation of triangular clusters with densities of 0.01 mol nm^{-2} and enrichment ratios of 20 (top) and 2.5 (bottom). (**f–i**) Quantitative analysis of α- and β-subunit content in GlyR. Shown are an example of a localization data set of β-GlyR–mEOS2 (**f**) and magnification with the corresponding Voronoï diagram (**g**). We segmented individual GlyRs (red contours) by combining thresholding of the first-rank density by the average localization density with a shortest distance parameter of 50 nm (**h**). Magenta points represent the molecule's coordinates after blinking correction. Bar graphs show the distribution of the measured number of α-GlyR and β-GlyR subunits for various fluorescent proteins (black) and their corresponding binomial distributions (red) (**i**).

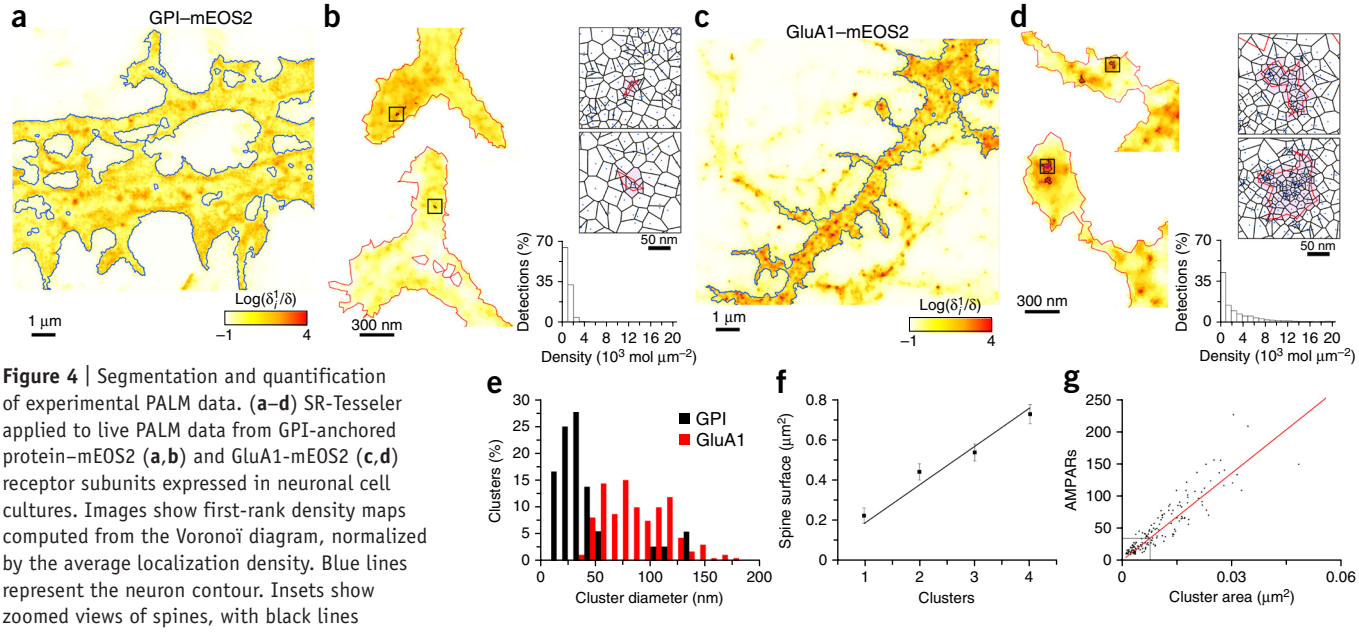

Figure 4 | Segmentation and quantification of experimental PALM data. (**a**–**d**) SR-Tesseler applied to live PALM data from GPI-anchored protein–mEOS2 (**a**,**b**) and GluA1-mEOS2 (**c**,**d**) receptor subunits expressed in neuronal cell cultures. Images show first-rank density maps computed from the Voronoï diagram, normalized by the average localization density. Blue lines represent the neuron contour. Insets show zoomed views of spines, with black lines representing the cluster contours. Histograms show the distribution of first-rank density for the two proteins. (**e**–**g**) Cluster analysis of 159 clusters and 36 clusters identified in 62 spines and 29 spines in cells expressing GluA1-mEOS2 and GPI-mEOS2, respectively, reflecting three different single-molecule experiments. (**e**) Synaptic cluster size distribution for the indicated proteins. (**f**) Number of nanodomains as a function of spine area for GluA1-mEOS2 (R^2 = 0.98, n = 62 spines; error bars indicate s.e.m.). (**g**) Number of AMPARs plotted as a function of the nanodomain surface area (R^2 = 0.92, n = 159 nanodomains).

shape from which we could extract the dendritic protein organization. We computed potential clusters using a threshold $\delta^1{}_i > 2\delta_N$, where δ_N is the average localization density inside the neuron contour (**Fig. 4b**,**d**). We further analyzed the cluster distributions after blinking correction from 159 or 23 clusters obtained from 62 or 29 spines of three cells expressing GluA1-mEOS2 or three cells expressing GPI-mEOS2, respectively (**Fig. 4e**,**f**).

For dSTORM data analysis (**Fig. 5**), the stochastic blinking pattern of organic fluorophores prevents the use of blinking-correction methods, but SR-Tesseler analysis nevertheless extracted quantitative information about GluA1 organization. Our analysis of the background area, using a threshold $\delta^1{}_i > \delta_B$ combined with a shortest distance parameter $\Delta^1{}_i < 30$ nm, where δ_B is the average localization density inside the background area, revealed isolated clusters corresponding to fluorescent secondary antibodies sticking nonspecifically to the coverslip (**Fig. 5b**,**c**). From an analysis of these clusters, we estimated the experimental resolution (33.9 nm ± 12.9 nm (±s.e.m.) at full-width at half-maximum (FWHM); **Fig. 5d**) and the number of localizations per fluorophore (22 localizations, interquartile range (IQR) of 13–40, n = 853; **Fig. 5e**), which we then used as a reference for receptor quantification. We could efficiently segment dendritic objects using two levels of segmentation, which revealed isolated AMPARs as well as a dense molecular organization inside the spine composed of single AMPARs surrounding a few clusters (**Fig. 5b**,**c**). We defined single AMPARs as objects inside the dendrite composed of one or several fluorophores and having a diameter $\omega_1 \leq d \leq \omega_2$, with ω_1 = 8 nm and ω_2 = 59 nm being the minimum and the maximum diameters, respectively, defined as 95% of the Gaussian fitting the reference distribution (**Fig. 5f**,**g**). We defined AMPAR nanodomains as clusters composed of several AMPARs inside the dendrite with a diameter $d > \omega_2$ (**Fig. 5h**).

SR-Tesseler analysis of both PALM and dSTORM data yielded quantitative results similar to those in recently published work[24,31–33]. AMPARs are clustered in nanodomains with mean diameters of 81.29 nm (IQR, 61.03–107.71 nm) and an average of 2.56 (±0.16, s.e.m.) nanodomains per spine for PALM and 73.24 nm (IQR, 62.21–97.17 nm) and 2.4 (±0.13, s.e.m.) for dSTORM. As a comparison, K-Ripley analysis performed on the whole image did not provide any obvious clustering because of the complex multiscale organization of neuronal cells (**Supplementary Fig. 3b**). However, when we analyzed regions of interest centered on spines, we were able to measure similar nanodomains of 91.2 nm (IQR, 83.2–112 nm) (**Supplementary Fig. 3c**). In contrast, we could not clearly identify clustering with the GPI-mEOS2 protein, with only 0.79 (±0.19, s.e.m.) clusters per spine with a width of 33.2 nm (IQR, 24.5–44.8 nm), corresponding to the resolution of the instrument.

We extracted multiple additional physiological parameters from these analyses. For example, both PALM and dSTORM data analyses revealed a linear relationship between nanodomain area and AMPAR content, with a measured density of 4,507 AMPARs µm^{-2} (R^2 = 0.92, n = 159 nanodomains) for PALM data and 2,100 AMPARs µm^{-2} (R^2 = 0.95, n = 225 nanodomains) for dSTORM data (**Figs. 4g** and **5i**). Discrepancies could be due to differences in labeling, overexpression (in the case of tagged receptors) or differences between live and fixed neurons. dSTORM data analysis revealed an average of 13.51 (IQR, 9.15–23.45) AMPARs per nanodomain and showed that spines had 19.22 single AMPARs (±0.67, s.e.m.). These results suggest that nanodomains are potential crystalline structures concentrating about 63% of the AMPARs within the spine.

DISCUSSION

SR-Tesseler uses Voronoï tessellation to automatically segment SMLM data. Because information is directly computed from the coordinates of localized molecules, SR-Tesseler does not require any image reconstruction before analysis, which is known to influence the quantifications. SR-Tesseler allows quantification of molecular

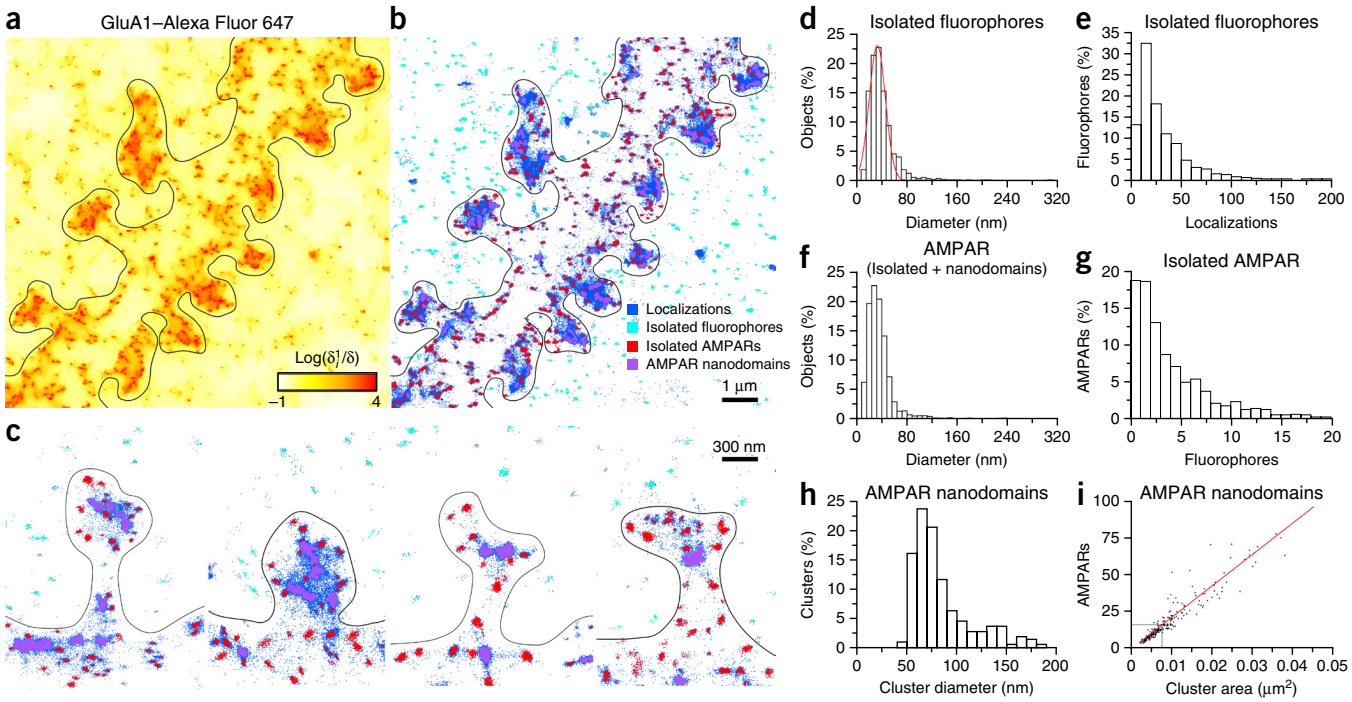

Figure 5 | Segmentation and quantification of experimental dSTORM data. (**a**–**c**) SR-Tesseler applied to dSTORM data of fixed cultured neurons labeled with GluA1–Alexa Fluor 647. (**a**) First-rank order density map computed from the Voronoï diagram on 715,994 localizations, normalized by the average localization density. Black lines represent the neuron cell contour obtained from the diffraction-limited low-resolution image. (**b**) Color-coded image of localizations with respect to the segmentation results. (**c**) Magnification of four spines composed of 16,039, 11,118, 14,928 and 12,257 localizations (left to right), color-coded as in **b**. (**d**–**g**) Distributions of the diameter of isolated fluorophores (**d**; red line shows the Gaussian fit), the number of localizations per isolated fluorophore (**e**), the diameter of isolated AMPARs and nanodomains (**f**) and the number of fluorophores per isolated AMPAR (**g**). Statistics were performed on the data set described in **a**. (**h**,**i**) Diameter distribution of the AMPAR nanodomains (**h**) and the number of AMPARs as a function of the area of AMPAR nanodomains (**i**). Statistics were performed on six data sets including 4,886,336 localizations, 92 spines and 225 nanodomains.

organization at various cellular levels and stoichiometry determination of both genetically and immunolabeled proteins.

SR-Tesseler is insensitive to cell shape, molecular organization, background and noise. This is very important for efficient and nonbiased comparisons of different biological conditions affecting molecular organization and for quantifications of various proteins and cell types. It provides visual feedback on the segmentation and statistics directly on the localization map through a very simple and intuitive graphical user interface. Its multiscale capability can be seen as a Matriochka analysis, which allows protein organization to be deciphered at multiple levels of organization.

However, whereas SR-Tesseler can provide precise quantitative information on protein organization (for example, morphology, surface and/or counting), the interpretation of the stoichiometry and counting from the number of localizations requires careful controls and calibration on well-characterized reference biological samples. This is important in order to avoid misinterpretations arising from varying labeling or photoconversion efficiency or from incomplete protein folding.

We expect SR-Tesseler to become a method of reference for the investigation of molecular organization of one or multiple proteins, in two and three dimensions. Combined with and designed for powerful localization-based super-resolution microscopy techniques, this analysis method could provide unprecedented insight into the molecular organization of cells.

METHODS

Methods and any associated references are available in the online version of the paper.

Note: Any Supplementary Information and Source Data files are available in the online version of the paper.

ACKNOWLEDGMENTS

We thank D. Nair and K. Haas for the GluA1-mEOS2 and GPI-mEOS2 acquisitions, G. Giannone and O. Rossier for the integrin-β3–mEOS2 PALM data and M. Lakadamyali for providing GlyR data and feedback on the manuscript. This work was supported by the Ministère de l'Enseignement Supérieur et de la Recherche (ANR NanoDom, Labex BRAIN and ANR-10-INBS-04 France-BioImaging), the European Research Council (ERC; grant nano-dyn-syn to D.C.), the Centre National de la Recherche Scientifique, the Conseil Régional d'Aquitaine and the Institut National de la Santé et de la Recherche Médicale.

AUTHOR CONTRIBUTIONS

F.L. developed the software and carried out the simulations. F.L. and J.-B. S. designed the analysis method. E.H. and D.C. designed the biological experiments. A.K. developed the single-molecule localization software. C.B. and A.B. worked on the quantitative analysis and the molecular counting. All the authors contributed to the manuscript. J.-B.S. came up with the original idea and supervised the work.

COMPETING FINANCIAL INTERESTS

The authors declare no competing financial interests.

1. Betzig, E. *et al.* Imaging intracellular fluorescent proteins at nanometer resolution. *Science* **313**, 1642–1645 (2006).

2. Hess, S.T., Girirajan, T.P. & Mason, M.D. Ultra-high resolution imaging by fluorescence photoactivation localization microscopy. *Biophys. J.* **91**, 4258–4272 (2006).
3. Rust, M.J., Bates, M. & Zhuang, X. Sub-diffraction-limit imaging by stochastic optical reconstruction microscopy (STORM). *Nat. Methods* **3**, 793–795 (2006).
4. Heilemann, M. *et al.* Subdiffraction-resolution fluorescence imaging with conventional fluorescent probes. *Angew. Chem. Int. Edn. Engl.* **47**, 6172–6176 (2008).
5. Folling, J. *et al.* Fluorescence nanoscopy by ground-state depletion and single-molecule return. *Nat. Methods* **5**, 943–945 (2008).
6. Klein, T., Proppert, S. & Sauer, M. Eight years of single-molecule localization microscopy. *Histochem. Cell Biol.* **141**, 561–575 (2014).
7. Sage, D. *et al.* Quantitative evaluation of software packages for single-molecule localization microscopy. *Nat. Methods* **12**, 717–724 (2015).
8. Ripley, B.D. Modelling spatial patterns. *J. R. Stat. Soc. B* **39**, 172–212 (1977).
9. Scarselli, M., Annibale, P. & Radenovic, A. Cell type–specific β2-adrenergic receptor clusters identified using photoactivated localization microscopy are not lipid raft related, but depend on actin cytoskeleton integrity. *J. Biol. Chem.* **287**, 16768–16780 (2012).
10. Muranyi, W., Malkusch, S., Müller, B., Heilemann, M. & Kräusslich, H.-G. Super-resolution microscopy reveals specific recruitment of HIV-1 envelope proteins to viral assembly sites dependent on the envelope c-terminal tail. *PLoS Pathog.* **9**, e1003198 (2013).
11. Sengupta, P. *et al.* Probing protein heterogeneity in the plasma membrane using PALM and pair correlation analysis. *Nat. Methods* **8**, 969–975 (2011).
12. Ester, M., Kriegel, H.-P., Jörg, S. & Xu, X. A density-based algorithm for discovering clusters in large spatial databases with noise. *Proc. 2nd International Conference on Knowledge Discovery and Data Mining* 226–231 (1996).
13. Endesfelder, U. *et al.* Multiscale spatial organization of RNA polymerase in *Escherichia coli*. *Biophys. J.* **105**, 172–181 (2013).
14. Nan, X. *et al.* Single-molecule superresolution imaging allows quantitative analysis of RAF multimer formation and signaling. *Proc. Natl. Acad. Sci. USA* **110**, 18519–18524 (2013).
15. Li, W. *et al.* Single protein molecule detection by glass nanopores. *ACS Nano* **7**, 4129–4134 (2013).
16. Deschout, H., Shivanandan, A., Annibale, P., Scarselli, M. & Radenovic, A. Progress in quantitative single-molecule localization microscopy. *Histochem. Cell Biol.* **142**, 5–17 (2014).
17. Baddeley, D., Cannell, M.B. & Soeller, C. Visualization of localization microscopy data. *Microsc. Microanal.* **16**, 64–72 (2010).
18. Okabe, A., Boots, B. & Sugihara, K. *Spatial Tessellations: Concepts and Applications of Voronoi Diagrams* (John Wiley & Sons, 1992).
19. Garrido, S., Moreno, L., Abderrahim, M. & Martin, F. Path planning for mobile robot navigation using Voronoi diagram and fast marching. in *Proc. International Conference on Intelligent Robots and Systems* 2376–2381 (IEEE, 2006).
20. Alliez, P., Colin de Verdière, E., Devillers, O. & Isenburg, M. Isotropic surface remeshing. *Proc. Shape Modeling International* 49–58 (IEEE Computer Society, 2003).
21. Beheiry, M.E. & Dahan, M. ViSP: representing single-particle localizations in three dimensions. *Nat. Methods* **10**, 689–690 (2013).
22. Baddeley, D. *et al.* Optical single-channel resolution imaging of the ryanodine receptor distribution in rat cardiac myocytes. *Proc. Natl. Acad. Sci. USA* **106**, 22275–22280 (2009).
23. Fortune, S. A sweepline algorithm for Voronoï diagram. *Proc. Second Annual Symposium on Computational Geometry* 313–322 (ACM, 1986).
24. Nair, D. *et al.* Super-resolution imaging reveals that AMPA receptors inside synapses are dynamically organized in nanodomains regulated by PSD95. *J. Neurosci.* **33**, 13204–13224 (2013).
25. Rossier, O. *et al.* Integrins β1 and β3 exhibit distinct dynamic nanoscale organizations inside focal adhesions. *Nat. Cell Biol.* **14**, 1057–1067 (2012).
26. Schneider, C.A., Rasband, W.S. & Eliceiri, K.W. NIH Image to ImageJ: 25 years of image analysis. *Nat. Methods* **9**, 671–675 (2012).
27. Williamson, D.J. *et al.* Pre-existing clusters of the adaptor Lat do not participate in early T cell signaling events. *Nat. Immunol.* **12**, 655–662 (2011).
28. Owen, D.M., Williamson, D.J., Magenau, A. & Gaus, K. Sub-resolution lipid domains exist in the plasma membrane and regulate protein diffusion and distribution. *Nat. Commun.* **3**, 1256 (2012).
29. Durisic, N., Laparra-Cuervo, L., Sandoval-Alvarez, A., Borbely, J.S. & Lakadamyali, M. Single-molecule evaluation of fluorescent protein photoactivation efficiency using an *in vivo* nanotemplate. *Nat. Methods* **11**, 156–162 (2014).
30. Annibale, P., Vanni, S., Scarselli, M., Rothlisberger, U. & Radenovic, A. Identification of clustering artifacts in photoactivated localization microscopy. *Nat. Methods* **8**, 527–528 (2011).
31. Macgillavry, H.D., Song, Y., Raghavachari, S. & Blanpied, T.A. Nanoscale scaffolding domains within the postsynaptic density concentrate synaptic AMPA receptors. *Neuron* **78**, 615–622 (2013).
32. Fukata, Y. *et al.* Local palmitoylation cycles define activity-regulated postsynaptic subdomains. *J. Cell Biol.* **202**, 145–161 (2013).
33. Hosy, E., Butler, C. & Sibarita, J.B. Organization and dynamics of AMPA receptors inside synapses—nano-organization of AMPA receptors and main synaptic scaffolding proteins revealed by super-resolution imaging. *Curr. Opin. Chem. Biol.* **20**, 120–126 (2014).
34. Giannone, G. *et al.* Dynamic superresolution imaging of endogenous proteins on living cells at ultra-high density. *Biophys. J.* **99**, 1303–1310 (2010).

ONLINE METHODS

Quantitative parameters computed from the Voronoï diagram. Given that each polygon P_i of a seed s_i has an area A_i and that the kth-rank neighboring polygons $P^k_{i,j}$, $k > 1$, are defined as the n^k_i polygons of area $A^k_{i,j}$ sharing common edges with $P^{k-1}_{i,j}$ (**Fig. 1b**), various quantitative parameters can be computed for each seed.

The area of s_i at the kth rank is defined by

$$A_i^k = A_i + \sum_k \sum_{j=1}^{n_i^k} A_{i,j}^k$$

The density of s_i at the kth rank is defined by

$$\delta_i^k = \left(1 + \sum_k n_i^k\right) / A_i^k$$

The mean distance of s_i at the kth rank is defined by

$$d_i^k = \sum_{j=1}^{n_i^k} d(s_i, s_{i,j}^k) / \sum_k n_i^k$$

Where $d(s_i, s_j)$ defines the Euclidian distance between s_i and s_j, and $s^k_{i,j}$ defines the seeds of the kth rank of s_i.

The shortest distance defines the distance between s_i and its closest seed using

$$\Delta_i = \min(d(s_i, s_{i,j}^1))$$

The shape index ρ^k_i of s_i at the kth rank is defined by the ratio of the minor axis to the major axis of the ellipse best fitting s^k_i.

K-Ripley function. The principle of the K-Ripley function clustering method is to compare the experimental localization distribution with a reference spatially uniform distribution. If, for a given distance r, the average number of localizations is statistically greater than the number obtained by the reference distribution, given by πr^2, the molecules are organized in clusters. The K-Ripley function is defined as

$$K(r) = \frac{1}{n} \sum_{i=1}^{n} Np_i(r) / \lambda$$

where $Np_i(r)$ is the number of points in the vicinity of the ith detection at a distance r and λ is the localization density. A normalization of the K-function such that the expected value is 0, known as the H-Ripley function, is defined as

$$H(r) = \sqrt{K(r)/\pi} - r$$

The traditional way to compute the cluster radius is to retrieve the value of r maximizing $H(r)$, as it represents the radius of maximum aggregation. Previous work demonstrated that this value varies between the radius and the diameter of the clusters[35].

Simulations. We have simulated several single-molecule data sets organized in clusters of various densities. Simulations consist of 15 µm × 15 µm images with randomly placed, nonoverlapping clusters of 50-nm radius, each containing a given number of randomly distributed molecules (**Fig. 3a**). For each simulation, we changed the number of clusters (50 and 300), the molecule density inside the clusters ($\phi_1 = 0.01$ mol/nm^2 and $\phi_2 = 0.0025$ mol/nm^2) and the density outside the clusters (between 0 and 40% of the density inside clusters). We defined R as the enrichment ratio between the density of molecules inside the clusters and the density of molecules outside the clusters. Enrichment ratios R of ∞, 20, 10, 5 and 2.5 correspond to density ratios outside clusters of 0%, 5%, 10%, 20% and 40%, respectively.

We also simulated a mixed population of 300 clusters with a density ϕ_1 and an R ratio of 5; 200 clusters were circular with a 50-nm radius (as in **Fig. 3b**,**c**), and 100 were triangular inside a 50-nm circle (**Fig. 3e**).

To test the efficiency of our method with respect to the localization accuracy, we degraded our simulation data by randomizing the molecule position with various localization accuracies (0, 5, 10 and 20 nm).

Analysis of well-characterized nanotemplates. Histograms of single, double and triple peaks of the GlyR α- and β-subunits were computed after blinking correction of the segmented objects. We determined the photoactivation efficiency for the β-GlyR condition by computing the exact solution of the dimeric stoichiometry binomial distribution with the observed peaks. For the α-GlyR condition, peaks were fitted using a trimeric stoichiometry binomial distribution (by least-squares optimization)[29].

Cluster analysis. Once clusters were identified, cluster size was analyzed by principal-component analysis (PCA) by linear least-squares fitting. We computed object lengths and widths by determining the s.d. along the principal components and multiplying them by 2.35, equivalent to the FWHM of a Gaussian distribution. Object diameter was defined as the average of the object's length and width, whereas areas and numbers of localizations were computed directly from the segmentation outline provided by the Voronoï-based method.

Benchmarking. One practical limitation of neighboring methods, such as Ripley functions, is that they are time consuming without software optimization. Hence, the algorithm is of complexity $O(N^2)$ in the case of brute-force implementation, where N is the number of localizations. Because the Voronoï diagram is a structure that allows natural navigation within the neighboring molecules, we implemented the H-Ripley functions using the Voronoï diagram structure. As expected, we obtained a speedup factor of more than two orders of magnitude compared with the standard brute-force algorithm, showing a complexity of $O(M \log(N))$, where M is the number of neighbors. As an example, with our Voronoï method and brute-force it took 36 min and 5,451 min, respectively, to compute the H-Ripley function on 220,775 molecules for a search radius ranging from 16 nm to 320 nm with $\delta r = 16$ nm (**Supplementary Fig. 3d**). This emphasizes that the Voronoï structure is perfectly adapted to the type of data provided by single-molecule localization techniques and can also be used

doi:10.1038/nmeth.3579

with time-consuming existing methods such as Ripley or pair-correlation. Nevertheless, other space-partitioning techniques are more suited for speeding up neighboring techniques such as the H-Ripley function or pair-correlation. For instance, it only took 10 min to perform the same H-Ripley analysis with a Quadtree implementation[36] (**Supplementary Fig. 3d**).

Correction for artifacts due to multiple single-molecule localizations. Accurate segmentation and quantifications of single-molecule data require consideration of possible multiple localizations and blinking[30,37,38]. In the case of genetically encoded fluorescent proteins, these multiple localizations occur within a distance tolerance ω and a blinking-time interval tolerance τ, which have to be precisely estimated to avoid over- or undercounting. The photophysical properties of the fluorophores can be described by the distribution of three main parameters: the number of blinks per molecule before photobleaching (N_{blinks}), the fluorescent on-time (T_{on}) before a blinking or photobleaching event, and the fluorescent off-time (T_{off}) between two blinking events (**Supplementary Fig. 4a**).

Multiple localizations issuing from the same molecule are reassigned to the barycenter position (**Supplementary Fig. 4b**). As ω and τ depend on the localization accuracy and the photophysics of the fluorophore under the experimental conditions and may fluctuate from one experiment to another, they are estimated for each data set. The search radius ω is defined as twice the average localization accuracy of the microscope. It can be fixed and global or dependent on each localization precision, using either

$$\omega = 2\sigma / \sqrt{N_{\text{ph}}}$$

or

$$\omega = 2\sqrt{\frac{\sigma^2 + (a^2/12)}{N_{\text{ph}}} + \frac{4\sqrt{\pi}\sigma^3 b^2}{aN_{\text{ph}}^2}}$$

where σ is the s.d. of the PSF emitter when fitted with a Gaussian model, N_{ph} is the number of photons per localization, a is the pixel size and b is the background signal[39]. These definitions of the search radius may be of importance when the local density of fluorescent molecules is high (greater than 0.5 mol/μm^2), but they have no real impact otherwise. To avoid an $O(N^2)$ complexity of the search algorithm (where N is the number of localizations of the data set), we used a Quadtree structure[36] to efficiently perform the neighborhood queries with a time complexity of $O(\log(N))$. The time interval τ is computed experimentally in two steps as in ref. 30. First initialized to $\tau_0 = 20$ frames, histograms of the off times (**Supplementary Fig. 4c**), blinks (**Supplementary Fig. 4d**) and on times (**Supplementary Fig. 4e**) were computed from all multiple localizations identified within the neighborhood ω and time interval τ. Second, the off-time histogram was fitted with an exponential decay function (**Supplementary Fig. 4c**), and τ was adjusted to three times the half-life of the exponential. Finally, all the multiple localizations were identified and replaced by a single detection positioned at their barycenter (**Supplementary Fig. 4b**), and the new Voronoï diagram was computed from the new list of localizations. As a control, we estimated the corrected number of molecules by dividing the number of molecules obtained with $\tau = 0$ (number of bursts) by the number of blinks per molecule. We computed the number of blinks per molecule by fitting the blinking distribution (**Supplementary Fig. 4d**) with a geometric distribution and the on-time distribution (**Supplementary Fig. 4e**) with a single exponential decay as in ref. 37. The difference between the number of molecules determined by the off-time method and that determined by the blinking method for our experimental data (n = 4,000,714 localizations, 6 cells, and 2 different proteins) was 1.66% ± 0.91%.

Code availability. The software is freely available for academic use as Supplementary Software or (including updated versions) at http://www.iins.u-bordeaux.fr/team-sibarita-SR-Tesseler. Source code is available upon signing of a material transfer agreement.

35. Kiskowski, M.A., Hancock, J.F. & Kenworthy, A.K. On the use of Ripley's K-function and its derivatives to analyze domain size. *Biophys. J.* **97**, 9 (2009).
36. Samet, H. The Quadtree and related hierarchical data structures. *ACM Comput. Surv.* **16**, 187–260 (1984).
37. Lee, S.-H., Shin, J.Y., Lee, A. & Bustamante, C. Counting single photoactivatable fluorescent molecules by photoactivated localization microscopy (PALM). *Proc. Natl. Acad. Sci. USA* **109**, 17436–17441 (2012).
38. Puchner, E.M., Walter, J.M., Kasper, R., Huang, B. & Lim, W.A. Counting molecules in single organelles with superresolution microscopy allows tracking of the endosome maturation trajectory. *Proc. Natl. Acad. Sci. USA* **110**, 16015–16020 (2013).
39. Thompson, R.E., Larson, D.R. & Webb, W.W. Precise nanometer localization analysis for individual fluorescent probes. *Biophys. J.* **82**, 2775–2783 (2002).

nature COMMUNICATIONS

ARTICLE

Received 22 Jul 2015 | Accepted 17 Jan 2016 | Published 16 Mar 2016

DOI: 10.1038/ncomms10773 OPEN

Mapping the dynamics and nanoscale organization of synaptic adhesion proteins using monomeric streptavidin

Ingrid Chamma[1,2], Mathieu Letellier[1,2], Corey Butler[1,2,5], Béatrice Tessier[1,2], Kok-Hong Lim[3,†], Isabel Gauthereau[1,2], Daniel Choquet[1,2,4], Jean-Baptiste Sibarita[1,2], Sheldon Park[3], Matthieu Sainlos[1,2,*] & Olivier Thoumine[1,2,*]

The advent of super-resolution imaging (SRI) has created a need for optimized labelling strategies. We present a new method relying on fluorophore-conjugated monomeric streptavidin (mSA) to label membrane proteins carrying a short, enzymatically biotinylated tag, compatible with SRI techniques including uPAINT, STED and dSTORM. We demonstrate efficient and specific labelling of target proteins in confined intercellular and organotypic tissues, with reduced steric hindrance and no crosslinking compared with multivalent probes. We use mSA to decipher the dynamics and nanoscale organization of the synaptic adhesion molecules neurexin-1β, neuroligin-1 (Nlg1) and leucine-rich-repeat transmembrane protein 2 (LRRTM2) in a dual-colour configuration with GFP nanobody, and show that these proteins are diffusionally trapped at synapses where they form apposed *trans*-synaptic adhesive structures. Furthermore, Nlg1 is dynamic, disperse and sensitive to synaptic stimulation, whereas LRRTM2 is organized in compact and stable nanodomains. Thus, mSA is a versatile tool to image membrane proteins at high resolution in complex live environments, providing novel information about the nano-organization of biological structures.

[1] Interdisciplinary Institute for Neuroscience, UMR 5297, Centre National de la Recherche Scientifique, 33077 Bordeaux, France. [2] Interdisciplinary Institute for Neuroscience, University of Bordeaux, 33077 Bordeaux, France. [3] Department of Chemical and Biological Engineering, University at Buffalo, Buffalo, New York 14260, USA. [4] Bordeaux Imaging Center, UMS 3420 Centre National de la Recherche Scientifique, University of Bordeaux, US 4 INSERM, 33077 Bordeaux, France. [5] Imagine Optic, 18 rue Charles de Gaulle, 91400 Orsay, France. † Present address: Conagen, Bedford, Massachusetts 01730, USA. * These authors jointly supervised this work. Correspondence and requests for materials should be addressed to M.S. (email: sainlos@u-bordeaux.fr) or to O.T. (email: olivier.thoumine@u-bordeaux.fr).

Critical cellular functions including adhesion and signalling are performed by dynamic macromolecular platforms at the cell membrane. Synaptic neuronal contacts are examples of such complex structures, where protein concentration is extremely high and lies in a very confined and compartmentalized space[1]. Recently developed fluorescence-based super-resolution imaging (SRI) techniques, including STimulated Emission Depletion (STED)[2], PhotoActivation Localization Microscopy (PALM)[3,4], direct STochastic Optical Reconstruction Microscopy (dSTORM)[5,6] and universal Point Accumulation for Imaging in Nanoscale Topography (uPAINT)[7,8], provide 20–50 nm resolution maps of single-molecule localization in biological samples, allowing a better understanding of the organization and turnover of these submicron multisubunit assemblies[9]. To accompany such progress in imaging power, there is a pressing need for efficient labelling strategies relying on small and penetrating probes that provide high signal-to-noise ratio and minimal linkage error with respect to target proteins[10,11].

Protein labelling has relied for a long time on the use of antibodies, which have the strong advantage of targeting endogenous proteins. Yet, full-length antibodies are relatively large (10–15 nm) compared with nanoscale biological objects, thereby causing potential steric hindrance and localization bias[11,12]. Moreover, because of their divalence, antibodies may induce protein crosslinking at the cell surface. The recent expansion of antibody fragments such as Fab, scFv or VhH is promising improvements[13,14]; however, their development including antigen preparation is time-consuming[15]. Alternative labelling approaches consist of the use of recombinant proteins fused to fluorescent proteins (FPs, photoactivatable or photoswitchable proteins)[3,16], reactive moieties such as modified enzymes to bind small dye-labelled synthetic molecules[17,18] or small peptide tags for subsequent conjugation with exogenous fluorescent ligands[19,20]. However, FPs usually have weaker fluorescence compared to organic dyes, and the insertion of a FP or enzyme moiety (25–35 kDa) may affect proper protein folding and/or function[21,22].

In this context, we searched for an efficient and orthogonal labelling approach combining minimal tag size on the protein of interest, probe penetrability in confined regions, absence of artefact due to multivalence and compatibility with multicolour imaging. We propose a new method based on streptavidin monomers (mSA) to deliver bright organic fluorophores to proteins that are enzymatically biotinylated on a 15-amino-acid acceptor peptide (AP) tag[23]. This targeted biotinylation strategy was previously developed in combination with monovalent streptavidin to track membrane molecule dynamics using quantum dots[24]. However, monovalent streptavidin remains a relatively large heterotetramer (molecular weight of 60 kDa and ~6 nm across) and is difficult to produce because of the precise 3-to-1 stoichiometry that is required among the subunits[24]. mSA is a structural monomer evolved from wild-type streptavidin tetramer with the aim of maximizing aqueous stability (denaturation temperature of 60 °C) while maintaining sufficient biotin affinity ($K_d = 2.8$ nM)[25,26]. The resulting mSA is a stable 3-nm labelling probe with a molecular weight of 12.5 kDa, which is simple to produce and to couple to various fluorophores for SRI applications.

We demonstrate that fluorescently conjugated mSA is compatible with a wide range of microscopy techniques, including uPAINT, Fluorescence Recovery After Photobleaching (FRAP), STED and dSTORM, in both live and fixed conditions. We further show that, unlike antibodies or streptavidin, mSA labels its targets without crosslinking and penetrates deep into live tissues. We applied mSA-based labelling to probe several synaptogenic adhesion proteins in neurons, including the presynaptic neurexin-1β (Nrx1β), and its postsynaptic binding partners neuroligin-1 (Nlg1), and leucine-rich-repeat transmembrane protein 2 (LRRTM2), against which good antibodies compatible with live cell imaging are lacking. We demonstrate differential nanoscale organization and dynamics of Nlg1 and LRRTM2, which may underlie divergent physiological roles at the synapse.

Results

mSA labels biotinylated proteins at the cell surface. Recombinant mSA was produced in bacteria, purified by affinity chromatography via a 10-His N-terminal tag and covalently conjugated to photostable organic dyes Atto 594 or Atto 647N for uPAINT and STED experiments, respectively, or to Alexa 647 for dSTORM imaging, using standard N-hydroxysuccinimide (NHS) ester coupling onto solvent-exposed primary amines (Supplementary Fig. 1). Fluorophore-conjugated mSA was used to label membrane proteins in neurons, COS-7 or HEK-293 cells that incorporate an extracellular AP tag. Biotinylation of the AP tag occurred during protein maturation by co-expressed *Escherichia coli* biotin ligase, $BirA^{ER}$ (ref. 17). When added to the extracellular imaging solution, the mSA–dye conjugate bound specifically to cells co-expressing AP-tagged proteins and $BirA^{ER}$, and not to cells expressing either haemagglutinin (HA)-tagged proteins and $BirA^{ER}$, or AP-tagged proteins but lacking $BirA^{ER}$ (Supplementary Fig. 2a–d). mSA labelling was efficient on all cell types and membrane proteins tested and produced images with high signal-to-noise ratio. The relatively fast dissociation kinetics of mSA ($k_{off} = 1.05 \times 10^{-3}\,s^{-1}$)[25,26] allow efficient release of bound mSA with excess free biotin. In this regard, addition of 200 μM biotin to the labelling solution resulted in rapid loss of the mSA label (Supplementary Fig. 2e,f). Such reversible binding may be exploited to visualize internalized protein complexes using competition with modified biotin having reduced membrane permeability[27], and synthesized for this study (Supplementary Fig. 3 and Supplementary Movie 1). Covalent labelling or labelling with high-affinity streptavidin derivatives, for example, monovalent tetramer ($k_{off} \sim 4.2 \times 10^{-6}\,s^{-1}$)[17,24,28], would not allow such measurements. Taken together, these results demonstrate the high specificity of mSA labelling for recombinant biotinylated proteins in a cellular context.

mSA reports on protein dynamics without crosslinking. To evaluate the impact of probe valence on observed protein dynamics, we used uPAINT[8] to measure the diffusion of biotinylated AP-tagged Nlg1 (AP-Nlg1) in neurons that were labelled with divalent biotin antibody, tetrameric streptavidin or mSA conjugated with Atto 594 (Fig. 1a and Supplementary Fig. 1). The three probes were added at a low concentration (1 nM) to isolate single Nlg1 molecules diffusing on the cell surface. Neurons electroporated with AP-Nlg1 exhibited a twofold stronger surface labelling with Nrx1β-Fc and twofold higher anti-Nlg1 signal in western blots than control neurons expressing empty vector or Homer1c-green fluorescent protein (GFP), indicating a ratio of approximately one overexpressed AP-Nlg1 molecule for one endogenous Nlg1 molecule (Supplementary Fig. 4). In immature neurons, at 7 days *in vitro* (7 DIV), the distribution of AP-Nlg1 diffusion coefficients after mSA labelling was centred around 0.1 $\mu m^2\,s^{-1}$, revealing fast Brownian motion (Fig. 1b,c). When the movement of AP-Nlg1 was tracked with Atto-conjugated biotin antibody or tetrameric streptavidin, the measured diffusion coefficients were shifted towards lower values (Fig. 1b,c) and there was a concomitant

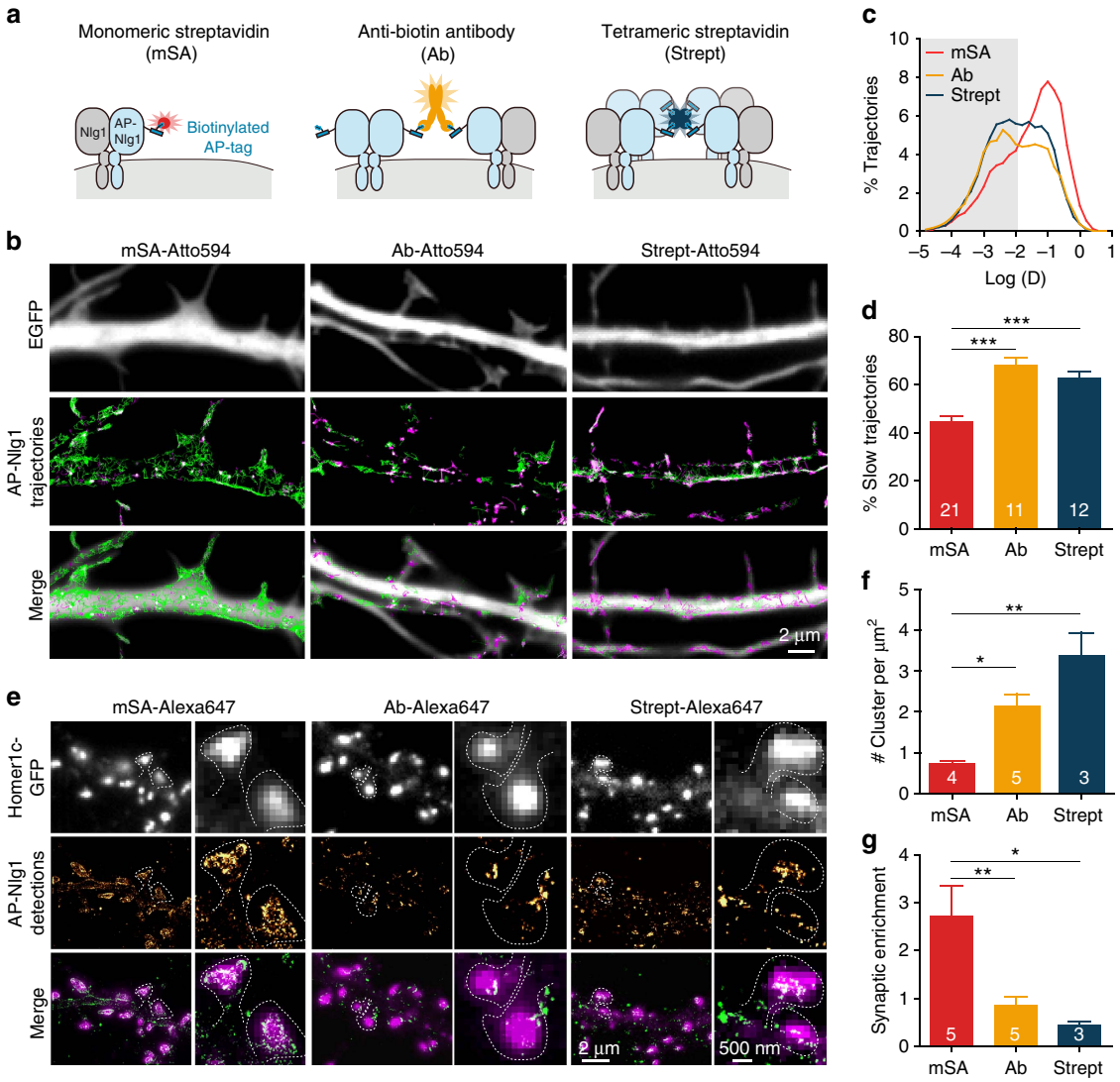

Figure 1 | Super-resolution imaging of AP-Nlg1 with mSA or biotin antibody or tetrameric streptavidin. (**a**) Schematic diagram of AP-Nlg1 labelled with three different probes (mSA, monoclonal biotin antibody or streptavidin), conjugated to Atto 594 for uPAINT or Alexa 647 for dSTORM. (**b**) Examples of DIV 7 neurons co-expressing EGFP as a volume marker, AP-Nlg1 and BirA^{ER}, and labelled as described above. Middle panels display AP-Nlg1 trajectories calculated from stacks of 4,000 images with 20-ms exposure time (green: fast-diffusing pool, that is, $D>0.01\,\mu m^2\,s^{-1}$; magenta: slow diffusing pool, that is, $D<0.01\,\mu m^2\,s^{-1}$). Merged images show EGFP (grey) overlaid with AP-Nlg1 trajectories. Note that mSA explores larger surface areas with faster diffusion than multivalent ligands. (**c**) Distribution of AP-Nlg1 diffusion coefficients in a semi-log plot, where the grey-shaded area represents slow trajectories (that is, with $D<0.01\,\mu m^2\,s^{-1}$). (**d**) Corresponding percentage of slow trajectories measured in the three different conditions (***$P<0.0001$). Data are from three different experiments. (**e**) Examples of DIV 15 neurons co-expressing Homer1c-GFP, AP-Nlg1 and BirA^{ER}, and labelled with the three Alexa647-conjugated probes shown in **a**. Top panels: Homer1c-GFP signal showing mature synapses (white). Middle panels: super-resolved AP-Nlg1 detection maps generated from 40,000 frames with 20-ms integration time. Bottom panels: merged images showing AP-Nlg1 detections (green) overlaid with Homer1c-GFP (magenta). Note the presence of large AP-Nlg1 aggregates in anti-biotin and streptavidin-labelled neurons. (**f**) Histogram showing the number of Nlg1 clusters per μm^2 in the three conditions (**$P<0.01$). (**g**) Histogram showing the synaptic enrichment of AP-Nlg1 compared with the shaft (**$P<0.01$, *$P<0.05$). Data are from two different experiments. Numbers in the bar charts represent the number of cells examined.

increase in the fraction of slowly diffusing molecules (Fig. 1d), defined as $D<0.01\,\mu m^2\,s^{-1}$ (Supplementary Fig. 5). The surface area covered by AP-Nlg1 trajectories was also higher with mSA than with biotin antibody or streptavidin (Fig. 1b). Together, these results suggest that divalent and tetravalent probes alter AP-Nlg1 distribution and dynamics through a combination of protein crosslinking and steric hindrance.

mSA prevents aggregation compared with multivalent probes. To examine the effects of probe size and valence on Nlg1 distribution at the nanoscale, we used dSTORM to image Nlg1 in mature neurons (DIV 15)[5,29,30]. Membrane-bound AP-Nlg1 was labelled with 100 nM mSA, biotin antibody or streptavidin conjugated with Alexa 647 for 10 min before fixation and observation. In contrast to our uPAINT experiments, which rely on sparse labelling and short acquisition sequences to focus on protein dynamics, dSTORM uses high-density labelling combined with long acquisition times (800 s) to produce a static representation of the overall protein organization. In parallel, postsynaptic densities were identified using co-expressed Homer1c-GFP[31,32]. mSA labelling was fairly diffuse in the shaft and highly concentrated at synapses (Fig. 1e). In contrast, both biotin antibody and streptavidin induced the aggregation of

AP-Nlg1 into numerous small clusters on dendrites (Fig. 1e,f), which are most likely caused by ligand-mediated receptor crosslinking. The anti-biotin-labelled AP-Nlg1 was found mostly on the edge of the synapses around rather than inside, presumably because the antibody has limited accessibility to the synaptic cleft because of its large size. With its intermediate size, tetrameric streptavidin penetrated well inside synapses, but because of massive extrasynaptic clustering was less enriched than anti-biotin at synapses compared with shaft levels. Overall, the enrichment of AP-Nlg1 at Homer1c-GFP-positive puncta was significantly higher for mSA compared with streptavidin and antibody (Fig. 1g), indicating that mSA enables a more accurate visualization of receptor localization and organization at the nanometre scale.

mSA efficiently labels Nlg1 in the confined synaptic cleft. To assess the ability of mSA-labelled Nlg1 to dynamically access the synaptic cleft (20 nm across), we performed uPAINT experiments on live DIV 10–15 neurons expressing AP-Nlg1, and labelled using either mSA or biotin antibody conjugated to Atto594. Using mSA, we observed a gradual decrease in AP-Nlg1 diffusion across neuronal development (Supplementary Fig. 6a–c), revealing the stabilization of Nlg1 associated with an increase in synapse density and maturation[33]. On DIV 15, AP-Nlg1 trajectories recorded with mSA populated both the dendritic shaft and synapses and substantially overlapped with the synaptic Homer1c-GFP staining (Fig. 2a and Supplementary Movie 2), whereas AP-Nlg1 trajectories obtained with biotin antibody were mostly localized on the dendritic shaft and confined to areas around the postsynaptic density. Quantitatively, 85% of synapses contained mSA-labelled Nlg1, while only 40% contained antibody-labelled Nlg1 (Fig. 2b), and the synaptic area covered by mSA-labelled Nlg1 was fourfold higher than antibody-labelled Nlg1 (30% versus 8%, respectively; Fig. 2c). mSA-labelled Nlg1 exhibited fast diffusion in extrasynaptic compartments and slower diffusion at synapses (Fig. 2d), reflecting interactions with presynaptic axonal adhesion protein, Nrx and/or postsynaptic scaffolding proteins[32]. In contrast, anti-biotin labelling showed consistently slower diffusion across the entire neuronal surface, similar to the observations on DIV 7 (Fig. 1c). An additional level of immobilization of mSA-labelled AP-Nlg1 on DIV 15 was observed on incubation with soluble dimeric Nrx1β-Fc (Supplementary Fig. 6d,e), which is consistent with the preferential anchorage of Nlg1 to synaptic PSD-95 triggered by Nrx1β binding[32]. These observations show that mSA can be used to label both fast- and slow-moving AP-Nlg1 in developing neurons, and to visualize trapping events in mature synapses without introducing steric and valence bias compared with divalent antibodies.

mSA labels target proteins in organotypic brain tissue. Given the small size and high labelling efficiency of mSA, we tested its capability to label neurons in dense organotypic tissue. We co-expressed GFP, AP-Nlg1 and BirA^{ER} in individual CA1 pyramidal neurons from 150-µm-thick mouse organotypic

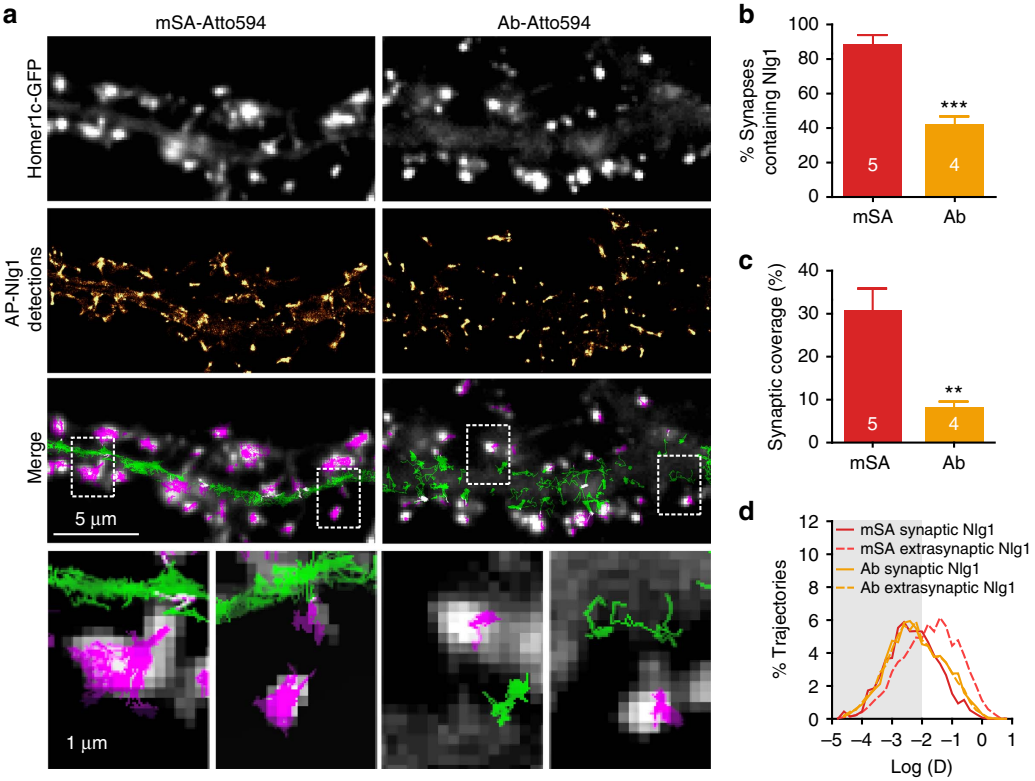

Figure 2 | Different ability of mSA and biotin antibody to label AP-Nlg1 within the synaptic cleft in live conditions. (**a**) DIV 15 neurons expressing Homer1c-GFP, AP-Nlg1 and BirA^{ER} were labelled with mSA or anti-biotin conjugated to Atto594 to track individual AP-Nlg1 molecules by uPAINT. From top to bottom: Homer1c-GFP signal staining mature synapses; super-resolved AP-Nlg1 detection maps; merged images showing extrasynaptic AP-Nlg1 trajectories (green) and synaptic trajectories (magenta) overlaid with Homer1c-GFP signals (grey); insets show that mSA-stained Nlg1 fills the entire synaptic area, whereas antibiotin remains on the edge of the postsynaptic density. (**b**) Percentage of synapses containing AP-Nlg1 labelled with mSA or biotin antibody (***$P<0.0001$). (**c**) Percentage of the synaptic area occupied by AP-Nlg1 when labelled with mSA or anti-biotin (**$P<0.01$). (**d**) Semi-log distribution of synaptic (solid lines) and extrasynaptic (dashed lines) diffusion coefficients for AP-Nlg1 measured with the two different probes. Data are from two different experiments. Numbers in the bar charts represent the number of cells analysed.

hippocampal slices using single-cell electroporation. Slices were labelled by one-step incubation with 100 nM mSA-Atto 647N (for STED) or mSA-Alexa647 (for dSTORM), then rinsed and observed live (STED) or after fixation (dSTORM). The mSA-labelling of AP-Nlg1 was highly specific since it stained only GFP-co-expressing cells throughout the slice with extremely low background, and localized exclusively to somatodendritic regions (Fig. 3a,b and Supplementary Movie 3). The photostability of Atto dyes combined with the thermal stability of mSA allowed an extensive live STED imaging of optical sections at 37 °C down to 40 µm deep. Zoom on dendritic portions showed specific enrichment of Nlg1 in spines compared with GFP (Fig. 3c,d and Supplementary Movie 4), which is also observed in dissociated hippocampal cultures (Fig. 1e–g).

Using conventional confocal microscopy, we evaluated how well mSA penetrates into brain slices compared with streptavidin and biotin antibodies. mSA and tetrameric streptavidin were able to label AP-Nlg1 expressed in live electroporated neurons within a few minutes, although the labelling efficiency of streptavidin decreased rapidly with depth, suggesting an impact of the probe size and/or valence in reaching deep tissues (Supplementary Fig. 7a,b). At the same sample depth (~15 µm below the surface of the slice), the anti-biotin signal was not detectable after a 10-min live labelling, but became apparent after 1 h (Supplementary Fig. 7c). Finally, we used astigmatism-based three-dimensional (3D) dSTORM to image the distribution of mSA-labelled AP-Nlg1 in small dendritic regions on the surface of a slice from Nlg1 knockout (KO) mice, revealing high enrichment of Nlg1 in spines (Fig. 3e,f and Supplementary Movie 5). These results show that mSA penetrates deep into thick tissues, where it can be used to label target proteins at high density and with specificity for immediate application in SRI. Interestingly, a similar AP-Nlg1 localization was observed in STED images made on organotypic slices from wild-type mice, and in STORM images made on organotypic slices from Nlg1 KO mice, where AP-Nlg1 expressed in CA1 cells replaces endogenous Nlg1.

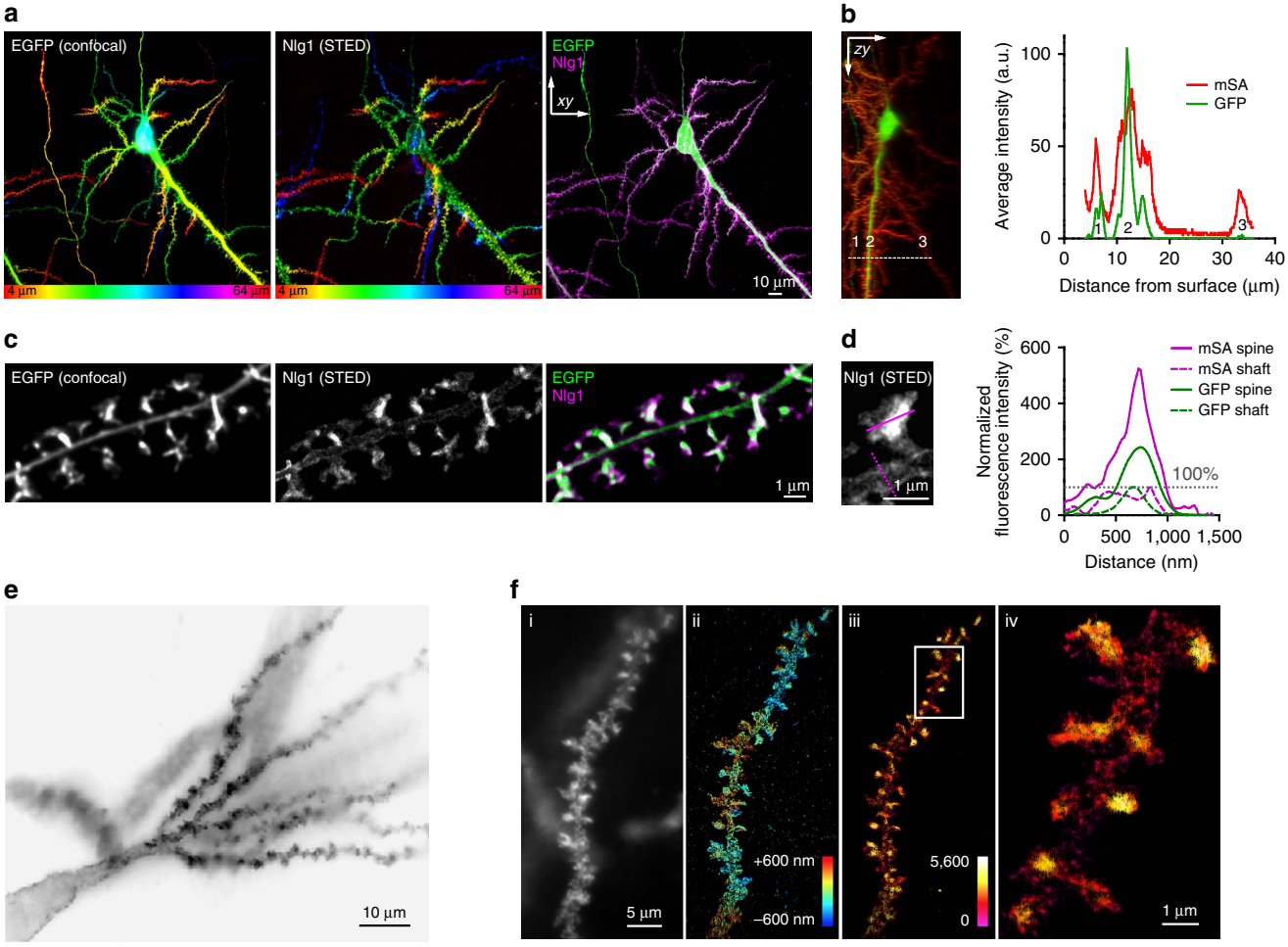

Figure 3 | Super-resolution imaging of AP-Nlg1 in organotypic hippocampal slices. (**a**) Confocal (EGFP, left), STED (mSA-Atto 647N, middle) and merged (right) images acquired from live neurons expressing GFP, AP-Nlg1 and BirA^{ER} in organotypic hippocampal slices. Images are projections of a z-stack of 60 planes taken by 1-µm increments and colour-coded with respect to sample depth. (**b**) Linescan measurements of mSA-Atto 647N and GFP staining along the *z* axis. The reduction in mSA-Atto 647N intensity with the sample depth likely reflects reduced laser penetration rather than weaker staining, since the GFP signal also decreases with depth. (**c**) High-magnification deconvoluted STED projection of mSA-labelled Nlg1 in a hippocampal slice shows the accumulation of Nlg1 at dendritic spines. (**d**) Linescans of GFP and mSA-Atto 647N fluorescence intensity in the shaft membrane and in a dendritic spine normalized to the respective fluorescence of GFP and Atto 647N in the shaft. (**e**) Wide field image of mSA-Alexa647 selectively labelling one neuron expressing GFP, AP-Nlg1 and BirA^{ER}, a few microns deep from the surface of an organotypic brain slice. (**f**) Astigmatic-based 3D dSTORM imaging in an organotypic brain slice from Nlg1 KO mice: (i) wide field image of mSA-Alexa647-labelled AP-Nlg1. (ii) 3D dSTORM-reconstructed image of a dendritic segment based on 1,038,506 single-molecule localizations from 64,000 images. The image is colour-coded with respect to the *z* distance (−600 to +600 nm). (iii) Normalized localization detection maps integrated within $z = \pm 400$ nm. (iv) Magnified view of iii showing the enrichment of Nlg1 in dendritic spines.

mSA and GFP nanobody similarly probe protein diffusion. Monomeric VhH antibodies (nanobodies) against GFP and red fluorescent protein have been previously used for SRI, where their small size provides smaller linkage error relatively to the target structure[13,14]. We thus sought to compare mSA to these well-characterized tools. To this end, we labelled the same axonal molecular target, Nrx1β, using both approaches and compared the measured diffusion dynamics and membrane organization. On the one hand, we labelled Nrx1β carrying a biotinylated N-terminal AP tag with mSA-Atto594. On the other hand, Nrx1β fused with an N-terminal GFP tag was labelled with Atto594-conjugated GFP nanobody, resulting in a specific enrichment at excitatory pre-synapses immunostained for the vesicular transporter VGlut1 (Fig. 4a). Single-molecule trajectories were then recorded for each labelling scheme using uPAINT in DIV 15 neurons (Fig. 4b,c). The distributions of diffusion coefficients were very similar for the two probes (Fig. 4d), with a major fast diffusion peak centred around $\sim 0.5\,\mu m^2\,s^{-1}$, representing free diffusion in extrasynaptic compartments, and a minor slower diffusion peak around $0.005\,\mu m^2\,s^{-1}$, representing Nrx1β confined at presynaptic terminals[34,35]. These results show that, in agreement with their small size and monomeric nature, mSA and nanobody labelling lead to similar diffusion measurements. Given their orthogonality, the two approaches may thus be combined for dual-colour SRI.

The AP tag can be inserted into small extracellular loops. An advantage of using mSA is that the short 15-amino-acid AP tag can be readily incorporated into extracellular protein domains, such as protein loops, without perturbing the native function. To demonstrate the use of the AP tag in a system that may not be amenable for GFP fusion, we inserted the AP sequence in the first extracellular loop of the alpha-amino-3-hydroxy-5-methyl-4-isoxazole-propionic acid (AMPA) receptor auxiliary protein stargazin (AP-Stg)[36] (Fig. 4e). Using mSA-Atto594, we observed the localization and dynamics of AP-Stg in DIV 15 neurons by uPAINT (Fig. 4f). AP-stargazin localized at synapses where its diffusion was reduced, consistent with previously published work[37] (Fig. 4f,g). Thus, the mSA-labelling strategy can be successfully applied to situations where the use of a GFP tag may not be allowed for structural or functional reasons. To further illustrate this point, we inserted the mCherry

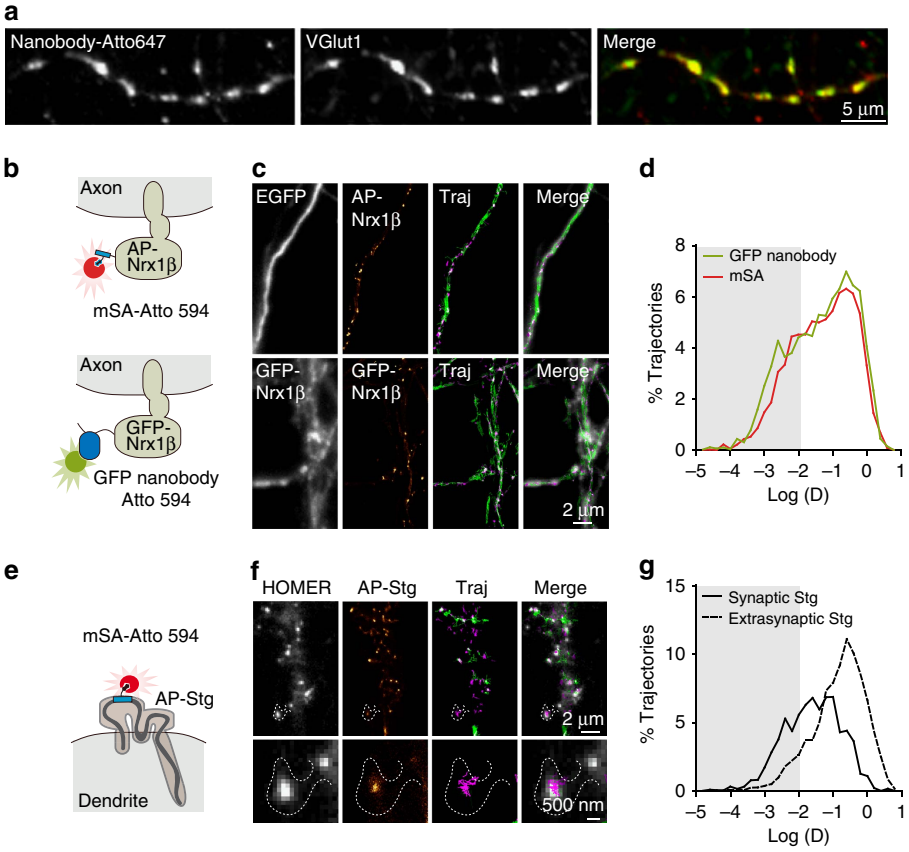

Figure 4 | Comparison of mSA and GFP nanobody. (**a**) DIV 15 axons expressing GFP-Nrx1β were live-labelled using anti-GFP nanobody-Atto647, followed by immunolabelling for VGlut1 to stain pre-synaptic glutamatergic terminals. The merged image shows the colocalization between GFP-Nrx1β (red) and VGlut1 (green). (**b**) Schematics showing the labelling of AP-Nrx1β with mSA-Atto594 (top) and GFP-Nrx1β with GFP nanobody-Atto594 (bottom). (**c**) Examples of axonal regions from DIV 15 neurons expressing EGFP, AP-Nrx1β and BirA^{ER} (top); or GFP-Nrx1β (bottom). From left to right: GFP signal, Nrx1 β detection maps, colour-coded Nrx1β trajectory maps (green: fast-diffusing pool, that is, $D > 0.01\,\mu m^2\,s^{-1}$; magenta: slow diffusing pool, that is, $D < 0.01\,\mu m^2\,s^{-1}$), merged image showing Nrx1β trajectories overlaid with GFP (grey). (**d**) Distributions of the diffusion coefficients obtained for AP-Nrx1β or GFP-Nrx1β (mSA, $n = 6$; GFP nanobody, $n = 5$ cells from two different experiments). (**e**) Schematics showing the structure of the AMPA receptor auxiliary protein stargazin (Stg) with the insertion of an AP tag in the first extracellular protein loop. (**f**) Example of DIV 15 neurons co-expressing the synaptic marker Homer1c-GFP, AP-Stg and BirA^{ER}. AP-Stg individual molecules were tracked using mSA-Atto594 by uPAINT. Super-resolved AP-Stg localization and trajectory maps were reconstructed from 4,000 images of 20-ms exposure time, with the same colour code as in **b**. (**g**) Diffusion coefficient distribution of AP-Stg inside and outside synapses ($n = 6$ cells from two different experiments).

FP (256 amino acids) in the extracellular loop of stargazin in place of the AP tag (15 amino acids). When expressed in heterologous COS-7 cells, this fusion protein formed numerous vesicular aggregates enriched in a perinuclear area, suggesting that mCherry-stg is retained in intracellular transport compartments, and not properly expressed at the cell membrane, possibly because of protein misfolding (Supplementary Fig. 8). In contrast, fusing mCherry to the C terminus of stargazin resulted in very clear membrane localization. This experiment clearly shows that AP tags can be advantageous compared with large domains such as FPs for the tagging of complex membrane proteins.

Dual-colour imaging of *trans*-synaptic adhesive contacts. Postsynaptic Nlg1 interacts with presynaptic Nrx1β to form *trans*-synaptic contacts[38]. To visualize the dynamic organization of mature Nrx1β/Nlg1 complexes, we used mSA in combination with GFP nanobody[13,14] for dual-colour uPAINT analysis. Neurons expressing either AP-Nlg1 or a blue fluorescent protein Nrx1b fusion (BFP-Nrx1β) were co-cultured for 2 weeks, and the individual AP-Nlg1 and BFP-Nrx1β molecules on the surface of dendrites and axons, respectively, were labelled with mSA-Atto 594 and GFP nanobody-Atto 647N for tracking (Fig. 5a,b and Supplementary Movie 6). Both BFP-Nrx1β and AP-Nlg1 showed decreased diffusion at Homer1c-GFP-positive areas, resulting in an increase in the slowly moving fraction (Fig. 5b,c), which is consistent with the formation of functional *trans*-synaptic complexes. The images reconstructed from all single-molecule detections indicate that every synapse contains one to two domains of Nrx1β and Nlg1 hot spots facing each other (Fig. 5d), with an average diameter of 85 ± 3 nm for Nrx1β and 91 ± 2 nm for Nlg1 (Fig. 5e,f). Given the dilute labelling conditions, these domains reflect the trapping of a small number of molecules at the synapse, whose intensity compared with diffusive molecules is amplified by the temporal integration of long-emitting fluorescent signals coming from the same location. Indeed, the domain size is in agreement with the confinement diameter measured from the mean squared displacement of synaptic Nlg1 molecules (Supplementary Fig. 5).

Addition of ethylene glycol tetra-acetic acid (EGTA) as a calcium chelator decreased the number of synaptic Nrx1β and Nlg1 confinement domains (Fig. 5d) and increased the diffusion of both proteins (Supplementary Fig. 9). Both changes are likely caused by a dissociation of calcium-dependent Nrx1β/Nlg1 bonds[39], followed by lateral motion of the two proteins. We also used dual-colour uPAINT to examine the dynamics of Nrx1β/Nlg1 adhesion in response to synaptic stimulation in live conditions. We treated neurons with 20 μM N-methyl-D-aspartate (NMDA) for 10 min to chemically induce synaptic depression[40] and monitored Nrx1β and Nlg1 dynamics by uPAINT. NMDA caused a specific and time-dependent decrease in BFP-Nrx1β and AP-Nlg1 molecules from the cell surface (Fig. 5g,h), whereas their number remained constant under control conditions. Such a loss of the Nrx1β/Nlg1 complex thus represents coordinated, activity-dependent destabilization of *trans*-synaptic contacts at the single-molecule level.

Differential dynamics of Nlg1 and LRRTM2 at synapses. To gain insight into the membrane dynamics of other synaptogenic proteins, we examined the behaviour of another excitatory postsynaptic adhesion molecule, LRRTM2, that competes with Nlg1 for the binding to presynaptic neurexins[41–43]. We first used the same dual-colour uPAINT analysis described above to simultaneously image AP-LRRTM2 in dendrites and BFP-Nrx1β in axons. Similarly to Nlg1, LRRTM2 was highly concentrated at synapses, where it formed a small number of confinement domains of 118 ± 4 nm diameter overlapping with BFP-Nrx1β (Supplementary Fig. 10). However, the average diffusion coefficient of LRRTM2 was significantly lower than that of Nlg1, reflecting the fact that most LRRTM2 molecules (80%) were localized at synapses, while very few (20%) diffused freely on dendritic shafts (Fig. 6a–c). For comparison, the synaptic and dendritic fractions of Nlg1 were 60% and 40%, respectively.

To confirm that Nlg1 and LRRTM2 also exhibited differential dynamics at the population level, we performed FRAP experiments. We labelled AP-Nlg1 and AP-LRRTM2 at the cell surface with 100 nM mSA-Atto594 and photobleached individual synapses using a focused 561-nm laser beam. Fluorescence recovery was analysed for up to 30 min (Fig. 6d,e). Control FRAP experiments on Nlg1-GFP showed similar recovery curves (Supplementary Fig. 11). The recovery curves were fitted with a diffusion-reaction model described previously, which includes three adjustable parameters: the fraction of adhesion molecules trapped at the synapse, their steady-state exchange rate and the diffusion coefficient of free molecules[44]. We used the fastest AP-Nlg1 and LRRTM2 observed in uPAINT to estimate the diffusion coefficient of free molecules ($\sim 0.1\,\mu m^2\,s^{-1}$) and adjusted the two other parameters to obtain the best fit. The exchange rate was approximately threefold lower for AP-LRRTM2 than for AP-Nlg1, and the trapped fraction was higher (81% versus 73%, respectively). Therefore, FRAP predicts a longer synaptic residence time for LRRTM2 than for Nlg1, consistent with the uPAINT data.

Differential nanoscale organization of Nlg1 and LRRTM2. Finally, to gain insight on the nanoscale organization of Nlg1 and LRRTM2, we imaged Nlg1 and LRRTM2 by dSTORM in mature neurons (Fig. 7a–d). Unlike in uPAINT, originally diffusing molecules appear with a similar intensity to confined ones because of fixation, thus contributing to a homogenous signal in the shaft and spines. This effect was especially prominent for Nlg1, which was more diffusive than LRRTM2, resulting in a lower synaptic enrichment when compared with shaft levels (2.7 ± 0.6 versus 5.3 ± 0.8, respectively). Furthermore, the dense labelling allows the identification of many simultaneous Nlg1-trapping events in the dendritic spine, yielding a fairly disperse localization with respect to the synapse centroid (Fig. 7e), but occasionally forming one or two clusters of similar sizes as those observed with uPAINT (average diameter 98 ± 6 nm; Fig. 7f,g). In contrast, LRRTM2 seemed to visit a more restricted postsynaptic area, mostly forming one compact mass comprising several small subclusters (107 ± 7 nm) and being localized at a shorter distance from the centroid (Fig. 7b,d–g). This specific scattering of Nlg1 was not due to an increase in postsynaptic size compared with LRRTM2 (Fig. 7h). In summary, the two Nrx partners, Nlg1 and LRRTM2, differed considerably in their postsynaptic nano-organization and dynamics.

Finally, to rule out the possibility of a localization artefact due to AP-Nlg1 overexpression, saturating synaptic binding sites, we designed a rescue strategy by replacing endogenous Nlg1 with similar levels of exogenous AP-Nlg1. To this aim, we either co-expressed a short hairpin RNA to Nlg1 together with a resistant AP-Nlg1 construct in rat cultures, or expressed AP-Nlg1 in primary hippocampal cultures from Nlg1 KO mice. Western blots and Nrx1β-binding assays confirmed that exogenous AP-Nlg1 levels roughly reached those of endogenous Nlg1 in both approaches (Supplementary Fig. 4). STORM images performed with mSA-Alexa647 on these cultures revealed a very similar distribution of rescue AP-Nlg1 compared with what we had previously observed using AP-Nlg1 expression alone, with a

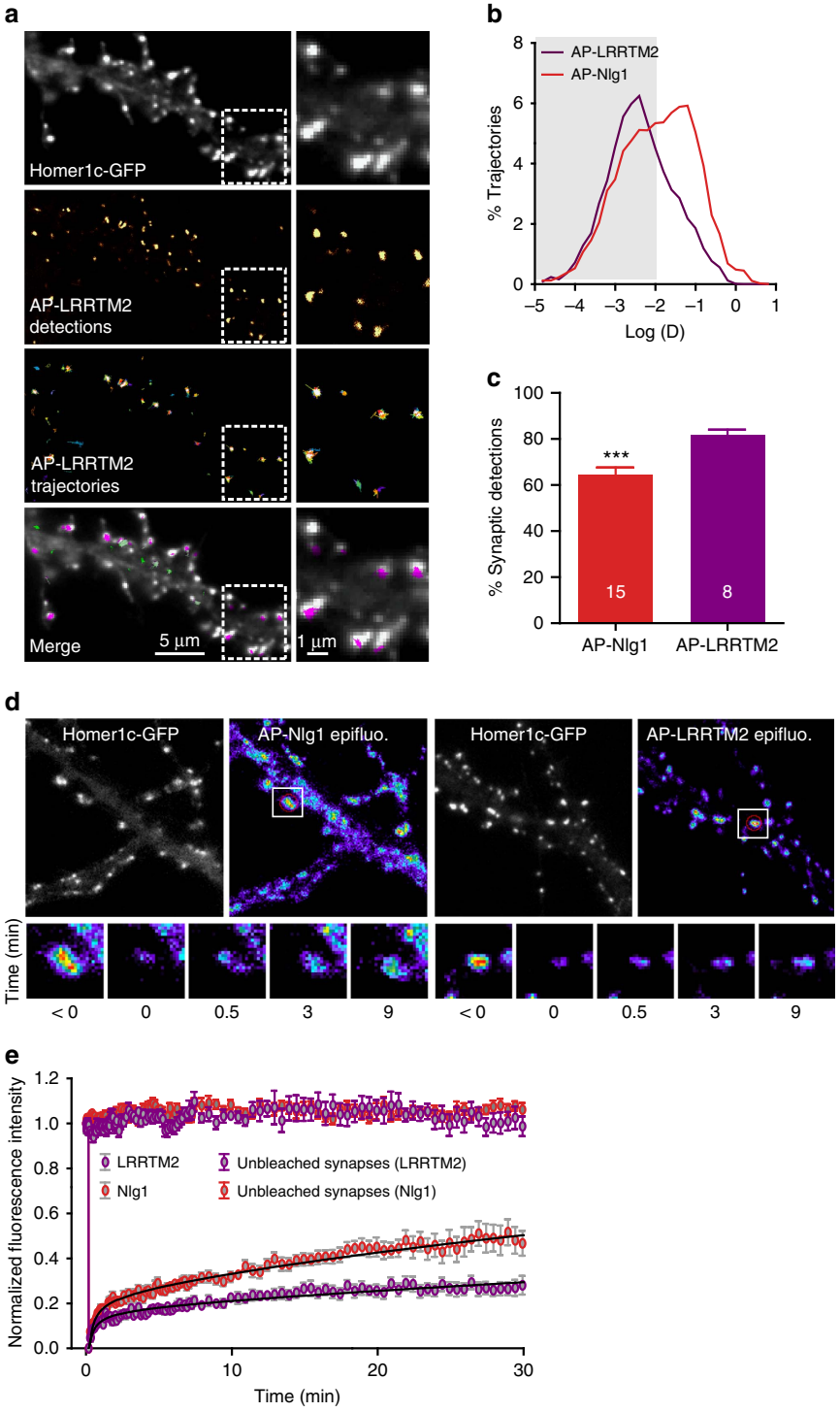

Figure 6 | Comparison of Nlg1 and LRRTM2 dynamics in mature hippocampal neurons. (**a**) DIV 15 neurons expressing AP-LRRTM2, Homer1c-GFP and $BirA^{ER}$ were labelled using mSA-Atto 594 for uPAINT imaging of single LRRTM2 molecules. Super-resolved localization and trajectory maps are shown (green, fast-diffusing molecules, magenta, slow-moving molecules). Note the absence of diffusion on dendritic shafts. (**b**) Semi-log distribution of AP-LRRTM2 and AP-Nlg1 diffusion coefficients. (**c**) Corresponding percentage of synaptic LRRTM2 and Nlg1 detections by uPAINT (LRRTM2, $n=8$; Nlg1, $n=15$ cells from three different experiments). (**d**) FRAP experiments performed on AP-Nlg1 and AP-LRRTM2 labelled with mSA-Atto594. (**e**) Corresponding normalized fluorescence recovery curves. The intensity of unbleached synapses is shown as control for observational photobleaching. Solid lines represent fits of the mean data points with the diffusion-reaction equation given in the Methods. The parameters obtained for Nlg1 and LRRTM2 were the fraction of free molecules $\phi=0.27$ and 0.19 and the turnover rate of adhesions $k_{reac}=1.4\times10^{-2}$ and $5.0\times10^{-3}\,min^{-1}$, respectively. The ratio of all synaptic molecules versus free molecules ($1/\phi$) gives 3.5 for Nlg1 and 5.1 for LRRTM2, closely corresponding to the synaptic enrichment values measured by dSTORM (Nlg1, $n=25$; LRRTM2, $n=18$; Nlg1 unbleached, $n=10$; LRRTM2 unbleached, $n=8$ cells for each condition from three different experiments).

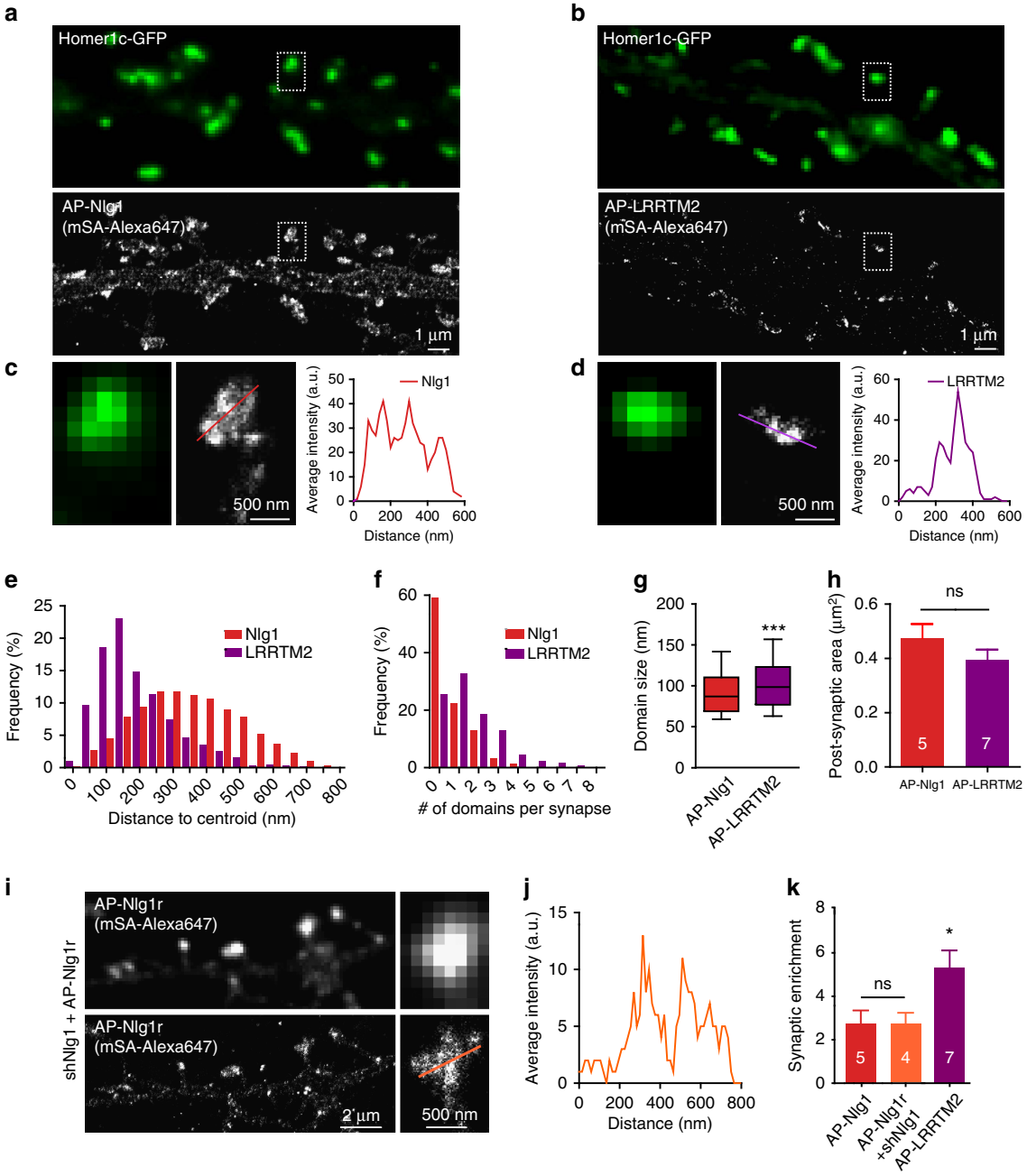

Figure 7 | Comparison of Nlg1 and LRRTM2 organization in mature hippocampal neurons. (**a**,**b**) DIV 15 neurons expressing either AP-Nlg1 or AP-LRRTM2, plus Homer1c-GFP and BirA^{ER} were labelled at high density with mSA-Alexa 647 for dSTORM imaging. Integrated densities over 40,000 frames are shown. (**c**,**d**) AP-Nlg1 and LRRTM2 fluorescence across linescans represented in **a,b** insets show local fluorescence accumulation within synapses. (**e**) Dispersion of AP-Nlg1 and AP-LRRTM2 molecules within synapses represented as the distribution of distances from individual synaptic detections relatively to the centroid of the Homer1c-GFP signal (LRRTM2, $n=7$; Nlg1, $n=5$). (**f**) Distribution of the number of locally enriched AP-Nlg1 and AP-LRRTM2 domains within synapses (LRRTM2, $n=7$; Nlg1, $n=5$). (**g**) The median sizes of AP-Nlg1 and AP-LRRTM2 locally enriched synaptic domains (Nlg1, 87.00, IQR 68–110, $n=5$; LRRTM2, 98.35, IQR 76–122, $n=7$; $^{***}P<0.0001$). (**h**) Synaptic area in DIV 15 neurons electroporated with AP-Nlg1 or AP-LRRTM2 based on the Homer1c-GFP signal. (**i**) Representative STORM image of AP-Nlg1r expressed on a knockdown background in DIV 15 rat neurons, shown with the corresponding low-resolution mSA-Atto647 labelling. (**j**) Average intensity corresponding to the linescan in **i** showing local AP-Nlg1r fluorescence accumulation within a spine in a knockdown background, similar to AP-Nlg1. (**k**) Synaptic enrichment of AP-Nlg1, AP-Nlg1r co-expressed on a knockdown background and AP-LRRTM2 with respect to shaft levels (AP-Nlg1, 2.73 ± 0.62, $n=5$; AP-Nlg1r, 2.54 ± 0.34, $n=4$; AP-LRRTM2, 5.29 ± 0.81 $n=7$; $^{*}P<0.05$). Data are from three different experiments for AP-Nlg1 and AP-LRRTM2, and two experiments for AP-Nlg1r.

scheme, we were able to explore real-time single-molecule dynamics at the nanoscale level (uPAINT), and to map representative protein organization at a precise time point to measure local densities within immobile structures (STED and dSTORM).

Antibodies are commonly used for labelling; however, high-quality antibodies compatible with live imaging are not always available, a critical issue for the synaptic adhesion molecules studied here. Furthermore, our comparison of monomeric (mSA), dimeric (antibody) and tetrameric (streptavidin) probes clearly

shows that, for live SRI applications, probe multivalence affects the measurements by generating artificial nanoscale clusters and biasing protein diffusion. For single-particle-tracking applications, mSA-Atto conjugates represent a significant improvement over large and multivalent nanoparticles such as antibody- or streptavidin-coated quantum dots, which often get sequestered at the periphery of the postsynaptic density because of steric hindrance[31,32,47]. However, because of their resistance to photobleaching compared with organic fluorophores, nanoparticles will remain a method of choice to track molecules for long durations, even more so with the recently developed non-blinking fluorescent nanoparticles[48,49]. mSA labelling is in many regards comparable to that of anti-GFP nanobody labelling, an example of monovalent detection recently used in SRI[13]. In some cases, however, labelling with mSA may be advantageous if the use of GFP as an antigenic tag is problematic. Indeed, the 15-amino-acid AP tag, which is similar in size to other commonly used epitopes, such as FLAG or c-Myc, can be readily inserted between structural domains or within protein loops with minimal perturbation of the native function. We demonstrated this point by fusing the AP tag on a short extracellular loop of stargazin that was previously targeted with an engineered HA tag[36], whereas FP insertion at this location resulted in a dramatic mislocalization of the resulting fusion construct.

A benefit of developing an orthogonal technique of comparable capability includes the potential for dual-colour SRI. To this end, we simultaneously applied mSA and GFP nanobody labelling of *trans*-synaptic contacts in hippocampal neurons to reveal a differential dynamic organization of the two main Nrx1β adhesion partners at excitatory synapses, namely Nlg1 and LRRTM2. We showed a diffusional trapping of presynaptic Nrx1β and postsynaptic Nlg1, resulting in selective *trans*-synaptic apposition of those proteins at axon–dendrite contacts. Labelling of Nrx1β/Nlg1 complexes was rapid with both mSA and GFP nanobody, neither of which affected their intrinsic interaction. In contrast, some labelling strategies, such as GFP complementation, have intrinsically slower kinetics owing to GFP folding and can artificially increase the binding strength between Nrx and Nlg, thus enhancing synaptogenesis[38]. That Nrx1β escaped synapses more readily than Nlg1 on EGTA treatment suggests that the molecule may be retained at pre-synapses through extracellular calcium-dependent interactions, for example, with Nlgs and LRRTMs. This observation is consistent with the report that the Nrx intracellular domain is dispensable for Nlg1-induced presynaptic differentiation[50]. Nlg1 may be anchored at the synapses not only via extracellular interactions with Nrxs but also via intracellular interactions with PSD-95, which may be promoted by Nrx1β binding[32].

Whether adhesion molecules are functionally regulated by synaptic activity remains an important, unresolved issue. Nlg1 interacts directly with the extracellular domain of NMDA receptors[51] and Nlg1 knockdown affects NMDAR-mediated synaptic transmission[52,53]. In addition, the synaptogenic effect induced by Nlg1 expression is abolished by chronic blockade of NMDA receptor activity[53], whereas synapse elimination caused by the absence of Nlgs and LRRTMs is promoted by calcium-calmodulin kinase II (CamKII)-dependent synaptic activity[54]. Our results show that both Nlg1 and Nrx1β *trans*-synaptic clusters rapidly vanish on NMDA treatment, suggesting that Nlg1 plays a role in activity-dependent synaptic remodelling through NMDA receptor activity. Proteolytic shedding of Nlg1 at the cell membrane by the metalloprotease MMP9 (ref. 55) or altered export of Nlg1 through phosphorylation by CamKII (ref. 56) provide possible mechanisms. In contrast to Nlg1, LRRTM2 is less mobile and is confined in more compact synaptic domains, suggesting that the molecule plays a strong role in maintaining *trans*-synaptic connectivity. This specific function of LRRTM2 might be achieved through direct extracellular interactions with presynaptic Nrxs or with postsynaptic AMPA receptors[43], the latter playing a retrograde role on presynaptic differentiation[57]. Indeed, alternative splicing of presynaptic Nrx3 decreases both postsynaptic LRRTM2 and AMPA receptor levels[58], and LRRTM knockdown alters AMPA receptor-mediated synaptic transmission and plasticity[52]. Both the number and size of synaptic LRRTM2 clusters match the recently identified AMPA receptor nanodomains[59], suggesting that they may be structurally and/or functionally related. One interesting mechanism could be that extrasynaptic surface-diffusing AMPA receptors get dynamically trapped at Nrx1β/Nlg1 adhesions through PSD-95 scaffolds[31,33], and then become stabilized at synapses by more durable interactions with LRRTM2.

Obtaining a more integrated view of the molecular ultrastructure of the synapse requires multicolour SRI of adhesion molecules, scaffolding proteins and neurotransmitter receptors. The penetrability and labelling efficiency reached with mSA, together with targeted expression of adhesion proteins such as Nrx and Nlg in intact organisms[60] and improved optical detection in deep tissue[61], should enable further investigation of activity-dependent modulation of synaptic protein organization with high spatial and temporal resolution. In addition to addressing specific questions in neuroscience, the mSA-based labelling strategy constitutes a significant progress towards developing a robust staining technique for fluorescence-based super-resolution microscopy, which should stimulate its application to a wide range of questions in fundamental biology.

Methods

DNA plasmids. The AP-Nlg1, AP-Nrx1β, pDisplay-HA-6His-AP-CFP and BirA^{ER} constructs[21,23] were kind gifts from A. Ting (MIT, Boston). HA-Nlg1 and short hairpin RNA to Nlg1 (shNlg1) were obtained from P. Scheiffele (Biozentrum, Basel). The AP-Nlg1 rescue was generated by changing the nucleotide sequence of AP-Nlg1 recognized by the shNlg1 5′-gaaggtactggaaatctg-3′ to 5′-gaGggCacGggTaaCTtg-3′, using silent mutations. Myc-LRRTM2 (ref. 43) was a gift from J. de Wit (Leuwen, Belgium). Nlg1 with GFP insertion at position 728aa (Nlg1-GFP) was generously provided by T. Dresbach (Goettingen, Germany)[62]. AP-LRRTM2 was generated using the In-Fusion HD Cloning kit (Clontech), replacing the myc-tag from myc-LRRTM2 by the AP Tag (amino-acid sequence GLNDIFEAQKIEWHE). The AP tag sequence was amplified from pDisplay-HA-6His-AP-CFP. Oligonucleotides used were as follows: LRRTM2-1F, 5′-ACTAGTTGTCCACCCAAATG-3′; LRRTM2-2R, 5′-GCTAGCCGCCATACCCAG-3′; AP-5F, 5′-GGTATGGCGGC TAGCggcctgaacgatatcttcg-3′; AP-6R, 5′-GGGTGGACAACTAGTctcgtgccactc gatctt-3′. Homer1cGFP was a gift from S. Okabe (Tokyo University, Japan). BFP-Nrx1β was derived from human GFP-Nrx1β (gift from M. Missler, Münster University, Germany) by replacing the GFP sequence by PCR-amplified-EBFP2 from pEBFP2-Nuc (obtained from Addgene, plasmid 14893). AP-SEP-transferrin receptor was a kind gift from D. Perrais (IINS Bordeaux). HA-stargazin[36] was a gift from R. Nicoll (UCSF, USA). AP-stargazin was obtained by inserting a synthetic fragment containing the AP tag between residues 50 and 51 (in the first extracellular loop, same position as HA-stargazin) using HindIII and BspEI restriction sites. For comparison of the impact of FP insertion, mCherry was inserted into the same stargazin construct either at the same position as the AP tag (first extracellular loop, between residues 50 and 51, AgeI and NheI restriction sites) or at position −56 (BglII site) with respect to the C terminus (cytoplasmic tail). The plasmid for bacterial expression of the anti-GFP nanobody[14] was a kind gift from Alexis Gautreau (LEBS, Gif-sur-Yvette, France). mSA was subcloned from the previously described pRSET-A vector[25,26] into pET-IG, a homemade vector derived from pET-24 (Novagen) and engineered to incorporate after the start codon a decahistidine tag immediately followed by a Tobacco Etch Virus cleavage site (-ENLYFQS-) and no tag on the C terminus.

Protein expression and purification. Nrx1β-Fc was obtained as follows. Conditioned medium from a stable hygromycin-resistant HEK cell line producing Nrx1β-Fc lacking splice insert 4 was collected, and recombinant Nrx1β-Fc was purified on a protein G column (HiTrap Protein G HP, GE Healthcare) to a concentration of 0.6–1.0 mg ml^{-1} (refs 31,32). mSA was produced similarly to previously reported methods[25,26], with slight modifications. Briefly, pET-IG-mSA was transformed into E. Coli BL21 codon plus (DE3)-RIL and expressed for 12 h at

16 °C in 300 ml using an autoinduction protocol[63]. The cells were harvested and resuspended in 9% NaCl, transferred into a conical tube and kept at −80 °C until purification. The cell pellet was thawed and resuspended in 40 ml of freshly prepared denaturing lysis buffer (50 mM Tris acetate, pH 8.0, 8 M urea and 40 µl Protease Cocktail III from Calbiochem) and gently mixed for 30 min at 4 °C. Cells were lysed by sonication and lysates were cleared by centrifugation at 10,000*g* (60 min, 4 °C). HIS-Buster Cobalt Affinity gel (AMOCOL, 1 ml) was added and incubated with the supernatant for 2 h at 4 °C. The resin was collected, washed extensively with washing buffer (50 mM TrisOAc, pH 8.0, 300 mM NaCl, 5 mM imidazole and 8 M urea, freshly prepared) and the protein was eluted with 3 × 1 ml of elution buffer (50 mM TrisOAc, pH 8.0, 300 mM NaCl, 500 mM imidazole, 8 M urea, freshly prepared). The elution fractions were added drop by drop to 40 ml of ice-cold PBS buffer (5 mM Na_2HPO_4, 5 mM NaH_2PO_4 and 150 mM NaCl) containing 0.3 mg ml^{-1} d-biotin, 0.2 mg ml^{-1} oxidized glutathione and 1 mg ml^{-1} reduced glutathione under rapid stirring to refold the protein. The precipitates were removed by centrifugation. The refolded protein was concentrated to ∼1 mg ml^{-1} using Amicon Ultra centrifugal filters with a 10-kDa cutoff. The anti-GFP nanobody was expressed in the same conditions as mSA and purified under native conditions by affinity chromatography using the HIS-Buster Nickel Affinity gel. The protein was dialysed in PBS buffer and concentrated to ∼1 mg ml^{-1} using Amicon Ultra centrifugal filters with a 10-kDa cutoff. mSA and anti-GFP nanobody were kept at 4 °C and used for coupling to fluorophores within 24 h. The modified, negatively charged biotin (Biot-DDDY-COOH) to reduce membrane permeability[27] was obtained by manual standard Fmoc-based solid-phase peptide synthesis.

Protein and antibody coupling to fluorophores. All proteins (mSA, anti-GFP nanobody, streptavidin (85878, Sigma-Aldrich), mouse monoclonal anti-biotin (03-3700, Invitrogen)) were prepared in PBS at ∼1 mg ml^{-1}. Coupling to Atto 647N, Atto 594 and Alexa 647 was performed following the recommended procedures from the manufacturers (ATTO-TEC and Life Technologies) with the corresponding NHS ester derivatives of each dye. Briefly, labelling was conducted in the dark at room temperature for 1 h. Excess dye was removed using Sephadex G-25 medium (PD MiniTrap G-25, GE Healthcare) by elution with PBS. mSA-Atto 647N, mSA-Atto 594, mSA-Alexa 647 and the Atto 647N-GFP nanobody were further purified to homogeneity by size exclusion chromatography with a Superdex 75 HiLoad 16/60 column (GE Healthcare) on an AKTA purifier system (GE Healthcare) using PBS as a running buffer. Labelled proteins were concentrated to ∼0.2 mg ml^{-1} using Amicon Ultra centrifugal filters with a 10-kDa cutoff. All proteins were aliquoted and flash-frozen for storage at −80 °C until use.

Cell culture and electroporation. Gestant rat females were purchased weekly (Janvier Labs, Saint-Berthevin, France), while wild-type and Nlg1 KO mouse strains obtained from F. Varoqueaux and N. Brose (MPI Goettingen) were raised in our animal facility. Animals were handled and killed according to European ethical rules. Dissociated hippocampal neurons from E18 Sprague–Dawley rat embryos or P0 mice (from Nlg1 WT or KO background) were prepared as described[64], and electroporated with the Amaxa system (Lonza) using 500,000 cells per cuvette. The following plasmid combinations were used: (GFP or Homer1c-GFP) + $BirA^{ER}$ + (AP-Nlg1, AP-LRRTM2, AP-STG or AP-Nrx1β) (1.5:1.5:1.5 µg DNA), BFP-Nrx1β or GFP-Nrx1β (4.5 µg DNA), Nlg1-GFP (4 µg DNA). Electroporated neurons were resuspended in Minimal Essential Medium supplemented with 10% horse serum (MEM-HS) and plated on 18-mm coverslips previously coated with 1 mg ml^{-1} polylysine for 2 h at a concentration of 50,000 cells per coverslip. Three hours after plating, coverslips were flipped onto 60-mm dishes containing a glial cell layer in Neurobasal medium (NB for rat cultures or NB-A for mouse cultures) supplemented with 2 mM L-glutamine and 1 × NeuroCult SM1 Neuronal supplement (STEMCELL Technologies) and cultured for 2 weeks at 37 °C and 5% CO_2. Astrocyte feeder layers were prepared from the same embryos, plated between 20,000 and 40,000 cells per 60-mm dish and cultured in MEM (Fisher Scientific, cat. no. 21090-022) containing 4.5 g l^{-1} Glucose, 2 mM L-glutamine and 10% horse serum (Invitrogen) for 14 days. For biochemistry experiments, electroporated neurons from rats or mice were seeded in a six-well plate coated with 1 mg ml^{-1} polylysine for 2 h at a concentration of 500,000 cells per well. Three hours after plating, the medium was replaced by conditioned Neurobasal medium (rat) or Neurobasal-A medium (mice), supplemented with 2 mM L-glutamine and 1 × NeuroCult SM1 Neuronal supplement (STEMCELL Technologies) and renewed every 3–4 days. Ara-C (3.4 µM) was added at DIV 3 and DIV 13. COS-7 and HEK-293 cells were cultured in DMEM (GIBCO/BRL) supplemented with 10% fetal bovine serum, 100 units ml^{-1} penicillin and 100 µg ml^{-1} streptomycin. Heterologous cells were electroporated with TfR-SEP-AP + $BirA^{ER}$ (1.5:2 µg DNA for 2 million cells) or stargazin-mcherry (3.5 µg DNA for 2 million cells) constructs with the Amaxa system (Lonza) using 500,000 cells per cuvette.

Neuronal lysates. DIV 14 mouse or rat neuronal cultures were rinsed in ice-cold PBS, and then scraped into 100 µl RIPA buffer (50 mM HEPES, 10 mM EDTA, 0.1% sodium dodecyl sulfate, 1% IGEPAL CA-630 and 0.5% sodium deoxycholate, pH = 7.2). Homogenates were kept 15 min on ice and centrifuged at 8,000*g* for 15 min at 4 °C to remove cell debris. Ten microlitres per condition were loaded for western blots.

SDS–PAGE and immunoblotting. Samples were separated by TGX stain-free precast gels (4-15% gradient, Bio-Rad), ultraviolet-activated with ChemiDoc Touch system (Bio-Rad) for direct imaging of total proteins and then transferred to nitrocellulose membranes for immunoblotting analysis. After blocking with 5% non-fat dried milk in Tris-buffered saline Tween-20 (TBST; 28 mM Tris, 136.7 mM NaCl, 0.05% Tween-20, pH 7.4) for 45 min at room temperature, membranes were incubated with rabbit anti-Nlg1 (129013, Synaptic systems) diluted at 1:1,000 with 0.5% non-fat dried milk in TBST, followed by horse radish peroxidase-conjugated anti-rabbit antibody (Jackson ImmunoResearch) for 1 h at room temperature. Target proteins were detected by chemiluminescence with Super signal West Dura (Pierce) on the ChemiDoc Touch system (Bio-Rad). The theoretical molecular weight of Nlg1 is 93 kDa, but the apparent molecular weight in immunoblots is ∼130 kDa, likely due to glycosylations[65]. For quantification, the intensity of the chemiluminescence signal of each lane was normalized by the total protein signal on the same lane, revealed by the stain-free technology.

Organotypic cultures and single-cell electroporation. Organotypic hippocampal slice cultures were prepared from either wild-type or Nlg1 KO mice (C57Bl6/J strain), as described below[66]. Briefly, animals at postnatal day 4–6 were quickly decapitated and their brains placed in ice-cold Gey's balanced salt solution under sterile conditions. Hippocampi were dissected out and coronal slices (350 µm) were cut using a tissue chopper (McIlwain) and incubated with serum-containing medium on Millicell culture inserts (CM, Millipore). The medium was replaced every 2–3 days. After 3–4 days in culture, CA1 pyramidal cells were processed for single-cell electroporation with plasmids encoding enhanced GFP (EGFP) along with AP-Nlg1 and $BirA^{ER}$ in equal proportions. The pipette containing 33 ng µl^{-1} total DNA was placed close to the soma of individual CA1 pyramidal neurons. Electroporation was performed by applying three square pulses of negative voltage (10 V, 20 ms duration) at 1 Hz, and then the pipette was gently removed. Three to five neurons were electroporated per slice, and the slice was placed back in the incubator for several days before imaging.

Single Molecule Tracking (uPAINT). uPAINT experiments were carried out as previously reported[8]. Cells were mounted in Tyrode solution (15 mM D-glucose, 108 mM NaCl, 5 mM KCl, 2 mM $MgCl_2$, 2 mM $CaCl_2$ and 25 mM HEPES, pH 7.4) containing 1% globulin-free BSA (Sigma) in an open Inox observation chamber (Life Imaging Services, Basel, Switzerland). The chamber was placed on an inverted microscope (Nikon Ti-E Eclipse) equipped with an EMCCD camera (Evolve, Roper Scientific, Evry, France), a thermostatic box (Life Imaging Services) providing air at 37 °C and an apochromatic (APO) total internal reflection fluorescence (TIRF) × 100 oil 1.49 numerical aperture (NA) objective. BFP- and GFP-expressing cells were detected using a mercury lamp (Nikon Xcite) and the following filter sets (SemROCK, USA): BFP (excitation: FF01-379/34; dichroic: FF-409Di03; emission: FF01-440/40); EGFP (excitation: FF01-472/30; dichroic: FF-562Di02; emission: FF01-593/40). Cells expressing the different AP constructs, or BFP- or GFP- Nrx1β, were labelled using low concentrations of Atto 594-conjugated mSA, Atto 594-conjugated streptavidin and Atto 594-anti-biotin, or Atto 647N- and 594-conjugated GFP nanobody (1 nM) to isolate single molecules. The GFP nanobody recognizes BFP, given the high sequence homology with GFP. A four-colour laser bench (405; 488; 561; and 642 nm, 100 mW each; Roper Scientific) is connected through an optical fibre to the TIRF illumination arm of the microscope. Laser powers were controlled through acousto-optical tunable filters driven by the Metamorph software (Molecular Devices, USA). Atto 594 and Atto 647N were excited with the 561- and 642-nm laser lines through a four-band beam splitter (BS R405/488/561/635, SemRock). Samples were imaged by oblique laser illumination, allowing the excitation of individual Atto-conjugated ligands bound to the cell surface, without illuminating ligands in solution. Fluorescence was collected using FF01-617/73 and FF01-676/29 nm emission filters (SemRock), respectively, placed on a filter wheel (Suter). Stacks of 2,000–4,000 consecutive frames were obtained from each cell, with an integration time of 20–50 ms. Multicolour fluorescent 100-nm beads (Tetraspeck, Invitrogen) were used to register long-term acquisitions and correct for lateral drifts. In some experiments, EGTA (10 mM) was applied directly in the bath and left for 10 min. For NMDA experiments, a Gilson perfusion system was used to perfuse and change the medium up to 1 h during acquisitions. Neurons were perfused with Tyrode solution containing the fluorescent labels during the whole acquisition time. Cells were recorded in control solution for 10 min, treated with 20 µM NMDA in Tyrode for 10 min and allowed to recover in control solution for 10 min. Control cells were kept in Tyrode solution the whole time. Acquisitions were steered using the Metamorph software (Molecular Devices) in a streaming mode at 50 Hz. Cycles of two consecutive series of acquisitions were made sequentially up to 1 h. One series corresponds to GFP (20 frames, 50 Hz), mSA-Atto 594 (1,500 frames, 50 Hz) and Atto 647N-GFP nanobody (1,500 frames, 50 Hz).

Trajectory analysis and image reconstruction. Image stacks were analysed using a custom programme running on Metamorph based on wavelet segmentation for localization and simulated annealing algorithms for tracking, described earlier[67,68]. The programme allows both the reconstruction of the super-resolution image by summing the positions of localized single molecules into a single image, and tracking of localized molecules through successive images. The instantaneous

diffusion coefficient, D, was calculated for each trajectory from linear fits of the first 4 points of the mean square displacement (MSD) function versus time. Slow trajectories were defined as trajectories with diffusion coefficients below $0.0093 \sim 0.01\ \mu m^2\,s^{-1}$ (Supplementary Fig. 4). This threshold corresponds to molecules exploring a region smaller than that defined by the spatial resolution of the system ($\sim 0.054\ \mu m$, full-width at half-maximum) during the time used to fit the initial slope of the MSD (4 points, 20 ms) and is given by $D_{threshold} = (0.054\ \mu m)^2/(4 \times 4 \times 0.02\ s) \sim 0.0093\ \mu m^2\,s^{-1}$, as described earlier[16]. Spatial resolution was determined using fixed Atto samples. Overall, 415 two-dimensional (2D) distributions of single-molecule positions belonging to long trajectories (>10 frames) were measured by bi-dimensional Gaussian fitting and the resolution determined as $2.3\sigma_{xy}$, where σ_{xy} is the pointing accuracy. For trajectory analysis, synapses were identified by wavelet-based image segmentation of the Homer1c-GFP postsynaptic marker. The corresponding binary masks were used to sort single-particle data analyses to specific synaptic regions. For NMDA experiments, each mSA and nanobody sequence was analysed separately as described, and data were pooled over 10-min intervals, to obtain representative trajectories of protein populations. The percentage of synapses containing Nlg1 was defined as the ratio between synapses containing at least 10 detections of AP-Nlg1 over the total number of synapses on super-resolved images obtained in the same conditions for mSA and biotin antibody. Synaptic coverage was determined from super-resolved detection maps as the ratio between threshold areas containing detections over a whole synaptic region determined from the low-resolution Homer1c signal. The percentage of synaptic detection is defined as the number of detections within synapses defined by Homer1c divided by the total number of detections. For dual-colour imaging of Nlg1 and Nrx1β, areas with high signal density were identified as domains by wavelet segmentation. Their number and size were extracted from 2D isotropic Gaussian fitting, and their length was determined as the full-width at half-maximum. In the supplemental figures, the number of objects per frame was analysed using the 'Analyse Particles' plugin in ImageJ and averaged per stack of 2,000 frames acquired every 50 ms, and the number of trajectories per 10 µm was determined as the average number of trajectories per dendritic segments of 10 µm. MSD analysis was performed by filtering trajectories with $D<0.01$ or $D>0.01\ \mu m^2\,s^{-1}$ (Supplementary Fig. 4). The MSD curve as a function of time for $D<0.1\ \mu m^2\,s^{-1}$ was fitted by one-phase association curve on GraphPad to extract the confinement area, which was estimated to be ~ 118 nm.

dSTORM. Primary cultured neurons co-expressing Homer1c-GFP, BirA^{ER} and AP-Nlg1 or CA1 neurons in organotypic slice cultures from Nlg1 KO mice that were single-cell-electroporated with GFP, BirA^{ER} and AP-Nlg1 were surface-labelled with a high concentration (100 nM) of mSA-Alexa647, biotin antibody-Alexa647 or streptavidin-Alexa647 in Tyrode solution for 10 min, and were rinsed and fixed with 4% PFA–0.2% glutaraldehyde in PBS–BSA 1% for 10 min at room temperature or 2 h at 4 °C. dSTORM imaging of cultured neurons and astigmatic-based 3D dSTORM imaging of organotypic brain slices on neurons located close to the coverslip surface was performed. We used an inverted motorized microscope (Nikon Ti, Japan) equipped with a $\times 100$ 1.49NA PL-APO objective and a perfect focus system, allowing long acquisition in oblique illumination mode. Both the ensemble and single-molecule fluorescence were collected by using a quad-band dichroic filter (Di01-R405/488/561/635, Semrock). The fluorescence was collected using a sensitive EMCCD (Evolve, Photometrics, USA). For 3D imaging in organotypic brain slices, astigmatism was applied using an adaptive optics system (MicAO—Imagine Optic). 3D calibration was established using 100-nm fluorescent beads (Tetraspeck, Life Technologies) adhered to the slice surface. Single-molecule localization and reconstruction was performed online with automatic feedback control of the lasers using WaveTracer module, enabling optimal single-molecule density during the acquisition[68]. The acquisition and localization sequences were driven by MetaMorph (Molecular Devices) in a streaming mode at 50 frames per second (20-ms exposure time) using an area equal to or less than 256×256 pixel region of interest. The brain slice was mounted in an oxygen-scavenging imaging buffer[6] and sealed between two glass coverslips. Images were composed of 1,038,506 localizations analysed from 64,000 frames, over which sample drift was corrected by localizing and tracking the displacement of cellular autofluorescence. Super-resolution reconstructions were generated with the VISP software[69], and detection density maps were generated with a neighbourhood radius of 400 nm. The resulting lateral resolution is 20 nm for primary neuronal cultures and 50 nm for slice cultures, while the axial resolution is ~ 50 nm. The number of clusters per µm^2 was determined by wavelet segmentation based on areas with strong signal intensity compared with neighbouring areas[67,68] on the super-resolved dSTORM images generated from 40,000 frames. Synaptic enrichment was defined as the ratio between the average number of synaptic detections (area given by the Homer1c-GFP signal) and the average number of extrasynaptic detections. The dispersion of Nlg1 and LRRTM2 molecules compared with Homer centroid was computed as the distribution of the distances between each detection event and the Homer centroid. Enrichment domains were defined by wavelet segmentation of areas with higher labelling densities relatively to neighbouring environment as illustrated by the linescans in Fig. 7, and their number per synapse was counted for LRRTM2 and Nlg1. Domain sizes were extracted from 2D isotropic Gaussian fittings as the average full-width at half-maximum.

STED imaging and data analysis. CA1 neurons co-expressing EGFP, BirA^{ER} and AP-Nlg1 in organotypic slices from wild-type mice were surface-labelled with high concentration of mSA-Atto647N (100 mM) in Tyrode solution for 10 min, rinsed, observed live using a commercial STED microscope (TCS SP5, Leica) and thermostated to 37 °C. STED illumination of Atto 647N was performed using a 633-nm pulsed laser providing excitation, and a pulsed bi-photon laser (Mai Tai; Spectra-Physics) tuned to 765 nm and going through a 100-m optical fibre to enlarge pulse width (100 ps) used for depletion. A doughnut-shaped laser beam was achieved through two lambda plates. Fluorescence light between 650 and 740 nm was collected using a photomultiplier, using a HCX PL-APO CS $\times 100$/1.40 NA oil objective and a pinhole open to one time the Airy disk (60 µm). A fivefold zoomed area of 512×512 pixels, corresponding to a pixel size of 30 nm, was scanned at 50 Hz. In-depth acquisitions were performed by scanning hippocampal slices with an increment of 1 µm in z over 60 µm. When indicated, raw data were deconvoluted using the measured point spread function of the system and the Richardson–Lucy algorithm with Huygens Professional (Huygens Software). 3D reconstructed movies were made using Imaris (Bitplane).

FRAP experiments and analysis. Neurons electroporated with Homer1c-GFP, BirA^{ER} and AP-Nlg1 or AP-LRRTM2 and cultured for 2 weeks were labelled with high concentration of mSA-Atto594 (100 nM) for 10 min, and then rinsed, mounted in Tyrode solution and observed under the same set-up used for uPAINT. The laser bench (comprising 488, 561 and 642 nm lasers, 100 mW each, Roper Scientific) has a second optical fibre output connected to an illumination device containing galvanometric scanning mirrors (ILAS, Roper Instrument) steered by MetaMorph. It allows precise spatial and temporal control of the focused laser beam at any user-selected region of interest within the sample for targeted photobleaching. Switching between the two fibres for alternating between imaging and bleaching is performed in the millisecond range using a mirror. Oblique illumination acquisition was performed using the 561-nm laser at low power (300 µW at the front of the objective) to precisely image molecules accumulated at the substrate level. After acquiring a 10-s baseline at 0.5–1 Hz frame rate, rapid selective photobleaching of two to three synapses was achieved at higher laser power (3 mW at the front of the objective) during 200–300 ms. Fluorescence recovery was then recorded immediately after the bleach sequence for 30 min at a 0.5–1 Hz frame rate. Observational photobleaching was kept very low, as assessed by observing control synapses nearby. Data were plotted as normalized fluorescence intensity versus time and fitted by the formula[44]: $\phi\ [1 - \mathrm{erf}(1/(2\sqrt{k_{diff}t})] + (1-\phi)[1 - \exp(-k_{reac}t)]$, where ϕ is the fraction of synaptic Nlg1 or LRRMT2 molecules diffusing freely with coefficient D, k_{diff} (in min^{-1}) is a characteristic diffusive rate equal to D/r^2 (where r is the radius of the bleached area), $(1-\phi)$ the fraction of molecules trapped in adhesive interactions with presynaptic Nrx1β and k_{reac} (in min^{-1}) the turnover rate of bound molecules. In this model, the synaptic enrichment of Nlg1 or LRRTM2 at synapses is equal to the total number of molecules (bound + free) versus free molecules, that is, the ratio $1/\phi$. In control experiments, FRAP was performed on DIV 15 neurons electroporated with Nlg1-GFP using a 488-nm laser power of either 0.4 or 4 mW at the front of the objective.

Confocal microscopy. Single electroporated neurons from organotypic slice culture co-expressing GFP, BirA^{ER} and AP-Nlg1 were surface-labelled with mSA-Atto 647N, biotin antibody-Atto594 or streptavidin-Atto 647N in artificial cerebrospinal fluid (ACSF) (in mM, 125 NaCl, 2.5 KCl, 2 $CaCl_2$, 1 $MgCl_2$, 25 $NaHCO_3$, 1.25 NaH_2PO_4 and 25 glucose, pH 7.4) for 10 min or 1 h, rinsed and fixed with 4% PFA–0.2% glutaraldehyde in PBS–BSA 1% for 2 h at 4 °C. Images were acquired on a commercial Leica DMI6000 TCS SP5 microscope using a $\times 63$, 1.4 NA oil objective and a pinhole opened to one time the Airy disk. Images of 512×512 pixels were acquired at a scanning frequency of 400 Hz.

Statistics. Statistical values are given as mean ± s.e.m., unless otherwise stated. Statistical significance was calculated using GraphPad Prism. All data sets comparing two conditions were tested by the non-parametric Mann–Whitney test. Data sets containing more than two conditions were compared by one-way analysis of variance test, followed by a *post hoc* Dunn's test. Sample size was based on two to three different cultures per condition, 2–10 cells per experiment. Randomization of samples was performed for all experiments. When critical comparison of different labelling conditions was involved, experiments and image analysis were performed blindly.

References

1. Triller, A. & Choquet, D. New concepts in synaptic biology derived from single-molecule imaging. *Neuron* **59,** 359–374 (2008).
2. Willig, K. I. *et al.* Nanoscale resolution in GFP-based microscopy. *Nat. Methods* **3,** 721–723 (2006).
3. Manley, S. *et al.* High-density mapping of single-molecule trajectories with photoactivated localization microscopy. *Nat. Methods* **5,** 155–157 (2008).
4. Shroff, H., Galbraith, C. G., Galbraith, J. A. & Betzig, E. Live-cell photoactivated localization microscopy of nanoscale adhesion dynamics. *Nat. Methods* **5,** 417–423 (2008).

5. Dani, A., Huang, B., Bergan, J., Dulac, C. & Zhuang, X. Superresolution imaging of chemical synapses in the brain. *Neuron* **68,** 843–856 (2010).
6. Heilemann, M. *et al.* Subdiffraction-resolution fluorescence imaging with conventional fluorescent probes. *Angew. Chem.– Int. Ed. Engl.* **47,** 6172–6176 (2008).
7. Sharonov, A. & Hochstrasser, R. M. Wide-field subdiffraction imaging by accumulated binding of diffusing probes. *Proc. Natl Acad. Sci. USA* **103,** 18911–18916 (2006).
8. Giannone, G. *et al.* Dynamic superresolution imaging of endogenous proteins on living cells at ultra-high density. *Biophys. J.* **99,** 1303–1310 (2010).
9. Huang, B., Babcock, H. & Zhuang, X. Breaking the diffraction barrier: super-resolution imaging of cells. *Cell* **143,** 1047–1058 (2010).
10. Fernández-Suárez, M. & Ting, A. Y. Fluorescent probes for super-resolution imaging in living cells. *Nat. Rev. Mol. Cell Biol.* **9,** 929–943 (2008).
11. Deschout, H. *et al.* Precisely and accurately localizing single emitters in fluorescence microscopy. *Nat. Methods* **11,** 253–266 (2014).
12. Lau, L., Lee, Y. L., Sahl, S. J., Stearns, T. & Moerner, W. E. STED microscopy with optimized labeling density reveals 9-fold arrangement of a centriole protein. *Biophys. J.* **102,** 2926–2935 (2012).
13. Ries, J., Kaplan, C., Platonova, E., Eghlidi, H. & Ewers, H. A simple, versatile method for GFP-based super-resolution microscopy via nanobodies. *Nat. Methods* **9,** 582–584 (2012).
14. Rothbauer, U. *et al.* Targeting and tracing antigens in live cells with fluorescent nanobodies. *Nat. Methods* **3,** 887–889 (2006).
15. Van Bockstaele, F., Holz, J.-B. & Revets, H. The development of nanobodies for therapeutic applications. *Curr. Opin. Investig. Drugs* **10,** 1212–1224 (2009).
16. Rossier, O. *et al.* Integrins β(1) and β(3) exhibit distinct dynamic nanoscale organizations inside focal adhesions. *Nat. Cell Biol.* **14,** 1057–1067 (2012).
17. Liu, D. S., Phipps, W. S., Loh, K. H., Howarth, M. & Ting, A. Y. Quantum dot targeting with lipoic acid ligase and HaloTag for single-molecule imaging on living cells. *ACS Nano* **6,** 11080–11087 (2012).
18. Xue, L., Karpenko, I. A., Hiblot, J. & Johnsson, K. Imaging and manipulating proteins in live cells through covalent labeling. *Nat. Chem. Biol.* **11,** 917–923 (2015).
19. Sekine-Aizawa, Y. & Huganir, R. L. Imaging of receptor trafficking by using alpha-bungarotoxin-binding-site-tagged receptors. *Proc. Natl Acad. Sci. USA* **101,** 17114–17119 (2004).
20. Grunwald, C. *et al.* Quantum-yield-optimized fluorophores for site-specific labeling and super-resolution imaging. *J. Am. Chem. Soc.* **133,** 8090–8093 (2011).
21. Liu, D. S., Loh, K. H., Lam, S. S., White, K. a & Ting, A. Y. Imaging trans-cellular neurexin-neuroligin interactions by enzymatic probe ligation. *PLoS ONE* **8,** e52823 (2013).
22. Stadler, C. *et al.* Immunofluorescence and fluorescent-protein tagging show high correlation for protein localization in mammalian cells. *Nat. Methods* **10,** 315–323 (2013).
23. Howarth, M., Takao, K., Hayashi, Y. & Ting, A. Y. Targeting quantum dots to surface proteins in living cells with biotin ligase. *Proc. Natl Acad. Sci. USA* **102,** 7583–7588 (2005).
24. Howarth, M. *et al.* A monovalent streptavidin with a single femtomolar biotin binding site. *Nat. Methods* **3,** 267–273 (2006).
25. Lim, K. H., Huang, H., Pralle, A. & Park, S. Engineered streptavidin monomer and dimer with improved stability and function. *Biochemistry* **50,** 8682–8691 (2011).
26. Demonte, D., Drake, E. J., Lim, K. H., Gulick, A. M. & Park, S. Structure-based engineering of streptavidin monomer with a reduced biotin dissociation rate. *Proteins* **81,** 1621–1633 (2013).
27. Strassberger, V., Trüssel, S., Fugmann, T., Neri, D. & Roesli, C. A novel reactive ester derivative of biotin with reduced membrane permeability for *in vivo* biotinylation experiments. *Proteomics* **10,** 3544–3548 (2010).
28. Fairhead, M., Krndija, D., Lowe, E. D. & Howarth, M. Plug-and-play pairing via defined divalent streptavidins. *J. Mol. Biol.* **426,** 199–214 (2014).
29. Jones, S. a, Shim, S.-H., He, J. & Zhuang, X. Fast, three-dimensional super-resolution imaging of live cells. *Nat. Methods* **8,** 499–508 (2011).
30. Klein, T. *et al.* Live-cell dSTORM with SNAP-tag fusion proteins. *Nat. Methods* **8,** 7–9 (2011).
31. Mondin, M. *et al.* Neurexin-neuroligin adhesions capture surface-diffusing AMPA receptors through PSD-95 scaffolds. *J. Neurosci.* **31,** 13500–13515 (2011).
32. Giannone, G. *et al.* Neurexin-1β binding to neuroligin-1 triggers the preferential recruitment of PSD-95 versus gephyrin through tyrosine phosphorylation of neuroligin-1. *Cell Rep.* **3,** 1996–2007 (2013).
33. Czöndör, K. *et al.* Unified quantitative model of AMPA receptor trafficking at synapses. *Proc. Natl Acad. Sci. USA* **109,** 3522–3527 (2012).
34. Fu, Y. & Huang, Z. J. Differential dynamics and activity-dependent regulation of alpha- and beta-neurexins at developing GABAergic synapses. *Proc. Natl Acad. Sci. USA* **107,** 22699–22704 (2010).
35. Neupert, C. *et al.* Regulated dynamic trafficking of neurexins inside and outside of synaptic terminals. *J. Neurosci.* **35,** 13629–13647 (2015).
36. Tomita, S., Fukata, M., Nicoll, R. a & Bredt, D. S. Dynamic interaction of stargazin-like TARPs with cycling AMPA receptors at synapses. *Science* **303,** 1508–1511 (2004).
37. Opazo, P. *et al.* CaMKII triggers the diffusional trapping of surface AMPARs through phosphorylation of stargazin. *Neuron* **67,** 239–252 (2010).
38. Tsetsenis, T., Boucard, a. a., Arac, D., Brunger, a. T. & Sudhof, T. C. Direct visualization of trans-synaptic neurexin-neuroligin interactions during synapse formation. *J. Neurosci.* **34,** 15083–15096 (2014).
39. Saint-Michel, E., Giannone, G., Choquet, D. & Thoumine, O. Neurexin/ neuroligin interaction kinetics characterized by counting single cell-surface attached quantum dots. *Biophys. J.* **97,** 480–489 (2009).
40. Beattie, E. C. *et al.* Regulation of AMPA receptor endocytosis by a signaling mechanism shared with LTD. *Nat. Neurosci.* **3,** 1291–1300 (2000).
41. Ko, J., Fuccillo, M. V, Malenka, R. C. & Südhof, T. C. LRRTM2 functions as a neurexin ligand in promoting excitatory synapse formation. *Neuron* **64,** 791–798 (2009).
42. Siddiqui, T. J., Pancaroglu, R., Kang, Y., Rooyakkers, A. & Craig, A. M. LRRTMs and neuroligins bind neurexins with a differential code to cooperate in glutamate synapse development. *J. Neurosci.* **30,** 7495–7506 (2010).
43. de Wit, J. *et al.* LRRTM2 interacts with Neurexin1 and regulates excitatory synapse formation. *Neuron* **64,** 799–806 (2009).
44. Thoumine, O., Lambert, M., Mège, R.-M. & Choquet, D. Regulation of N-cadherin dynamics at neuronal contacts by ligand binding and cytoskeletal coupling. *Mol. Biol. Cell* **17,** 862–875 (2006).
45. Hughes, L. D., Rawle, R. J. & Boxer, S. G. Choose your label wisely: water-soluble fluorophores often interact with lipid bilayers. *PLoS ONE* **9,** e87649 (2014).
46. de Boer, E. *et al.* Efficient biotinylation and single-step purification of tagged transcription factors in mammalian cells and transgenic mice. *Proc. Natl Acad. Sci. USA* **100,** 7480–7485 (2003).
47. Biermann, B. *et al.* Imaging of molecular surface dynamics in brain slices using single-particle tracking. *Nat. Commun.* **5,** 3024 (2014).
48. Mahler, B. *et al.* Towards non-blinking colloidal quantum dots. *Nat. Mater.* **7,** 659–664 (2008).
49. Wu, S. *et al.* Non-blinking and photostable upconverted luminescence from single lanthanide-doped nanocrystals. *Proc. Natl Acad. Sci. USA* **106,** 10917–10921 (2009).
50. Gokce, O. & Sudhof, T. C. Membrane-tethered monomeric neurexin LNS-domain triggers synapse formation. *J. Neurosci.* **33,** 14617–14628 (2013).
51. Budreck, E. C. *et al.* Neuroligin-1 controls synaptic abundance of NMDA-type glutamate receptors through extracellular coupling. *Proc. Natl Acad. Sci. USA* **110,** 725–730 (2013).
52. Soler-Llavina, G. J., Fuccillo, M. V, Ko, J., Sudhof, T. C. & Malenka, R. C. The neurexin ligands, neuroligins and leucine-rich repeat transmembrane proteins, perform convergent and divergent synaptic functions in vivo. *Proc. Natl Acad. Sci. USA* **108,** 16502–16509 (2011).
53. Chubykin, A. a *et al.* Activity-dependent validation of excitatory versus inhibitory synapses by neuroligin-1 versus neuroligin-2. *Neuron* **54,** 919–931 (2007).
54. Ko, J., Soler-Llavina, G. J., Fuccillo, M. V, Malenka, R. C. & Südhof, T. C. Neuroligins/LRRTMs prevent activity- and Ca2 + /calmodulin-dependent synapse elimination in cultured neurons. *J. Cell Biol.* **194,** 323–334 (2011).
55. Peixoto, R. T. *et al.* Transsynaptic signaling by activity-dependent cleavage of neuroligin-1. *Neuron* **76,** 396–409 (2012).
56. Bemben, M. a *et al.* CaMKII phosphorylation of neuroligin-1 regulates excitatory synapses. *Nat. Neurosci.* **17,** 56–64 (2014).
57. Tracy, T. E., Yan, J. J. & Chen, L. Acute knockdown of AMPA receptors reveals a trans-synaptic signal for presynaptic maturation. *EMBO J.* **30,** 1577–1592 (2011).
58. Aoto, J., Martinelli, D. C., Malenka, R. C., Tabuchi, K. & Südhof, T. C. Presynaptic neurexin-3 alternative splicing trans-synaptically controls postsynaptic AMPA receptor trafficking. *Cell* **154,** 75–88 (2013).
59. Nair, D. *et al.* Super-resolution imaging reveals that AMPA receptors inside synapses are dynamically organized in nanodomains regulated by PSD95. *J. Neurosci.* **33,** 13204–13224 (2013).
60. Desbois, M., Cook, S. J., Emmons, S. W. & Bülow, H. E. Directional trans-synaptic labeling of specific neuronal connections in live animals. *Genetics* **200,** 697–705 (2015).
61. Galland, R. *et al.* 3D high- and super-resolution imaging using single-objective SPIM. *Nat. Methods* **12,** 641–644 (2015).
62. Dresbach, T., Neeb, A., Meyer, G., Gundelfinger, E. D. & Brose, N. Synaptic targeting of neuroligin is independent of neurexin and SAP90/PSD95 binding. *Mol. Cell Neurosci.* **27,** 227–235 (2004).
63. Studier, F. W. Protein production by auto-induction in high density shaking cultures. *Protein Expr. Purif.* **41,** 207–234 (2005).

64. Kaech, S. & Banker, G. Culturing hippocampal neurons. *Nat. Protoc.* ***1,*** *2406–2415 (2006).*
65. Dean, C. *et al.* Neurexin mediates the assembly of presynaptic terminals. *Nat. Neurosci.* **6,** 708–716 (2003).
66. Stoppini, L., Buchs, P. A. & Muller, D. A simple method for organotypic cultures of nervous tissue. *J. Neurosci. Methods* **37,** 173–182 (1991).
67. Izeddin, I. *et al.* Wavelet analysis for single molecule localization microscopy. *Opt. Express* **20,** 2081–2095 (2012).
68. Kechkar, A., Nair, D., Heilemann, M., Choquet, D. & Sibarita, J. B. Real-time analysis and visualization for single-molecule based super-resolution microscopy. *PLoS ONE* **8,** e62918 (2013).
69. Hajj, B. *et al.* Whole-cell, multicolor superresolution imaging using volumetric multifocus microscopy. *Proc. Natl Acad. Sci. USA* **111,** 17480–17485 (2014).

Acknowledgements

We thank D. Perrais, M. Missler, S. Okabe, P. Scheiffele, T. Dresbach and A. Ting for the generous gift of DNA plasmids; F. Neca and Z. Karatas for molecular biology; the Cell culture facility of the Institute (especially E. Verdier and P. Durand) ; the animal facility of the University of Bordeaux (in particular A. Lacquemant and A. Gautier); the biochemistry facility of Bordeaux Neurocampus; J. Gilardin for the technical support; G. Giannone and O. Rossier for helpful advice and preliminary experiments; the Bordeaux Imaging Center, in particular P. Legros for STED microscopy; and C. O'Hare for critical reading of the initial manuscript. This work received funding from the Centre National de la Recherche Scientifique, Agence Nationale pour la Recherche (grants Synapse-2Dt, Nanodom and SynAdh), Conseil Régional Aquitaine, Fondation pour la Recherche Médicale and the national infrastructure France BioImaging (grant ANR-10INBS-04-01).

Author contributions

I.C., M.S. and O.T. designed research and wrote the article. O.T. did initial proof-of-concept experiments and I.C. performed all subsequent imaging experiments. M.L. provided electroporated organotypic brain slices. C.B. and I.C. performed dSTORM experiments and analysis. B.T. and I.G. generated DNA constructs. B.T. performed biochemistry experiments. K.H.L. and S.P. provided the initial constructs of mSA. I.G., I.C. and M.S. produced and labelled protein probes. J.-B.S. provided the STORM set-up and software for single-molecule analysis. M.S. and O.T. coordinated and oversaw the research project. All authors discussed the results and commented on the manuscript.

Additional information

Supplementary Information accompanies this paper at http://www.nature.com/naturecommunications

Competing financial interests: The authors declare no competing financial interests.

Reprints and permission information is available online at http://npg.nature.com/reprintsandpermissions/

How to cite this article: Chamma, I. *et al.* Mapping the dynamics and nanoscale organization of synaptic adhesion proteins using monomeric streptavidin. *Nat. Commun.* 7:10773 doi: 10.1038/ncomms10773 (2016).